



Journal of Science

Volume: 17, Issue: 1, Year: 2021

Contact

Manisa Celal Bayar University

Institute of Natural and Applied Sciences

Campus of Şehit Prof Dr İlhan Varank 45140 Yunusemre – MANİSA, TURKEY

Tel: (00 90) 236 201 27 05

Fax: (00 90) 236 241 21 49

e-mail: cbujos@gmail.com

Web: <http://dergipark.gov.tr/cbayarfbe>

“CBU Journal of Science is indexed by ULAKBIM-TUBITAK TR-DIZIN”



ISSN 1305-130X

E-ISSN 1305-1385

CBUJOS is published quarterly at Manisa Celal Bayar University Printing House

“CBU Journal of Science is a refereed scientific journal”



Celal Bayar University Journal of Science

Owner

Manisa Celal Bayar University,

Editors : Assoc. Prof. Dr. Kamil ŞİRİN

Assoc. Prof. Dr.. Emine KEMİKLİOĞLU

Assistant Editor: Assoc. Prof. Dr. Mustafa AKYOL

Layout Editor & Secretary

Dr. İlker Çetin KESKİN

International Scientific Advisory Board

Prof. Dr. Arianit REKA; State University of Tetova, Macedonia

Prof. Dr. Tomasz NIEMIEC; Warsaw University of Life Sciences, Poland

Prof. Dr. Alyani ISMAIL; Universiti Putra, Malaysia

Prof. Dr. Iuliana APRODU; Dunarea de Jos University, Romania

Assoc. Prof. Dr. Johanan Christian PRASANNA; Madras Christian College, South India

Assoc. Prof. Dr. Noureddine ISSAOUI; Université de Monastir, Tunisie.

Assoc. Dr. Edward Albert UECKERMANN; North-West University, South Africa

Assoc. Dr. Zhi-Qiang ZHANG; The University of Auckland, Holland

Assist. Prof. Dr. Young Ki KIM; Pohang University of Science and Technology, South Korea

Assist. Prof. Can BAYRAM; University of Illinois, USA

Assist. Prof. Dr. Mona MIRHEYDARI; Rutgers University, USA

Assist. Prof. Dr. Donatella ALBANESE; Università Degli Studi Di Salerno, Italy

Assist. Prof. Dr. Jinghua JIANG; The University of Memphis, USA

Assist. Prof. Dr. Jens OLDELAND; University of Hamburg, Germany

Dr. Cheng CHENG; Apple Inc., USA

Dr. Sajedah AFGHAH; Microsoft Corporation, USA

Dr. Jinghua JIANG; The University of Memphis

National Scientific Advisory Board

Prof. Dr. Mustafa Ersöz; Selçuk University

Prof. Dr. Oğuz Gürsoy; Mehmet Akif University

Prof. Dr. Mehmet Çevik; İzmir Katip Çelebi University

Prof. Dr. Sezgin Çelik; Yıldız Teknik University

Prof. Dr. Osman Dayan; Çanakkale Onsekiz Mart University

Prof. Dr. Serdar İplikçi; Pamukkale University

Prof. Dr. Yasin Üst; Yıldız Teknik University

Prof. Dr. Mahmut Kuş; Konya Teknik University

Prof. Dr. Ertuğ Gundüz; Hacettepe University

Prof. Dr. Tülin Aydemir; Manisa Celal Bayar University

Prof. Dr. Sezai Taşkın; Manisa Celal Bayar University

Prof. Dr. Fatma Şaşmaz Ören; Manisa Celal Bayar University

Assoc. Prof. Dr. Fatih Doğan; Çanakkale Onsekiz Mart University

Assoc. Prof. Dr. Erol Akpınar; Abant İzzet Baysal University

Assoc. Prof. Dr. Yeliz Yıldırım; Ege University

Assoc. Prof. Dr. Serap Derman; Yıldız Teknik University

Assoc. Prof. Dr. Hayati Mamur; Manisa Celal Bayar University

Assoc. Prof. Dr. Fatih Selimefendigil; Manisa Celal Bayar University

Assoc. Prof. Dr. Özlem Çağındı; Manisa Celal Bayar University

Assoc. Prof. Dr. Osman Çulha; Manisa Celal Bayar University

Assoc. Prof. Dr. Ali Demir; Manisa Celal Bayar University

Assoc. Prof. Dr. Ali Konuralp; Manisa Celal Bayar University

Assist. Prof. Dr. Nil Mansuroğlu; Ahi Evran University

Assist. Prof. Dr. Zeynep Çipiloğlu Yıldız; Manisa Celal Bayar University



CBU Journal of Science

Celal Bayar University Journal of Science (CBUJOS) covers scientific studies in the fields of Engineering and Science and publishes accounts of original research articles concerned with all aspects of experimental and theoretical studies. CBU Journal of Science is a refereed scientific journal published four times annually (March, June, September and December) by Institute of Natural and Applied Sciences of Manisa Celal Bayar University. CBU Journal of Science considers the original research articles written in English for evaluation.

CBU Journal of Science is indexed by TUBİTAK ULAKBİM TR-DİZİN, EBSCOhost and also is included in DOAJ, Cite Factor, Journal TOCS, Advanced Science Index and OAJI databases. Digital Object Identifier (DOI) number will be assigned for all the articles being published in CBU Journal of Science.

Instructions for Authors and Article Template can be found on the main page of MCBU Institute of Natural and Applied Sciences (<http://fbe.cbu.edu.tr>)





Vol: 17, Issue: 1, Year: 2021

Contents

Research Article

Pages

Thermal Behaviours of Flower Shape BSA@Cu(II) Hybrid Nanostructures DOI: 10.18466/cbayarfbe.811643 Burcu Somtürk Yılmaz , Serkan Dayan, Cevahir Altınkaynak, Nilgün Kalaycıoğlu Özpozan, Nalan Özdemir	1-9
Newly Axially Silicon (IV) Phthalocyanine Photosensitizer: Design, Synthesis and Photo-chemical Properties DOI: 10.18466/cbayarfbe.821910 Gülçin Ekiner, Hülya Yanık	11-16
The Impact of European Green Deal on Turkey's Iron and Steel Industry: Decomposition Analysis of Energy-Related Sectoral Emissions DOI: 10.18466/cbayarfbe.823265 Abdulkadir Bektaş	17-29
Modeling of Inverse Kinematic Analysis of Open-Source Medical Assist Robot Arm by Python DOI: 10.18466/cbayarfbe.776697 Mehmet Gül	31-34
Static Analysis of the Slotted Upper Plate of Low Pressure Casting Machine DOI: 10.18466/cbayarfbe.779687 Yasemin Nur Aydın, Onur Özaydın, Alper Akış	35-41
Effect of Meteorological Parameters on PM10 Concentrations in Ardahan by Wavelet Coherence Analysis DOI: 10.780314/cbayarfbe.738596 Necla Barlık	43-49
The Effect of Addition of ZnO to Granite Body on Sintering and Mechanical Properties DOI: 10.18466/cbayarfbe. 814870 Savaş Elmas	51-57
Boole approximation method with residual error function to solve linear Volterra integro-differential equations DOI: 10.801544/cbayarfbe.791302 Kübra Erdem Biçer, Hale Gül Dağ	59-66
Existence and Uniqueness Results for a Computer Virus Spreading Model with Atangana-Baleanu Derivative DOI: 10.18466/cbayarfbe.716573 Sümeysra Uçar	67-72
Attenuation of Docetaxel-induced Oxidative Stress and Apoptosis in HEK 293 Human Embryonic Kidney Cells by Curcumin Treatment DOI: 10.18466/cbayarfbe.752495 Süleyman İlhan	73-78
Filler Type and Particle Distribution Effect on Some Properties of Polymer Composites DOI: 10.18466/cbayarfbe. 787883 Bayram Poyraz, Şevki Eren, Serkan Subaşı	79-89



Evaluation of the Bearing Capacity of Shallow Strip Foundations Resting on Sandy Soils with Analytical and Numerical Methods

DOI: 10.18466/cbayarfbe.705653

Emrah Dađlı, Ömer Faruk Çapar

91-100






Metakaolin and Red-Mud Based Geopolymer: Resistance to Sodium and Magnesium Sulfate Attack

DOI: 10.18466/cbayarfbe.790946

Ouiame Chakkor, Mehmet Fatih Altan, Orhan Canpolat

101-113

Thermal Behaviours of Flower Shape BSA@Cu(II) Hybrid Nanostructures

Burcu Somtürk Yılmaz¹, Serkan Dayan², Cevahir Altinkaynak³, Nilgün Kalaycıoğlu Özpozan¹, Nalan Özdemir^{1*}

¹Department of Chemistry, Faculty of Science, Erciyes University, 38039 Kayseri, Turkey

²Drug Application and Research Center, Erciyes University, 38280 Kayseri, Turkey

³Department of Plant and Animal Production, Avanos Vocational School, Nevşehir Hacı Bektaş Veli University, 50500 Nevşehir, Turkey

*ozdemir@erciyes.edu.tr

*Orcid: 0000-0002-8930-5198

Received: 16 October 2020

Accepted: 3 March 2021

DOI: 10.18466/cbayarfb.811643

Abstract

In this study, flower shape hybrid protein-inorganic hybrid nanostructures were synthesized using a common protein (bovine serum albumin, BSA) and metal ion (Cu^{2+}) at different protein concentrations (0.01, 0.02, 0.05, and 0.1 mg mL⁻¹) and pHs (PBS pH:6-9) at +4 °C for investigation of thermal properties the first time in detail. These synthesized protein-inorganic hybrid nanostructures (BSA-Cu₃(PO₄)₂. 3H₂O hNFs) were defined using SEM, EDX, elemental mapping XRD, FTIR, etc. Morphologies of BSA-Cu₃(PO₄)₂.3H₂O hNFs were characterized by SEM. Element analysis of BSA-Cu₃(PO₄)₂.3H₂O hNFs was achieved by EDX. Peak positions of BSA-Cu₃(PO₄)₂. 3H₂O hNFs were investigated using XRD. And, the FTIR technique was used to substantiate the creation of hNFs. Also, the thermal behavior such as glass transition and crystallization of BSA-Cu₃(PO₄)₂.3H₂O hNFs were investigated in detail using thermal gravimetric analysis (TGA).

Keywords: BSA, Copper phosphate, Hybrid nanoflowers, Thermal analysis

1. Introduction

Protein-inorganic hybrid nanostructures obtained from biomolecules and metal ions are a material that focuses on biological and chemical applications. Furthermore, bioinorganic hybrid nanostructures can show not only a combination of properties of different components but also synergistic properties resulting from the interplay between biological molecules and inorganic substances [1-4]. Because of the unified structural properties and functional practices of biomolecules and nanomaterials, particular attention is paid to the production of bioinorganic hybrids owing to their high composition elasticity and good biocompatibility [5-9].

Nanoflower can be distinguished among nanomaterials by their properties. These nanostructures have attracted the attention of scientists because of the properties of the nano-layers, which let a higher surface-to-volume rate comparatively traditional spherical nanoparticle [10].

Recently there has been a noticeable increase in the synthesis of hybrid nanostructures. In 2012, Zare et al. firstly synthesized the protein-inorganic hybrid nanostructures and reported the formation method of flower-like protein-inorganic hybrid nanostructures using Cu (II) ion as inorganic component and some proteins and enzymes (lactalbumin, laccase, carbonic anhydrase, lipase, and BSA) as an organic component [11]. Flower-shaped hybrid nanostructures are created as a result of a hierarchical unit of nano-sized leaf-shaped structures and growth mechanisms. These nano-sized leaf-shaped structures come together to connect and form structures with flower-like shapes. For this reason, the synthesized structures were named "flower-shaped nanostructures" (Nanoflowers).

In recent years, many studies have been carried out using some small or macromolecules (biomolecules) such as proteins, enzymes, DNA, etc. for synthesis of organic-inorganic hybrid nanomaterials [12-16] Bovine serum albumin (BSA) was used as a protein in some of these studies for different purposes. Yılmaz et al., synthesized BSA-Cu (II) hybrid nanoflowers (BSA-

hNF), and these synthesized structures were used as adsorbents for the detection of cadmium and lead ions in various samples such as hair, food [17]. Zhang et al., synthesized BSA/Zn₃(PO₄)₂ hybrid materials. Then, these synthesized structures were used for the adsorption of Cu²⁺ [18]. Zhang et al., Mn₃(PO₄)₂@BSA hybrid nanoflower synthesized used as a new support material [19].

Although there are many studies on protein-inorganic hybrid nanoflowers, there are very few studies on the thermal behavior of these hybrid nanoflowers [20, 21]. Song et al. reported a new and easy method for the synthesis of flower-like cobalt phosphate nanocrystals (Co₃(PO₄)₂ nanoflowers). Subsequently, they formed an excellent nano biocatalyst system through biomimetic mineralization of cobalt phosphate with Co-type nitrile hydratase (NHase). The encapsulated NHase (NHase@Co₃(PO₄)₂) showed high catalytic efficiencies and stability. They examined the thermal properties of the synthesized nanocrystals. According to the TGA curve, when the temperature rose above 100 °C, there was a sudden tilt due to the water loss of the crystal. However, the NHase@Co₃(PO₄)₂ curve fell again in the 200-350 °C range due to the degradation of the proteins, confirming the successful incorporation of NHase. Munyemana et al. synthesized protein-inorganic hybrid materials with hierarchical nanostructures. They used manganese as the inorganic component and collagen as protein. The as-prepared CL-Mn₃(PO₄)₂ nanoflowers exhibited good catalytic activity towards water oxidation. At the same time, Thermogravimetric analysis (TGA) was performed under a nitrogen atmosphere, employing a heating rate of 10 °C min⁻¹ from 25 °C to 500 °C.

The thermal properties of BSA@inorganic hybrid nanostructures (BSA-Cu₃(PO₄)₂.3H₂O hNFs) have not been studied. In our study, for the first time, the thermal behavior of BSA-Cu₃(PO₄)₂.3H₂O hybrid nanoflowers was investigated using TGA. At the same time, these synthesized hybrid nanoflowers were characterized by SEM, EDX, FTIR, elemental mapping, and XRD analysis.

2. Materials and Methods

2.1. Materials

All chemical reagents were analytically pure. Bovine serum albumin (lyophilized powder) and Copper (II) sulfate pentahydrate (CuSO₄·5H₂O), potassium phosphate dibasic (KH₂PO₄), calcium chloride dihydrate (CaCl₂·2H₂O), magnesium chloride (MgCl₂·6H₂O), sodium chloride (NaCl), potassium chloride (KCl), sodium phosphate (Na₂HPO₄) were obtained from Sigma-Aldrich. In all experiments, pure water was used.

2.1.1. Preparation of flower shape protein-inorganic hybrid nanoflowers (BSA@Cu₃(PO₄)₂.3H₂O hNFs)

BSA@Cu₃(PO₄)₂.3H₂O hNFs were fabricated using available methods [22-26]. Initial, CuSO₄·5H₂O stock solution (120 mM) was prepared made ready using pure water. Later, certain volume of this solution was added to 8 mL of 10 mM PBS solution (pH:6-9) including at different concentrations BSA (0.01- 0.1 mg/mL). These mixtures were strongly vortexed 30 s and then were incubated for 3 days at 4 °C. Following incubation, each reaction tube was centrifuged throughout for 20 min at 6,500 rpm. Finally, the collected hNFs were dried at room temperature.

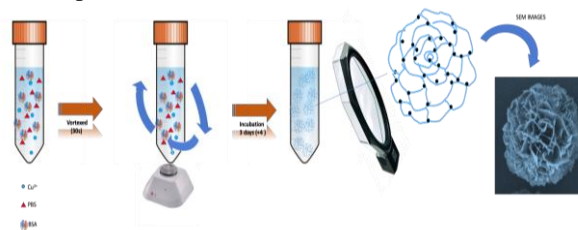


Fig 1. A synthesis scheme of BSA@Cu₃(PO₄)₂.3H₂O hNFs.

2.1.2. Characterization of BSA@Cu₃(PO₄)₂.3H₂O hNFs

The morphologies of the BSA@Cu₃(PO₄)₂.3H₂O hybrid nanoflowers were achieved using Scanning electron microscopy (SEM) (ZEISS EVO LS10). The powder diffraction spectra of the synthesized nanoflowers were determined with X-ray diffraction analysis (XRD) (BRUKER AXS D8). For determining weight and atomic percentage of elements such as Cu, N, P, O, Cl in BSA@Cu₃(PO₄)₂.3H₂O hNFs were used

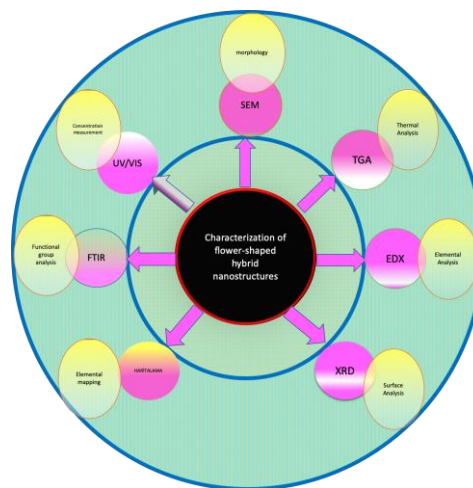


Fig 2. Characterization scheme of BSA@Cu₃(PO₄)₂.3H₂O hNFs.

Energy-dispersive X-ray (EDX) (ZEISS EVO LS10). Bond vibration of hNFs was investigated using the Fourier Transform Infrared Spectroscopy (FTIR) (Perkin Elmer Spectrum 400) spectrum. The thermal properties of BSA@Cu₃(PO₄)₂.3H₂O hNFs were investigated utilizing TGA (Perkin Elmer Diamond).

2.1.3. Determination of thermal properties of BSA@Cu₃(PO₄)₂·3H₂O hNFs hybrid Nanoflowers

The thermal properties of BSA@Cu₃(PO₄)₂·3H₂O hNFs were investigated utilizing TGA (Perkin Elmer Diamond). The scanning temperature for each sample was adjusted from 50 °C to 1200 °C (rate of 15 °C min⁻¹).

3. Results and Discussion

3.1. Preparation and characterization of BSA@Cu₃(PO₄)₂·3H₂O hNFs

BSA@Cu₃(PO₄)₂·3H₂O hNFs were prepared by mixing Cu²⁺ ions and BSA at +4 °C for 3 days in PBS solution (Figure 1). The nucleation and growth phase, which are important in BSA@Cu₃(PO₄)₂·H₂O hNFs formation, are briefly discussed. In nucleation phase, Cu²⁺ ions react with phosphate groups to form copper phosphate nanocrystals. Then, the amine groups in the protein molecules (BSA) are connected to the Cu²⁺ ions through the coordination reaction to start nucleation. In the growth phase, anisotropic growth occurs and hNFs are formed completely.

The morphologies and elemental mapping of hNFs were defined using SEM. Chemical and crystal structures of hNFs were defined using FTIR, EDX, and XRD techniques. To sight the formation of nanoflowers, SEM images of the hNFs were taken.

BSA@Cu₃(PO₄)₂·3H₂O hNFs were synthesized at different pH (pH: 6-10) and concentrations (0.01, 0.02, 0.05 and 0.1, mg mL⁻¹) at +4°C. And the differences in the morphology of the synthesized the hNFs were examined by SEM images (Figure 3-7).

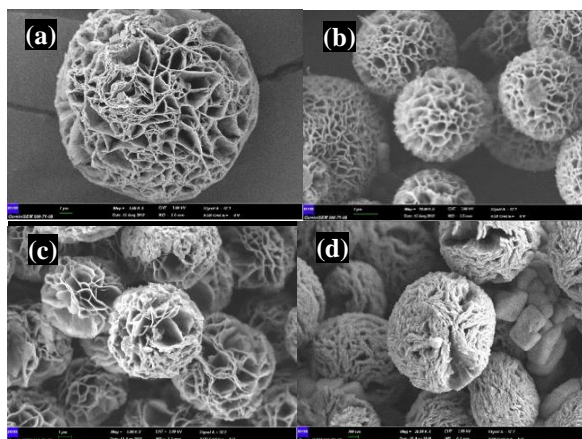


Fig 3. SEM images of BSA@Cu₃(PO₄)₂·3H₂O hNFs prepared at different protein concentrations (pH:6) a) 0.01 mg/mL b) 0.02 mg/mL c) 0.05 mg/mL d) 0.1 mg/mL.

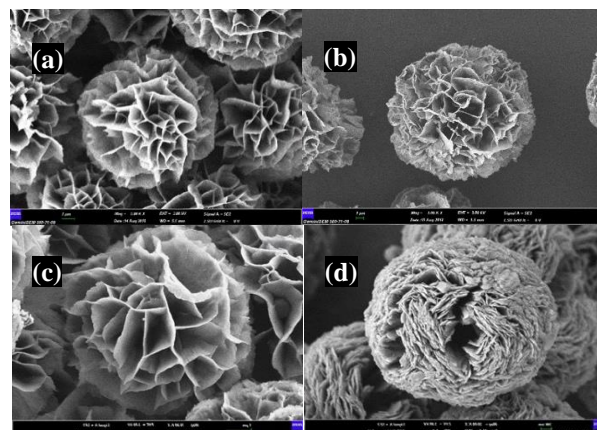


Fig 4. SEM images of BSA@Cu₃(PO₄)₂·3H₂O hNFs prepared at different protein concentrations (pH:7.4) a) 0.01 mg/mL b) 0.02 mg/mL c) 0.05 mg/mL d) 0.1 mg/mL.

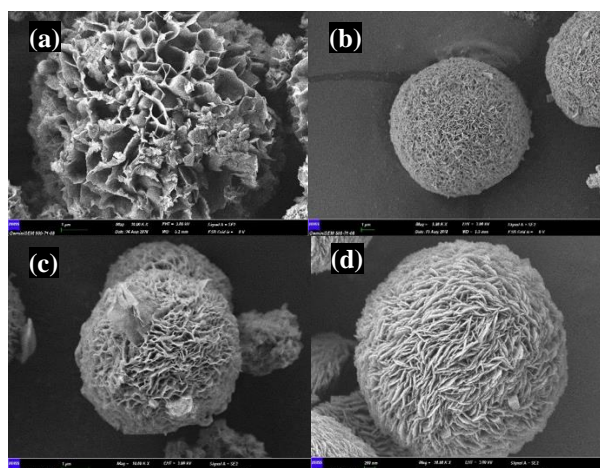


Fig 5. SEM images of BSA@Cu₃(PO₄)₂·3H₂O hNFs prepared at different protein concentrations (pH:8) a) 0.01 mg/mL b) 0.02 mg/mL c) 0.05 mg/mL d) 0.1 mg/mL.

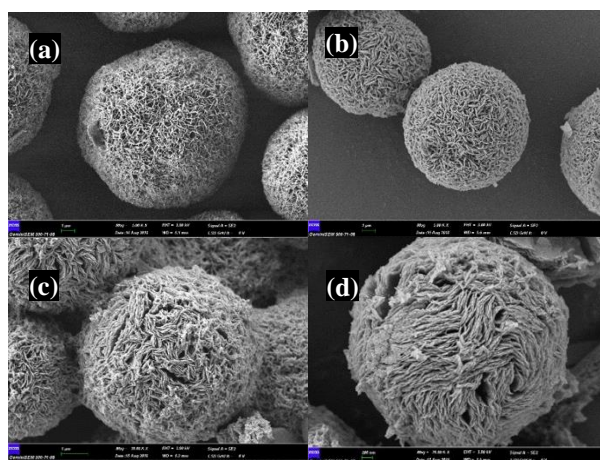


Fig 6. SEM images of BSA@Cu₃(PO₄)₂·3H₂O hNFs prepared at different protein concentrations (pH:9) a) 0.01 mg/mL b) 0.02 mg/mL c) 0.05 mg/mL d) 0.1 mg/mL.

The formations of the $\text{BSA}@Cu_3(\text{PO}_4)_2 \cdot 3\text{H}_2\text{O}$ hNFs were explored using different concentrations of BSA ($0.1\text{-}0.01\text{ mg mL}^{-1}$) and pHs (pH:6-10). When BSA concentration decreases from 0.1 to 0.01 mg mL^{-1} were observed significant distinctions in the morphology of $\text{BSA}@Cu_3(\text{PO}_4)_2 \cdot 3\text{H}_2\text{O}$ hNFs (Fig.3-7). However, as the concentration increased, it showed that all leaves were stiffly intertwined and there were no pores, yet cracks occurred over the surfaces of the $\text{BSA}@Cu_3(\text{PO}_4)_2 \cdot 3\text{H}_2\text{O}$ hNF for both concentrations. On the surface of the $\text{BSA}@Cu_3(\text{PO}_4)_2 \cdot 3\text{H}_2\text{O}$ hNFs synthesized in 0.1 mg mL^{-1} BSA concentration, pores were comparatively formed. $\text{BSA}@Cu_3(\text{PO}_4)_2 \cdot 3\text{H}_2\text{O}$ hNFs synthesized in 0.02 mg mL^{-1} and 0.01 mg mL^{-1} BSA concentrations have quite uniform and spherical pores.

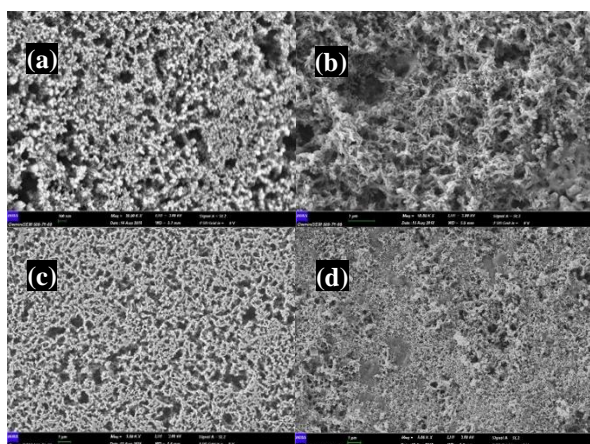


Fig 7. SEM images of $\text{BSA}@Cu_3(\text{PO}_4)_2 \cdot 3\text{H}_2\text{O}$ hNFs prepared at different protein concentrations (pH:10) a) 0.01 mg/mL b) 0.02 mg/mL c) 0.05 mg/mL d) 0.1 mg/mL .

The effect of pH values (pH 6-9) on the morphology of the $\text{BSA}@Cu_3(\text{PO}_4)_2 \cdot 3\text{H}_2\text{O}$ hNFs was investigated. The isoelectric point of BSA used in the study is $\sim 4.5\text{-}5$, and the protein net charge above or below of this value varies positive and negative. The formation of hybrid nanostructures below pH 5 and above pH 10 did not occur. Since pH is above 10, BSA is loaded with a very negative charge, and pH is under 5, with a very positive charge, protein molecules that are highly positive or highly negative repel each other and as a result of this repulsion, the formation of nanostructures is prevented. EDX analysis of $\text{BSA}@Cu_3(\text{PO}_4)_2 \cdot 3\text{H}_2\text{O}$ hNFs synthesized at pH 7.4 at different BSA concentrations is shown in figure 8.

The EDX analysis (Fig. 8) of $\text{BSA}@Cu_3(\text{PO}_4)_2 \cdot 3\text{H}_2\text{O}$ hNFs were performed to determine elemental composition of the hybrid structures. The synthesized HNFs include 2 major components: protein (Bovine serum albumin) and metal phosphate ($\text{Cu}_3(\text{PO}_4)_2 \cdot 3\text{H}_2\text{O}$) nanocrystals. The peak of N and Cu, O and P in the EDX spectrum of the $\text{BSA}@Cu_3(\text{PO}_4)_2 \cdot 3\text{H}_2\text{O}$ hNFs come from BSA and $\text{Cu}_3(\text{PO}_4)_2 \cdot 3\text{H}_2\text{O}$ nanocrystals, respectively.

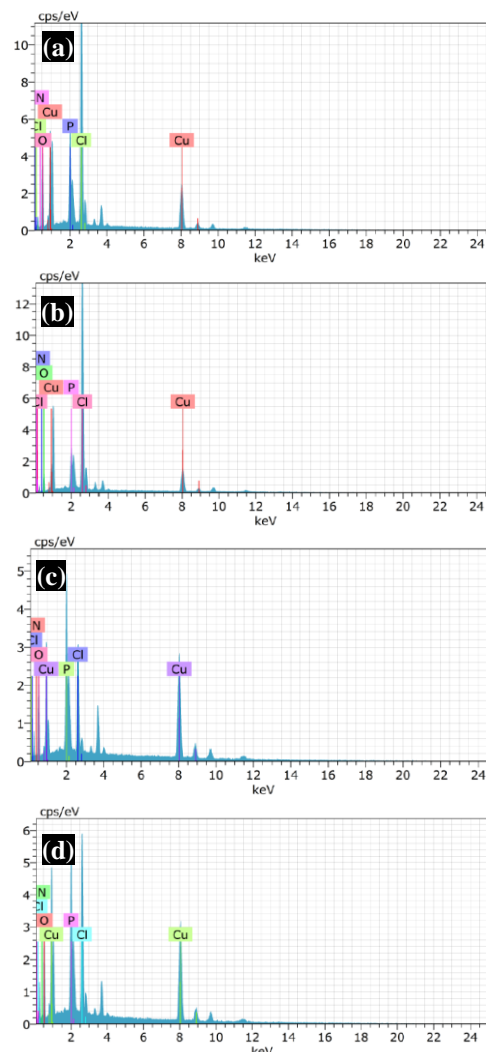


Fig 8. EDX analysis of the $\text{BSA}@Cu_3(\text{PO}_4)_2 \cdot 3\text{H}_2\text{O}$ hNFs synthesized at different BSA concentration a) 0.01 mg/mL , b) 0.02 mg/mL , c) 0.05 mg/mL , d) 0.1 mg/mL .

Table 1. wt % of elements in $\text{BSA}@Cu_3(\text{PO}_4)_2 \cdot 3\text{H}_2\text{O}$ hNFs synthesized at different concentrations.

Element	wt % of elements at different concentrations			
	0.01 mg/mL	0.02 mg/mL	0.05 mg/mL	0.1 mg/mL
N	%5.23	%5.96	%5.88	%6.88
Cu	%25.25	%25.20	%43.14	%37.64
O	%35.50	%21.49	%24.38	%27.68
P	%10.93	%8.69	%16.46	%13.89

Zeta potential measurements of $\text{BSA}@Cu_3(\text{PO}_4)_2 \cdot 3\text{H}_2\text{O}$ hNFs were taken. At pH 6, $\text{BSA}@Cu_3(\text{PO}_4)_2 \cdot 3\text{H}_2\text{O}$ showed a negative load with hNF -19.6 mV zeta potential. The zeta potentials of hNFs at pHs 7.4, 8, and 9 were -27.5 mV, -30.3 mV, and -35.6 mV, respectively.

The chemical structure and formation of the $\text{BSA}@Cu_3(\text{PO}_4)_2 \cdot 3\text{H}_2\text{O}$ hNFs were appraised by using FTIR (PerkinElmer Spectrum 400). The FTIR spectrum revealed the characteristic peaks of $\text{BSA}@Cu_3(\text{PO}_4)_2 \cdot 3\text{H}_2\text{O}$ hNFs (Fig. 9).

The FTIR spectrum revealed $\text{BSA}@Cu_3(\text{PO}_4)_2 \cdot 3\text{H}_2\text{O}$ hNFs characteristic peaks (Figure 9). The bending vibrations of $\text{O}=\text{P}=\text{O}$ groups were observed between ~ 535 cm^{-1} and ~ 557 cm^{-1} . $\text{P}=\text{O}$ and $\text{P}-\text{O}$ stretching bands appeared at ~ 926 cm^{-1} and ~ 979 cm^{-1} . The typical BSA's vibration bands at ~ 1520 - 1640 cm^{-1} belong to the NH_2 groups and the stretching bands at 3048 - 3300 cm^{-1} are connected to the CH_2 and CH_3 groups.

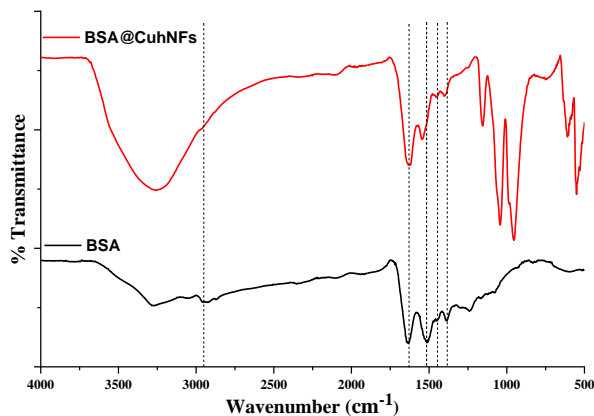


Fig 9. FTIR spectra of BSA and $\text{BSA}@Cu_3(\text{PO}_4)_2 \cdot 3\text{H}_2\text{O}$ hNFs.

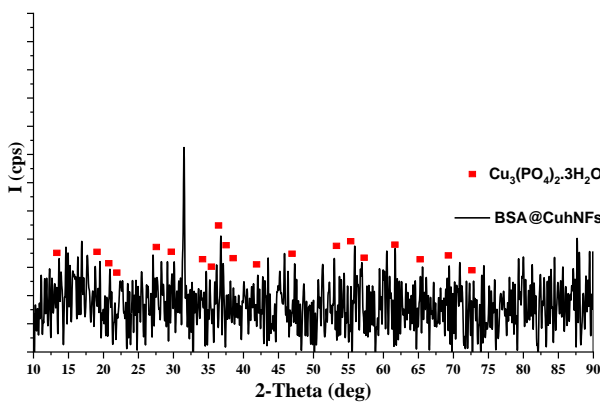


Fig 10. X-ray diffraction patterns of $\text{BSA}@Cu_3(\text{PO}_4)_2 \cdot 3\text{H}_2\text{O}$ hNFs [black line, $Cu_3(\text{PO}_4)_2 \cdot 3\text{H}_2\text{O}$, JCPDS card (00-022-0548)].

Also, $\text{BSA}@Cu_3(\text{PO}_4)_2 \cdot 3\text{H}_2\text{O}$ hNFs were characterized using XRD analysis (Fig. 10). The crystal structure of hNFs were brighten with the diffraction peaks of $Cu_3(\text{PO}_4)_2 \cdot 3\text{H}_2\text{O}$ in the $\text{BSA}@Cu_3(\text{PO}_4)_2 \cdot 3\text{H}_2\text{O}$ hNFs, which were compatible with them of JCPDS card (00-022-0548).

It is seen from Fig. 11, Cu, N, O, and P elements are homogeneously distributed inside the $\text{BSA}@Cu_3(\text{PO}_4)_2 \cdot 3\text{H}_2\text{O}$ hNFs

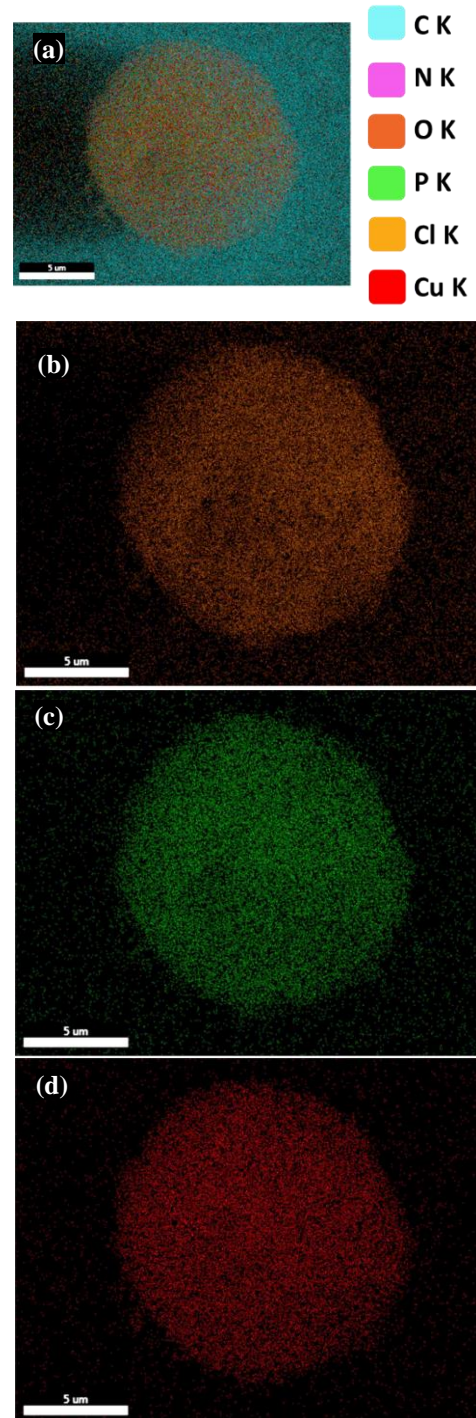


Fig 11. Elemental mapping of $\text{BSA}@Cu_3(\text{PO}_4)_2 \cdot 3\text{H}_2\text{O}$ hNFs a) mix, b) O, c) P, d) Cu

3.2. Thermal Studies of BSA@Cu₃(PO₄)₂.3H₂O hNFs

Thermal analysis studies were performed to confirm the optimum conditions of the fabricated hybrid nanoflowers at different concentrations of BSA and pH.

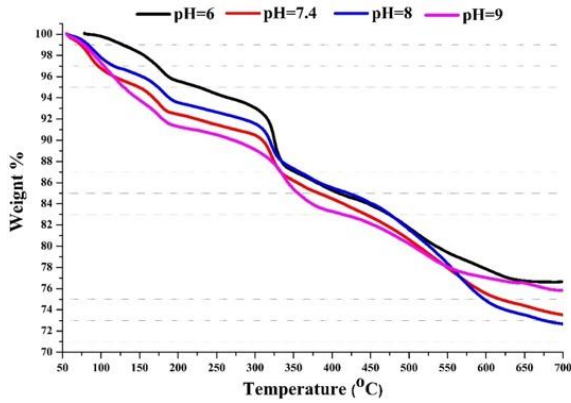


Fig 12. TGA results of the synthesized BSA@Cu₃(PO₄)₂.3H₂O hNFs with different pH at 0.01 mg/mL BSA concentration.

Table-2.TGA data of the synthesized BSA@Cu₃(PO₄)₂.3H₂O hNFs (0.01 mg/mL)

Hybrid Nanoflowers	Step	DTG _{max} / °C	T _{on} ^o C	T _{end} ^o C	Mass loss/ %
BSA@Cu ₃ (PO ₄) ₂ .3H ₂ O hNFs (0.01mg/mL), pH=6	I	133	78.6	214.3	4.72
	II	324	214.3	353.3	8.32
	III	506	353.3	644.6	10.19
	IV	-	644.6	700.0	0.12
BSA@Cu ₃ (PO ₄) ₂ .3H ₂ O hNFs (0.01mg/mL), pH=7.4	I	93	61.7	122.6	3.79
	II	167	122.6	204.9	3.46
	III	318	204.9	362.4	6.67
	IV	524	362.4	636.9	11.05
	V	-	636.9	700.0	1.12
BSA@Cu ₃ (PO ₄) ₂ .3H ₂ O hNFs 0.01mg/mL), pH=8	I	102	63.2	128.9	3.11
	II	173	128.9	221.4	3.53
	III	316	221.4	373.1	6.79
	IV	516	373.1	623.4	12.34
	V	-	623.4	700.0	1.39
BSA@Cu ₃ (PO ₄) ₂ .3H ₂ O hNFs (0.01mg/mL), pH=9	I	131	58.6	212.8	8.70
	II	314	212.8	389.3	7.60
	III	489	389.3	573.2	6.22
	IV	-	573.2	700.0	1.45

* T_{on} – thermal degradation onset temperature, T_{max} – maximum weight loss temperature, T_{end} – final thermal degradation temperature

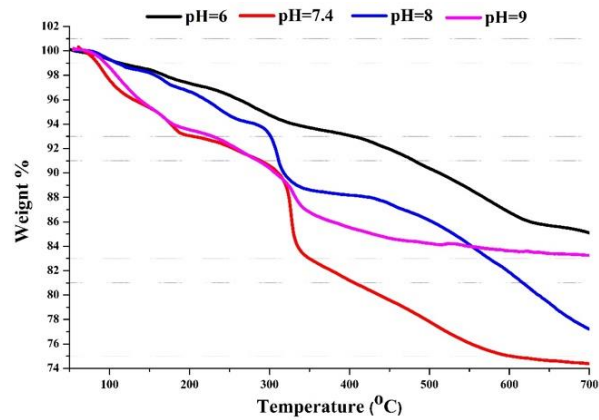


Fig 13. TGA results of the synthesized BSA@Cu₃(PO₄)₂.3H₂O hNFs with different pH at 0.02 mg/mL BSA concentration.

Table-3.TGA data of the synthesized BSA@Cu₃(PO₄)₂.3H₂O hNFs (0.02 mg/mL)

Hybrid Nanoflowers	Step	DTG _{max} / °C	T _{on} ^o C	T _{end} ^o C	Mass loss/ %
BSA@Cu ₃ (PO ₄) ₂ .3H ₂ O hNFs (0.02mg/mL), pH=6	I	231	68.5	360.9	6.30
	II	528	360.9	643.9	7.80
	III	-	643.9	700.0	0.68
BSA@Cu ₃ (PO ₄) ₂ .3H ₂ O (0.02mg/mL), pH=7.4	I	109	73.6	120.3	3.36
	II	180	120.3	220.0	3.62
	III	322	220.0	366.8	10.41
	IV	498	366.8	611.7	7.46
	V	-	611.7	700.0	0.53
BSA@Cu ₃ (PO ₄) ₂ .3H ₂ O (0.02mg/mL), pH=8	I	194	81.2	253.6	5.31
	II	304	253.6	351.9	6.00
	III	545	351.9	700.0	11.39
BSA@Cu ₃ (PO ₄) ₂ .3H ₂ O (0.02mg/mL), pH=9	I	125	86.5	200.8	5.97
	II	272	200.8	356.3	6.95
	III	485	356.3	700.0	3.32

* T_{on} – thermal degradation onset temperature, T_{max} – maximum weight loss temperature, T_{end} – final thermal degradation temperature

According to SEM analysis and literature information, BSA@Cu₃(PO₄)₂.3H₂O hNFs in the optimum conditions were prepared as pH:7.4 and 0.02 mg/ml BSA concentration. Of course, this result was obtained to obtain the nanoflower structure in a smooth morphology and we determined the thermal behavior of the same materials in this study. The pH values were used as 6, 7.4, 8, and 9, as well as, the BSA concentrations were also screened as 0.01, 0.02, 0.05, and 0.1 mg/ml. Also, thermal decomposition steps and thermal degradation onset temperature (T_{on}), and final thermal degradation temperature (T_{end}) of decomposition temperatures were determined. The screening temperature range for

materials degraded in 4 steps as generally was carried out between 50 to 700 °C. The common result of all thermal curves is that the degradation steps of the materials produced at pH 7.4 are more pronounced and orderly and, the irregularities in thermal curves were observed with increasing BSA concentration

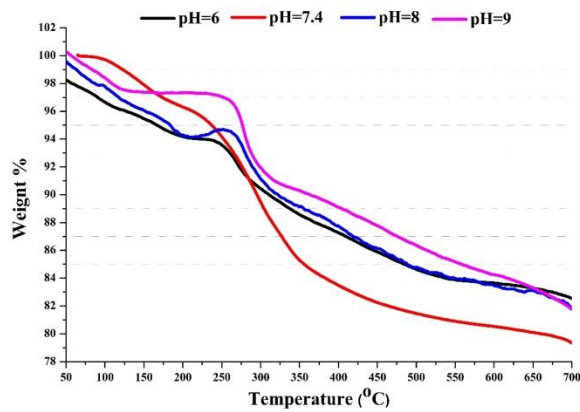


Fig 14. TGA results of the synthesized BSA@Cu₃(PO₄)₂.3H₂O hNFs with different pH at 0.05 mg/mL BSA concentration.

Table-4. TGA data of the synthesized BSA@Cu₃(PO₄)₂.3H₂O hNFs (0.05 mg/mL)

Hybrid Nanoflowers	Step	DTG _{max} / °C	T _{on} ^o C	T _{end} ^o C	Mass loss/ %
BSA@Cu ₃ (PO ₄) ₂ .3H ₂ O (0.05mg/mL), pH=6	I	120	57.4	202.1	3.84
	II	261	202.1	295.5	3.52
	III	387	295.5	539.8	6.67
	IV	540	539.8	700.0	1.45
BSA@Cu ₃ (PO ₄) ₂ .3H ₂ O (0.05mg/mL), pH=7.4	I	141	85.5	197.9	3.54
	II	288	197.9	437.6	13.86
	III	482	437.6	700.0	3.20
BSA@Cu ₃ (PO ₄) ₂ .3H ₂ O (0.05mg/mL), pH=8	I	127	52.5	204.6	5.23
	II	287	204.6	339.3	4.80
	III	517	339.3	700.0	7.57
BSA@Cu ₃ (PO ₄) ₂ .3H ₂ O (0.05mg/mL), pH=9	I	88	57.3	124.1	2.43
	II	283	124.1	347.9	7.22
	III	546	347.9	700.0	8.59

* T_{on} – thermal degradation onset temperature, T_{max} – maximum weight loss temperature, T_{end} – final thermal degradation temperature

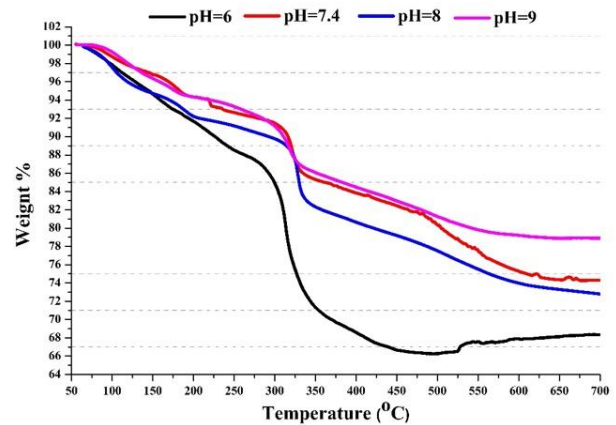


Fig 15. TGA results of the synthesized BSA@Cu₃(PO₄)₂.3H₂O hNFs with different pH at 0.1 mg/mL BSA concentration.

Table-5. TGA data of the synthesized BSA@Cu₃(PO₄)₂.3H₂O hNFs (0.1 mg/mL)

Hybrid Nanoflowers	Step	DTG _{max} / °C	T _{on} ^o C	T _{end} ^o C	Mass loss/ %
BSA@Cu ₃ (PO ₄) ₂ .3H ₂ O (0.1mg/mL), pH=6	I	164	68.3	250.6	11.45
	II	313	250.6	354.2	17.52
	III	425	354.2	700.0	2.64
BSA@Cu ₃ (PO ₄) ₂ .3H ₂ O (0.1 mg/mL), pH=7.4	I	176	74.8	267.8	7.60
	II	320	267.8	409.5	8.66
	III	524	409.5	700.0	9.29
BSA@Cu ₃ (PO ₄) ₂ .3H ₂ O (0.1 mg/mL), pH=8	I	97	64.3	129.8	4.45
	II	180	129.8	220.5	3.66
	III	327	220.5	366.9	10.08
	IV	497	366.9	700.0	8.90
BSA@Cu ₃ (PO ₄) ₂ .3H ₂ O (0.1 mg/mL), pH=9	I	135	76.7	201.3	5.69
	II	304	201.3	359.5	8.56
	III	473	359.5	700.0	6.84

* T_{on} – thermal degradation onset temperature, T_{max} – maximum weight loss temperature, T_{end} – final thermal degradation temperature

According to the obtained thermal analyses data, the TGA degradation step took place generally in the IV - V step and the decomposition temperatures were obtained in approximately the same regions for all nanomaterials. Then, the TG curve of the selected BSA@Cu₃(PO₄)₂.3H₂O hNFs (0.02 mg/mL) material for the most ideal nanoflower production was realized similar to the others. Also, the produced hNFs at pH 7.4 were noted to have more regular and gradual degradation among themselves.

4. Conclusion

Herein, flower shape hybrid protein-inorganic nanostructures (BSA-Cu₃(PO₄)₂. 3H₂O hNFs) were synthesized using BSA and Cu²⁺ ions at different protein concentrations and pHs at +4 °C. This synthesized BSA-Cu₃(PO₄)₂.3H₂O hNFs were defined using SEM, EDX, elemental mapping XRD, FTIR, etc. Also, using thermal gravimetric analysis (TGA) was investigated by the thermal behavior of nanoflowers. Thermal analyses of the synthesized BSA@Cu₃(PO₄)₂.3H₂O hNFs were examined as a detailed parameter.

Acknowledgement

This study was conducted at the Department of Chemistry, Erciyes University, and was supported by Erciyes University Scientific Research Projects Unit with the project coded FDK-2016-6637.

Author's Contributions

Burcu Somtürk Yılmaz: Conceptualization, Methodology, Validation, Formal analysis, Investigation, Writing - original draft, Writing - review & editing.

Serkan Dayan: Conceptualization, Methodology, Validation, Formal analysis, Investigation, Writing - original draft, Writing - review & editing.

Cevahir Altınkaynak: Conceptualization, Methodology, Validation, Formal analysis, Investigation, Writing - original draft, Writing - review & editing.

Nilgün Kalaycıoğlu Özpozan: Conceptualization, Methodology, Validation, Formal analysis, Investigation, Writing - original draft, Writing - review & editing.

Nalan Özdemir: Conceptualization, Methodology, Validation, Formal analysis, Investigation, Writing - original draft, Writing - review & editing, Supervision. Project administration, Funding acquisition.

Ethics

There are no ethical issues after the publication of this manuscript.

References

1. Cui, J, Jia, S, Organic-inorganic hybrid nanoflowers: A novel host platform for immobilizing biomolecules. *Coordination Chemistry Reviews*, 2017, 352, 249–263.
2. Shcharbin, D, Halets-Bui, I, Abashkin, V, Dzmitruk, V, Loznikova, S, Odabaşı, M, Acet, Ö, Önal, B, Özdemir, N, Shcharbina, N, Bryszewska, M, Hybrid metal-organic nanoflowers and their application in biotechnology and medicine *Colloids and Surfaces B: Biointerfaces*, 2019, 182, 110354.
3. Talens-Perales, D, Fabra, M, Martínez-Argente, L, Marín-Navarro, J, Polaina, J, Recyclable thermophilic hybrid protein-inorganic nanoflowers for the hydrolysis of milk lactose. *International Journal of Biological Macromolecules*, 2020, 15, 602–608.
4. Salehiabar, M, Nosrati, H, Javani, E, Aliakbarzadeh, F, Manjili, H.K, Davaran, S, Danafar, H, Production of biological nanoparticles from bovine serum albumin as controlled release carrier for curcumin delivery, *International Journal of Biological Macromolecules*, 2018, 115, 83–89.
5. Zoubi, W, Muhammad, K, Siti, F, Nisa, N, Young, G, Recent advances in hybrid organic-inorganic materials with spatial architecture for state-of-the-art applications *Progress in Materials Science*, 2020, 112, 100663.
6. Zhang, L, Jin, F, Zhang, T, Zhang, L, Xing, J, Structural influence of graft and block polycations on the adsorption of BSA. *International Journal of Biological Macromolecules*, 2016, 85, 252-257.
7. Nosrati, H, Rakhshbahar, A, Salehiabar, M, Afroogh, S, Manjili, H, Danafar, H, Davaran, S, Bovine serum albumin: An efficient biomacromolecule nanocarrier for improving the therapeutic efficacy of chrysin *Journal of Molecular Liquids*, 2018, 271, 639–646.
8. Canepa, J, Torgerson, J, Kim, D.K, Lindahl, E, Takahashi, R, Whitelock, K, Heying, M, Wilkinson, S.P, Characterizing osmolyte chemical class hierarchies and functional group requirements for thermal stabilization of proteins. *Biophysical Chemistry*, 2020, 264, 106410.
9. Zeng, X, Liu, G, Tao, W, Ma, Y, Zhang, X, He, F, Pan, J, Mei, L, Pan, G, A drug-selfgated mesoporous antitumor nanopatform based on pH-sensitive dynamic covalent bond, *Adanced. Functional Mateials*, 2017, 27, 160-178.
10. Zhu, J, Niu, Y, Li, Y, Gong, Y, Shi, H, Huo, Q, Liu, Y, Xu, Q, Stimuli-responsive delivery vehicles based on mesoporous silica nanoparticles: recent advances and challenges. *Journal of Mathematical Chemistry B*, 2017, 5, 1339–1352.
11. Ge, J, Lei, J, Zare, R.N, Protein inorganic hybrid nanoflowers. *Nature Nanotechnology*, 2012, 7, 428-432.
12. Zhang, B, Li, P, Zhang, H, Wang, H, Li, X, Tian, L, Ali, N, Ali, Z, Zhang, Q, Preparation of lipase/Zn₃(PO₄)₂ hybrid nanoflower and its catalytic performance as an immobilized enzyme, *Chemical Engineering Journal*, 2016, 29, 287–297.
13. Gulmez, C, Altınkaynak, C, Özdemir, N, Atakisi, O, Proteinase K hybrid nanoflowers (P-hNFs) as a novel nanobiocatalytic detergent additive, *International Journal of Biological Macromolecules*, 2018, 119, 803–810.
14. Wu, T, Yang, Y, Cao, Y, Song, Y, Xu, L, Zhang, X, Wang, S, Bioinspired DNA-Inorganic Hybrid Nanoflowers Combined with a Personal Glucose Meter for Onsite Detection of miRNA, *ACS Applied Materials & Interfaces*, 2018, 10, 42050–42057.
15. Dayan, S, Altınkaynak, C, Kayaci, N, Doğan, Ş.D, Özdemir, N, Kalaycıoğlu Ozpozan, N, Hybrid nanoflowers bearing tetraphenylporphyrin assembled on copper(II) or cobalt(II) inorganic material: A green efficient catalyst for hydrogenation of nitrobenzenes in water, *Applied Organometallic Chemistry*, 2020, 34(3), 5381.
16. Aydemir, D, Geçili, F, Özdemir, N, Ulusu, N.N, Synthesis and characterization of a triple enzyme-inorganic hybrid nanoflower (TrpE@ihNF) as a combination of three pancreatic digestive enzymes amylase, protease and lipase, *Journal of Bioscience and Bioengineering*, 2020, 129(6), 679-686.
17. Yılmaz, E, Ocsoy, I, Ozdemir, N, Soylak, M, Bovine serum albumin-Cu(II) hybrid nanoflowers: An effective adsorbent for

- solid phase extraction and slurry sampling flame atomic absorption spectrometric analysis of cadmium and lead in water, hair, food and cigarette samples. *Analytica Chimica Acta*, 2016, 906, 110-117.
18. Zhang, H, Wang, T, Zheng, Y, Yan, C, Gu, W, Ye, L, Comparative toxicity and contrast enhancing assessments of $Gd_2O_3@BSA$ and $MnO_2@BSA$ nanoparticles for MR imaging of brain glioma. *Biochemical and Biophysical Research Communications*, 2018, 499, 488-492.
 19. Zhang, Z, Zhang, Y, He, L, Yang, Y, Liu, S, Wang, M, Fang, S, Fu, G, A feasible synthesis of $Mn_3(PO_4)_2@BSA$ nanoflowers and its application as the support nanomaterial for Pt catalyst. *Journal of Power Sources*, 2015, 284, 170-177.
 20. Song, Y, Gao, J, He, Y, Zhou, L, Ma, L, Huang, Z, Jiang, Y, Preparation of a Flowerlike Nanobiocatalyst System via Biomimetic Mineralization of Cobalt Phosphate with Enzyme. *Industrial & Engineering Chemistry Research*, 2017, 56, 14923-14930.
 21. Munyemanai J, He, H, Ding, S, Yin, J, Xi, P, Xiao, J, Synthesis of manganese phosphate hybrid nanoflowers by collagen-templated biomineralization. *RSC Advances*, 2018, 8, 2708.
 22. Noma, S.A.A, Somtürk Yılmaz, B, Ulu, A, Özdemir, N, Ateş, B, Development of l-asparaginase@hybrid Nanoflowers (ASNase@HNFs) Reactor System with Enhanced Enzymatic Reusability and Stability. *Catalytic Letters*, 2020, DOI: <https://doi.org/10.1007/s10562-020-03362-1>
 23. Somturk, B, Yılmaz, I, Altinkaynak, C, Karatepe, A, Ozdemir, N, Ocsöy, I, Synthesis of urease hybrid nanoflowers and their enhanced catalytic properties. *Enzyme and Microbial Technology*, 2016, 86, 134-142.
 24. Somturk, B, Hancer, M, Ocsöy, I, Özdemir, N, Synthesis of copper ion incorporated horseradish peroxidase-based hybrid nanoflowers for enhanced catalytic activity and stability, *Dalton Transactions*, 2015, 44, 13845–13852.
 25. Altinkaynak, C, Gulmez, C, Atakisi, O, Özdemir, N, Evaluation of organic-inorganic hybrid nanoflower's enzymatic activity in the presence of different metal ions and organic solvents. *International Journal of Biological Macromolecules*, 2020, 164, 162-171.
 26. Altinkaynak, C, Kocazorbaz, E, Özdemir, N, Zihnioglu, F, Egg white hybrid nanoflower (EW-hNF) with biomimetic polyphenol oxidase reactivity: Synthesis, characterization and potential use in decolorization of synthetic dyes. *International Journal of Biological Macromolecules*, 2018, 109, 205–211.

Newly Axially Silicon (IV) Phthalocyanine Photosensitizer: Design, Synthesis and Photo-chemical Properties

Gülçin Ekiner ^{1*} , Hülya Yanık ¹ 

¹Kocaeli University, Center for Stem Cell and Gene Therapies Research and Practice, 41001, Kocaeli, Turkey

* gulcinekiner@gmail.com

* Orcid No: 0000-0003-0999-8586

Received: 5 November 2020

Accepted: 1 March 2021

DOI: 10.18466/cbayarfbe.821910

Abstract

Phthalocyanines as used a photosensitizer in photodynamic therapy, π phthalocyanines exhibit their long wavelength absorption and the ability to produce high singlet oxygen for tumor destruction with 650 to 900 nm fluorescence. In this study, new axially substituted silicon (IV) phthalocyanine (**PS-4**) was synthesized to determine photo-chemical properties using 2-methoxyethanol as an axial ligand to increase singlet oxygen quantum yield. Structural characterization of this new axially substituted silicon (IV) phthalocyanine were performed by IR, mass, ¹H NMR and UV-Vis spectroscopic techniques. As axially substituted silicon (IV) phthalocyanine (**PS-4**) is thought to be a promising PDT agent, photo-chemical properties for cancer treatment with PDT have been investigated.

Keywords: Axially, Silicon (IV) phthalocyanine, Photodynamic Therapy, Photosensitizer

1. Introduction

Photodynamic Therapy (PDT), a cancer treatment method, is alternative to traditional treatment methods (surgery, radiation therapy, chemotherapy). PDT is a triple combination of the photosensitizer (PS), molecular oxygen (O₂) and light of appropriate wavelength. None of these components is toxic by itself. The basis of PDT is photo-chemical reactions induced *via* excitation PS by illumination with appropriate wavelength. Free radicals and singlet oxygen (¹O₂) are formed by the interaction of this PS with molecular oxygen (O₂) [1-3]. They interact with many biological molecules (such as fats, proteins and nucleic acids) cause death in cancer cells through apoptosis or necrosis [4].

Photosensitizers are designed to absorb red light because of the therapeutic window range between 650 nm and 900 nm. [5]. The ideal photosensitizer: *i*) have high light absorption (650-900 nm) *ii*) have high triplet quantum yield, *iii*) have high singlet oxygen quantum yield, *iv*) have high photo stability, *v*) have high selectivity for the target tissue, *vi*) non-toxic at dark conditions *vii*) have quick cleansing from the body after PDT treatment [5].

Phthalocyanines (Pcs) are known as second generation photosensitizers. These compounds are suitable for

substitution to various structures as a chemical modification. They also have intense light absorption at longer wavelengths (650-750 nm) and are capable of producing effective singlet oxygen. Furthermore, due to the high fluorescence properties, these compounds provide follow-up in the body as well as the therapeutic properties are used for the diagnosis of cancer cells [6]. Disadvantages of phthalocyanines are non-solubility in organic solvents and aggregation due to planar ring. Axially, non-peripheral or peripheral substituted phthalocyanines can be designed to get over these disadvantages. The substituents can also affect photo-chemical-physical properties of the Pcs parallel to increasing their solubility [7-9]. Despite all these features and studies, an ideal photosensitizer for PDT still has not found. For this reason, researchers have been studying on phthalocyanine compounds due to its properties as explained above.

Silicon phthalocyanines (SiPcs) have solubility, and can absorb in the near IR region. These molecules are promising photosensitizers as photosensitive substances for PDT [10, 11]. SiPcs also produce a strong absorption peak in the red region in the UV-Vis spectrum, as well as long-lasting triplet state and high singlet oxygen production [12]. The first axially substituted SiPc (Pc4) synthesized as PS and approved for clinical trials [13].

In this study, we studied on axially substituted silicon phthalocyanine set down the effect of ligand for improved the photo-chemical properties for PDT treatment. 2-methoxyethanol was chosen as axial ligand to increase solubility and decrease aggregation. For this purpose, axially substituted SiPc (**PS-4**) was synthesized and characterized. Photo-chemical properties were investigated to conformity PDT.

2. Materials and Methods

2.1. Materials

1,2-dicyanobenzene (1), 1,2,3,4-tetrahydronaphthalene anhydrous 99% (tetralin), silicon tetrachloride 99%, N,N-diisopropylethylamine (hunig's base), tributylamine 99%, 2-methoxyethanol, solvents and chemicals were commercially purchased from Aldrich. All reaction solvents were purified as described by Perrin and Armarego [14]. Mass spectra were recorded using MALDI (matrix assisted laser desorption ionization) using BRUKER Micro-ex LT using 2,5-dihydroxybenzoic acid (DHB) as matrix. The FT-IR spectra were recorded between 4000 and 650 cm^{-1} using a Perkin-Elmer Spectrum 100 FT-IR spectrometer with an attenuated total re-ATR accessory containing zinc selenite (ZnSe) crystal. The electronic absorption spectra in the UV-Vis region were recorded with a Thermo scientific 2001 UV spectrophotometer using a 1 cm quartz cuvette at room temperature. ^1H NMR spectra were recorded in $\text{DMSO}-d_6$ and CDCl_3 solutions on a Varian 400 MHz spectrometer.

2.2. Investigation of Photo-chemical Properties

Photo-chemical properties (singlet oxygen quantum yields and photo-degradation quantum yields) of **PS-4** were investigated with photo-chemical measurement system at Figure 1. For photo-chemical measurements, a 300 W-quartz lamp was used as the light source, a water filter and a 600 nm filter were used to filter ultraviolet and infrared radiation. In addition, for the same purpose, filters which have the appropriate wavelength (670 nm)

for the wavelength of the photosensitizers were used. Light intensities were measured with a POWER MAX5100 (Mol electron detector incorporated) power meter.

2.3. Singlet Oxygen Quantum Yield (Φ_{Δ})

Singlet oxygen quantum yield (Φ_{Δ}) determinations were accomplished as is described in the literature [15]. 1,3-diphenylisobenzofuran (DPBF) was added as a singlet oxygen trap after the photosensitizer compounds were dissolved in DMSO. Then, the mixture was exposed to light and UV-Vis spectra are taken to examine the change in absorption at 417 nm of the DPBF compound.

Generally, 3 mL portion of phthalocyanine solutions ($C=8 \times 10^{-6}$ M) containing the DPBF was irradiated in the Q band region with the photo-irradiation. Equation 2.1 was employed for the calculations:

$$\Phi_{\Delta} = \Phi_{\Delta}^{std} \frac{R \cdot I_{abs}^{std}}{R^{std} \cdot I_{abs}} \quad (2.1)$$

2.4. Photo-degradation Quantum Yield (Φ_d)

Photo-degradation quantum yield (Φ_d) determinations were accomplished as is described in the literature [15]. The photo-chemical measurement system shown in Figure 1 is also used for photo-degradation measurements. For this purpose, after **PS-4** was dissolved in DMSO, it was exposed to light at certain intervals and then the UV-Vis spectra are taken to determine the change of phthalocyanine's Q band. Photo-degradation quantum yield was determined using equation 2.2.

$$\Phi_d = \frac{(C - C_0) V \cdot N_A}{I_{abs} St} \quad (2.2)$$

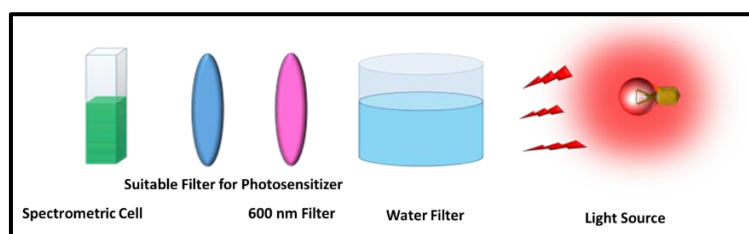


Figure 1. Schematic presentation of the photo-chemical measuring device

2.5. Experimental

2.5.1. Synthesis of 1,3-diiminoisoindoline (2)

Dry methanol (300 mL) was added to phthalonitrile (25

g, 0.195 mol, 2 eq.) and sodium methoxide (5.1 g, 0.094 mol, 1 eq.). Ammonia gas was slowly passed through this mixture at room temperature. This process was continued with an 11 hour. After this, the temperature was increased

to 65 °C and the process was continued for 3 hours. The reaction temperature was then brought to room temperature. The precipitate was filtered through a G3 filter. Solids washed with water, ethanol and then dried in vacuo. The pale yellow compound of molecular formula $C_8H_7N_3$ has a melting point of 194-196 °C and is consistent with the literature [16] Yield 90% (25.5 g).

2.5.2. Synthesis of Dichlorosilicon (IV) Phthalocyanine (3)

Tetralin (20 mL), tributylamine (10 mL) and silicon tetrachloride (2.5 mL, 5.09 g, 0.03 mol, 3 eq.) were added to 1,3-diiminoisoindoline (2) (3 g, 0.02 mol, 2 eq). The reaction temperature was brought to boiling temperature for 4 hours. The reaction temperature was cooled down to room temperature and then ethanol was added for the precipitation. The resulting solids were filtered through a G3 filter and washed with ethanol and acetone for three times, respectively. Finally, solid compound dried in a vacuo. A dark navy blue color with molecular formula $C_{32}H_{18}Cl_2N_8Si$ is obtained and consistent with the literature [16]. Yield 55% (1.74 g). $C_{32}H_{18}N_8Cl_2Si$, MW: 613.54. m.p. >250 °C. FT-IR ν_{max}/cm^{-1} : 3056 (Ar-H), 1609, 1532, 1473, 1429, 1335, 1290, 1163, 1119, 1079, 913, 783,760, 727, 693. MS (MALDI-TOF) (DIT): m/z: Calc. for $C_{32}H_{18}Cl_2N_8Si$ 613.54; found: 613.94 $[M]^+$. 1H NMR (400 MHz, DMSO- d_6) δ (ppm): 7.83 (16H, s, CH_{ar}). ^{13}C NMR (100 MHz, DMSO- d_6) δ (ppm): 169.63, 134.72, 133.65, 133.08, 124.00, 123.41.

2.5.3. Synthesis of Phthalocyanine (PS-4)

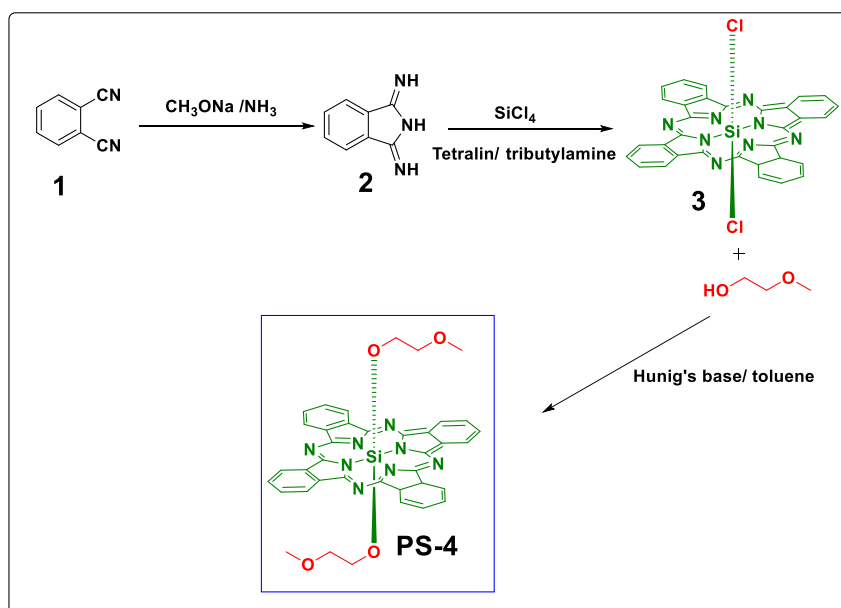
Dry toluene (4 mL), hunig's base (1 mL) and (0.2 g, 0.04 mol) excess of 2-methoxyethanol were added

dichlorosilicon (IV) Pc (3). Reaction temperature was heating to 115°C for 24 hours. The reaction temperature was brought to room temperature. Reaction mixture was added to water and then filtered. The precipitate was washed with water, ethanol and then dried in vacuo. The blue solid product was purified by preparative thin layer chromatography (TLC) using silica gel, and dichloromethane/ethanol (25:1) solvent system as eluent. Yield: 24% (28 mg). $C_{38}H_{32}N_8O_4Si$, MW: 692.81. m.p. >250 °C. FT-IR ν_{max}/cm^{-1} : 3048, 2954, 2863, 1615, 1596, 1531, 1449, 1413, 1393, 1327, 1282, 1257, 1159, 1091, 1053, 967, 913, 831, 814, 751, 663. MS (MALDI-TOF) (DHB) m/z: Calc. for $C_{38}H_{32}N_8O_4Si$, 692.81; found: 692.73 $[M]^+$. 1H NMR (400 MHz, $CDCl_3$) δ (ppm): 9.64 (8H, m, CH_{ar}), 8.34 (8H, m, CH_{ar}), 4.21 (4H, m, O- CH_2), 3.64 (4H, m, - CH_2), 2.35 (6H, t, O- CH_3). UV-vis (DMSO): λ_{max} , nm (log ϵ): 674 (5.12), 604 (4.39), 354 (4.66).

3. Results and Discussion

3.1. Synthesis

The synthesis steps of axially silicon (IV) phthalocyanine (PS-4) were given in Scheme 1. The synthesis of 1,3 diiminoisoindolin (2) and dichlorosilicon (IV) phthalocyanine (3) were applied from the literature [16]. Synthesis yield of compounds (2 and 3) were 90% and 55%, respectively. We investigated the reaction conditions for di-axially substitution and used Hunig's base (N,N-isopropylethylamine) in this study [17]. For the synthesis of axially di silicon (IV) phthalocyanine (PS-4), dichlorosilicon (IV) phthalocyanine (3) and excess of 2-methoxyethan-1-ol were used. PS-4 was characterized by different spectroscopic techniques such as FT-IR, 1H -NMR, UV-Vis, MALDI-TOF mass.



Scheme 1. Synthetic route of PS-4

FT-IR spectrum of **PS-4**, C-O peak was observed at 1091 cm^{-1} and aliphatic peaks were observed at 2954 and 2863 cm^{-1} , respectively (Figure.3). In the MALDI-TOF mass spectrum of **PS-4**, the molecular ion peaks was observed at 692.72 [M]^+ (Figure.4).

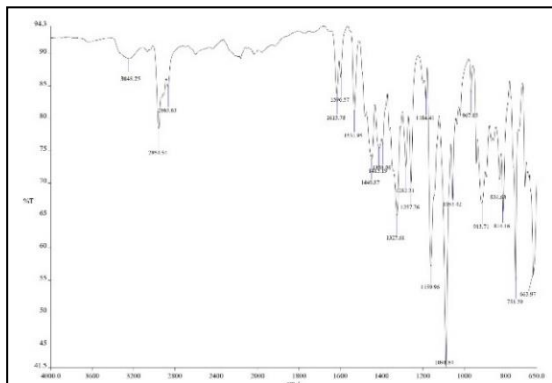


Figure 2. FT-IR spectrum of **PS-4**.

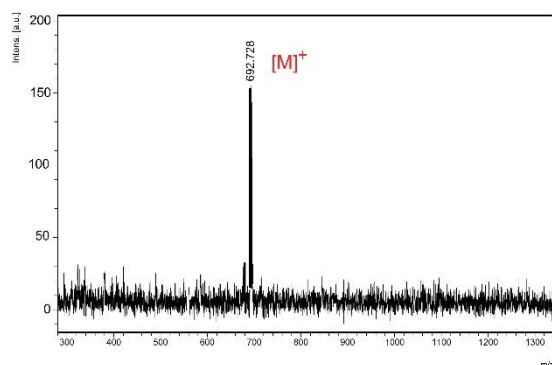


Figure 3. MALDI-TOF mass spectrum of **PS-4**.

$^1\text{H-NMR}$ spectrum was analyzed using CDCl_3 solvent. Spectrum for **PS-4**, the aromatic protons appeared at 9.64 ppm and 8.34 ppm (Figure.4). Original source in the form of a reference at the end of the table caption.

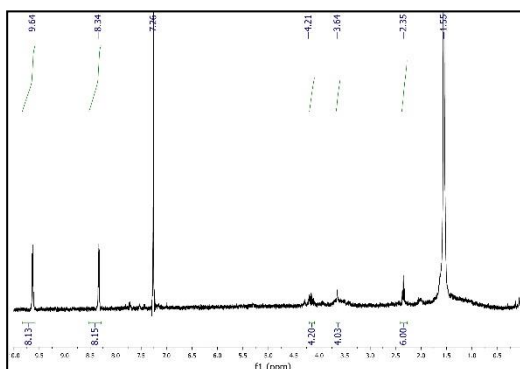


Figure 4. $^1\text{H NMR}$ spectrum of **PS-4**.

3.2. Ground State Electronic Absorption Spectrum and Aggregation Study

The electronic absorption behavior of studied axially silicon (IV) phthalocyanine (**PS-4**) was determined by UV-Vis spectroscopy. Generally, phthalocyanines exhibit two specific absorption bands. Q band was observed at $650\text{-}800\text{ nm}$ in the visible region of the spectrum and B band was observed $350\text{-}450\text{ nm}$ in the ultraviolet region, due to $\pi \rightarrow \pi^*$ transitions.

The aggregation behavior of axially silicon (IV) phthalocyanine (**PS-4**) was also studied at different concentrations in DMSO for determination of the concentration effect on aggregation. The Lambert–Beer law was obeyed for this compound at the concentrations ranging from $12\text{ }\mu\text{M}$ to $2\text{ }\mu\text{M}$. The studied **PS-4** exhibited solubility in DMSO, DMF and chloroform. The silicon (IV) phthalocyanine (**PS-4**) was not aggregated at the working concentration range in DMSO (Figure 5).

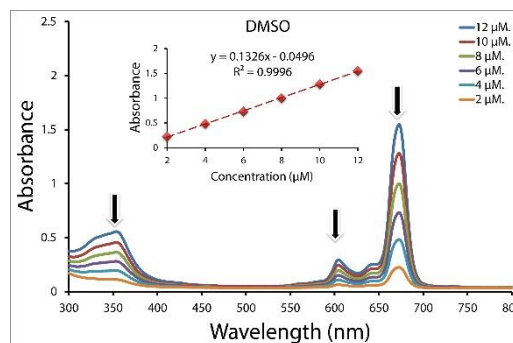


Figure 5. Ground state electronic absorption spectra of **PS-4** in DMSO at different concentrations ($12\text{ }\mu\text{M}$ - $2\text{ }\mu\text{M}$).

3.3. Singlet Oxygen Quantum Yield (Φ_{Δ})

Singlet oxygen production was determined using the chemical method. In this method, singlet oxygen production rate was determined from the decrease of DPBF absorbance at 417 nm which was used as a singlet oxygen trap. The DPBF absorption did not change during the measurement. Accordingly, DPBF absorption did not decrease in dark or photosensitizer-free solutions (Figure 6). The obtained Φ_{Δ} value for axially silicon (IV) phthalocyanine (**PS-4**) in DMSO was given in Table 1 and this value was compared with and SiPcCl_2 . The singlet oxygen generation ability of **PS-4** was found higher than dichloro silicon (IV) phthalocyanine ($\Phi_{\Delta}=0.15$). This result showed that axial substituents effected singlet oxygen generations for silicon (IV) phthalocyanine.

Table 1. Photo-chemical data SiPcCl₂ and PS-4 in DMSO solutions.

Compound	Q band λ_{\max} , (nm)	log ϵ	Φ_a ($\times 10^{-5}$)	Φ_{Δ}
SiPcCl ₂	672- 701 ^a	4.71- 4.47 ^a	-	0.15 ^b
PS-4	674	5.12	4.8	0.26

a Data from reference [18].

b Data from reference [19].

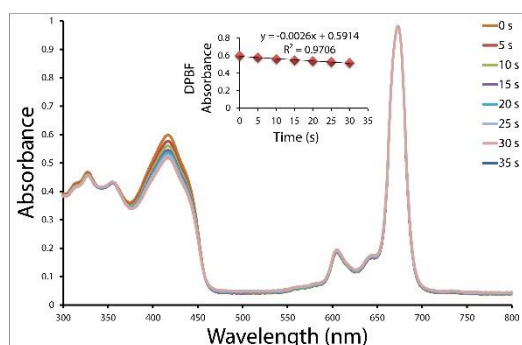


Figure 6. UV-Vis absorption changes of PS-4 for determination of singlet oxygen quantum yield ($c = 1 \times 10^{-5} M$).

3.4. Photo-degradation Quantum Yield (Φ_a)

The photo-degradation is a process in which the photosensitizer is disrupted by light irradiation. It is an important parameter for molecules that are used to determine the stability of photosensitizers and are especially intended for use in photocatalytic reaction as PDT. An ideal photosensitizer should be able to remain for a certain period of time to achieve its photodynamic efficiency in malignant tissue. In this study, the photo-degradation property of the studied PS-4 was determined in DMSO. The absorption band of PS-4 diminished during light irradiation (Figure 7).

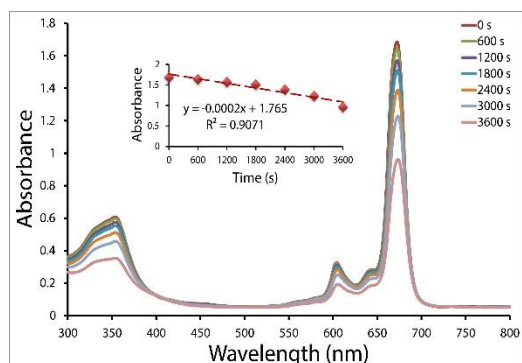


Figure 7. UV-Vis absorption change of PS-4 for determination of photo-degradation quantum yield ($c = 1 \times 10^{-5} M$).

Spectral changes of PS-4 during light irradiation showed that photo-degradation is not photo-transformation. In the absorption spectrum, new bands were not observed. However, the absorption band intensity decreased. Considering these results, PS-4 showed moderate stability to light irradiation in DMSO.

4. Conclusion

This study described successfully synthesized novel axially substituted silicon (IV) phthalocyanine (PS-4). PS-4 was characterized using by spectroscopic methods such as FT-IR, ¹H NMR, mass as well as UV-Vis spectroscopy. Photo-degradation quantum yield and singlet oxygen quantum yield of silicon phthalocyanine (PS-4) were investigated in DMSO solutions.

The ground state absorption spectrum of PS-4 showed characteristic absorption for phthalocyanine in DMSO solution. The study showed that the addition of the 2-methoxyethanol group as an axial ligand has increased solubility and so on decrease aggregation. As a result of this, the singlet oxygen quantum yield of PS-4 ($\Phi_{\Delta} = 0.26$) was slightly higher than the compared to SiPcCl₂ ($\Phi_{\Delta} = 0.15$).

Finally, the studied phthalocyanine (PS-4) could have potential to be used as a candidate photosensitizer for photodynamic therapy.

Acknowledgement

Authors would like to thank Meltem Göksel who contributed to the preparation of this publication.

Author's Contributions

Gülçin Ekineker: Performed the experiment, manufactured the samples and characterized them spectroscopic methods. Drafted and wrote the manuscript, and commented result analysis.

Hülya Yanık: Aided in interpreting the results and worked on the manuscript.

Ethics

There are no ethical issues after the publication of this manuscript.

References

- Ekineker, G, Nguyen, C, Bayır, S, Dominguez Gil, S, İşi, Ü, Daurat, M, Godefroy, A, Raehm, L, Charnay, C, Oliviero, E, Ahsen, V, Gary-Bobo, M, Durand, J-O, and Dumoulin, F. 2019. Phthalocyanine-based mesoporous organosilica nanoparticles: NIR photodynamic efficiency and siRNA photochemical internalization, *Chemical Communications*; 55, 11619-11622.



2. Macdonald, I J, and Dougherty, T. J. 2001. Basic principles of photodynamic therapy, *Journal of Porphyrins and Phthalocyanines* 5, 105-129.
3. Tarhouni, M, Durand, D, Önal, E, Aggad, D, İsci, Ü, Ekiner, G, Brégier, F, Jamoussi, B, Sol, V, Gary-Bobo, M, and Dumoulin, F. 2018. Triphenylphosphonium-substituted phthalocyanine: Design, synthetic strategy, photoproperties and photodynamic activity, *Journal of Porphyrins and Phthalocyanines*; 22, 552-561.
4. Hopper, C. 2000. Photodynamic therapy: a clinical reality in the treatment of cancer, *The lancet oncology*; 1, 212-219.
5. Plaetzer, K, Krammer, B, Berlanda, J, Berr, F, and Kiesslich, T. 2009. Photophysics and photochemistry of photodynamic therapy: fundamental aspects, *Lasers Med Sci*; 24, 259-268.
6. Lo, P-C, Rodríguez-Morgade, M S, Pandey, R -K, Ng, D. K. P, Torres, T, and Dumoulin, F. 2020. The unique features and promises of phthalocyanines as advanced photosensitisers for photodynamic therapy of cancer, *Chemical Society Reviews*.
7. Bartlett, M-A, Mark, K, and Sundermeyer, J. 2018. Synthesis, spectroscopy and singlet oxygen quantum yield of a non-aggregating hexadecamethyl-substituted phthalocyanine silicon (IV) derivative, *Inorganic Chemistry Communications*; 98, 41-43.
8. Barut, B, Demirbas, U, Ozel, A, and Kantekin, H. 2017. Novel water soluble morpholine substituted Zn(II) phthalocyanine: Synthesis, characterization, DNA/BSA binding, DNA photocleavage and topoisomerase I inhibition, *International journal of biological macromolecules*; 105, 499-508.
9. Skupin-Mrugalska, P, Szczolko, W, Gierlich, P, Konopka, K, Goslinski, T, Mielcarek, J and Düzgüneş, N. 2018. Physicochemical properties of liposome-incorporated 2-(morpholin-4-yl) ethoxy phthalocyanines and their photodynamic activity against oral cancer cells, *Journal of Photochemistry and Photobiology A: Chemistry*; 353, 445-457.
10. Baş, H, Biyiklioglu, Z. 2018. Synthesis and electropolymerization properties of axially disubstituted silicon phthalocyanines bearing carbazole units, *Inorganica Chimica Acta*; 483, 79-86.
11. Goksel, M, Biyiklioglu, Z, Durmus, M. 2017. The water soluble axially disubstituted silicon phthalocyanines: photophysicochemical properties and in vitro studies, *Journal of biological inorganic chemistry : JBIC : a publication of the Society of Biological Inorganic Chemistry*; 22, 953-967.
12. Bispo, M, Pereira, P. M. R, Setaro, F, Rodríguez-Morgade, M. S, Fernandes, R, Torres, T, Tomé, J. P. C. 2018. A Galactose Dendritic Silicon (IV) Phthalocyanine as a Photosensitizing Agent in Cancer Photodynamic Therapy, *ChemPlusChem*; 83, 855-860.
13. Baron, E. D, Malbasa, C. L, Santo-Domingo, D, Fu, P, Miller, J. D, Hanneman, K. K, Hsia, A. H, Oleinick, N. L, Colussi, V. C, Cooper, K. D. 2010. Silicon phthalocyanine (Pc 4) photodynamic therapy is a safe modality for cutaneous neoplasms: results of a phase I clinical trial, *Lasers in surgery and medicine*; 42, 728-735.
14. Armarego, W, Perrin, D. 1980. Purification of laboratory chemicals, *Pergamon Press, Oxford* 102, pp.102-103.
15. Yanık, H, Aydın, D, Durmuş, M, Ahsen, V. 2009. Peripheral and non-peripheral tetrasubstituted aluminium, gallium and indium phthalocyanines: Synthesis, photophysics and photochemistry, *Journal of Photochemistry and Photobiology A: Chemistry*; 206, 18-26.
16. Lowery, M. K, Starshak, A. J, Esposito, J. N, Krueger, P. C, Kenney, M. E. 1965. Dichloro (phthalocyanino) silicon, *Inorganic Chemistry*; 4, 128.
17. Rășădean, D. M, Gianga, T. M, Swan, A. H, Kociok-Köhn, G, Pantoş, G. D. 2018. Chiral Phthalocyanines through Axial Coordination, *Organic letters*; 20, 2645-2648.
18. Göksel, M, Durmuş, M, Atilla, D. 2017. Synthesis and photophysicochemical properties of a set of asymmetrical peptide conjugated zinc (II) phthalocyanines bearing different fluorophore units, *Inorganica Chimica Acta*; 456, 95-104.
19. Atmaca, G. Y, Dizman, C, Eren, T, Erdoğan, A. 2015. Novel axially carborane-cage substituted silicon phthalocyanine photosensitizer; synthesis, characterization and photophysicochemical properties, *Spectrochimica Acta Part A: Molecular and Biomolecular Spectroscopy*; 137, 244-249.

The Impact of European Green Deal on Turkey's Iron and Steel Industry: Decomposition Analysis of Energy-Related Sectoral Emissions

Abdulkadir Bektaş^{1*} 

¹The Ministry of Energy and Natural Resources, Nasuh Akar Mah. Türk Ocağı Cad.

No: 2 06520 Cankaya – Ankara, Turkey

*kadirbektas35@gmail.com

*Orcid: 0000-0003-0199-2251

Received: 8 November 2020

Accepted: 1 March 2021

DOI: 10.18466/cbayarfbe.823265

Abstract

The European Union has put forward a vision under the EU Green Deal's name to take the lead in its priorities, fulfill the Agreement's criteria, and subsequently accept the first EU climate law on March 5, 2020. The law framework aims to impose tax obligations on consumption goods imported by the EU from abroad, especially on energy-intensive sectors, by applying the carbon border adjustment mechanism. Our main goal is to determine what kind of measures can be taken to ensure that the iron and steel industry is least affected by the EU border carbon regulation. We are an absolute exporter, are least affected by the EU carbon border adjustment. For this reason, the change in energy-related greenhouse gas emissions from the iron and steel industry from 1998 to 2018 was analyzed using the Logarithmic Mean Divisia Index (LMDI) model to investigate the potential effects of carbon border adjustment in the iron and steel industry. The analyzes were made with five significant factors that determine the change of emissions. These factors are; changes in economic activity, activity mix, energy intensity, energy mix, and emission factors. Analysis has suggested that the economic activity effect has raised CO₂ emissions. This method indicates that the energy intensity's impact could be the first key determinant of GHG emissions. Turkey should attempt to implement low-carbon development policies and reduce energy-related emissions in the iron & steel sector are the least impacted by the EU's carbon border adjustment.

Keywords: Carbon Border Adjustment, Decomposition Analysis, Energy, Greenhouse Gas Emissions, Iron and Steel Industry.

1. Introduction

Today, the phenomenon of climate change, which shows its effects in the form of excessive rainfall, floods, and extreme temperatures, has been one of the priority issues in the European Union, as in the whole world. The adverse effects of climate change have been primarily observed on agriculture and food security, water resources, public health, land and marine ecosystems, and coastal regions. The Special Report of the Intergovernmental Panel on Climate Change (IPCC) on the effects of global warming above 1.5 °C of pre-industrial levels confirms that the global effects of climate change increase with the average global temperature. Furthermore, the dramatic effects would be seen worldwide in 2 °C due to climate change. European Union accelerated its efforts to take more precautions and reduce these impacts on combating climate since it considers climate change an urgent

problem due to the severe disasters in the world ecosystem, biodiversity, health, and food system.

The Paris Agreement aims to keep global temperature rise well below 2 °C and take measures to keep it at 1.5 °C. Its aim is to become carbon-neutral (zero-emission) by the middle of this century. As stated in the IPCC report [1], to limit the temperature increase to 1.5, net-zero CO₂ emissions at the global level should be achieved around 2050, and neutrality should be ensured for all other greenhouse gases later in the century. In this context, the European Union put forward a vision on December 11, 2019, in the name of the European Green Deal (EGD) to take the lead in terms of its interests and fulfill the Paris Climate Agreement's requirements [2]. The European Commission, in this new growth plan, is committed to becoming the world's first climate-neutral bloc by 2050. This plan also aims to transform the EU into a fair and prosperous society where greenhouse gas emissions are net zero in 2050.

The decoupling of economic growth and resource use has been achieved based on a modern, climate-neutral, resource-efficient, and competitive economic structure. In the transition into a climate-neutral economy, the industry has a prominent key role. All manufacturing value chains, including energy-intensive industries, would face the main challenges. In March 2020, the European Commission proposed “A New Industrial Strategy for Europe.” This document underpins the essential role of industry in the transition towards a carbon-neutral economy. The industry needs to reduce its carbon footprints, offer accessible, clean technology solutions, and create new business models to accelerate the transition.

The European Green Deal is a new growth strategy for the European Union that would provide more gain than they would spend. It is a vision that includes making the EU economy a global leader while meeting the Paris Agreement’s long-term emission targets by taking advantage of the opportunities obtained in this way. For this purpose, the EU has announced that it would implement various applications in many areas. “Carbon border adjustment mechanism,” which the EU plans to implement against commercial partners in 2021, is its most important application, which would profoundly affect our trade with the EU since the EU is our most important export and import partner [3]. The EU aims to impose a severe tax liability on imported products, primarily to energy-intensive sectors. Therefore, energy-intensive sectors would be severely affected, such as steel, cement, glass, and aluminum.

The EU green deal strategy would have a direct effect on trade ties with the Turkish bloc and this can be used to turn efficient infrastructure in the country. As a developing country, Turkey needs increasing amounts of energy demand. The main policy objective is to maintain its energy supply and keep up with the demand to support its economic growth as its population increases. It needs to urgently transform its energy system to reduce its reliance on imports, which constitute 3 out of 4 units of total primary energy supply. With an increasing economy and population, the country’s imported energy costs have reached unprecedented levels, driving a large proportion of Turkey’s current account deficit. Therefore, Turkey also wants to use hydrocarbons that are its domestic capital. In this respect, greenhouse gas emissions that cause global warming need to be analyzed in detail based on sectors that are likely to be subject to carbon border regulation. Emissions originated from the iron and steel industry, which is one of the intensive energy sectors and of which we are an absolute exporter, would be examined. Our main objective is to decide what kind of steps can be taken to ensure that the EU border carbon regulation is least impacted on the iron and steel industry. Logarithmic Mean Divisia Index (LMDI) method has been used to decompose changes in GHG

emissions for the iron and steel industry from 1998-2018. It is used to decompose GHG emissions into five driving forces in the iron and steel industry; changes in economic activity, activity mix, energy intensity, energy mix, and emission factors (EF). Four types of fuel were used in the analyzes; solid, liquid, gas, and other fuels. The biomass fuel type was not considered, as CO₂ emissions from biomass were not included in the total CO₂ emissions from fuel combustion. The results have shown that 1) the economic activity impact (GDP) is the most critical determining factor behind the change in CO₂ emissions. 2) Similarly, the sectoral energy structure also had an increasing effect on emissions, and 3) energy density, energy composition, and emission factors have a decreasing effect on emissions.

2. European Green Deal

The European Commission presented “The European Green Deal,” which reveals the European Union’s new strategic vision for 2050 with the perspective of “combating climate change and economic growth” and includes regulations that concern almost all sectors in December 2019. It is a long-term strategic vision for a thriving, prosperous, competitive, and climate-neutral economy by 2050. The strategy demonstrates how, by investing in real technical solutions, motivating people, and associating activity in critical areas such as industrial policy, finance, or science, Europe can lead the way to climate neutrality while maintaining social justice for a just transition. The EU has indeed begun modernizing and changing the economy with a goal of climate neutrality. It decreased greenhouse gas emissions by 23% between 1990 and 2018, while the economy expanded by 61%. There are severe breakthroughs in energy efficiency and renewable energy in achieving this success. As expected by the Paris Agreement, the European Union intends to reduce its emissions by 40 percent by 2030, update the 2030 target to 55 percent with the European Green Deal, and meet a reduction target of 100 percent as set out in the 2050 target. Achieving a 55 percent reduction in greenhouse gas emissions would take measures in all economic sectors. A climate-neutral transition can be done only with the contributions of everybody. The EU Parliament approved an amendment that increased this target to 60% on October 7.

The Commission estimates that meeting the current environment and energy goals for 2030 would require an additional EUR 260 billion of annual investment, about 1.5 percent of GDP in 2018. Apart from the current 2030 and 2050 emission targets, the “Green Deal for Europe” requires additional funding. In response to the additional financing requirement, it is stated that the European Commission would present the “Sustainable Investment Plan for Europe.” As part of the plan, it is envisaged to establish a “Just Transition Fund,” the “Just Transition Fund,” and a Just Transition

Mechanism of € 100 billion. As part of the Green Deal, the Commission presented on January 14, 2020, a European Green Deal Investment Plan of at least € 1 trillion over the next decade to stimulate sustainable investment. Green Deal consists of 47 actions under the main headings of Climate, Energy, Industry, Transportation, Agriculture, Biodiversity, Environmental Pollution, Financing, Leadership, and Working Together. Based on the point that the specified comprehensive transformation cannot be achieved only by Europe's efforts, the EU intends to lead international studies in this direction; it is observed that it aims to encourage its partners to take similar steps by sharing its expertise, and financial resources. Since the driving factors that cause climate change and biodiversity exceed national borders, "The Green Consensus" gear up in terms of the environmental target cannot be achieved by Europe acting alone. Therefore, it aims to share its dialogue, expertise, and financial support with neighboring and partner countries at the EU cooperation point. On the other hand, to avoid being disadvantaged in international competition and prevent carbon leakage, the European Union foresees significant changes in its foreign trade and international investment and financing policies. These changes can be listed with the following subtitles;

- 1- Failure to sign new free trade agreements with countries that do not ratify the Paris Agreement
- 2- Carbon border adjustment mechanism
- 3- Funding
- 4- Standards and eco-labeling

According to the Green Deal, the EU requires the candidate country to "ratify and effectively implement the Paris Agreement" for liberalization agreements, such as the free trade agreement it would make with other countries. The text considers ratification sufficient for the country to be a member but goes further and suggests a condition of practical implementation.

2.1 Green Deal Evaluation in Turkey-EU Trade: Carbon Border Regulation

The European Union (EU), consisting of 27 countries, is the world's largest political and economic organization. Although it constitutes about 7% of the world population, the EU is among the world's largest economic and trade actors. In addition to this, the EU is a significant market for our country with its large and diversified market structure, advanced infrastructure opportunities, technical standards, and health measures applied in the same way in all member countries, current market size, and future trade potential. When the EU is considered a single block, it ranks second in world exports and imports of goods, taking 15.2% of world goods exports and 14.7% of world imports. With a trade surplus of \$ 209 billion in service trade, the EU is the world's largest exporter and importer. With an

intense and diversified market structure, the EU offers our exporters countless opportunities at every stage of the value chain by importing essential products such as agricultural products, raw materials, and energy and importing investment chemical and various consumer goods. Having an import volume of approximately 2.1 trillion dollars, the EU is increasing its import volume in many sectors day by day. With this import size, these sectors offer a tremendous market opportunity to our exporters.

For all these reasons, the "carbon border adjustment mechanism," which the EU plans to implement against commercial partners in 2021, stands as the most critical topic. In case the worldwide differences in climate action persist, it is aimed to create a carbon regulation mechanism at a new frontier in combating the risk of carbon leakage. With this mechanism, it is envisaged to ensure that the goods imported into the EU under the World Trade Organization rules and other international obligations of the EU are priced to reflect their carbon content [3]. In short, it is understood that this EGD implementation, which would cause the most significant impact on a global scale, has been taken against countries that do not take obligations to protect the EU from the competition and to prevent carbon leaks. The EU imposes strict obligations on carbon-intensive businesses to be carbon neutral while pricing the carbon through the European Union Emission Trading System (EU ETS) and charging these businesses' costs. EU companies and environmentalists criticized that a country business with no emission obligation abroad exports the same type of goods to the EU without any cost.

Moreover, since it is costly to produce such products within the EU due to the carbon price, buying the same product by importing from a country with no abatement obligation does not mean that the obligating EU country reduces its emissions. (For example, steel is cheaper to import from Turkey came to an automobile company in Germany) Such consequences, called carbon leakage, could increase global emissions since the importer country (Germany in the example) was not deducted from its emissions. Therefore, in recent years, EU countries have focused primarily on reducing consumption-based emissions and production. In this sense, the border carbon adjustment mechanism can solve both problems [4]. This framework recommends the "carbon border adjustment mechanism" to reduce carbon leakage caused by exports in selected carbon-intensive sectors. In other words, the EU seeks to defend its carbon pricing market and its export leakage to different countries while pursuing more ambitious emission reduction goals. It also needs to keep commodity prices competitive against substitution for imported goods, increasing jobs by reducing imports.

In particular, the EU would like to give priority the mining (coal, iron and steel, petroleum, chemical, and fertilizer raw materials) and sugar, malt, textile, glass, paper, plastic, ceramic, cement, steel, sectors as those that may be exposed to carbon leakage. It is understood that they have targets, such as creating funds and additional investments for the revenues to be generated by these mechanisms.

As the EU is the world's largest trade bloc with a non-EU trade figure of around 3.9 trillion euros, the border tax regulation can have severe global impacts. Half of the foreign trade with EU member states such as Turkey, a country that this application would be greater than the effect of the form. To be established on January 1, 1996, together with the Customs Union trade volume between Turkey and the EU gained momentum in 2019, 161.6 billion dollars (exports: \$ 88.0 - imports: \$ 73.5) as incurred and most of our EU countries has continued to be an essential trading partner. 4% of the total EU exports to Turkey were made. The EU has a share of 48.7% in our exports with 88.0 billion dollars in 2018 and ranks first in our total exports. Our country has a share of 4% of the total imports in the EU. Besides, the EU ranks first in imports as well as in our country's exports. According to 2019 figures, Turkey 210.3

billion dollars to 73.5 billion dollars of the total imports of goods (35.0 % share) were realized from the EU. In 2019, the ratio of exports to imports in our country's trade with the EU was 119.7%.

Table-1 shows the import-export with the EU between 2013-2019.

The 'iron-steel, aluminum, cement, glass, and ceramic' industries are among the energy-intensive sectors and are considered to be affected by the policy changes envisaged by the EU under the European Green Deal (EGD), are expected to be included in the list. Because 75% of the EU's carbon emissions come from the energy sector, the energy sector's transformation is expected to form the Green Deal's backbone, which would also be a prerequisite for decarbonizing other sectors. Considering that our exports to the EU in products and services with a high risk of carbon leakage (COMMISSION et al., 2019) are at the level of 28.2 billion dollars, the issue should be addressed and protected in our country holistically. Improving the competitiveness of our exporters in the EU market is considered essential. Due to Turkey's developing country, there is an increasing amount of energy demand.

Table 1. Our foreign trade with the European Union (Billion US \$)

EU (28)	Foreign Trade	2019	2018	2017	2016	2015	2014	2013
Total exports		180,8	177,2	164,5	149,2	151,0	166,5	161,5
Total imports		210,3	231,2	238,7	202,2	213,6	251,1	260,8
	Export	88,0	88,9	77,9	71,9	67,3	72,4	67,4
	% export	48,7%	50,2%	47,4%	48,2%	44,6%	43,5%	41,7%
A-European Union (E.U. 28)	Import	73,5	84,7	88,8	80,7	82,6	93,3	96,9
	% import	35,0%	36,6%	37,2%	39,9%	38,7%	37,2%	37,1%
	Foreign trade volume	161,6	173,6	166,7	152,7	149,9	165,7	164,2
	Export-Import	14,5	4,2	-10,9	-8,8	-15,3	-21,0	-29,5
	Coverage Rate	120%	105%	88%	89%	81%	78%	120%

According to National Energy and Mines, it is required to use hydrocarbons in the domestic capital position. In this respect, it can be stated that there are essential steps to be taken in EGD and climate change. To carry out the necessary studies in this area, greenhouse gas emissions that cause global warming should be analyzed in detail based on sectors that are likely to be subject to border carbon regulation.

2.2 Development of Turkey's energy-related GHG Emissions

According to the Turkish Statistical Institute, Turkey's total greenhouse gas emissions in 2018 are 520.9 million tons (Mt) of CO₂ equivalent. This value represents an increase of 240.7 Mt CO₂ equivalent, with

an increase of 86 percent compared to 1998 [5]. Population growth, the growing economy, and the increase in demand for energy are among the main reasons for increased emissions. While energy-related emissions had the highest share in total emissions with 71.6 percent, this rate was only 0.8% for the iron and steel industry. Turkey showed increased emissions during the period mentioned in terms of both quantity and proportionate emissions from the iron and steel sector has shown a downward trend. This tendency shows us that the iron and steel industry is taking firm steps towards becoming a cleaner, lower-emission sector on an annual basis. Sectoral emissions based on years are given in detail in Table-2.

Table 2. The energy-related greenhouse gas emissions in Turkey, kt CO₂ eq. (1998–2018)

Years	Total Emissions	Energy Sector	Manufacturing Industry and Construction	Iron and Steel Sector	Transport Sector	Other Energy Sectors
1998	280 231	195 864	55 470	6 152	32 782	37 704
1999	277 650	193 817	47 365	5 576	34 617	35 753
2000	298 760	216 054	57 936	6 566	36 465	37 764
2001	280 301	199 233	45 656	6 732	36 455	31 397
2002	286 003	205 832	57 112	6 461	36 234	32 930
2003	305 261	220 300	66 682	6 197	37 825	36 232
2004	314 669	226 139	63 857	5 057	42 048	39 561
2005	337 140	243 965	63 004	5 482	42 041	42 709
2006	358 292	259 959	70 084	4 524	45 424	42 236
2007	391 422	290 771	71 874	4 640	52 099	45 279
2008	387 590	287 279	47 354	3 977	48 166	64 410
2009	395 596	292 501	46 226	2 912	47 907	70 959
2010	398 883	287 047	52 332	2 644	45 392	67 773
2011	427 831	308 666	52 585	3 990	47 386	74 656
2012	447 255	320 489	61 052	4 298	62 525	61 586
2013	439 326	307 523	52 978	4 638	68 865	56 384
2014	458 369	325 767	54 438	4 992	73 559	56 079
2015	472 595	340 907	59 585	5 288	75 798	65 327
2016	497 742	359 671	60 071	4 190	81 841	65 201
2017	523 753	379 901	60 180	4 327	84 659	73 391
2018	520 942	373 101	59 578	4 215	84 502	62 868
Difference	240.711	177.237	93.326	4.108	-1.937	51.719

Table-2 and Figure-1 show that the total emissions (85.9%) and energy sector emissions (90.5%) increased significantly between 1998-2018. One of the most important reasons behind this increase is considerable GDP development (Million \$ at current prices), which increased by 184.4% in the same period. During the same period, the average GDP growth was 4.6. The economic growth effect increases the demand for energy, which naturally causes a severe increase in energy-related emissions. While the share of the iron and steel industry in GDP increased from 1.3 percent to 3.2 percent in the specified period, it corresponds to a considerable increase of 575.8% in terms of the value it creates.

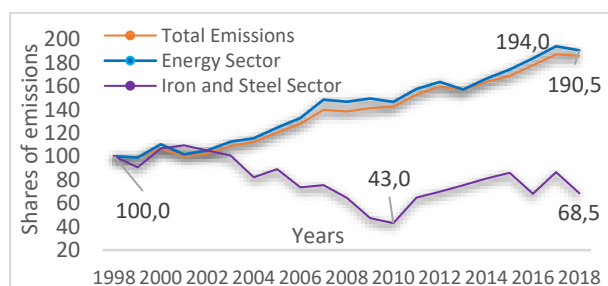


Figure 1. The change of energy-related sectoral emission shares, 1998–2018

In the same period, sectoral energy intensity decreased by 68 percent, followed by a 31.5 percent decrease in emissions. Detailed data are given in Table-3.

Table 3. The development of the indicators of the iron and steel industry by years (1998-2018)

Years	Iron and Steel Industry Emissions Rate (%)	Share of GDP (%)	Energy intensity (toe/1000 \$)
1998	2,2%	1,3%	1,07
1999	2,0%	1,2%	1,22
2000	2,2%	1,2%	1,33
2001	2,4%	1,5%	1,21
2002	2,3%	1,4%	1,22
2003	2,0%	1,5%	0,95
2004	1,6%	1,9%	0,56
2005	1,6%	1,8%	0,50
2006	1,3%	2,1%	0,39
2007	1,2%	2,4%	0,32
2008	1,0%	3,1%	0,23
2009	0,7%	2,0%	0,39
2010	0,7%	2,1%	0,38
2011	0,9%	2,9%	0,29
2012	1,0%	2,7%	0,29
2013	1,1%	2,5%	0,30
2014	1,1%	2,5%	0,30
2015	1,1%	2,2%	0,39
2016	0,8%	2,0%	0,45
2017	1,0%	2,6%	0,39
2018	0,8%	3,2%	0,34

2.3 Turkey's Iron and Steel Industry Structure

Three integrated iron and steel manufacturing plants are currently operating in Turkey (Ereğli, İskenderun ve Karabük). There are 31 electric arc furnace mills operating in Turkey in addition to these plants.

As of 2018, 39.4 million tons of 51.8 million tons of crude steel capacity belongs to facilities producing from scrap and 12.4 million tons from iron ore [6]. In recent years, steel production and consumption, another major steel producer that decompose in the country's positive direction, Turkey in 2007-2012, among the top 15 steel producers in the country, after China and India, increasing fastest production 3. In 2011 and 2012, after achieving the country's position with the fastest increase in production, production decreased for three consecutive years in the 2013-2015 period. Turkey's crude steel production in 2015, by 7.4%, down from 34.04 million tons, down 31.52 million tons recovery in 2016 and 2017, starting with Turkey, crude steel production in 2018; It has managed to rank 2nd in Europe and 8th in the world (Figure-2).

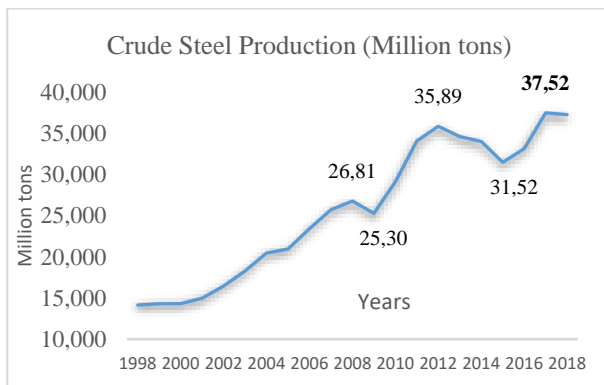


Figure 2: The Value Created by the Steel Industry, 1998–2018

Table 1. The basic indicators for Turkey iron and steel industry ([6])

Indicators	Unit	2016	2017	2018
Industrial Sector Total Energy Consumption	ktoe	33.253,7	35.318,3	36.155,0
Iron and Steel Industry Energy Consumption	ktoe	7.629,5	8.540,8	8.490,4
Share of Iron and Steel Industry	%	22,9	24,2	23,5
Specific Energy Consumption	tep/tons	0,230	0,228	0,229
Crude Steel Production	million tons	33.163	37.524	37.312
Iron and Steel Export	million tons	15.081	16.275	19.748
	Billion (\$)	6.921	9.172	11.051
Iron and Steel Import	million tons	17.000	15.802	14.019
	Billion (\$)	8.531	10.063	10.657
Per Capita Crude Steel Consumption	kg/person	454	475	447

Turkey's crude steel production in August 2020 totaled 3.2 million tons, an increase of 22.9% compared to the same month of the previous year. In the January-August period, crude steel production increased by 0.6% to 22.7 million tons.

The sector reached the Capacity Utilization Rate in 2018 at the level of 71.9%. In 2018, 19.5 million tons of iron and steel were exported, and 11.1 billion dollars of income was provided to our country. This figure corresponds to 6.6% of our total exports [6]. In 2018, the highest exports were made to EU countries (9.062 thousand tons; 7.840 million). The primary indicators related to the sector are given in Table-4.

Despite all the contractionary impact of the pandemic period, the Turkish steel sector to ensure the first eight months as a 0.6% production increase in production and a 13% increase in a show of Turkey's steel consumption has increased optimistic expectations for the final months of the year. However, in our domestic market, 50% of the consumption is met with imports, reducing capacity utilization rates. Consequently, the increase in consumption is not fully reflected in domestic production. On the other hand, the practices of the EU Commission continue to restrict our steel exports. While talking about quota restriction, dumping investigation, non-tariff transaction tax, it is now seen that EUROFER has requested tax implementation for the past years. On the other hand, the practices of the EU Commission continue to restrict our steel exports. While talking about quota restriction, dumping investigation, non-tariff transaction tax, it is now seen that EUROFER has requested tax implementation for the past years.

3. Literature Review

There are various types of decomposition analysis in the literature. These are generally grouped under two main headings as index decomposition analysis and SDA-Structural Decomposition Analysis. Both methods are used to measure the effects of economic growth, sectoral changes and technological developments, changes in the environment, and socio-economic indicators. The additive Divisia Index method was preferred due to its suitability of analytical structure, ease of use, and straightforward interpretation of the results. Therefore, the LMDI (Logarithmic Mean Divisia Index) method developed by Ang (Ang, 2005), one of the leading index decomposition analyzes, is employed. The analyses were made with five significant factors that determine the change.

LMDI, an important index decomposition analysis, has been a popular method used to analyze energy consumption changes and the factors affecting carbon emissions in many sectors over time. Therefore, it is seen that it is used in the analysis of different sectors in many countries. For example; China [[7]–[9]], Greece [10], India [11], Pakistan ([12], Nigeria [13], Spain [14], Mexico [15], Philippines [16] ve Turkey [17]–[21]. Studies frequently use five primary factors, industrial operation, industry structure, energy structure, energy intensity, and emission factor. Some other researchers have added three other factors to examine these factors affecting GHG emissions in many industries, especially the industrial sector, such as efficiency, investment intensity research & development [22]. Gonzalez ve Martinez [15] analyzed the factors determining the greenhouse gas emissions of 16 important sectors of the Mexican economy in 1965–2003 using the decoupling method. They state that economic activity and structural factors led to an increase in electricity generation emissions during this period. Energy density and fuel composition factors had a lowering effect on emissions. Zhang et al. [7], Emodi et al. [13], Moreover, Sumabat et al. [16] used the LMDI technique to analyze CO₂ emissions from power generation in China, Nigeria, and the Philippines. They stated that the most important contribution to CO₂ emissions from electricity generation is due to the effect of economic activity. On the other hand, they said that energy density reduces emissions.

Although decomposition analyzes are used in many different sectors, it is generally seen in the literature that scientific researchers are carried out in energy-intensive industries and sub-sectors. There a few studies in this field concerning Turkey. They are listed below;

Akbostancı et al. [17] studied Turkish manufacturing greenhouse gases covering 57 industries in Turkey from 1995 to 2001 by applying the LMDI technique and established improvements in industrial growth and

energy intensity are the primary main drivers of greenhouse gas alterations. Coal is the primary determinant of fuel, while the steel and iron industries are the most polluting sectors in Turkey's industrial market, with CO₂ emissions overwhelming the industry.

Lise [18] found that economic growth is the most crucial factor in rising CO₂ emissions relatively rapidly in developing economies. On the other hand, the decreasing energy intensity of the economy accounted for a modest decrease in CO₂ emissions in Turkey during the 1980-2003 period.

Akbostancı et al. [19] decomposed and analyzed the CO₂ emissions of five Turkish economy sectors between 1990 and 2013. These sectors are manufacturing, electricity and heat, transport, and residential industries. They found that the main factors that cause a shift in CO₂ emissions are energy intensity and economic activity. In altering GHG pollution, the first two sectors (Manufacturing and electricity) are the most crucial. Besides, particularly for the Manufacturing sector, the fuel mixture portion reduces CO₂ emissions during an economic downturn.

Tunç et al. [20] also used the LMDI technique to assess the definitive factor determining carbon dioxide emissions from Turkey's three main sectors (agriculture, manufacturing, and services). To investigate the impacts of different macroeconomic policies on GHG emissions, Tunç and his colleagues decomposed and analyzed Turkey's GHG emissions for the period 1970-2006, using alterations in the production and use of various energy resources. The investigation concluded that economic growth is the most significant increase in greenhouse gases. On the other hand, energy intensity decreases CO₂ in the periods 1980-1990 and 1995-2008, and the manufacturing system is not a significant factor in lowering carbon dioxide emissions.

Rüstemoğlu [22] attempted to determine and evaluate the factors that, using the LMDI decomposition technique increased or decreased CO₂ emissions for Turkey and Iran between 1990 and 2011. Economic growth and the population are the key determinants of CO₂ emissions for both nations. Surprisingly, the third crucial deciding factor in Iranian carbon emissions may be the effect of energy intensity. It has, on the other hand, a minimally reduced impact on Turkey.

Ediger and Havuz [23] used the LMDI model to investigate sectoral energy usage in the Turkish economy. While there is a clear correlation between primary energy and the GDP, studies show substantial sectoral energy use variations during 1982, 1988-1989, 1994, and 1998-2000. They stated that government policies seem to be the vital driving force for improving the relationship between the Turkish economy and the

oil economy. Such policies would include improving the composition of final energy requirements, improving the quality of materials and energy, and replacing more acceptable products and oils. Furthermore, researchers have done much scientific investigation on the iron and steel industry of many countries.

Sun et al. [24] have paid attention to China's iron & steel industry as a significant energy-consuming manufacturing sector and one of the most significant caused by carbon dioxide (CO₂) emissions. The logarithmic mean division index (LMDI) technique is used to decompose the overall change in CO₂ emissions into four factors: the effect of the emission factor, the effect of the energy structure, energy consumption, and the effect of steel production. The findings revealed that the effects of steel production are the key factor responsible for the increase in CO₂ emissions, while energy consumption contributes most to reducing CO₂ emissions. Moreover, there is a weak negative contribution to the increase in CO₂ emissions from the emission factor effect. Correlation equations are also suggested to determine the complicated relationship between the change in energy use or output of steel and CO₂ emissions change.

Tian et al. [9] have examined the energy-related GHG emission trajectories, characteristics, and driving forces for Chinese ISI for 2001-2010. Using the logarithmic mean Divisia index (LMDI) decomposition analysis, the driving forces for such emission changes are examined. The findings indicate that the Chinese ISI has undergone a rapid increase in GHG emissions related to energy at an annual average growth rate of 70 million tons of CO₂ eq. The output scale effect is the key driving force for the rise in GHG emissions related to Energy in the Chinese ISI. In contrast, the effect of the energy intensity effect and the effect of the emission factor adjustment compensates for the overall increase the energy structure has a marginal effect.

Hasanbeigi et al. [25] aim to examine influential factors that have influenced the steel industry's energy usage in the past. They analyze the patterns in energy use of leading medium-sized and large-sized steel enterprises in China during 2000-2030. The research also uses a refined analysis of the Logarithmic Mean Divisia Index decomposition to measure the effects of different variables in influencing past and future energy consumption trends. Their forecast outcome indicates that key steel companies' final energy usage peaks in 2020 under scenarios 1 and 2 (low and medium scrap usage) and 2015 under scenario 3 (high scrap use). The three scenarios generated with the forward-looking decomposition study for 2010-2030 show that the structural effect and the pig iron ratio play a crucial role in decreasing final energy use during 2010-2030, contrary to experience during 2000-2010.

Wang et al. [26] analyze the iron and steel (IS) industry of China since it is the largest emitter of air contaminants and plays an essential part in achieving a green economy. They have used the logarithmic mean Divisia index (LMDI) method to examine the influencing factors of the IS industry's air pollutant emissions from environmental regulatory impact dimensions, the effect of pollutant generating intensity, the effect of energy structure, the effect of technological development and the effect of economic impact. Based on China's IS industry's empirical study from 2005 to 2015, three significant findings can be summarized. First, in controlling air pollution in the IS industry, environmental policy plays a decisive role. Second, environmental legislation and technological development have inhibitory effects on emissions of air pollutants. In contrast, the intensity impact of the production of pollutants and the scale effect encourage emissions to some degree. Third, the industry's decoupling efforts have steadily shifted from weak to strong.

Khan et al. [12] have used the LMDI method to calculate changes in CO₂ emissions in Pakistan over 1900-2017. The goal of this was to reduce the changes in CO₂ emissions. They have used five variables: activity effect, structural effect, intensity effect, fuel-mix effect, and emission factor effect. The three key factors responsible for changes in the country's overall CO₂ emissions have been established as the effects of the activity effect, structural effect, and intensity effect. The activity impact is the largest contributor to overall changes in the level of CO₂ emissions among all the effects. The structural effect positively affects CO₂ emissions, reflecting a change in economic activity to more energy-intensive sectors. Nevertheless, the strength effect has a negative emission relationship, which is a sign of improvements in energy efficiency. They have concluded that policymakers should promote the diversification of the energy and production mix into more energy-efficient economic sub-sectors.

To achieve emission reduction targets for determining to make a low-carbon transition of Turkey, we conduct a specific investigation on the Turkish high-energy intensive sector, iron, and steel, for the period 1998-2018 by employing the LMDI method.

To achieve emission reduction targets for determining to make a low-carbon transition of Turkey, we conduct a specific investigation on the Turkish high-energy intensive sector, iron, and steel, for the period 1998-2018 by employing the LMDI method.

Table 5. The change in greenhouse gas emissions in the iron and steel industry, kt CO₂ eq. (1998–2018).

Years	ΔC_{act}	ΔC_{str}	ΔC_{int}	ΔC_{mix}	ΔC_{emf}	ΔC_{tot}
	Activity effect	Structure effect	Intensity effect	Energy-mix effect	Emission factor effect	Total effect
1999-1998	-526	-523	787	-316	2	-576
2000-1999	418	76	507	-14	3	990
2001-2000	-2.005	1.208	-620	1.586	-2	166
2002-2001	1.068	-186	59	-1.213	0	-271
2003-2002	1.794	26	-1.584	-496	-3	-264
2004-2003	1.403	1.555	-2.916	-1.177	-5	-1.140
2005-2004	1.132	-235	-640	173	-4	425
2006-2005	457	800	-1.221	-983	-11	-958
2007-2006	972	434	-977	-309	-4	116
2008-2007	495	973	-1.144	-986	0	-662
2009-2008	-621	-1.497	1.824	-771	-0	-1.066
2010-2009	491	152	-75	-838	3	-268
2011-2010	240	997	-853	926	36	1.346
2012-2011	188	-172	-27	366	-46	308
2013-2012	387	-340	99	194	-0	340
2014-2013	-79	-23	15	440	1	354
2015-2014	-417	-691	1.345	1.179	-1.120	295
2016-2015	5	-543	664	-769	-454	-1.097
2017-2016	-50	1.170	-640	-104	-238	137
2018-2017	-331	874	-569	-129	39	-115
Total	5.019	4.055	-5.969	-3.240	-1.805	-1.940

4. Methodology

The LMDI method developed by Ang (Ang, 2005) was used in the formula below to determine the change in greenhouse gas emissions caused by the iron and steel industry and the effect of five factors thought to be determinant in the formation of this change

$$C = \sum_{ij} C_{ij} = \sum_{ij} Q \frac{Q_i E_i E_{ij} C_{ij}}{Q Q_i E_i E_{ij}} = \sum_{ij} Q S_i I_i M_{ij} U_{ij} \quad (1)$$

Where C is the total CO₂ emissions of the Turkish iron and steel industry; i specifies the i-th combustion sector; j represents the jth type of fuel $S_i = Q_i/Q$ represents the industrial structure, $I_i (=E_i/Q_i)$ represents the energy intensity of sector i; $M_{ij} (=E_{ij}/E_i)$ is the fuel-mix variable, and $U_{ij} (=C_{ij}/E_{ij})$ represents the CO₂ emissions factor of fuel j consumed in i sector [27].

The LMDI into the five components as illustrated;

- (i) The economic activity effect (ΔC_{act});
- (ii) The structure effect (shown as ΔC_{str});
- (iii) The sectoral energy intensity effect (shown as ΔC_{int});
- (iv) The sectoral energy-mix effect (shown as ΔC_{mix}); and
- (v) The emissions factor effect (denoted as ΔC_{emf}) in additive form.

5. Results and Discussion

The LMDI method developed by Ang (Ang, 2005) has been applied to determine the change in greenhouse gas emissions caused by the iron and steel industry into the effect of five for the period 1998-2018.

The LMDI can be expressed as:

$$\Delta C_{act} = \sum_{ij} \frac{C_{ij}^T - C_{ij}^0}{\ln C_{ij}^T - \ln C_{ij}^0} \ln \left(\frac{Q^T}{Q^0} \right) \quad (2)$$

$$\Delta C_{str} = \sum_{ij} \frac{C_{ij}^T - C_{ij}^0}{\ln C_{ij}^T - \ln C_{ij}^0} \ln \left(\frac{S_i^T}{S_i^0} \right) \quad (3)$$

$$\Delta C_{int} = \sum_{ij} \frac{C_{ij}^T - C_{ij}^0}{\ln C_{ij}^T - \ln C_{ij}^0} \ln \left(\frac{I_i^T}{I_i^0} \right) \quad (4)$$

$$\Delta C_{mix} = \sum_{ij} \frac{C_{ij}^T - C_{ij}^0}{\ln C_{ij}^T - \ln C_{ij}^0} \ln \left(\frac{M_{ij}^T}{M_{ij}^0} \right) \quad (5)$$

$$\Delta C_{emf} = \sum_{ij} \frac{C_{ij}^T - C_{ij}^0}{\ln C_{ij}^T - \ln C_{ij}^0} \ln \left(\frac{U_{ij}^T}{U_{ij}^0} \right) \quad (6)$$

Table-5 shows that economic activity and structural effect increase emissions, while density, energy composition, and emission factors decrease emissions.

5.1 Economic activity effect:

GDP is both an indicator of a country's economic performance and a measure of national wealth. It also shows the effect on total primary energy consumption resulting from an increase in production. Increasing economic output increases the activity effect and increases the growth rate in energy consumption. It positively contributes to the increase in energy consumption. If production falls, the economic activity effect reduces energy demand growth and negatively affects energy consumption change. The economic activity effect naturally harmed emissions in 1999, 2001, and 2009, when the economic recession (Table-5). However, despite the favorable growth rates of 5.2% in 2014, 6.1% in 2015, 7.5% in 2017, and 2.8% in 2018, there was a decrease in energy-related emissions in the iron and steel sector. This fact is related to the reduction in steel production compared to the previous year. The cumulative effect of economic activity rise of 5 kt GHG from 1998 to 2018 (Table-5).

5.2 Sectoral Structure Effect

The structural effect is the factor that indicates the change in the proportional value of each sector within the total economic activity (GDP). In other words, it is the change in total energy consumption resulting from the change (increase or decrease) in the total production composition of the iron and steel industry. For example, while the share of iron and steel production in GDP was 1.22% in 1999, this value was lower than 1.24% in 2000. This result creates an emission-increasing effect for the 2000-1999 period. The iron and steel industry's share in the total production composition between 2018-1998 increased from 1.34% to 3.18%. (Table -3) It led to a 4.0 Mtons increase in emissions due to the sectoral structure effect (Table-5).

5.3 Sectoral energy intensity effect

Energy density is the amount of energy used per unit output or process required. The density of the iron and steel industry is calculated as toe / 1000 \$ in this study. Therefore, density is an indicator of the toe's energy consumed for \$ 1000 in the sector. It is expected that the sectors' energy density would be lower with apply advanced, effective, and efficient production techniques and make improvements in material and fuel quality. Since technological change and progress need less energy to produce the same amount of product. In other words, much more product is expected to be obtained with the same amount of energy. [28]. Therefore, while energy density increases in the early stages of the developing economy and sectors, technological developments in the developed economy and sectors reduce the energy density and make production more efficient. Many studies in recent years have shown that

reducing its density limits or reduces energy-related greenhouse gas emissions. [7], [17], [19], [29]–[30].

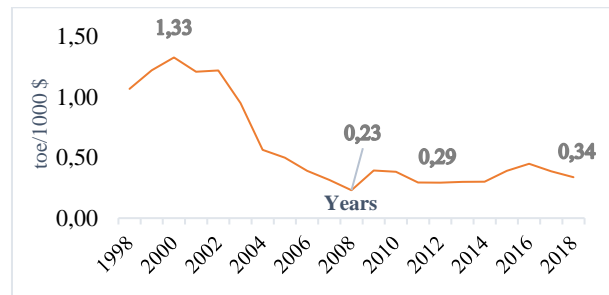


Figure 3. Energy intensity of the iron and steel industry by years (toe/1000 \$).

The iron and steel industry's energy intensity started to decline in 1999, and this trend continued until 2008 when the global economic recession occurred. The increasing intensity in 2009 started to decrease again in 2010 and 2011. Energy intensity, which has a steady-state between 2011 and 2014, started to increase in 2015 and reached the highest point of the last quarter of 2016. Since 2017, the sector has started to recover, and the energy intensity has started to decline again. Although the density effect took positive values in many years between 1998 and 2018, it generally has negative values. Especially in the period 2000-2008, the decrease in intensity significantly reduces the sectoral-based emissions. The downward trend was broken in 2009 with a high positive value. The impact of the global economic crisis in the iron and steel industry was felt seriously. Figure-3 shows that the density effect was not very useful in the 2010-2014 period. Decreases followed the increases in 2015 and 2016 in 2017 and 2018. It was determined that in 2015 and 2016, more energy consumption and lower revenue was obtained for unit product production. In particular, Turkey's steel production showed a drop for the third time in succession in 2015, while world steel production, the global financial crisis in 2009, and then-induced decline, declined for the first time in 2015. In the post-2016 period, the sector has taken advantage of significant energy use and technologies and energy-saving techniques and has managed to take the density effect to negative values (Figure-3). This improvement contributed to the reduction of the sectoral intensity effect by approximately 6.0 Mt in total emissions. (Table-5)

5.4 Sectoral energy mix effect

This effect shows how industries are using existing fuels and are calculated by dividing the energy consumption of a fuel type by the total energy consumption of that sector. Until 2009, solid (coke, derived gases, hard coal) and liquid fuels (petroleum products) and a limited quantity of natural gas was widely used in the iron and steel industry. In the period 2009-2018, solid and liquid

fuels were replaced by a high-rate of natural gas. Although this fuel composition change caused the fuel composition effect to have positive values in the 1998-2018 period, it took negative values in general. It caused the sector emissions to decrease by 3.2 Mt in total (Table-5).

5.5 Emission Factor Effect

The emission factor effect, which shows the effect of the fuel efficiency used in the sector on the emissions, does not affect the sectoral emissions between 1998-2014. (Table -5). Since there is no change in the carbon content of the fuels used for this period, however, it is determined that the emission reductions were caused by the usage of lower emission factors of the solid fuels used in 2015, 2016, and 2017. The plant-based emission factors could not be calculated until 2015; therefore, the default values in the IPCC 2006 Guidelines were used, and facility-based EF was calculated with calculations based on elemental analysis of fuels used in Integrated Iron and Steel plants since 2015. The emission factor effect reduced emissions between 2015-2017 by applying facility-based EF (Table-5).

6. Conclusion

The European Green Deal, which reveals the European Union's new strategic vision for 2050 with the perspective of "combating climate change and economic growth," to increase its citizens' welfare, live in a clean and healthy environment, and secure future generations. EGD was announced in 2019, and it is a new growth strategy prepared for the European Union that would provide more than it would spend. As our most important export and import partner, the EU plans to implement carbon border regulation mechanisms against commercial partners in 2021, would require serious measures, especially for our energy-intensive sectors. Mechanisms would profoundly affect our trade. Besides, it included being a party to the Paris Agreement and fulfilling the requirements of the Agreement in all international trade agreements that the EU has recently negotiated. In the Green Deal, the EU declared that it would adopt this practice for all future trade agreements; therefore, it is anticipated that this issue would come to the agenda in updating the Customs Union, which aims to be initiated by our country. Also, considering the legislative and implementation changes envisaged by the EU in the titles of Industry, Agriculture, Transport, and Energy, it is considered that a much wider part of our exports to the EU would be affected by the EU's climate change measures. This EGD implementation, which is obvious to have the most significant impact on a global scale, both its possible effects were evaluated and discussed with the measures taken to have the least impact on our country's iron and steel industry. For this purpose, the change in the energy-related greenhouse gas emissions

originating from the iron and steel industry from 1998 to 2018 was analyzed into five driving forces using the LMDI, one of the effective decomposition methods. Because of the analysis, it has been determined that the economic activity impact (GDP) is the most crucial determining factor behind the change in CO₂ emissions. It increases the emissions by 5 Mt. The sectoral structure effect means the change in the sectors' proportional value within the total economic activity.

Furthermore, it affects that similar to economic activity and increases 4 Mt in the specified period. The other three factors were found to reduce emissions. The sectoral energy intensity reduced emissions by about 6 Mt, followed by the energy mix effect with 3.2 million. The emission factor reduced the total emissions by around 2 Mt in the specified period.

The steel industry is among the most energy-consuming industries in the world. Improving energy efficiency in the iron and steel sector through the presentation and implementation of the latest technologies and techniques is essential because its share of total energy consumption in Turkey, 7.5%, and industrial consumption is around 22.9%. Studies are carried out in high-energy consumption units to reduce energy consumption in the blast furnace, coke factories, arc furnace, annealing furnace, energy systems feeding the furnace, dust holding, and cooling water systems. Our steel industry's energy share in input costs ranks 2nd after raw materials and has a high ratio of around 15-25%. The share of energy in production costs is sufficient to show how vital energy has for the iron and steel industry.

For this reason, our steel industry has drawn a roadmap for the development of projects that increase energy efficiency and continues to work towards renovation by continually improving its technology. In our steel industry, energy efficiency studies started in the 80s; considering the studies carried out in the last ten years; Energy consumption per ton of crude steel has been reduced by 18-20%. It is necessary to speed up energy efficiency studies to ensure sustainable low carbon development. It would be beneficial to use higher technology products and encourage renewable and carbon-free gases and technologies, mainly hydrogen, by the state.

Regarding climate change, the average compared to other countries per tons of steel crude steel production in Turkey (about 1.5 tons) of CO₂ emissions caused stated under (0.69 tons of CO₂). This result is mainly due to the predominance of electric arc furnaces in production (69.8% of the factories are electric arc furnaces in 2014). Major producers such as Erdemir are also developing projects for energy and resource efficiency with multilateral development banks' support. These are admirable developments. However,

in the fight against climate change went ahead to say that Turkey's steel sector would be misleading. The road to be taken is long for the sector players who are still at awareness and capacity building.

Furthermore, technological advances in reducing greenhouse gas emissions can only solve a part of the problem. Absolute mitigation measures such as reducing consumption, ensuring energy and resource efficiency, making electrification, and ensuring

electricity production in all processes must be implemented urgently, with fully independent of fossil fuels. The usage of renewable energy sources can achieve the best solution as they are both viable and do not damage the environment like fossil fuels and to reduce the high reliance on imported resources and to meet the envisaged 2023 goals of greenhouse gas emission reduction by using domestic energy sources.

Author's Contributions

Abdulkadir Bektaş: Drafted and wrote the manuscript, performed the experiment and result analysis.

Ethics

There are no ethical issues after the publication of this manuscript.

References

1. IPCC. "Proposed outline of the special report in 2018 on the impacts of global warming of 1.5 °C above pre-industrial levels and related global greenhouse gas emission pathways, in the context of strengthening the global response to the threat of climate change". IPCC - Sr15 2, 17–20, 2018.
2. European Commission, Speech by President von der Leyen in the Plenary of the European Parliament at the debate on the European Green Deal https://ec.europa.eu/commission/presscorner/detail/en/speech_19_6751 (accessed at 21.02.2021).
3. European Commission, EU Green Deal (carbon border adjustment mechanism) <https://ec.europa.eu/info/law/better-regulation/have-your-say/initiatives/12228-Carbon-Border-Adjustment-Mechanism/> (accessed at 21.02.2021).
4. Claey's, G., Tagliapietra, S. and Zachmann, G. (2019) How to make the European Green Deal work", Bruegel Policy Contribution.
5. TURKSTAT (2020) Turkish Greenhouse gas inventory report 1990–2018. Ankara: TURKSTAT. Available at: <https://unfccc.int/documents/223580>.
6. SteelData is the largest online steel statistics bank of Turkey <http://www.steel-data.com/> (accessed at 31.10.2020)
7. Zhang, M. et al. (2013) "Decomposition analysis of CO2 emissions from electricity generation in China." *Energy Policy*, 52, pp. 159–165. doi: 10.1016/j.enpol.2012.10.013
8. Song, Y., Huang, J. B. and Feng, C. (2018) "Decomposition of energy-related CO2 emissions in China's iron and steel industry: A comprehensive decomposition framework," *Resources Policy*. Elsevier Ltd, 59(March), pp. 103–116. doi:
9. Tian, Y., Zhu, Q. and Geng, Y. (2013) "An analysis of energy-related greenhouse gas emissions in the Chinese iron and steel industry," *Energy Policy*, 56, pp. 352–361. doi:
10. Hatzigeorgiou, E., Polatidis, H. and Haralambopoulos, D. (2008) "CO 2 emissions in Greece for 1990–2002: A decomposition analysis and comparison of results using the Arithmetic Mean Divisia Index and Logarithmic Mean Divisia Index techniques," *energy*, 33(3), pp. 492–499. doi: 10.1016/j.energy.2007.09.014.
11. Paul, S. and Bhattacharya, R. N. (2004) "CO2 emission from energy use in India: A decomposition analysis," *Energy Policy*, 32(5), pp. 585–593. doi: 10.1016/S0301-4215(02)00311-7.
12. Khan, A., Jamil, F. and Khan, N. H. (2019) "Decomposition analysis of carbon dioxide emissions in Pakistan," *SN Applied Sciences*. Springer International Publishing, 1(9), pp. 1–8. doi: 10.1007/s42452-019-1017-z.
13. Emodi, N. V. and Boo, K. J. (2015) "Decomposition analysis of CO2 emissions from electricity generation in Nigeria," *International Journal of Energy Economics and Policy*, 5(2), pp. 565–573.
14. Cansino, J. M., Sánchez-Braza, A. and Rodríguez-Arévalo, M. L. (2015) "Driving forces of Spain's CO2 emissions: A LMDI decomposition approach," *Renewable and Sustainable Energy Reviews*. Elsevier, 48, pp. 749–759. doi: 10.1016/j.rser.2015.04.011.
15. González, D. and Martínez, M. (2012) "Decomposition analysis of CO2 emissions in the Mexican industrial sector," *Energy for Sustainable Development*, 16(2), pp. 204–215. doi: 10.1016/j.esd.2012.01.005.
16. Sumabat, A. K. et al. (2016) "Decomposition analysis of Philippine CO2 emissions from fuel combustion and electricity generation," *Applied Energy*, 164, pp. 795–804. doi: 10.1016/j.apenergy.2015.12.023.
17. Akbostanci, E., Tunç, G. I. and Türüt-Aşık, S. (2011) "CO2 emissions of Turkish manufacturing industry: A decomposition analysis," *Applied Energy*, 88(6), pp. 2273–2278. doi: 10.1016/j.apenergy.2010.12.076.
18. Lise, W. (2006) "Decomposition of CO 2 emissions over 1980–2003 in Turkey," *Energy Policy*, 34(14), pp. 1841–1852. doi: 10.1016/j.enpol.2004.12.021.
19. Akbostanci, E., Tunç, G. İ. and Türüt-Aşık, S. (2018) "Drivers of fuel based carbon dioxide emissions: The case of Turkey," *Renewable and Sustainable Energy Reviews*, 81(July 2017), pp. 2599–2608. doi: 10.1016/j.rser.2017.06.066.
20. İpek Tunç, G., Türüt-Aşık, S. and Akbostanci, E. (2009) "A decomposition analysis of CO2 emissions from energy use: Turkish case," *Energy Policy*, 37(11), pp. 4689–4699. doi: 10.1016/j.enpol.2009.06.019
21. Rüstemoğlu, H. (2016) "Environmental costs of economic growth : Determinants of CO2 emissions in Turkey and Iran," pp. 2151–2168. Shao, S. et al. (2016) "Using an extended LMDI model to explore techno-economic drivers of energy-related industrial CO2 emission changes: A case study for Shanghai (China)," *Renewable and Sustainable Energy Reviews*. Elsevier, 55, pp. 516–536. doi: 10.1016/j.rser.2015.10.081.
22. Shao, S. et al. (2016) "Using an extended LMDI model to explore techno-economic drivers of energy-related industrial CO2 emission changes: A case study for Shanghai (China)," *Renewable and Sustainable Energy Reviews*. Elsevier, 55, pp. 516–536. doi: 10.1016/j.rser.2015.10.081. Ediger, V. Ş. and

- Huvaz, O. (2006) "Examining the sectoral energy use in Turkish economy (1980-2000) with the help of decomposition analysis," *Energy Conversion and Management*, 47(6), pp. 732–745. doi: 10.1016/j.enconman.2005.05.022.
23. Ediger, V. Ş. and Huvaz, O. (2006) "Examining the sectoral energy use in Turkish economy (1980-2000) with the help of decomposition analysis," *Energy Conversion and Management*, 47(6), pp. 732–745. doi: 10.1016/j.enconman.2005.05.022.
 24. Sun, W. qiang et al. (2011) "Change in Carbon Dioxide (CO₂) Emissions From Energy Use in China's Iron and Steel Industry," *Journal of Iron and Steel Research International*. Elsevier, 18(6), pp. 31–36. doi: 10.1016/S1006-706X(11)60074-5.
 25. Hasanbeigi, A., Jiang, Z. and Price, L. (2014) "Retrospective and prospective analysis of the trends of energy use in Chinese iron and steel industry," *Journal of Cleaner Production*. Elsevier Ltd, 74(2014), pp. 105–118. doi: 10.1016/j.jclepro.2014.03.065.
 26. Wang, X. et al. (2020) "Factor decomposition and decoupling analysis of air pollutant emissions in China's iron and steel industry," *Environmental Science and Pollution Research*. Environmental Science and Pollution Research, 27(13), pp. 15267–15277. doi: 10.1007/s11356-020-07997-w.
 27. Ang, B. W. (2004) "Decomposition analysis for policymaking in energy: Which is the preferred method?," *Energy Policy*. Elsevier BV, 32(9), pp. 1131–1139. doi: 10.1016/S0301-4215(03)00076-4.
 28. Du, G. et al. (2018) "A decomposition analysis of energy-related CO₂ emissions in Chinese six high-energy intensive industries," *Journal of Cleaner Production*, 184, pp. 1102–1112. doi: 10.1016/j.jclepro.2018.02.304.
 29. Wang, C., Chen, J. and Zou, J. (2005b) "Decomposition of energy-related CO₂ emission in China: 1957-2000," *energy*. doi: 10.1016/j.energy.2004.04.002.
 30. Lin, B. and Tan, R. (2017) "Sustainable development of China's energy intensive industries: From the aspect of carbon dioxide emissions reduction," *Renewable and Sustainable Energy Reviews*. Elsevier Ltd, 77(February), pp. 386–394. doi: 10.1016/j.rser.2017.04.042.

Modeling of Inverse Kinematic Analysis of Open-Source Medical Assist Robot Arm by Python

Mehmet Gül¹ 

¹Computer Engineering, Faculty of Engineering, Şırnak University, Şırnak, Turkey

*mehmetgul@ymail.com

*Orcid: 0000-0002-4819-4743

Received: 3 August 2020

Accepted: 1 March 2021

DOI: 10.18466/cbayarfbe.776697

Abstract

Today, the epidemic diseases such as COVID-19 spreads very fast in the globalizing world and lethal effects on human health have had a noticeable effect on the health sector. For this situations, various disciplines have had different studies to minimize the effects of the epidemic. In such cases, it is a separate requirement that the use of the opportunities brought by technology. In this study, the kinematic analysis of the open-source robot arm was especially examined in terms of reducing the workload of individuals working in the healthcare sector. The open-source robot arm is articulated and has 5 degrees of freedom. The kinematic analysis is very important for determination of the working space of the robotic systems. The inverse kinematic analysis was done with Python programming language and the control module was developed to check the analysis. The control module shows the angle values depending on the joints of the robot arm. It is also shown the Px, Py, and Pz positions obtained depending on the position of the end effector in 3D space. On the other hand, Euler angle values are also specified, which are based on the position of the last position taken by the joints of the robot arm in the 3D space. In the study, the geometric approach method was used that is still popular in the inverse kinematic analysis. It is hoped that this study will inspire the development and use of professional and industrial kinds of the open-source robot arm.

Keywords: Open-Source Robot Arm, Inverse Kinematic Analysis, Python

1. Introduction

Robot technology is an advanced technology innovation that requires a multidisciplinary area of research. In robot technology, numerous disciplines such as computer science, information and sensor technology, mechanisms, control theory and artificial intelligence need to cooperate. The prevalence of robotic arms, which are frequently used in industrial applications, is expanding day by day. On the other hand, the sophisticated robotic arms are both expensive and hard to maintain systems. The fact that epidemic diseases such as COVID-19, which today threatens human health, is a global treat, has revealed the importance of the healthcare staff especially in hospital in pandemic situations. In this study, open-source humanoid robot arms were emphasized to reduce the workload of healthcare professionals. Any contribution that can be made in pandemic situations where human health is a need has significance. However, it is obvious that the use of advanced scale robotic systems in hospitals

would pose both maintenance and expense burdens. Considering these situations, it will provide a significant cost gain that the production of open-source robotic arms on a professional scale printed from 3D printers and the development of control software as an open-source compared to their professional scale equivalent. On the other hand, it is of special importance that spare parts and maintenance are also easily provided. Determining of the working space of the robot arm is one of the most important issues in the robotic systems. This determination of workspace is possible by kinematic analysis. The working space is expressed by the point coordinate that end effector on the robot arm will form in three-dimensional space. There are some solutions methods for determination of the location of robot arm in the working space. Those are listed mainly as graphical method, analytical method and numerical method. The graphical method and analytical method are limited by the number of joints and inadequate in defining some robot arms, although, both the amount of calculation and the reliability in the numerical method cannot be guaranteed for some cases [1, 2]. Two

different space is used in kinematic analysis, Cartesian space and Quaternion space. The transformation between two Cartesian coordinate systems can be reduced to one turn and one translation. It is among used the methodologies to represent rotation that Cayley-Klein parameters, Gibbs vector, Euler angles, and orthonormal matrices, while in robotics, homogeneous transformations based on 4x4 real matrices are predominantly used [3]. In the study, it was examined the kinematic analysis of open-source professional 5 degree of freedom robotic arm obtained from 3D printer by Denavit-Hartenberg (D-H) method [4].

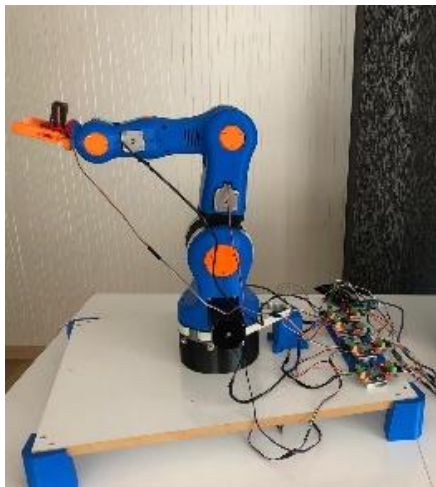


Figure 1. Medical Assist Robot arm printed from the 3D printer

Python programming language was used to determine the analysis of the workspace, and the position of the robot arm in the workspace was analyzed by the D-H method. It was examined the inverse kinematic analysis after determination of the working space of robot arm. kinematic analysis of the medical assist robot arm is open-source software format. Open-source medical assist robot arm is suitable for development (figure 1). The robot arm is also an articulated kind. Kinematic analysis is extremely important in robotic systems, in other words, it is equivalent to controlling robotic systems. In particular, inverse kinematic modelling continues to pose one of the major problems in today's robot research. On the other hand, the most popular method for controlling robotic arms is as yet dependent on manually designed scanning tables [5 – 8]. The D-H method is used to determine working space of robot arm and its position to control. The key to the D-H method is to demonstrate the relationship of the coordinate system of all joints. In the scope of the method, a series of D-H parameters are created.

2. Robot Arm Kinematic

In robotic systems, kinematic analysis is divided into two parts, forward and inverse kinematics. While the

inverse kinematic analysis examined, the complexity of the equations makes the solutions difficult, however this is not the case in forward kinematic analysis. The obvious reason for the complexity is not particularly linear. Although nonlinear equations cannot be combined, there are no one-to-one solutions. While nonlinear equations cannot combine, moreover, they do not have unique solutions. There are numerous studies in this searching area, while in certain studies the geometric approach is used for inverse kinematic analysis solutions [9], while in some other studies double quaternion is used [10]. Particularly in many recent studies, it is seen that artificial intelligence (AI) methods are used in inverse kinematic solutions of robotic systems [11 – 13]. Among the prominent studies, while the position/force values are used for the control of the dual robot system [14], the robot arm was controlled by calculating of the position/force values required for the B-Hand robots with 4 degrees of freedom [15].

2.1. Inverse Kinematic Analysis

Different approaches have been adopted for kinematic analysis of robotic systems and especially for inverse kinematic solutions. In the study [16], closed form solution and zero moment point approach were used in the robotic system with 18 DoF. In another study, optimal path in Cartesian space was performed using the particle swarm optimization (PSO) algorithm for inverse kinematic of the robot arm with two degrees of freedom [17]. Inverse kinematic analysis of the robot arm with two degrees of freedom was developed using the genetic algorithm approach by Chaitanyaa et al. [18]. Jones and Walker developed inverse kinematic analysis for the continuum robots within the structure of the modular approach [19]. Radavelli et al. performed the kinematic analysis of robotic systems by comparing DH convention and Dual Quaternion approaches [20].

In a study conducted in 2015, screw theory was used in the inverse kinematic analysis process [21]. In another conducted study, the metaheuristic methods were used to determine the working space of robots [22]. In the study [23], analytical inverse kinematic solution was done with data obtained from D-H tables. At the point when the literature is examined, especially, that are developed numerous different inverse kinematic analysis solutions in robotic systems. The studies of inverse kinematic solutions are limited compared to geometric approaches. It means that the geometric approach is still prominent in inverse kinematic solutions. The inverse kinematic analysis is a basic assignment for the operation and structure of robotic systems. Analysis of this critical problem continues to pose serious problems in the robotic systems. It is basic to make the most inverse kinematic calculations for complete control of the robotic system. In particular, serious problems are posed to determine the position of the robot and the calculation of all joint angles

corresponding to the position [24]. Although there are numerous packages available for numerical inverse kinematics, an initial value is required to find just one of the multiple solutions. Besides, normal requirements, for instance, it must be overcome that dependency and convergence of individual initial value configurations [25, 26].

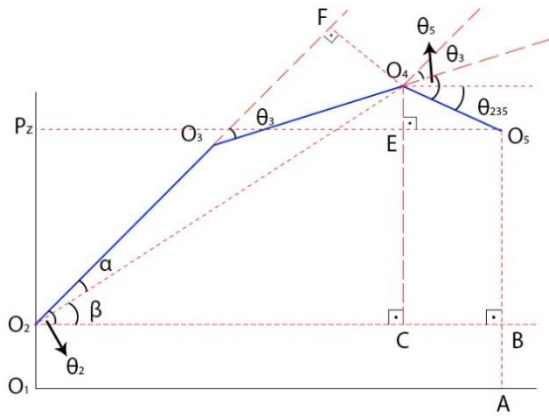


Figure 2. Solution of the inverse kinematic analysis of robot arm by geometric approach method

Briefly, inverse kinematic analysis in robotic systems is called the analysis of the end effector and how many different configurations can be performed. In other words, if n , o , a , and p variables and geometric variables are known, joint variables can be resolved in kinematic solutions θ_i ($i = 1, 2, \dots, 6$) [27]. The equation required for the solution of inverse kinematic is as follows. Geometric method is used for the inverse kinematic solution of the medical assist robot arm (figure 2).

3. Control Module of Robot Arm

In the study, it was examined the inverse kinematic analysis of the medical assist robot arm with Python programming language. The graphical user interface (GUI) was developed via Python to control inverse kinematic analysis. The model GUI was designed as shown in figure 3 below, the controlled system was simulated too. The robot arm is shown in figure 1 and it has 5 active joints. 3rd and 4th joints are connected to each other in form of twisting joints. The controlled functions via the GUI are as follows;

- Controlling the simulation process
- Monitoring of joint angle information
- Obtaining exposure information of the manipulator

In this study, an open-source robot arm was printed on the 3D printer and it was 5 DoF features that aims to help hospital staff. Additionally, the kinematic analysis was performed to control robot arm. Inverse kinematic analysis of the robot was performed via the GUI. In the solution of the kinematic equation, it was used homogeneous transformation theory. The GUI interface was prepared with Python programming language. The biggest advantage of the robot arm prepared within the scope of the study is that it has 5 DoF degree of freedom at a professional usage and its production cost is low. In the next phase of the study, which is aimed to reduce workload of healthcare staff as much as possible, robotic arm will be designed based artificial intelligence applications that will be created by parallel operation.

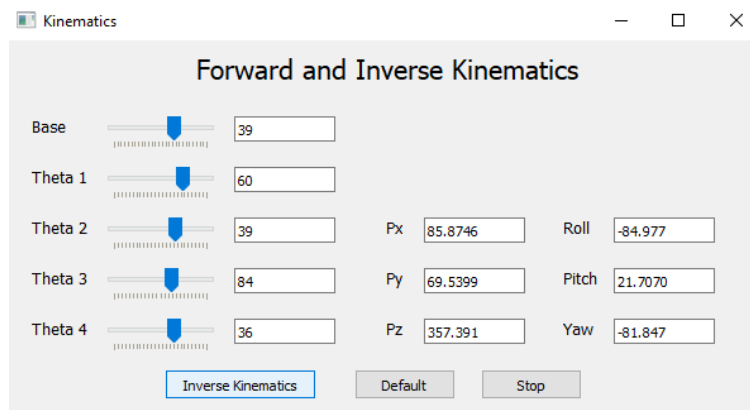


Figure 3. Control module prepared with Python programming language

In the prepared the GUI interface, in the inverse kinematic analysis, it is specified the position of P_x , P_y , and P_z depending on 5 angles obtained from the position of the end-effector. While the position of the end-effector is determined in the working space, Euler angles are also calculated and shown in the interface.

4. Conclusions and Recommendations

In this study, it was performed the inverse kinematic analysis of open-source robot arm with 5 DoF. In the inverse kinematic analysis process, it was determined conceivable inverse movement of the robot arm in the working space. During the analysis phase, the D-H

parameter table was created and an analysis was made based on the homogeneous transformation theory. The GUI interface was created via Python for analysis. It is hoped that this study will inspire the development of open-source robotic systems especially professional kinds robotic arm, and the development of kinematic analysis.

Author's Contributions

Mehmet Gül: Drafted and wrote the manuscript, performed the experiment and result analysis.




Ethics

There are no ethical issues after the publication of this manuscript.

References

1. Haibo, T, Hongwei, M, Juan, W. 2013. Workspace and Structural Parameters Analysis for Manipulator of Serial Robot Manipulator workspace analysis using the Monte Carlo method, *J. Transactions of the Chinese Society for Agricultural Machinery*, 44 p. 196-201.
2. Ming, Z, Qingzhong, H. 2013. The Workspace Analysis of the Articulated Palletizing Robot, *J. Modular Machine Tool & Automatic Manufacturing Technique*, 7 p. 68-74.
3. Funda, J, Taylor, RH, Paul, RP. 1990. On homogeneous transforms, quaternions, and computational efficiency, *IEEE Trans. Robot. Automation* 6, pages 382–388.
4. Klafter, RD, Chmielewski TA, Negin. M. 1989. *Robotic Engineering: An Integrated Approach*. Prentice Hall.
5. Mittal, RK, Nagrath, J. 2005. *Robotics and Control*, Tata McGraw-Hill.
6. McKerrow, PJ. 1991. *Introduction to Robotics*. Addison-Wesley.
7. Niku, SB. 2001. *Introduction to Robotics: Analysis, Systems, Applications*. Prentice Hall.
8. Denavit, J, Hartenberg, RS. 1955. A kinematic Notation for Lower- Pair Mechanism Based on Matrices. *ASME Journal of Applied Mechanics*, 215-221.
9. Liu, Y, Wang, D, Sun, J, et al. 2015. Geometric approach for inverse kinematics analysis of 6-dof serial robot, *IEEE International Conference on Information and Automation*, pages 852-855
10. Qiao, S, Liao, Q, Wei, S, Su, H. 2010. Inverse kinematic analysis of the general 6R serial manipulators based on double quaternions, *Mechanism and Machine Theory* 45, 193-199.
11. Almusawi, ARJ, Dülger, LC, Kapucu, S. 2016. A new artificial neural network approach in solving inverse kinematics of robotic arm (denso vp6242), *Computational Intelligence and Neuroscience*
12. Köker, R. 2013. A genetic algorithm approach to a neural-network-based inverse kinematics solution of robotic manipulators based on error minimization, *Information Sciences* 222, 528-543.
13. Duka, AV. 2014. Neural network based inverse kinematics solution for trajectory tracking of a robotic arm, *Procedia Technology* 12, 20-27.
14. Uchiyama, M, Iwasawa, N, Hakomori, K. 1987. Hybrid position/force control for coordination of two-arm robot. in *Proceedings of the IEEE International Conference on Robotics and Automation*, pp. 1242–1247.
15. Kopf, CD, Yabuta, T. 1988. Experimental comparison of master/slave and hybrid two arm position/force control. in *Proceedings of the IEEE International Conference on Robotics and Automation*, vol. 3, pp. 1633–1637.
16. Mandava, RK, Vundavilli, PR. 2016. Forward and inverse kinematic based full body gait generation of biped robot. *Proceedings of the International Conference on Electrical, Electronics and Optimization Techniques*, Mar 3-5, IEEE Xplore Press, Chennai, India, pp: 3301-3305. DOI: 10.1109/ICEEOT.2016.7755317
17. Sadiq, AT, Raheem FA, Abbas, NA. 2017. Optimal trajectory planning of 2-DOF robot arm using the integration of PSO based on D* algorithm and cubic polynomial equation. *Proceedings of the 1st International Conference for Engineering Researches*, (CER' 17), Middle Technical University, Baghdad-Iraq, pp: 458-467.
18. Chaitanyaa, G, Reddy, S. 2016. Genetic algorithm based optimization of a two Link planar robot manipulator. *Int. J. Lean Think.*, 7: 1-3.
19. Jones, BA, Walker, ID. 2006. Kinematics for multisection continuum robots. *IEEE Trans. Robot.*, 22: 43-55. DOI: 10.1109/TRO.2005.861458
20. Radavelli, L, Simoni, R, De Pieri E, Martins, D. 2012. A comparative study of the kinematics of robots manipulators by Denavit-Hartenberg and dual quaternion. *Mecánica Comput. Multi-Body Syst.*, 31: 2833-48
21. Chen, Q, Zhu S, Zhang, X. 2015. Improved inverse kinematics algorithm using screw theory for a sixDOF robot manipulator. *Int. J. Adv. Robotic Syst.*, 12: 140-140. DOI: 10.5772/60834
22. Raheem, FA, Sadiq AT, Abbas, NAF. 2019. Robot arm free Cartesian space analysis for heuristic path planning enhancement. *Int. J. Mech. Mechatron. Eng.*, 19: 29-42.
23. Sun, JD, Cao, GZ, Li, WB, Liang, YX, Huang, SD, 2017. Analytical inverse kinematic solution using the D-H method for a 6-DOF robot. *Proceedings of the 14th International Conference on Ubiquitous Robots and Ambient Intelligence*, Jun. 28-Jul. 1, IEEE Xplore Press, Jeju, South Korea, pp: 714-716. DOI: 10.1109/URAI.2017.7992807
24. Xiao WL, Henning S, Torsten L, et al. 2011. Closed-form inverse kinematics of 6R milling robot with singularity avoidance. *Prod Eng Devel* 5:103–110
25. Corke, PI. 1996. A robotics toolbox for matlab. *IEEE Robotics Automation Magazine*, vol. 3, no. 1, pp. 24–32
26. Kelmar L, Khosla, PK. 1990. Automatic generation of forward and inverse kinematics for a reconfigurable modular manipulator system," *Journal of Robotic Systems*, vol. 7, no. 4, pp. 599–619 [Online]. Available: <http://dx.doi.org/10.1002/rob.4620070406>
27. Wu Y, Cheng LH, Fan GF, et al. 2014. Inverse kinematics solution and optimization of 6-DOF handling robot. *Appl Mech Mater* 635–637:1355–1359

Static Analysis of the Slotted Upper Plate of Low Pressure Casting Machine

Yasemin Nur Aydın^{1,3*}, Onur Özyayın¹, Alper Akış^{2,3}

¹Cevher Wheels / R&D Department, İzmir, Turkey

²Numesys Inc. / Mechanical Business Unit, İzmir, Turkey

³Manisa Celal Bayar University /Department of Mechanical Engineering, Manisa, Turkey

*yaseminnuraydinn@gmail.com

*Orcid: 0000-0001-7083-2329

Received: 12 August 2020

Accepted: 11 March 2021

DOI: 10.18466/cbayarfbe.779687

Abstract

In this study, the process improvement / Kaizen case study of a casting mold set-up process, was examined. The aim of this work was reducing the set-up time and improving ergonomic conditions. Since existing operating conditions cause a waste of time, an air impact wrench had to be used in the mold assembly process. To be able to use the air impact wrench, a new geometry had to be implemented on casting mold and this design change was analyzed in ANSYS software to avoid a failure in working conditions. It was concluded that the maximum stress on the mold was not at a level where it would cause failure. After the initial geometry improvement process, a further ANSYS-Topology optimization process was conducted to reduce weight of the mold. As a result, the set-up time decreased. Consequently, big benefits in terms of cycle time, occupational health and safety, improvement in the process and cost have been achieved.

Keywords: ANSYS Static Structural, ANSYS Topology Optimization, Case Study, Kaizen, Process Improvement

1. Introduction

In today's conditions, parameters such as production speed, quality, cost and reliability have a great importance in the globalizing producer-consumer society. Process improvements have a critical value for competitive manufacturers, as they reduce cost and waste of time [1]. To improve their processes, manufacturers are inspired by a variety of principles like Kaizen, 6 Sigma and lean manufacturing [2, 3].

Kaizen states that improvement of the process by the manufacturers is as important as the quality of the product. It emphasizes that unknown or uncontrolled parameters are a risk in terms of sustainability of the product quality [4]. Many manufacturers implement improvements by applying the Kaizen principles in their work. Modarress et al. determined a case study and defined Kaizen costs to reduce existing costs of Boeing Commercial Aviation Company, improve quality, and reduce cycle time [5]. Venkataramana et al. studied a case to increase the export prices of crankshaft production, which is the domestic production of an automotive company in India. The production time was

decreased by 40%, the production capacity was increased, and production errors were reduced, resulting in a higher customer satisfaction [6]. Kumar et al. investigated the effects of Kaizen on production techniques and delivery times to increase the competition of small-scale industrial organizations in India [7]. Kumar et al. reduced the stock level, delivery time, cycle time by implementing the lean-Kaizen principle in a medium-sized enterprise, thereby achieving improved efficiency and improved product quality [8]. Özdağoğlu et al. studied on reducing the cycle time with Kaizen and lean manufacturing principles of a company producing PVC films [9].

Designers must optimize their designs in today's competitive market in terms of cost and time. For this reason, to survive in competitive and rapidly changing conditions, fast, efficient, functional and cost-effective designs should be introduced in this scope the efficient utilization of CAD and CAE software becomes compulsory. Additionally, topology optimization tools are widely used to improve designs without succumbing to unnecessary design iteration loops. Topology optimization is a useful method to reduce weight

without endangering safety or strength of the product [10, 11]. In the literature many topology optimization studies in many diverse applications can be found; some examples are truck chassis, deck lid and undercarriage [12], automotive chassis [13], automotive engine mounts [14], machine tools [15], cast iron feeding system [16], implants [17], [18].

In this study, an air impact wrench is selected to reduce the production cycle time and improve the process ergonomically. The manual mold assembly process is not suitable for hot working conditions of the casting shop due to dependence on manpower. For this reason, the mold geometry has been redesigned to allow the utilization of an air impact wrench. The maximum Von-mises stress (equivalent stress) values of the original geometry and the slotted geometry are compared using at ANSYS - Static Structural software. After the stresses are examined and no risk is found, slots are opened on the actual casting mold. Due to this slotted geometry, the air impact wrench reduces work cycle time by 11 minutes and the workstation is improved ergonomically. Finally topology optimization is conducted on the upper plate of casting mold and Von-Mises stress (Equivalent stress) results of the geometry obtained via topological optimization is examined.

2. Materials and Methods

Different sizes of casting molds are used in the casting factories depending on the product and molds on casting machines must be changed in accordance with the demands of production planning. This process is called mold assembly. Safety, set-up time and ergonomics are priorities of the mold assembly process. The reason for working on the mold assembly station is to provide better working conditions and reduce high cycle time as seen in Figure 1.



Figure 1. Working conditions and casting mold assembly process

Before making changes on actual casting mold, ANSYS software is used to determine safety risks of the new design by calculating stresses.

In the geometry shown in Figures 2.a and 2.b, structural steel material is used for the lower pusher plate and upper pusher plate, lower plate, upper plate, pillars where the slots are opened, bridge, centering shafts, upper plate dowel pins and centering bushings.

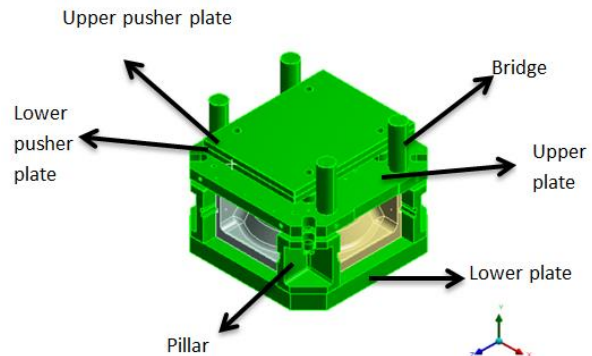


Figure 2.a. The representation of the lower pusher plate and upper pusher plate, lower plate, upper plate, pillars where the slots are opened, bridge.

Table 1. Torque information table required for screwing-loosening the bolt regulated by DIN EN ISO 4014-4018, DIN ISO 262, DIN 34800, DIN EN ISO 4762, DIN EN 20 273 standards [19].

Size	Streight Class	Assembly preload forces F_{MTab} in kN for $\mu_G =$							Tightening torques M_A in Nm for $\mu_K = \mu_G =$						
		0,08	0,10	0,12	0,14	0,16	0,20	0,24	0,08	0,10	0,12	0,14	0,16	0,20	0,24
M 18	8.8	107	104	102	99	96	91	85	220	259	295	329	360	415	462
	10.9	152	149	145	141	137	129	121	314	369	421	469	513	592	657
	12.9	178	174	170	165	160	151	142	367	432	492	549	601	692	769
M 20	8.8	136	134	130	127	123	116	109	308	363	415	464	509	588	655
	10.9	194	190	186	181	176	166	156	438	517	592	661	725	838	933
	12.9	227	223	217	212	206	194	182	513	605	692	773	848	980	1092

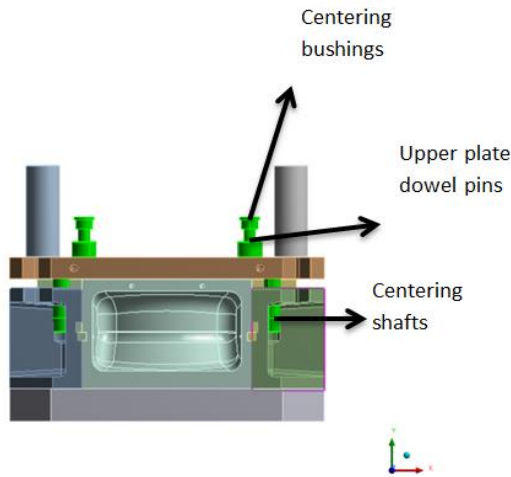


Figure 2.b. The representation of the centering shafts, upper plate dowel pins and centering bushings on the mold geometry.

In the geometry shown in Figure 3.a and 3.b, the side cores materials are cast iron, the upper core is hot work tool steel, and the bottom core is mold cast steel.

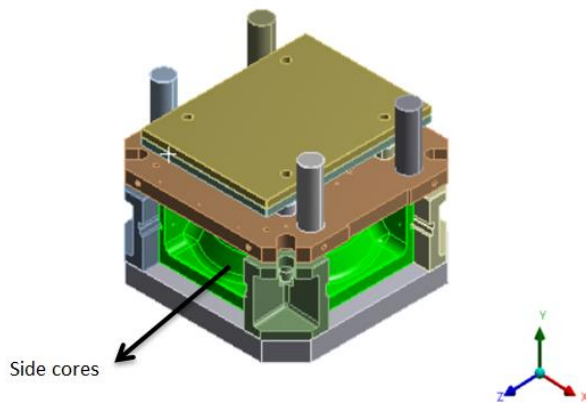


Figure 3.a. The representation of the side cores.

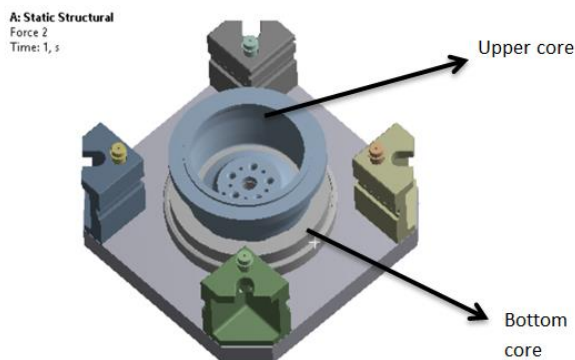


Figure 3.b. The representation of the upper core and bottom core on mold geometry.

After modelling the individual components, the contact conditions are defined. The number of mesh elements is 1.249.023 and the number of nodes is 1.872.114. As boundary conditions, the weights of the upper and lower plates in Figure 5.a were determined to be 1540,8 N. The force of the hydraulic press has been determined to be 62860,6 N applied to the cylindrical upper surfaces of the bridge elements. As a boundary condition, the surface of the mold that contacts the ground is taken as a fixed support as shown in Figure 4.

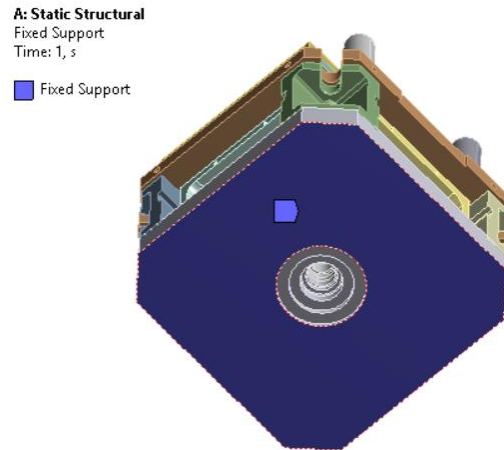


Figure 4. Fixed support surface of the mold that the contacts of the ground.

In order to compare the stress results, the same processes are repeated on the slotted geometry with same boundary conditions as shown in Figure 5.b.

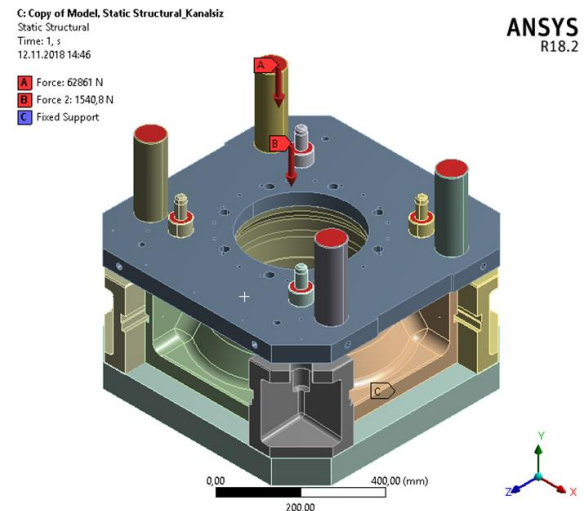


Figure 5.a. Force values shown on original geometry and display of fixed geometry (fixed support).

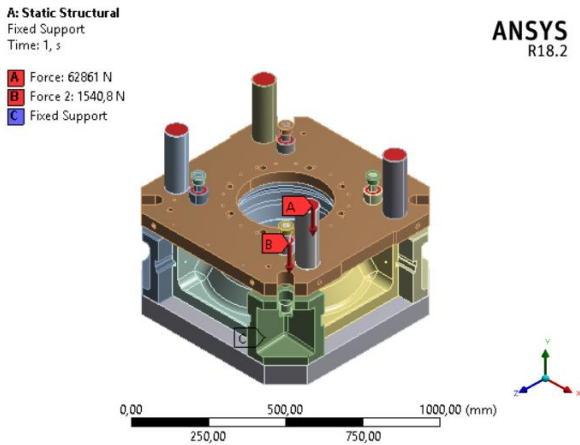


Figure 5.b. Force values shown on slotted geometry and display of fixed geometry (fixed support).

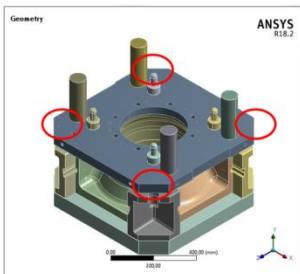


Figure 6.a. 3D geometry in ANSYS.



Figure 6.b. Actual view of the mold before revision.

The slots are applied in the red circled corners as shown in Figure 6.a. As seen in Figure 6.b, non-ergonomic condition is encountered during the casting mold assembly. Since the air impact wrench is not physically suitable for the region due to restricted space in the corners of the mold where the assembly process will be performed, it is necessary to implement a slot on the mold corners.

As shown on Figure 7.a and 7.b, certain material removal on the corners are necessary so that the torque wrench can reach bolts, also stud of the torque wrench should be extended for greater length. Air impact wrench has a specified working torque range of 250-1250 Nm to supply 773 Nm of torque as shown in Table 1.

To compare the static stresses on the slotted model, the slotted casting mold geometry is modeled as in Figure 8.a. The operation is carried out on the casting mold upper plate's corner as in Figure 8.b after positive evaluation of Ansys safety examination.

After the slotted geometry is created and the analysis conditions are prepared, topology optimization process is defined on the slotted geometry at ANSYS- Topology Optimization module. The aim of topology optimization is to reduce the amount of raw material during the mold production and to create a lighter upper plate design that supplies the tension values



Figure 7.a. Air impact wrench intermediate lever and end bits view.

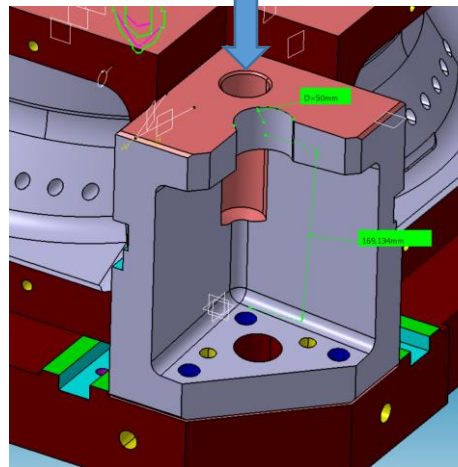


Figure 7.b. Dimensioning of the slot opened on the mold and 3D geometry.

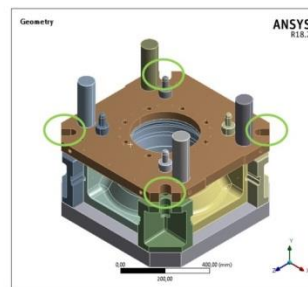


Figure 8.a. 3D geometry in ANSYS.



Figure 8.b. Image of the slotted mold.

In this way, the optimum design that will provide a reduction in raw material costs is created.

In order to perform topology optimization, the upper plate is chosen as the region where mass removal will be applied. The solution method is chosen based on the topology optimization as density based [20]. The parameter to be changed on the upper plate is mass, 75% of the mass is preserved (response constraint). As a result of the change in the mass, static analysis results of slotted and original geometry are examined. Design verification studies are carried out without any financial or time loss thanks to the simulations performed in computer environment [21].

3. Results and Discussion

3.1. Cycle Time Changing

Before the improvement process, the mold assembly process was 20,3 minutes on average. After improvement, process is decreased to 9,1 minutes on average because of the 6-month project implementation. In this way, the cycle time is reduced by 11,2 minutes as shown in Figure 9.

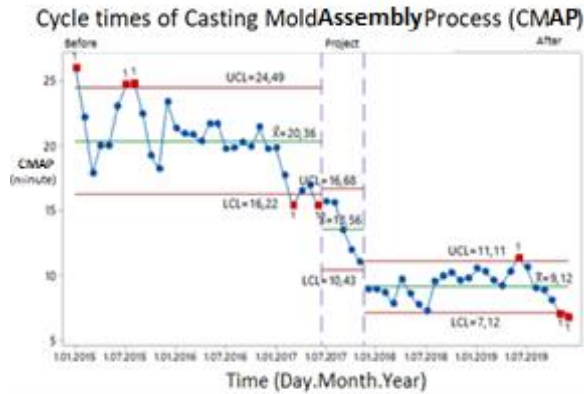


Figure 9. Before and after project cycle times of casting mold assembly process (CMCP)

An average of 11,2 minutes of change in cycle time means that a total of 101,1 minutes of profit is achieved per day in 3 shifts, assuming that an average of 3 molds are changed in the shift. Since the average cycle time of a rim is 330 seconds, it means $101,1 \text{ min} * 60 \text{ seconds} / 330 \text{ seconds} = 18,4$, meaning that there can be approximately 18 additional casting wheels per a day.

3.2. Slotted Geometry

The results of the original geometry and slotted upper plate geometry modeled in the ANSYS-Static Structural software are shown in Figure 10.a and 10.b.

In the original geometry shown in Figure 10.a, the maximum Von-Mises stress (Equivalent stress) caused by the boundary and loading conditions of the upper plate is 60,6 MPa. The maximum Von-Mises stress (Equivalent stress) caused by the same boundary conditions and load on the upper plate is shown in Figure 10.b and is found to be 46,7 MPa.

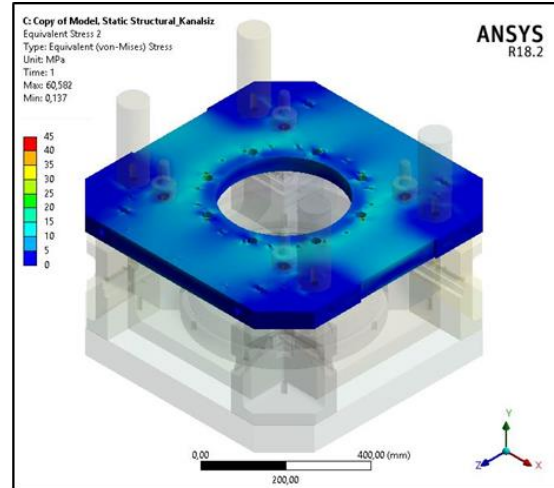


Figure 10.a. Von-Mises stress (Equivalent Stress) results of original geometry

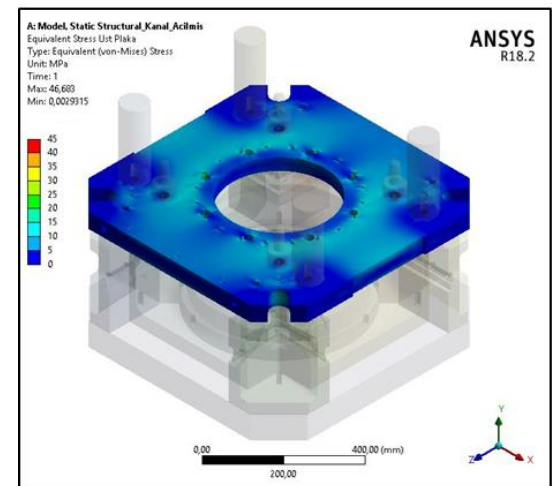


Figure 10.b. Von-Mises stress (Equivalent Stress) results of slotted geometry

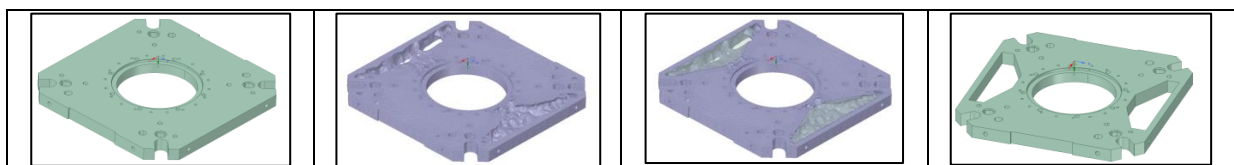


Figure 11. Topology optimization on slotted geometry

As a result, the maximum Von-Mises stress (Equivalent stress) value of the upper plate in slotted geometry is lower than the original geometry. It is concluded that the slot opened on the upper plate can be applied on the

molds according to the static stress value results. In this way, while the stress values are decreasing on the upper plate, the casting mold assembly cycle time has decreased by an average of 11, 2 minutes. So a lighter, more ergonomic, and safer solution was found.

3.3. Topology Optimization

The topology optimization is performed on the upper plate with ANSYS-Topology Optimization module as shown in Figure 11. 25% of the mass is reduced on the upper plate and a reduction of approximately 31 kg is achieved after optimizing the upper plate. However static stress values are also critical in the slotted geometry so a new static analysis of the new optimized geometry with the same boundary conditions as before is performed and the results were compared in Figure 12.a and 12.b.

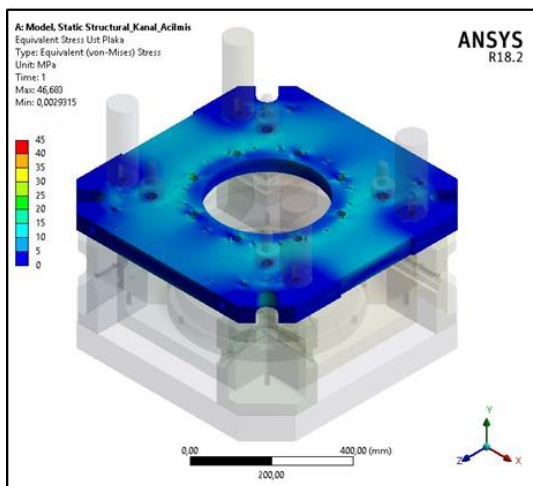


Figure 12.a. Slotted geometry analysis of the upper plate

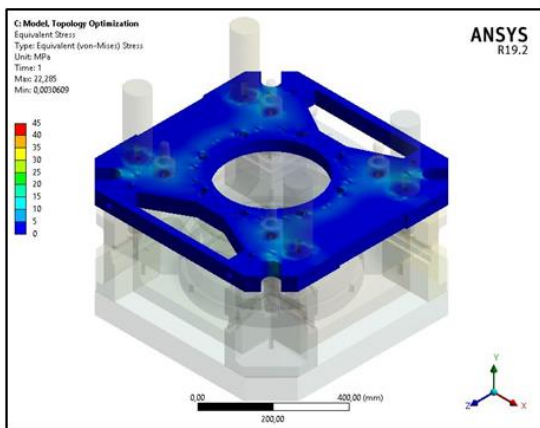


Figure 12.b. Optimized geometry analysis of the upper plate

At a first glance an axisymmetric 4-sided material removal would be expected, but actually the bridges on top of the mold are positioned as a rectangle and are not axisymmetric. As seen in Figure 12.a, under the boundary conditions of the slotted geometry, while the maximum Von-Mises stress (Equivalent Stress) of the upper plate is 46,6 MPa, as seen in Figure 12.b, the maximum Von-Mises stress in the optimized of the upper plate (Equivalent) Stress) is 22,2 MPa. The mass of the upper plate is reduced 31 kg. The decrease in the maximum Von-Mises stress indicates that the optimized

upper plate can be used in future mold designs. The decrease in the mass on the upper plate will provide mold casting with less cost and more functionality on the increased wheel dimensions designs.

4. Discussion

As a result of the work done,

- Field work was carried out to improve the casting mold assembly process. Air impact wrench was provided to supply the required torque level for the non-ergonomic changing procedure with a long cycle time and an improvement was made in the changing procedure.

- Suitable slots for the end bits and intermediate lever were opened in the corners to allow usage of the air impact wrench. After the geometry was slotted, the maximum Von-Mises stresses were taken into consideration. It was concluded that the stress on the upper plate decreased.

- As a result, the cycle time was reduced by 11,2 minutes, saving enough time to produce 18 wheels per day. In this way, the efficiency of the slotted geometry, which had less strain than the original geometry, in the changing process had a positive effect on the annual profit of the company.

- Topology optimization had been made on the upper plate of the casting mold to be produced in the future. 25% of the upper plate mass was reduced by 31 kg in total and the maximum Von Mises stress on the upper plate was also reduced. In this way, the cost of raw materials had been reduced and a better mold design had been created in terms of fatigue because of the decrease in tension.

In the future slotted geometry will carry out on casting mold and experimental work will investigate. This geometrical improving may applied to other wheel moulds. This approach may be used for other moulds, equipments and apparatus.

Acknowledgement

The authors would like to thank Cevher Wheels Company and Numesys Inc. for the permission to publish this article.

Author's Contributions

Yasemin Nur Aydın: Drafted and wrote the manuscript, performed the experiment and result analysis.

Onur Özeydin: Supervised the experimental and analytical progress, result interpretation and helped in manuscript preparation.

Alper Akış: Supervised the experimental and analytical progress, result interpretation and helped in manuscript preparation.

Ethics

There are no ethical issues after the publication of this manuscript.

References

1. Kabadayı, E. T. 2002. İşletmelerdeki Üretim Performans Ölçütlerinin Gelişimi, Özellikleri ve Sürekli İyileştirme ile İlişkisi. *Doğuş Üniversitesi Dergisi*; 61-75.
2. Joseph C. Chen, Y. L. 2010. From Value Stream Mapping Toward a Lean/sigma Continuous. *International Journal of Production Research*; 48: 1069–1086.
3. C-C Wang, K.-S. C.-H.-H. 2010. Application of 6-sigma Design System to Developing an Improvement Model for Multi-process Multi Characteristic. Vol. 225 Part B: *J. Engineering Manufacture*; 1205-1216.
4. Berger, A. 1997. Continuous improvement and kaizen: standardization and organizational designs. *Integrated Manufacturing Systems*; 110–117.
5. B. Modarress, A. A. 2005. Kaizen Costing for Lean Manufacturing: a Case Study. *International Journal of Production Research*; 43: 1751–1760.
6. K. Venkataramana, B. R. 2014. Application of Value Stream Mapping for Reduction of Cycle Time in a Machining Process. *Procedia Materials Science*; 6: 1187 – 1196.
7. Amit Kumar, A. a. 2013. Impacts of Kaizen in a Small-scale Industry of India: a Case Study. *International Journal of Lean Six Sigma*; 22-45.
8. Sunil Kumar, A. K. 2018. Process Improvement Through Lean-Kaizen Using Value Stream Map: A Case Study in India. *The International Journal of Advanced Manufacturing Technology*; 96: 2687–2698.
9. Aşkın Özdağoğlu, S. R. 2016. Applications of Kaizen and Cycle Time Reduction as Lean Production Techniques in a Semi-flexible PVC. *Int. Journal of Management Economics and Business*; 12: 25-37.
10. ANSYS Topology Optimization. 2017. White paper, ANSYS Inc., Canonsburg, PA U.S.A.; 1-4.
11. Dr.-Ing. Markus Stephan, D.-I. D.-P.-M. 2009. CFD Topology Optimization of Automotive Components. 4th European Automotive Simulation Conference EASC.
12. Chahande, R. Y. 1995. Automotive Applications of Topology Optimization. *Structural Optimization*; 9: 245-249.
13. Marco Cavazzuti, A. B. 2011. High performance automotive chassis design. *Struct Multidisc Optim*; 44: 45–56.
14. Chao Li, I. Y. 2015. Conceptual and Detailed Design of an Automotive Engine Cradle by Using Topology, Shape, and Size Optimization. *Structural and Multidisciplinary Optimization*; 51: 547–564.
15. Hüseyin Güçlü YAVUZCAN, M. Ö. 2015. Yatık Ağız Açma Ve Kalibre Etme Makinasının Yapısal Analizi Ve Ağırlık Optimizasyonu. *Gazi Üniversitesi Fen Bilimleri Dergisi*; 3(3): 555-564.
16. R. Tavakoli, P. D. 2009. Optimal Riser Design in Sand Casting Process with Evolutionary Topology Optimization. *Struct Multidisc Optim*; 205–214.
17. Vivien J. Challis, A. P.-C. 2010. Prototypes for Bone Implant Scaffolds Designed via Topology Optimization and Manufactured by Solid Freeform Fabrication. *ADVANCED ENGINEERING MATERIALS*; 12: 1105-1110.
18. Xiaojian Wang, S. X. 2016. Topological Design and Additive Manufacturing of Porous Metals for Bone Scaffolds and Orthopaedic Implants: A Review. *Biomaterials*; 83: 127-141.
19. Würth Industrie. Dimensioning metric screw assemblies. Wuerth Industrie: https://www.wuerth-industrie.com/web/media/en/pictures/wuerthindustrie/technikportal/dinokapitel/Kapitel_06_DINO_techn_Teil.pdf
20. M. P. Bendsue, O. S. 1999. Material Interpolation Schemes in Topology Optimization. *Archive of Applied Mechanics*; 69: 635-654.
21. Nişancı, M.C., Yurddaş, A. 2020. Compare Between the Results of the Casting Simulation and the Results of Experimental Production with Calculating the Interface Heat Transfer Coefficient of the Casting-Mold. *Celal Bayar University Journal of Science*; Volume 16, Issue 2, 2020, p 169-181 Doi: 10.18466/cbayarfbe.720791.

Effect of Meteorological Parameters on PM10 Concentrations in Ardahan by Wavelet Coherence Analysis

Necla Barlık^{1*} 

¹Ardahan University, Engineering Faculty, Department of Environmental Engineering, 75002 Ardahan, Turkey

*neclabarlik@ardahan.edu.tr

*Orcid: 0000-0003-0000-1903

Received: 17 May 2020

Accepted: 4 March 2021

DOI: 10.18466/cbayarfbe.738596

Abstract

In the city of Ardahan, the PM10 concentrations are high especially in winter and autumn due to heating in buildings. This paper investigates the impact of meteorological parameters (air temperature, air pressure, humidity and wind speed) on the PM10 concentrations in the city of Ardahan by using the Wavelet Coherence analysis. The data have been provided from the records of the Ministry of Environment and Urbanization Continuous Monitoring Center and the Turkish State Meteorological Service in between 2010-2020. The results of the study show that selected meteorological parameters have the different effects on the PM10 concentrations in a period of ten years. Wavelet coherence approach presents clearly the influence of meteorological factors on the PM10 concentrations, and the approach is quite useful in terms of the practical explanation of available data, also.

Keywords: Meteorological parameters, PM10, time series, wavelet coherence

1. Introduction

As world population increases, the share of particulate matter (PM) concentrations in air pollution problems in urban centers also increases. PM is a general term used to classify air pollutants containing air-suspended particles, varying in composition and size, resulting from various natural or anthropogenic activities. Anthropogenic origin PM emissions emitted from motor vehicles, electricity generation, industrial facilities and domestic heating sources. The coarse, particulate matter with aerodynamic diameters from 2.5 μm to 10 μm is classified as PM10 [1, 2].

Many studies have shown that there is a close relationship between PM10 pollution and human health deterioration [2, 3, 4]. For this reason, national and international organizations set limit values for different exposure times, taking into account the observed health effects. In the regulations of the EEA (European Environment Agency) and WHO (World Health Organization), the daily average limit values for PM10 are 50 $\mu\text{g}/\text{m}^3$. This value is 70 $\mu\text{g}/\text{m}^3$ for our country.

Better understanding of spatial and temporal variability of pollutant concentrations in the atmosphere is seen as an important component of air quality management and

health risk assessment. Low air quality and pollution events in any location are affected by a wide variety of factors such as pollutant emissions, meteorology and topography. Therefore, it is important to analyze pollutant concentrations in relation to these factors [5]. Many researchers were investigated influence of temperature, relative humidity, precipitation, air pressure and wind speed (or direction) on concentrations or pollution index of PM10 by using approaches such as basic statistical calculates [6], correlation [7], regression models [8, 9], Fourier transform [10], wavelet transform [11, 12] and neural networks [13] as spatially and temporally. Generally, temperature, relative humidity, precipitation and wind speed have correlated negative correlation with the PM10 concentration and air quality index (AQI), and positive correlation with daily temperature range and atmospheric pressure PM10 and AQI.

This paper analyzes the impact of meteorological variables such as air temperature, air pressure, humidity and wind speed to the concentration of PM10 in the city of Ardahan by using a linear regression and the Wavelet Coherence approach (WTC). Linear regression was used as a tool for basic analysis and relative comparison.

Wavelet transform is the improved version of Fourier transform. This analysis can be performed in several ways, a continuous wavelet transforms and a discrete wavelet transforms. The fields of application vary from science, engineering, medicine to finance such as wave propagation, data compression, signal processing, image processing, pattern recognition, computer graphics, the detection of aircraft and submarines, cell membrane recognition, blood pressure, heart rate, ECG analyses, internet traffic description and weather data etc. The application of wavelet analysis becomes more widely spread as the analysis technique becomes more generally known [14].

2. Materials and Methods

Ardahan is a small city located north east region of Turkey. In the city, which is 1829 m above sea level, the city's continental climate prevails. Winters are long, hard and snowy. The annual average temperature of Ardahan is 5°C. For this reason, the heating in the houses is carried out for about eight months.

2.1. The Data

In the city, there is a monitoring station of the Ministry of Environment and Urbanization Continuous Monitoring Center. PM10 hourly values of the 10 - year period, covering 2010 - 2020, were saved online from the measurements of the station [15]. Meteorological parameters such as temperature, humidity, pressure and wind speed were requested from the Turkish State Meteorological Service. Following analyzes were used 24-hour average values of the data.

2.2. Methodology

To analyze the relationship between the meteorological parameters and the PM10 concentrations a linear regression and WTC analysis have been performed. Regression analysis estimates potential relationship between two variables and mathematical description of this analysis is known well in literature. It was used as a tool for basic analysis and relative comparison, in here.

$$y(t) = mx(t) + n \quad (2.1)$$

where m and n are the regression coefficients, x(t) represents the time series of the meteorological parameters such as air temperature, air pressure, relative humidity and wind speed and y(t) represents the time series of PM10 for this study. For determination of the representation of the regression model is used a coefficient of r-square (r^2) which ranges from 0 to 1. As the coefficient approaches 1, the representation ability of the regression model increases.

WTC has been performed as the second methodological approach. A wavelet function is used in wavelet

transform. The wavelet transform is conducted by shifting (τ) and scaling (s) the mother wavelet (ψ) across the time series (x) as a function of time (x(t)). The definition of a continuous wavelet (CWT) is [16, 17]:

$$W_{x,\psi}(\tau, s) = \int_{-\infty}^{+\infty} x(t) \frac{1}{\sqrt{s}} \psi^* \left(\frac{t-\tau}{s} \right) dt \quad (2.2)$$

where * denotes the conjugate complex value.

Morlet wavelet is mostly preferred in applications since it is similar to normal distribution curve. Morlet wavelet, is given by [18]:

$$\psi(t) = \pi^{-1/4} e^{i\omega_0 t} e^{-t^2/2} \quad (2.3)$$

where $\pi^{1/4}$ and ω_0 are a normalization factor and a dimensionless frequency parameter, respectively

Wavelet coherence (WTC) can be explained the time and frequency components as well as the strength of correlation between the time series in the time-frequency space [19]. Therefore, the wavelet coherence can be supplies a better correlation between the meteorological parameters and the PM10 concentrations in comparison with the conventional correlation analysis. Following the WTC is defined as [16]:

$$R_{x,y}^2(\tau, s) = \frac{|S(s^{-1}W_{x,y}(\tau, s))|^2}{S(s^{-1}|W_x(\tau, s)|^2)S(s^{-1}|W_y(\tau, s)|^2)} \quad (2.4)$$

where S is a smoothing operator for performing time-frequency normalization processing and the squared of WTC coefficient, R^2 , is in the following range:

$$0 \leq R_n^2(s) \leq 1$$

If the coefficient equals 1, there is a perfect linear relation between the x(t) and y(t) if it equals 0, two series are independent. MATLAB codes have been used for wavelet coherence transformation. In wavelet coherence plots, red indicates a strong correlation between meteorological parameter and PM10 concentrations, while blue indicates zero or no correlation between these time series.

The coefficient of wavelet coherence is expressed by the term square, therefore it cannot reveal the difference between positive and negative correlations. Phase difference is used to provide information about backwards and forwards relationships between the two variables. The phase difference ($\phi_{x,y}$) characterizes the phase relationship between x(t) and y(t) [17]:

$$\phi_{x,y}(\tau, s) = \tan^{-1} \left(\frac{\Im[S(s^{-1}W_{x,y}(\tau, s))]}{\Re[S(s^{-1}W_{x,y}(\tau, s))]} \right) \quad (2.5)$$

where \Im and \Re denote an imaginary and a real operator, respectively. The definition range of $\phi_{x,y}$ is $[-\pi, \pi]$.

If $\phi_{x,y} \in (0, \pi/2)$, then the series moves together positively and $x(t)$ leads $y(t)$

If $\phi_{x,y} \in (\pi/2, \pi)$, then the series moves together negatively and $y(t)$ leads $x(t)$

If $\phi_{x,y} \in (-\pi/2, 0)$, then the series moves and $y(t)$ leads $x(t)$

If $\phi_{x,y} \in (-\pi, \pi/2)$, then the series moves and $x(t)$ leads $y(t)$

3. Results and Discussion

Ardahan, Turkey is one of the coldest cities. PM10 concentrations are particularly high in winter and autumn due in buildings to heating. The highest values of the PM10 concentrations have been recorded in January, February and December. Between January 2010 and January 2020, 13 days unhealthy ($> 261 \mu\text{g}/\text{m}^3$) and 335 days sensitive ($101 - 260 \mu\text{g}/\text{m}^3$) weather conditions were observed according to the average national AQI PM10 values. In approximately 30% of the period, the PM10 particles concentration is above the 24-hours limit set by WHO.

In this period, the average daily temperature was 5.19°C , while the hottest day was as 23.50°C on August 7, 2017 and the coldest day as -26.80°C on February 4, 2014. Air pressure varied between $800.50 - 830.60 \text{ hPa}$. If about 10-days records between 30.1 to 36.2 m/s are excluded in June 2015, the average wind speed has been 1.13 m/s . The average relative humidity was 68.03% .

There is no any industrial activity in the city. The share of pollution from traffic is also low in total pollution. The biggest natural source that can be shown to the high concentrations of PM10 in the city are the dust from the roads. The main source in terms of anthropogenic effects; are relatively low quality coals used in buildings for heating purposes. The amount of coal used for heating in 2018 was approximately 11 tons and the amount of natural gas was $15\,000 \text{ m}^3$ [20].

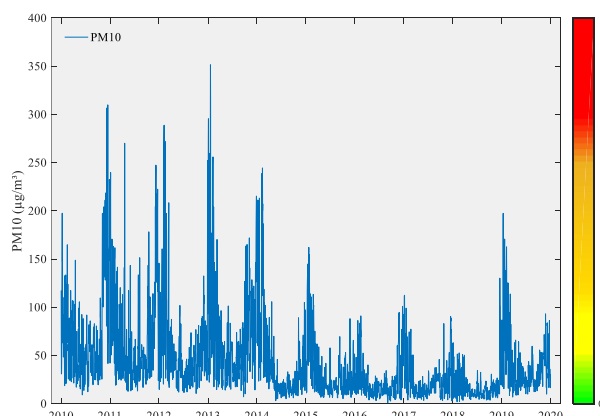


Figure 1. Daily values of the PM10 particle concentration between 2010-2020. The colormap shows the national air quality index (AQI)

Fig. 1 shows the time series of 24-hour the PM10 concentrations from January 2010 to January 2020. The time series are represented by 3468 sample points. The highest PM10 concentrations have been measured in January 2013, as $351.5 \mu\text{g}/\text{m}^3$. Since 2014, natural gas has been used in buildings for heating purposes. The decrease in the PM10 particles the concentrations after the use of natural gas is clearly seen in Fig. 1, also. Days exceeding the limit values are mostly seen before this date.

3.1. Linear Regression Analysis Between the Meteorological factors and the PM10 values

The linear regression approach was conducted to examine the effect of meteorological factors (air temperature, air pressure, relative humidity and wind speed) on changes in the PM10 concentration. Daily average the values of meteorological parameters and 24-hourly average PM10 the concentrations for the period 2010 - 2020 are presented in Fig. 2.

Fig. 3 shows correlations between the meteorological parameters and the PM10 particles concentration, as scatter plot. 10-day excessive wind speed signals, considered as noise, were not included in the analysis. While temperature and wind speed are negatively correlated with the PM10 concentration, air pressure and relative humidity are positive with PM10. The values of calculated the coefficients (r^2) between temperature, air pressure, relative humidity and wind speed and PM10 are: 0.18470 , 0.00018 , 0.02151 and 0.02376 , respectively. The correlation coefficient is the highest for temperature - PM10 and the lowest for air pressure - PM10.

The results of this study shows that the correlation between the PM10 concentrations and temperature is negative so the low PM10 concentrations has occurred at the high temperatures. In other words, decreased temperature has been associated with an increase in the PM10 concentrations. The relationship observed between wind speed and the PM10 concentrations is similar, also.

According to the results, the low PM10 concentrations have occurred in the low relative humidity rate. In other words, with increased the relative humidity, the concentration has increased as well, but the correlation between the PM10 concentrations and the relative humidity is weak.

Essentially, the time series in Fig.2 are very useful for practical analysis. It is clearly seen in the time series given in Fig. 2 that the PM10 concentrations decrease as the temperature and wind speed increase. Moreover, increases in wind speed and relative humidity also coincide with increases in the PM concentrations.

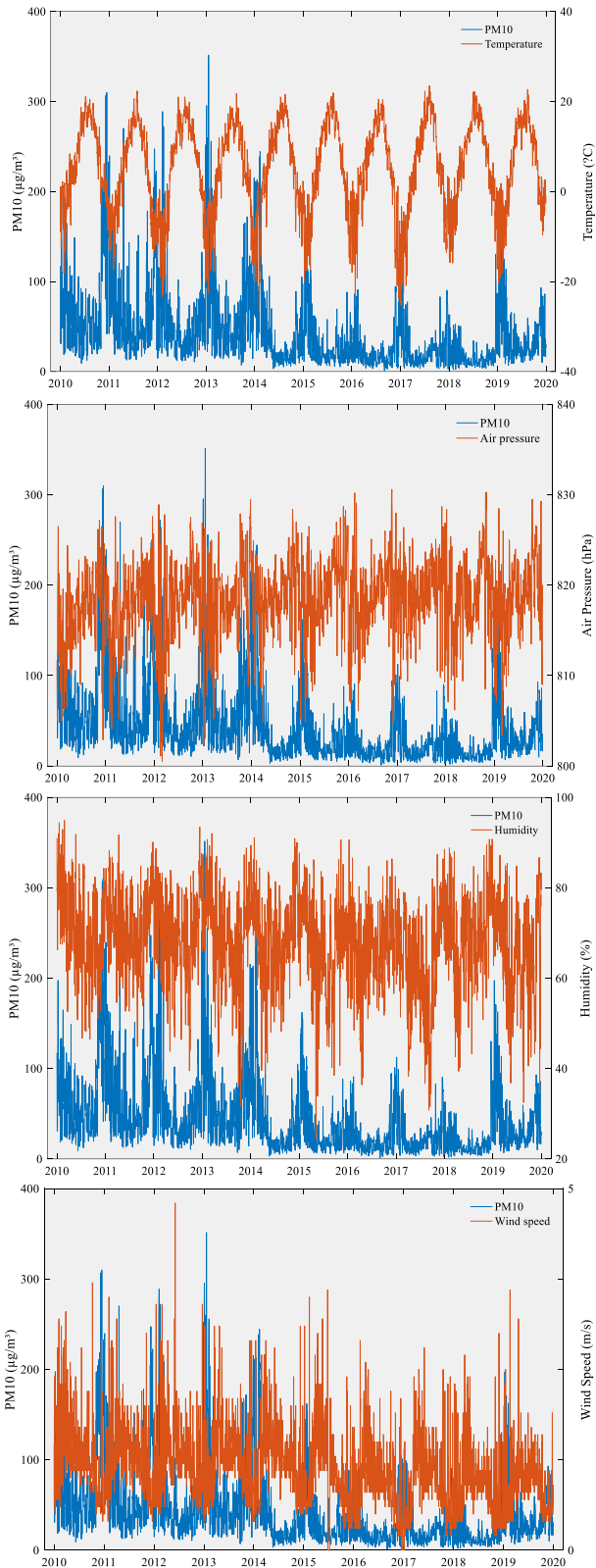


Figure 2. The time series of 24-hour the PM10 concentrations and meteorological parameters (temperature, air pressure, relative humidity and wind speed from top to bottom respectively) in 2010-2020

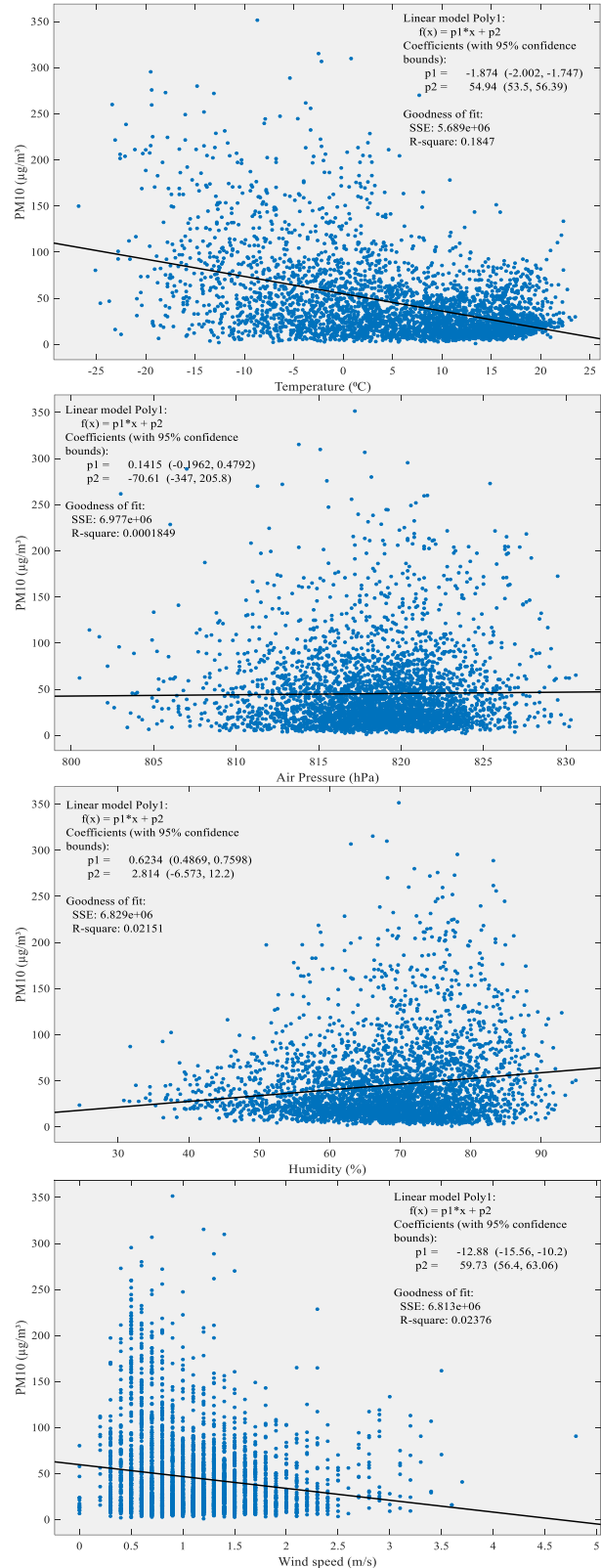


Figure 3. Correlations between the meteorological parameters (temperature, air pressure, relative humidity and wind speed from top to bottom respectively) and the PM10 concentrations in the period of 2010 -2020

However, the results of the regression analysis are not sufficient and strong to reveal the correlation between the time series. The regression statistics given above have a very low regression coefficient, which indicates that it is not appropriate to apply linear regression analysis to large interval time series. Also, as seen in Fig. 2, the PM10 concentration is not expected to be the same throughout the year due to meteorological factors. Detailed regression analysis between daily the PM10 emissions and the meteorological parameters is needed on a monthly scale. Low regression coefficients also require the application of different approaches in the analysis of the time series.

3.2. Wavelet coherence between the meteorological parameters and PM particles the concentration

The WTC plots show the regions the time series change together. WTC approach has been applied to show the relationships between the meteorological factors and the concentrations of PM10 in different time-frequency spaces. The phase difference between the time series is indicated by arrows on the graph [21]. The direction of the arrows shows the level and type of correlation in terms of time shifts, while also showing the relative bond between the phenomena.

The results of WTC analysis between the meteorological factors and PM10 the concentrations for the period of 2010 -2020, is presented in Fig. 4. Different WTC ranges are colored emphasizing to the significance of the regions, as from blue to red. This approach not only provides important information about the common behavior of the time series under study, but also gives an interesting idea of the phenomenon under study. In the WTC analysis of the temperature-PM10 series, the first characteristic period is between 4 and 32 days and has been out of phase many times over during observed time interval. In the period between 128 and 256 days, between time series is identified significant the correlation in time interval the end of 2012 and to the early 2014, also with out of phase. For the period about 256 days, the common behaviors of air temperature and PM10 concentration move out of phase during all observed time interval, in other words the correlation between time series is quite significant. This shows the high seasonal dependence between temperature and the PM10 variations. This is especially obvious in the days around new year's 2013-2014, 2014-2015, 2015-2016, 2016-2017 and 2017-2018.

According to WTC analysis applied between air pressure and PM10 the first characteristic period is between 32 and 64 days and has been out of phase time interval new year of 2014 and the end of 2015 and to the early 2017. From 2010 to the end of 2019 the common behaviors of two-series are out of phases for the period about 256 days and there are significant correlations. Also, dynamics of out phase has been seen the period

between 16 and 32 days in the winter of 2013 and the period between 32 and 64 days in the winter of 2015.

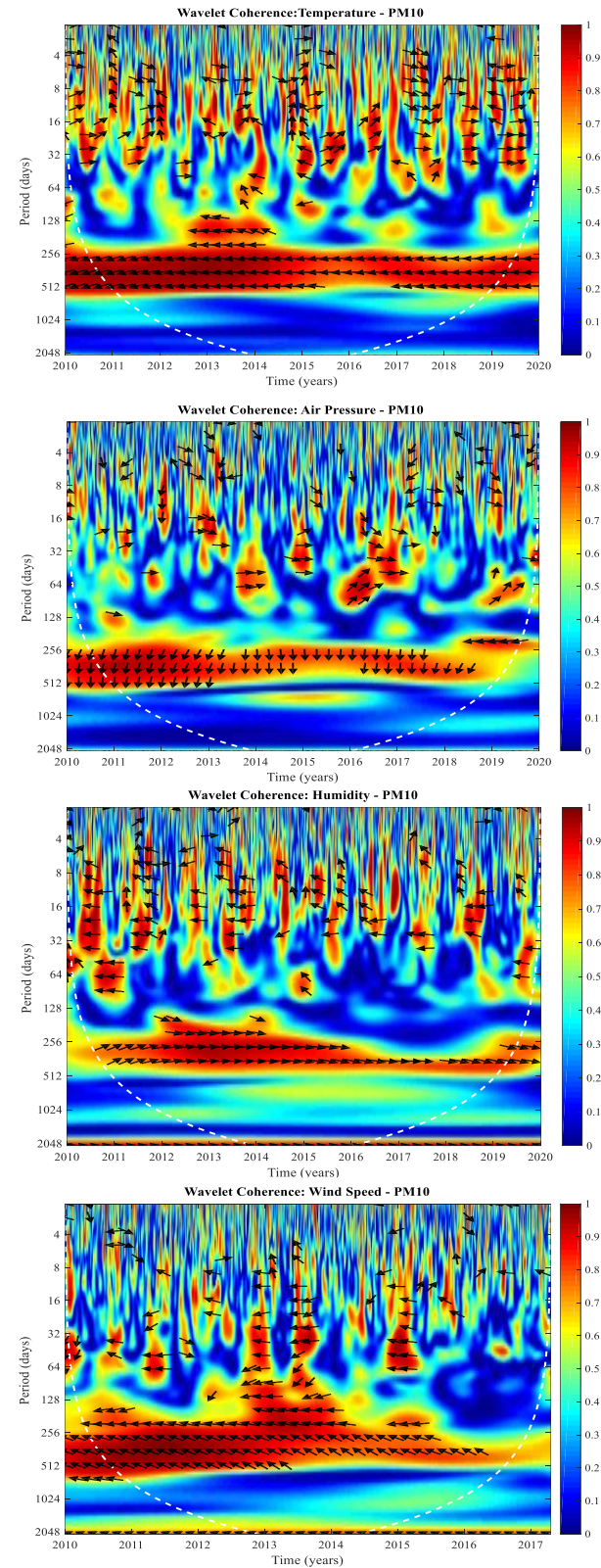


Figure 4. WTC of daily values of the meteorological factors (temperature, air pressure, relative humidity and wind speed from top to bottom respectively) and the PM10 concentrations in the period of 2010 -2020

For the period about 256 days, the common behaviors of relative humidity-PM10 and wind speed-PM10 move out of phase during all observed time interval such as in the series of air temperature-PM10 and pressure-PM10. In other words, the correlation between these series is significant, also. In the WTC graphic of the series of humidity-PM10 is seen out of phase the period between 8 and 32 days in between 2010 and 2011. This interval, which corresponds to the spring of 2010 indicates the rainy period. Besides, it is seen out of phase the period between 32 and 128 days in the autumn of 2011, indicates the snowy period. This case is especially evident in the days around the autumn periods for the whole of the studied time interval. In the WTC graphic of the series of wind speed-PM10 is seen out of phase in the period between 16 and 64 days both in the end of 2013 and new year's 2013 and 2014, in other words the correlation between time series is significant.

The common behaviors of between the meteorological factors and the PM10 move out of phase for the period about 256 days during all observed time interval. This is very interesting as the correlation between the series indicates positive and significant trend in about 256 days band. Again, in this period, the distribution of colors towards lighter red after 2015 (after the use of natural gas becomes widespread) is another interesting result, also.

4. Conclusion

In this paper, the influence of meteorological factors on the PM10 concentration in the period 2010-2020 in Ardahan has been analyzed by using the WTC approach.

According to records that are saved from monitoring stations of the Ministry of Environment and Urbanization Continuous Monitoring Center in Ardahan, the PM10 concentrations were seasonally high, especially in autumn and winter. The use of natural gas for heating in buildings has have a significant impact on the reduction of the PM10 concentrations in the city. According to the air quality index, all of the unhealthy ($> 261 \mu\text{g}/\text{m}^3$) weather conditions and a very important part of the sensitive ($101 - 260 \mu\text{g}/\text{m}^3$) weather conditions in the city has been recorded before the use of natural gas.

Meteorological conditions corresponding to the high values of PM10 concentrations have appeared in the scatter plot between time series. These values have varied in the following ranges: the air temperature values from -25°C to $+5^\circ\text{C}$, the air pressure values from 810 to 825 hPa, the values of relative humidity from 65 to 85% and wind speed from 0.5 to 1.5 m/s. The linear regressions between the time series show the PM10 concentrations sensitivity to meteorological conditions. However, regression statistics are characterized by a

very low coefficient of determination, indicating that it has the potential to discover other alternative approaches.

The WTC approach applied in this research not only allows a time-frequency analysis of the time series, but also helps to identify time frames where a significant correlation between the meteorological factors and the PM10 concentrations can be expected. Also, unlike linear regression, WTC analysis shows that a larger number of examples provide a better and more detailed analysis of the phenomenon studied, providing more information about the dynamic behavior and relationships of the time series.

In this study, periods in which meteorological variables have a significant effect on the PM10 concentrations were determined. From the WTC analysis it has been seen possible to produce useful results for a better understanding of meteorological conditions leading to increase the PM10 concentrations.

Acknowledgement

Thanks the Turkish State Meteorological Service as it supports the performing of the study by sharing meteorological parameters.

Author's Contributions

Necla Barlık: Drafted and wrote the manuscript, performed the experiment and result analysis.

Ethics

There are no ethical issues after the publication of this manuscript.

References

1. Miller, BG. Clean Coal Engineering Technology; 2nd Edition, Elsevier Inc.: Pennsylvania, US, 2017; pp. 419-420
2. Cheng, Z, Jiang, J, Fajardo, O, Wang, S and Hao, J. 2013. Characteristics and health impacts of particulate matter pollution in China (2001-2011). *Atmospheric Environment*; 65:186-194.
3. Kappos AD, Bruckmann P, Eikmann T, Englert N, Uwe H, Höpfe P, Koch E, Krause GH, Kreyling WG, Raufuss K, Rombout P, Schulz-Klemp V, Thiel WR and Wichmann HE. 2004. Health effects of particles in ambient air. *International Journal of Hygiene and Environmental Health*; 207(4):399-407.
4. Wilson JG, Kingham S, Pearce J and Sturman AP. 2005. A review of intraurban variations in particulate air pollution: Implications for epidemiological research. *Atmospheric Environment*; 39: 6444-6462.
5. Ştefan, S, Radu C and Belegante, L. 2013. Analysis of Air Quality In Two Sites With Different Local Conditions. *Environmental Engineering and Management Journal*; 12(2):371-379.
6. Guerra, SA, Lane, DD, Marotz, GA, Carter, RE, Hol CM and Baldauf, RW. 2006. Effects of Wind Direction on Coarse and Fine Particulate Matter Concentrations in Southeast Kansas. *Journal of the Air & Waste Management Association*; 56:1525-1531.
7. Galindo, N, Varea, M, Gil-Moltó J and Yubero, E. 2011. The

- Influence of Meteorology on Particulate Matter Concentrations at an Urban Mediterranean Location. *Water Air and Soil Pollution*; 2015: 365–372.
8. Bathmanabhan, S and Madanayak, SNS. 2010. Analysis and interpretation of particulate matter – PM10, PM2.5 and PM1 emissions from the heterogeneous traffic near an urban roadway. *Atmospheric Pollution Research*; 1:184-194.
 9. Sajjadi, SA, Zolfagharib, G, Adab, H, Allahabadi A and Delsouza, M. 2017. Measurement and modeling of particulate matter concentrations: Applying spatial analysis and regression techniques to assess air quality. *MethodsX*; 4:372-390.
 10. Tchepel, O and Borrego, C. 2010. Frequency analysis of air quality time series for traffic related pollutants. *Journal of Environmental Monitoring*; 12: 544–550.
 11. Li, L, Qian, J, Ou, CQ, Zhou, YX, Guo, C and Guo, Y. 2014. Spatial and temporal analysis of Air Pollution Index and its timescale-dependent relationship with meteorological factors in Guangzhou, China, 2001-2011. *Environmental Pollution*; 190:75-81.
 12. Anusasananan, P. 2019. Wavelet spectrum analysis of PM10 data in Bangkok, Thailand. *Journal of Physics: Conference Series*,1380:1-9.
 13. Biancofiore, F, Busilacchio, M, Verdecchia, M, Tomassetti, B, Aruffo, E, Bianco, S, Tommaso, SD, Colangeli, C, Rosatelli G and Carlo, PD. 2017. Recursive neural network model for analysis and forecast of PM10 and PM2.5. *Atmospheric Pollution Research*; 8(4): 652-659.
 14. Sifuzzaman, M, Islam, MR and Ali, MZ. 2009. Application of Wavelet Transform and its Advantages Compared to Fourier Transform. *Journal of Physical Sciences*; 13:121-134.
 15. Environment and Urban Ministry, Hava Kalitesi Veri Bankasi. <http://www.havaizleme.gov.tr/> (accessed at: 05.05. 2020).
 16. Torrence, C and Compo, GP. 1998. A practical guide to wavelet analysis. *Bulletin of the American Meteorological Society*; 79(1):61-78.
 17. Nie, Y, Chen, P, Zhang, T and Wang, E. Impacts of international oil price fluctuations on China's PM2.5 concentrations: a wavelet analysis. 2019. *Economic Research-Ekonomika Istrazivanja*;1-21.
 18. Grossmann, A and Morlet, J. 1984. Decomposition of hardy functions into square integrable wavelets of constant shape. *Society for Industrial and Applied Mathematics*; 15(4): 723-736.
 19. Loh, L. 2013. Co-movement of Asia-pacific with European and us stock market returns: A cross-time-frequency analysis. *Research in International Business and Finance*; 29:1-13.
 20. Environment and Urban Ministry. 2019. *Environmental Status Report for Ardahan 2018 (Turkish)*.
 21. Aguiar-Conraria, L, Azevedo N and Soares, MJ. 2008. Using wavelets to decompose the time–frequency effects of monetary policy. *Physica A*; 387: 2863–2878.

The Effect of Addition of ZnO to Granite Body on Sintering and Mechanical Properties

Savaş Elmas^{1*} 

¹Ceramic and Glass Department, Fine Arts Faculty, Çanakkale Onsekiz Mart University, Çanakkale, Turkey

*savaselm@comu.edu.tr

*Orcid: 0000-0003-2913-0303

Received: 22 October 2020

Accepted: 11 March 2021

DOI: 10.18466/cbayarfbe.814870

Abstract

In granite body, 1-3-5 wt% ZnO was replaced instead of feldspar and fired in an industrial continuous production kiln. Physical properties of the tiles were determined including dried strength, fired strength, water absorption, fired loss, and colorimeter values. X-Ray Diffraction (XRD), scanning electron microscope (SEM) and energy dispersive X-Ray (EDX) measurements for distinctive microstructural changes and phases formed were done. The fired strength values of the standard and 3% ZnO added body are 400 kg/cm², 511 kg/cm², respectively. Water absorption and firing shrinkage values are close to each other. In the analysis of the sample with 3% added ZnO with XRD, it was observed that the solubility of quartz was increased, mullite formation was prevented; besides 27.4 wt.% spinel phase and 13.8 wt.% albite formation was observed.

Keywords: Ceramics, characteristics, microstructure, porcelain stoneware (granite tile), sintering, ZnO

1. Introduction

In the competitive conditions increasing with globalization, efficiency and exceeding customer expectations force companies to obtain products with superior features. In ceramic production, granite tile has been in demand in recent years with its superior properties. Turkey's share in the world total in 2018 was 2.6 % with 335 million m²[1].

Many studies have been done in the literature on the production of porcelain stoneware [2-5]. Ceramic bodies consist of 3 basic raw materials. Clay gives properties such as workability, green strength, body color, rheology. Feldspars affect the solubility, the amount of the glassy phase, the viscosity and the formation temperature of the glassy phase. Quartz, with its inert structure, prevents the body from cracking during drying and deformation during firing [6-7]. The microstructure, which determines the properties of the material, includes the amount, shape and distribution of phases and pores. At the same time, the composition of the glassy phase formed, its homogeneity and the structural stress between different phases affects the properties [8]. Body undergoes some changes with its body firing. The removal of residual moisture below

200 °C, the removal of organics at 200-650 °C, conversion of kaolin into metakaolin at 450-600 °C, 500-600 °C quartz transformation, the initiation of reactions between 900-1000 °C silica and alumina, > 1000 °C eutectic formation and partial melting begins [9-11]. Liquid content increases after 1200 °C as a result of the increase in quartz solubility. Small mullite (primary) and γ -alumina crystals are formed between the degraded clay particles, while secondary mullite crystals are formed between the clay and feldspar [12]. Some oxides have been studied in the literature in the form of dopant to the vitrified body. In a study conducted by Bhattacharyya and Snehes [13] on the subject, it was observed that the addition of Cr₂O₃ to the porcelain body in the range of 0-4 wt.%, negatively affected the structural properties. In the same study, it was observed that the addition of 1-5 wt.% NiO, improved physical and mechanical properties at 1200 °C. Beside the mullite, nickel aluminate spinel phase was formed. It was observed that the addition of NiO also affected mullite morphology. With the addition of 5 wt.% NiO, maximum shrinkage, minimum porosity, high bulk density and maximum fired strength were observed at 1200 °C. In another study conducted by Bhattacharyya and Snehes [14] on the subject, it was observed that 1-5 wt% CoO was added and gave positive results in physical and mechanical properties as

a result of firing at 1100-1200 °C. Feldspar's solubility and mullitization were increased with the addition of CoO. The addition of 1 wt.% CoO has given the body optimum fired properties at low temperatures. In a study by Bhattacharya, Das and Mitra [15], TiO₂ was added to the porcelain body in the range of 3-6-9 wt.% and fired at 1200-1250-1300-1350-1400 °C. It was observed that excess liquid phase was formed at temperatures above 1300 °C and as a result, swelling occurred in the product. At 1300 °C, negligible porosity and maximum strength value of 45 MPa were observed. It was determined that with increasing TiO₂ amount, quartz amount decreased, mullite and liquid phase amount increased. After the 6 wt.% TiO₂ increase, no significant property change appears. In a study about the addition of ZnO to porcelain body (Chaudri 1974; transmited Bhattacharyya, Das and Mitra, 2005) it was observed that with the addition of 4% ZnO to the porcelain body, a minimum of mullite was formed [16]. In a study conducted by Iya, Noh, Razak, Sharip and Kutty [17], it was observed that the addition of 5 wt.% Fe₂O₃ at 1150 °C increased mullitization and the amount of liquid phase. Maximum strength value, bulk density and hardness values were reached to 138.94 MPa, 2.515 g / cm³, 829 HV, respectively. It has been observed that the maturing temperature is 100-120 °C lower than the standard body. The addition of Fe₂O₃ inside the porcelain body instead of quartz, the chemical analyzes of standard and Fe₂O₃ added bodies are respectively, 46.5% quartz, 35.4% aluminosilicate, 5.1% calcium, 13.1% sulfuric acid and 42% quartz, 32% mullite, 21% anorthite, 5% iron. The peaks are more precise with the addition of Fe₂O₃. By the help of the presence and interaction of anorthite and mullite crystals, bulk density and strength increased. This effect is evident especially with the addition of 5% Fe₂O₃. In a study by Tulyaganov, Agathopoulos, Fernandes and Ferreria [18] Li₂CO₃ was added to the porcelain structure at increasing rates of 1-7 wt.%. Positive results were achieved when Li₂O does not exceed 1.5 wt.%. In a study by Chaudhuri and Sarkar [19], mullite formation increased in the porcelain body where V₂O₅ and Nb₂O₅ additions were 3% and 2%, respectively; It has been found that they are effective nucleators for crystal formation. At the same time, while the amount of cristobalite was almost 0 % among other samples, it was found to be as high as 24.8% in only 2% Nb₂O₅ added body. In another study [20], FeO_{1.5}, CoO and NiO were added and the order of reducing viscosity was seen as FeO_{1.5}> CoO> NiO.

In this study, the addition of ZnO to the granite body was made as 1-3-5 wt.% and firing shrinkage, water absorption, fired strength, dried strength, fired losses were determined. In addition, crystalline phases after firing were detected by X-ray analysis (XRD); surface morphology, microstructure, phase and elemental analysis were investigated using energy dispersive X-

ray spectroscopy (EDX) and scanning electron microscopy (SEM).

2. Materials and Methods

The addition of ZnO instead of sodium feldspar in the prepared industrial body was made as 1-3-5 wt. %. The materials were prepared in the proportions specified in the recipe and at a density of 1650gr / lt, >63 microns residue with 3.6 %. After being kept in the dryer for 8-10 hours at 110 °C, water was added to the powder with a spray to obtain granules with a moisture value of 5-6%, then these granules were pressed to 300 kg / cm². Firing was carried out in an industrial continuous kiln at 1180-1185 °C in 63 minutes. Dwelling timey at the maximum temperature is 3 minutes. Chemical analysis of the raw materials used are shown in Table 1, and the prescriptions prepared are shown in Table 2. The strength measurement was made in a 3-point gabrielli brand strength device according to equation (Eq. 2.1).

$$S = \frac{30 \cdot P}{L \cdot h^2} \quad (2.1)$$

formula is used for strength (kg / cm²).

S: the breaking strength (kg/cm²)

P: the load breaking the tile (kg / cm²)

L: the width of the tile (cm) and

h : the thickness of the tile (cm)

In the water absorption process is used equation (Eq. 2.2) below:

$$\text{water absorbtion (\%)} = \frac{(w_2 - w_1)}{w_1} \cdot 100 \quad (2.2)$$

W₁ : dry weight

W₂: water absorbed weight (sample was kept in boiling water for 2 hours to cool, then it was wiped with a damp cloth then weighed).

XRD measurements were made by XRD Pan Analytic Empeyron Series 45kV, K alpha. Microstructure photos were measured by SEM-JEOL- JSM -7100 F. EDX measurements were made in Oxford Instruments x-max quorum 1mbar / Pa, 10mA, Au / Pa (80/20%) coating.

Color measurement was made on the Minolta CR 300 instrument. Color difference measurement is made with equation (Eq. 2.3).

$$\Delta E = \sqrt{(L2 - L1)^2 + (a2 - a1)^2 + (b2 - b1)^2} \quad (2.3)$$

ΔE: criterion for detecting color difference

L: lightness value

a: redness value

b: yellowness value

ZnO from Tekkim Kimya extra pure grade is used.

Table 1. Chemical analysis of used raw materials.

	SiO ₂	Al ₂ O ₃	Fe ₂ O ₃	TiO ₂	CaO	MgO	Na ₂ O	K ₂ O	ZnO	F.L.
Kaolin	52	34.05	0.80	0.30	0.15	0.30	0.15	1.30	-	12
Albite	69	19.6	0.017	0.04	0.95	0.11	10.30	0.23	-	0.12
Quartz sand	91	7	0.8	0.3	0.02	0.02		0.76	-	0.1
Clay	54	31.05	0.67	1.17	0.3	0.45	0.13	2.3	-	10.05
ZnO	-	-	-	-	-	-	-	-	99.6	0.1

F.L: Fired loss

Table 2. Used recipes.

Recipes	1	2	3	4
Kaolin	25	25	25	25
Albite	30	29	27	25
Quartz sand	5	5	5	5
Clay	40	40	40	40
ZnO	-	1	3	5

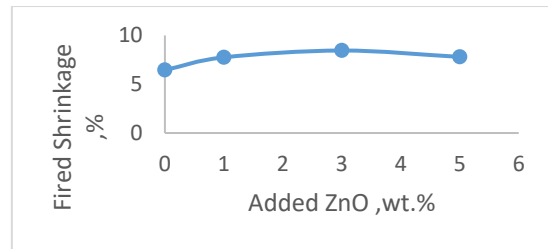


Figure 1. F. shrinkage % - added ZnO wt.% graphic.

3. Results and Discussion

3.1. Physical Measurements

The firing shrinkage increased up to 3 % ZnO addition, then decreased. In a study on the subject, it was found that the sintering degree increased with early sintering and consequently firing shrinkage and strength increased [21]. There is an increase up to 3 % ZnO addition in parallel with the increased sintering and firing shrinkage in the fired loss value. While the maximum value of the fired strength value was 400 kg/cm² in the standard body, it increased to 511 kg / cm² in the body with added 3 % ZnO. The water absorption value also showed a value close to the standard (0.05%) as 0.06% in the addition of 3% ZnO.

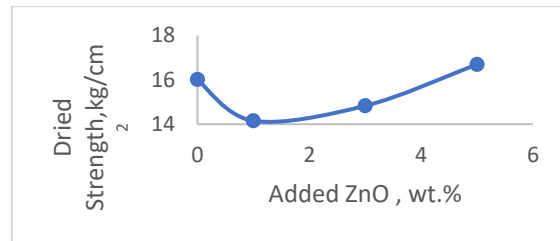


Figure 2. Dried strength- added ZnO wt.% graphic.

Table 3. Physical characteristics of bodies.

Recipes	1	2	3	4
Fired Shrinkage (%)	6.45	7.75	8.45	7.80
Fired Lost (%)	3.9	4.9	5	4.1
Dried Strength (kg/cm ²)	16.0	14.2	14.9	16.7
Fired Strength (kg/cm ²)	400	498	511	471
Water Absorption (%)	0.05	0.13	0.06	0.05

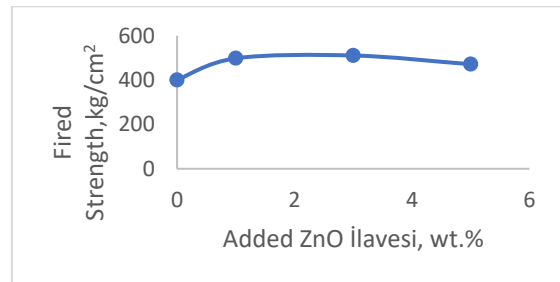


Figure 3. Fired strength - added ZnO wt.% graphic.

Table 4. Arithmetic mean, variance and standard deviation of measurements

	μ	σ^2	σ
Viscosity (sn)	57	191.3	13.83
Fired Shrinkage (%)	7.61	0.70	0.83
Fired Lost (%)	4.47	0.31	0.55
Dry Strength (kg/cm ²)	15.45	1.24	1.11
Fired Strength (kg/cm ²)	470	2455	49
Water Absorption (%)	0.07	0.001	0.04

μ = arithmetic mean, σ^2 =variance, σ = standard deviation

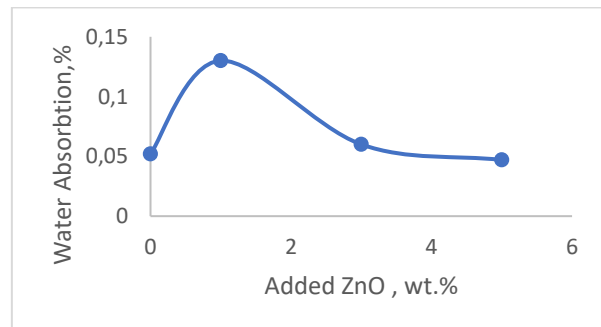


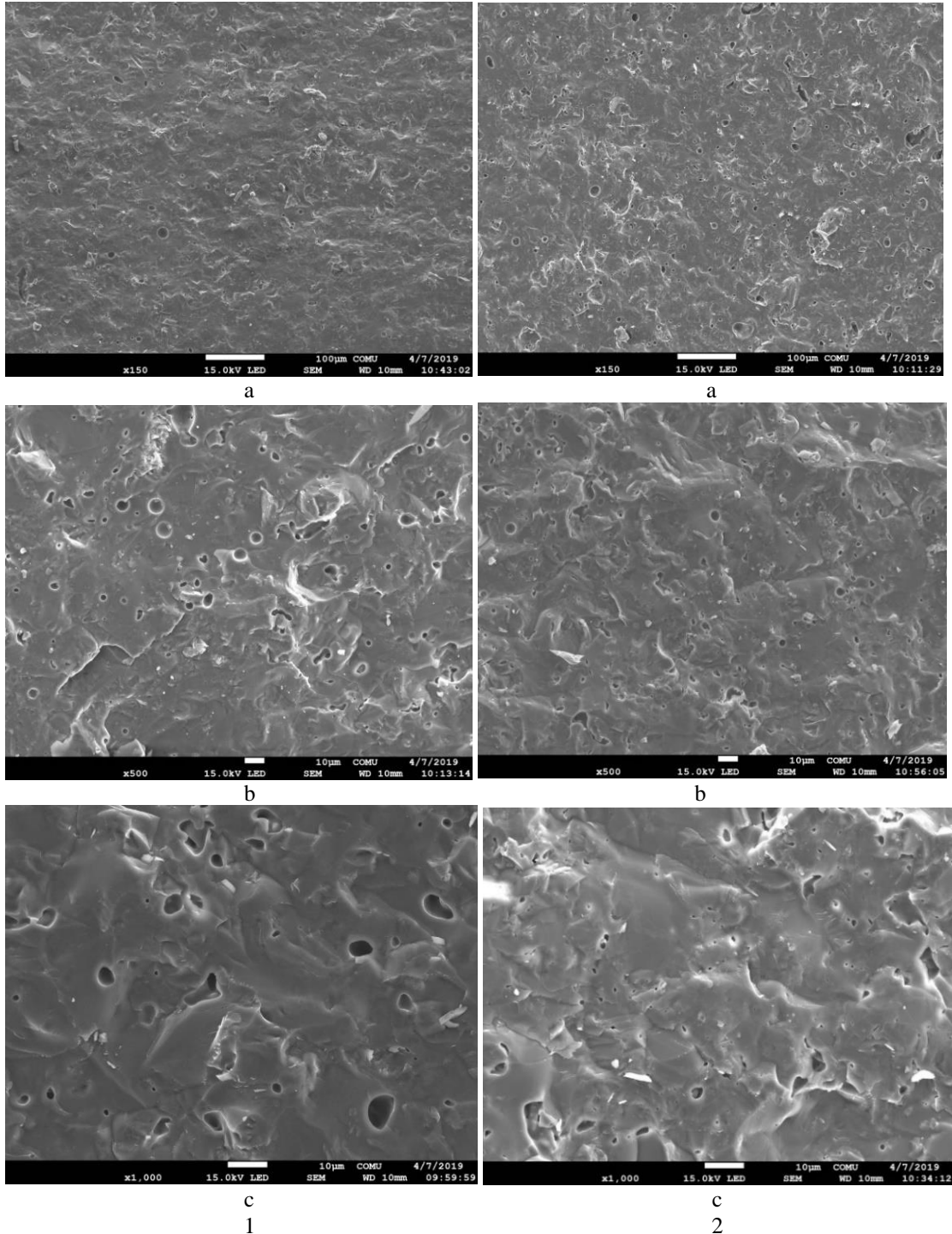
Figure 4. Water absorption % - added ZnO wt.% graphic

Physical characteristics of bodies are shown in Table 3. All trials meet the requirement of maximum 0.5% according to ISO 10545-3 water absorption standard and minimum 350 kg / cm² according to ISO 10543-5 bending strength requirement. The increase in firing shrinkage and fired strength and the decrease in water absorption by using ZnO up to 3% is an indication that it has a positive effect on sintering. It has been determined that the addition

of ZnO increases the viscosity of the slurry, that is, it impairs the rheological properties.

3.2. Microstructural Analyses

The SEM images of the standard and 3wt.% ZnO added samples are shown in Figure 5.1.a.b.c and Figure 5.2.a.b.c.



There is a decrease in the size of the pores on the fractured surface that shows close pores in the recipe 3 as seen at 500x and 1000x magnification. Pore sizes decrease according to feret diameter measurements. The lower the temperature of the liquid phase formation with eutectic reactions ($\text{Na}_2\text{O}-\text{K}_2\text{O}-\text{ZnO}-\text{Al}_2\text{O}_3-\text{SiO}_2$), the more positively it contributes to rapid firing[22]. The viscosity of the glassy phase should also be at an optimal level, which is high enough not to cause pyroplastic deformation, but low enough to respond easily and quickly to gas release. High level of glass phase formation is observed in both body types. Another reason for the increase in strength is that the closed pore volume

decreases due to the positive effect of ZnO on sintering. As seen Figure 6 and Figure 7 for EDX analyses, both standard and doped samples have high vitrification. Alkali metals and zinc were detected in the quartz base amorph matrix in the analysis performed on the sample added ZnO that is no.3. Zinc has diffused into the glassy matrix by showing its melting property. One reason for the increase in strength is thought to be the change in glassy matrix composition. The presence of carbon element in EDX analysis indicates short firing time that cannot provide enough time for organics to escape. In a study performed on stoneware tiles, C element was not found in EDX analysis of the standard sample [23].

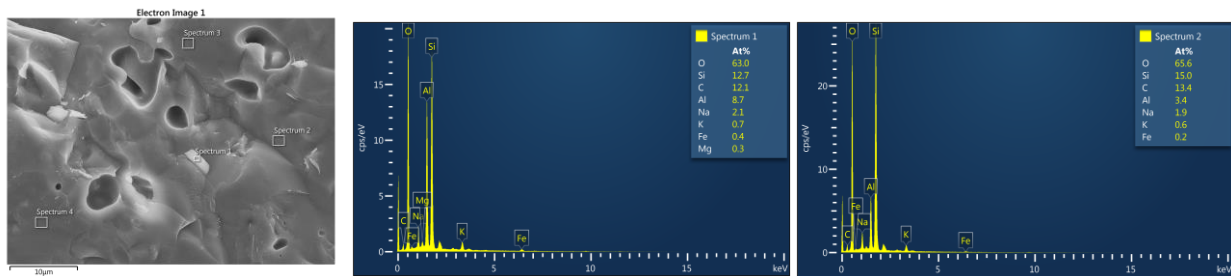


Figure 6. Standard (1 no) sample's EDX images.

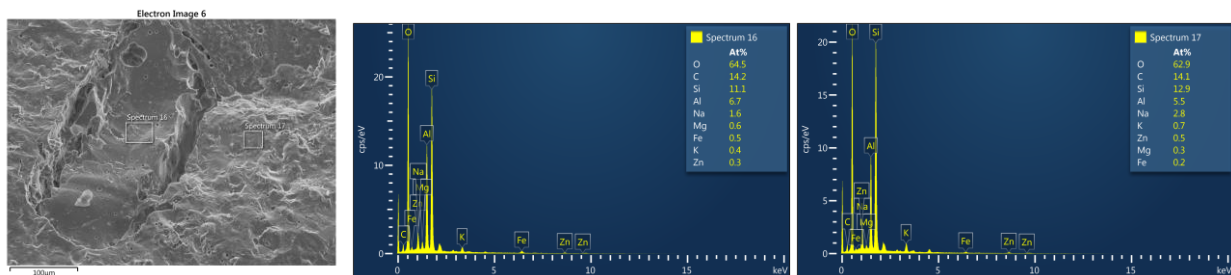


Figure 7. 3 wt. % added ZnO (no 3) sample's EDX images.

3.3. Crystalline Phase Analyses

The XRD graphics of the standard and 3wt. % added ZnO samples are shown in Figure 8. Rietveld method was used for quantitative analyzes. The presence of ZnO in the ceramic body decreased the viscosity of the liquid phase and increased the solubility of quartz by increasing its chemical activity; spinel phase was occurred, mullitization was prevented and albite formation was triggered. While quartz in the standard body was 77.2%, mullite 22.8%, in body no.3, quartz was 56.4%, cristobalite 2.5%, spinel 27.4% and albite 13.8%. It has been observed that the addition of NiO

also creates a spinel phase [13]. In the study conducted by Chaudhuri, it was observed that with the addition of 4 wt.% ZnO to the porcelain body, a minimum of mullite was formed[16]. With increasing quartz solubility, increased the amount of quartz in the glassy phase and thus cristobalite formation was observed in XRD [8]. In a study, it was determined that the addition of ZnO to the household porcelain body creates cristobalite and increases with the amount of ZnO added. In the same study, it was observed that the amount of quartz decreased [21].

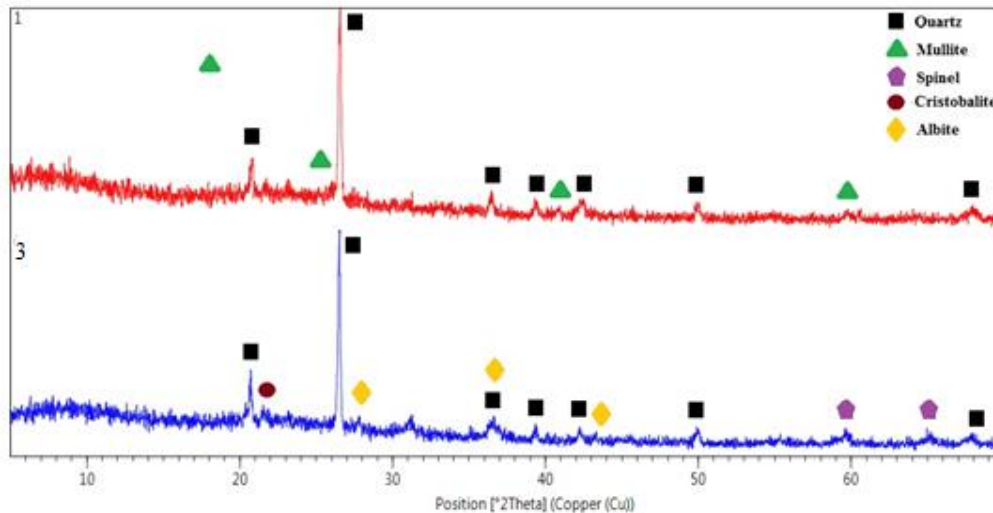


Figure 8. Standard (1) and 3 wt.% ZnO added sample (3).

3.4. Colour Analyses of the Samples

Colorimeter values of bodies are shown in Table 5. As a result of colorimeter measurements, it was determined that the L (lightness) value increased, a (redness) and b (yellowness) values decreased and -a value (green) increased with increasing ZnO. Especially in the 5% ZnO sample, the value of a decreases from 3.91 to 0.30 compared to the standard. L (lightness) value increases with increasing ZnO. With increased ZnO, the (yellowness) value of b decreased by 1% and reached the smallest value with 5% added value. When $\Delta E < 1$, the human eye cannot detect color difference. According to this, the color change that occurs in all doped samples can be detected by the human eye. Fired samples are shown in Figure 9.

Table 5. Colorimeter degrees of bodies.

Sample	L	a	b	ΔE
1	47.75	3.91	15.31	Std.
2	48.61	3.99	11.68	3.73
3	50.41	2.53	12.31	4.24
4	54.68	0.30	10.60	9.1

Std:Standard



Figure 9. Images of fired bodies.

3. Conclusion

According to study,

1. It has been determined that the added of 3 wt.% ZnO, increased the strength increase from 400 kg/cm² to 511 kg / cm², respectively, as standard and added samples.
2. While there was quartz 77.2% and 22.8% mullite in the standard body, 56.4% quartz, 2.5% cristobalite,

27.4% spinel and 13.8% albite were detected in 3% ZnO added body. With the addition of 3% ZnO, the liquid phase viscosity decreased and the amount of quartz in the body decreased, and the formation of cristobalite was triggered by the increasing amount of quartz in the liquid phase. Mullite formation was prevented and spinel phase formed.

3. It was determined that the L (openness value) value of the standard sample and the 5% ZnO added sample increased from 47.75 to 54.68. The values where a (redness) and b (yellowness) value are the smallest and the values that falls according to the standard are a: 0.3 and b: 10.70 in the 5% added ZnO.

In the production of wall tiles and sanitaryware, studies can be carried out on the use of ZnO in recipes to determine the effect of different compositions and firing times. The benefit / cost parameter can be revealed in a detailed work.

Author's Contributions

Savaş Elmas: Drafted and wrote the manuscript, performed the experiment and result analysis.



Ethics

There are no ethical issues after the publication of this manuscript.

References

1. TSF2019 Faaliyet Raporu. <https://serfed.com/upload/raporlar/TSF%202019%20FAAL%C4%B0YET%20RAPORU%20SON.pdf> (accessed at 15.10.2020)
2. Paganelli M. and Sighinolfi D., 2009. Effect of Quartz Particle Size on Porcelain Stoneware Sintering by Means of Optical Dilatometry. *Ceramic Forum International*, Volume 86.
3. Biesuz, M., Abate W.D., Sglavo V., 2018. Porselem stoneware consolidation by flash sintering. *Journal of American Ceramic Society*, Volume 101, pp.71-81.
4. Mahdi O.S., 2018. Study the Influence of Sintering on the Properties of Porcelain Stoneware Tiles. *International Journal of Applied Engineering Research* ISSN 0973-4562 Volume 13, Number 6, pp. 3248-3254.
5. Zanelli C., Raimondo M., Guarini G. and Dondi M., 2011. The vitreous phase of porcelain stoneware: Composition, evolution during sintering and physical properties. *Journal of Non-crystalline Solids*, Volume 357, pp. 3251-3260.
6. Fortuna D., 2000, Ceramic Technology-Sanitaryware. Gruppo Editoriale Faenza Editrice.
7. Ryan W., Radford C., 1987. Whitewares Productions, Testing and Quality Control. The Institute of Ceramics, Pergamon Press.
8. Lundin S. T., 1964. Microstructure of Porcelain pp.93-106 in Microstructure of Ceramic Materials, Proceedings of the American Ceramic Society Symposium, National Bureau of Standards Miscellaneous Publications No.257. National Bureau of Standard, Gaithersburg, MD.
9. Vari A. Drying and Firing of Ceramic Tiles, Modena-Italia , S.A.L.A.srl, via carlo Zucchi,21 A/B.
10. Worrall W.E., 1975. Clay and Ceramic Raw Materials, New York, Elsevier Applied Science Publishers.
11. Norton F.H., 1970. Fine Ceramics Technology and Applications, Florida, Robert E.Krieger Publishing Comp,INC.
12. Iqbal Y., Lee W. E., 2000, Microstructural Evolution in Triaxial Porcelain, *J.Am. Ceram. Soc.*, 83 [12] 3121-27.
13. Bhattacharyya S., Snehes T.S., 2015. Improvement of fired properties in porcelain system by the addition of transition metal oxides, *Journal of The Australian Ceramic Society*, Volume 51[1], 8-15.
14. Bhattacharya S., Snehis T.S., 2015. Effect of cobalt oxide additive on the fired properties of tri-axial ceramic, *Ceramics International* 41, 61-67.
15. Bhattacharyya S., Das S.K., Mitra N.K., 2005. Effect of titania on fired characteristics of triaxial porcelain, *Bull. Mater. Sci.*, Vol. 28, No. 5, August, pp. 445-452. © Indian Academy of Sciences.
16. S.P., 1974. *Ceram.Bull.*53, 169.
17. Iya S.G.D, Noh M.Z., Razak S.N.A., Sharip N., Kutty A.A., 2019. Effect of Iron (111) Oxide (Fe₂O₃) as an Additive and Substitution of Quartz with POFA on Physico- Mechanical Properties of Porcelain. *International Journal of Nanoelectronics and Materials* Volume 12, No.2, Apr 175-1847.
18. Tulyaganov D.U., Agathopoulos S., Fernandes H.R., Ferreira J.M.F., 2006. Influence of lithium oxide as auxiliary flux on the properties of triaxial porcelain bodies. *Journal of the European Ceramic Society*, 26 1131-1139.
19. Chaudhuri S.P., Sarkar P., 1995. Constitution of Porcelain Before and After Heat-Treatment. I: Mineralogical Composition, *Journal of the European Ceramic Society*, 15 1031-1035.
20. Kong L.B., Huang H., Zhang T.S., Gan Y.B., Ma j., Boey F., Zhang R.F., 2003. Effect of transition metal oxide on mullite whisker formation from mechanochemically activated powders. *Materials and Engineering*, A359 75-81.
21. Maslenikova G.N., Stoikova T.V., 2001. Household Porcelain with Mineralizing Additives. *Glass and Ceramics*, Vol.58, Nos 7-8.
22. Carrty William M., Senepati U., 1998. Porcelain-Raw Materials, Processing, Phase Evolution, and Mechanical Behaviour. *J.Am.Ceramic. Soc.*, 81[1] 3-20.
23. Selli N.T., 2015. Investigation of the Whiting Composition for the Porcelain Stoneware Tiles. *Acta Physica Polonica A* Vol.127 1202-1204.

Boole approximation method with residual error function to solve linear Volterra integro-differential equations

Kübra Erdem Biçer^{1*}, Hale Gül Dağ¹

¹Manisa Celal Bayar University, Mathematics, 45000, Manisa, Turkey

*kubra.erdem@cbu.edu.tr

*Orcid: 0000-0002-4998-6531

Received: 12 October 2020

Accepted: 1 March 2021

DOI: 10.18466/cbayarfbe.791302

Abstract

In this study, a numerical method is developed for the approximate solution of the linear Volterra integro-differential equations. This method is based Boole polynomial, its derivatives and the collocation points. The aim is to reduce the given problem, as the linear algebraic equation, to the matrix equation. This matrix equation is solved using Boole collocation points. As a result, the approximate solution is obtained in the truncated Boole series in the interval [a, b]. The exact solution and the approximate solution are included in the study. Also, the error analysis and residual correction calculations are performed in the study. The results have been obtained by using computer program MATLAB.

Keywords: Boole polynomials, linear Volterra integro-differential equation, collocation points, approximate solutions, Residual error analysis

1. Introduction

Integro-differential equations are a tool used to representing problems in fields such as physics, biology, chemistry, mechanics, astronomy, electrostatic, natural science, potential theory, economics. Since integro-differential equation classes are difficult to solve by analytical methods, numerical methods are preferred. For the numerical solution of integro-differential equation classes, the method based on the Bernoulli polynomial by Erdem Biçer et al. [1, 13], the method based on the Bessel polynomial by Yüzbaşı et al. [11, 28], the method based on the Laguerre polynomial by Baykuş Savaşaneril and Sezer [27] and the method based on the Dickson polynomial by Kürkçü [15] have been developed [14, 16-24]. In addition, the numerical methods such as Taylor collocation method [2], a multiscale Galerkin method [3], Bernstein polynomials method [4], Legendre collocation method [5], Euler wavelet method [6], Newton-Product method [7], homotopy-perturbation method [8], improved Bessel collocation method [9], Spectral collocation method [10], Hybrid Euler-Taylor matrix method [29] and Tau method [12] are included in the literature.

In this study, the numerical method is developed using Boole polynomial, its derivatives and collocation points for the approximate solution of the m th order linear

Volterra integro-differential equation which is a type of the integro-differential equations.

Charles Jordan has stated general form of Boole polynomial as follows [26,30-31]

$$R_n(x) = \sum_{m=0}^{n+1} \frac{(-1)^m}{2^m} \binom{x}{n-m}. \quad (1.1)$$

The defined form of the Boole polynomial is written as

$$\sum_{n=0}^{\infty} \frac{R_n(x)}{n!} t^n = \frac{2(1+t)^x}{2+t}. \quad (1.2)$$

The aim is to get Boole solution of the m th order linear Volterra integro-differential equation

$$\sum_{k=0}^m P_k(x) y^{(k)}(x) = g(x) + \lambda \int_a^x K(x,t) y(t) dt, \quad a \leq x, t \leq b \quad (1.3)$$

with the initial boundary conditions

$$\sum_{k=0}^{m-1} (a_{jk}y^k(a) + b_{jk}y^k(b)) = \lambda_j, \quad j = 0, 1, 2, 3, \dots, m-1. \quad (1.4)$$

The Boole solution of Eq. (1.3) is obtained in the following Boole series form

$$y(x) \cong y_N(x) = \sum_{n=0}^N a_n R_n(x) \quad (1.5)$$

where $R_n(x)$ is Boole polynomial and a_n , $n = 0, 1, 2, \dots, N$ are the unknown Boole coefficients.

2. Matrix relations of the linear Volterra integro-differential equation

In this section, the matrix relations to reduce the Eq. (1.3) to the matrix equation system and the matrix relation of conditions (1.4) are given. Firstly, the matrix form of the Boole polynomial, $\mathbf{R}(x)$, is written as

$$\mathbf{R}(x) = \mathbf{X}(x)\mathbf{H}^T \quad (2.1)$$

where

$$\mathbf{R}(x) = [R_0(x) \quad R_1(x) \quad R_2(x) \quad \dots \quad R_N(x)],$$

$$\mathbf{X}(x) = [1 \quad x \quad x^2 \quad \dots \quad x^N]$$

and

$$\mathbf{H} = \begin{bmatrix} 1 & 0 & 0 & \dots \\ -\frac{1}{2} & 1 & 0 & \dots \\ \frac{1}{2} & -2 & 1 & \dots \\ \vdots & \vdots & \vdots & \ddots \end{bmatrix}$$

The matrix relation of the Boole series form (1.5) is written as

$$y(x) = \mathbf{R}(x)\mathbf{A} \quad (2.2)$$

and its k th derivative is

$$y^{(k)}(x) = \mathbf{R}^{(k)}(x)\mathbf{A}. \quad (2.3)$$

The matrix form (2.1) is placed in the matrix relation (2.3) and the matrix relation is obtained as

$$y^{(k)}(x) = \mathbf{X}^{(k)}(x)\mathbf{H}^T\mathbf{A} \quad (2.4)$$

where

$$\mathbf{X}^{(k)}(x) = \mathbf{X}(x)\mathbf{E}^k. \quad (2.5)$$

First, the matrix form (2.5) is placed in the matrix relation (2.4), the new matrix relation is obtained as

$$y^{(k)}(x) = \mathbf{X}(x)\mathbf{E}^k\mathbf{H}^T\mathbf{A} \quad (2.6)$$

where the matrix \mathbf{E} is derivative transition matrix of $\mathbf{X}(x)$,

$$\mathbf{E} = \begin{bmatrix} 0 & 1 & 0 & 0 & \dots & 0 \\ 0 & 0 & 2 & 0 & \dots & 0 \\ \vdots & \vdots & \vdots & \vdots & \ddots & \vdots \\ 0 & 0 & 0 & 0 & \dots & N \\ 0 & 0 & 0 & 0 & \dots & 0 \end{bmatrix}, \quad \mathbf{A} = \begin{bmatrix} a_0 \\ a_1 \\ a_2 \\ \vdots \\ a_N \end{bmatrix}$$

In Eq. (1.3), the kernel function $K(x, t)$ is defined as follows for the Taylor polynomial and Boole polynomial, respectively

$$\left. \begin{aligned} K(x, t) &= \mathbf{X}(x)^t \mathbf{K} \mathbf{X}^T(t) \\ K(x, t) &= \mathbf{R}(x)^R \mathbf{K} \mathbf{R}^T(t) \end{aligned} \right\} \quad (2.7)$$

From these forms, the matrix relation is obtained as follows

$${}^R\mathbf{K} = (\mathbf{H}^T)^{-1} {}^t\mathbf{K} \mathbf{H}^{-1} \quad (2.8)$$

where

$${}^tK(x, t) = \sum_{m=0}^N \sum_{n=0}^N {}^t k_{mn} x^m t^n,$$

$${}^R K(x, t) = \sum_{m=0}^N \sum_{n=0}^N {}^R k_{mn} R_m(x) R_n(t),$$

and

$${}^t k_{mn} = \frac{1}{m! n!} \frac{\partial^{m+n} K(0,0)}{\partial x^m \partial t^n} \quad m, n = 0, 1, 2, \dots, N.$$

According to the relation (2.4), the corresponding matrix form of the conditions (1.4) is written as

$$\sum_{k=0}^{m-1} (a_{jk}\mathbf{X}(a) + b_{jk}\mathbf{X}(b))\mathbf{E}^k\mathbf{H}^T\mathbf{A} = \lambda_j, \quad j = 0, 1, 2, \dots, m-1. \quad (2.9)$$

3. Collocation method

The matrix relation (2.6), the kernel function for the Taylor polynomial and the matrix form (2.1) are placed in the Eq. (1.3). Then the matrix equation is obtained as

$$\sum_{k=0}^m P_k(x) \mathbf{X}(x)\mathbf{E}^k\mathbf{H}^T\mathbf{A} = g(x) + \lambda \mathbf{X}(x)^t \mathbf{K} \mathbf{C}(x)\mathbf{H}^T\mathbf{A} \quad (3.1)$$

where

$$\mathbf{C}(x) = \int_a^x \mathbf{X}^T(t)\mathbf{X}(t)dt = [c_{i,j}(x)],$$

$$c_{i,j}(x) = \frac{x^{i+j+1} - a^{i+j+1}}{i+j+1}, i, j = 0, 1, 2, \dots, N.$$

By using in Eq. (15) the collocation points x_i defined by

$$x_i = a + \frac{b-a}{N}i, \quad i = 0, 1, \dots, N \quad (3.2)$$

the system of the matrix equations is gained as

$$\sum_{k=0}^m P_k(x_i) \mathbf{X}(x_i) \mathbf{E}^k \mathbf{H}^T \mathbf{A} = g(x_i) + \lambda \mathbf{X}(x_i)^t \mathbf{K} \mathbf{C}(x_i) \mathbf{H}^T \mathbf{A} \quad (3.3)$$

or briefly the fundamental matrix equation is shown as

$$\left\{ \sum_{k=0}^m \mathbf{P}_k \mathbf{X} \mathbf{E}^k \mathbf{H}^T - \lambda \overline{\mathbf{X}} \overline{\mathbf{K}} \overline{\mathbf{C}} \mathbf{H}^T \right\} \mathbf{A} = \mathbf{G} \quad (3.4)$$

Where

$$\mathbf{P}_k = \begin{bmatrix} \mathbf{P}_k(x_0) & 0 & \dots & 0 \\ 0 & \mathbf{P}_k(x_1) & \dots & 0 \\ \vdots & \vdots & \ddots & \vdots \\ 0 & 0 & \dots & \mathbf{P}_k(x_N) \end{bmatrix}_{(N+1) \times (N+1)},$$

$$\mathbf{G} = \begin{bmatrix} g(x_0) \\ g(x_1) \\ \vdots \\ g(x_N) \end{bmatrix}_{(N+1) \times 1}, \quad \mathbf{R} = \begin{bmatrix} \mathbf{R}(x_0) \\ \mathbf{R}(x_1) \\ \vdots \\ \mathbf{R}(x_N) \end{bmatrix}_{(N+1) \times (N+1)},$$

$$\overline{\mathbf{X}} = \begin{bmatrix} \mathbf{X}(x_0) & 0 & \dots & 0 \\ 0 & \mathbf{X}(x_1) & \dots & 0 \\ \vdots & \vdots & \ddots & \vdots \\ 0 & 0 & \dots & \mathbf{X}(x_N) \end{bmatrix}_{(N+1) \times (N+1)^2},$$

$$\overline{\mathbf{K}} = \begin{bmatrix} \mathbf{K} & 0 & \dots & 0 \\ 0 & \mathbf{K} & \dots & 0 \\ \vdots & \vdots & \ddots & \vdots \\ 0 & 0 & \dots & \mathbf{K} \end{bmatrix}_{(N+1)^2 \times (N+1)^2},$$

$$\overline{\mathbf{H}}^T = \begin{bmatrix} \mathbf{H}^T \\ \mathbf{H}^T \\ \vdots \\ \mathbf{H}^T \end{bmatrix}_{(N+1)^2 \times (N+1)} \quad \text{and}$$

$$\overline{\mathbf{C}} = \begin{bmatrix} \mathbf{C}(x_0) & 0 & \dots & 0 \\ 0 & \mathbf{C}(x_1) & \dots & 0 \\ \vdots & \vdots & \ddots & \vdots \\ 0 & 0 & \dots & \mathbf{C}(x_N) \end{bmatrix}_{(N+1)^2 \times (N+1)^2}.$$

The fundamental matrix relation (3.4) is written as

$$\mathbf{W} \mathbf{A} = \mathbf{G} \quad \text{or} \quad [\mathbf{W}; \mathbf{G}] \quad (3.5)$$

where

$$\mathbf{W} = \sum_{k=0}^m \mathbf{P}_k \mathbf{X} \mathbf{E}^k \mathbf{H}^T - \lambda \overline{\mathbf{X}} \overline{\mathbf{K}} \overline{\mathbf{C}} \mathbf{H}^T.$$

As a result of the operations, a system of $(N + 1)$ of the linear algebraic equation is obtained with the unknown Boole coefficients a_0, a_1, \dots, a_N . The matrix form for the conditions (2.9) are written as

$$\mathbf{U}_j \mathbf{A} = [\lambda_j] \quad \text{or} \quad [\mathbf{U}_j; \lambda_j]; \quad j = 0, 1, 2, \dots, m - 1 \quad (3.6)$$

where

$$\mathbf{U}_j = \sum_{k=0}^{m-1} (a_{jk} \mathbf{X}(a) + b_{jk} \mathbf{X}(b)) \mathbf{E}^k \mathbf{H}^T = [u_{j0} \quad u_{j1} \quad u_{j2} \quad \dots \quad u_{jN}], \quad j = 0, 1, 2, \dots, m - 1.$$

To reach the solution of the Eq. (1.3) under conditions (1.4), the rows matrices (3.5) are replaced with m rows of the matrix (3.6). So, the new augmented matrix form is obtained as

$$[\widetilde{\mathbf{W}}; \widetilde{\mathbf{G}}] = \begin{bmatrix} w_{00} & \dots & w_{0N} & ; & g(x_0) \\ w_{10} & \dots & w_{1N} & ; & g(x_1) \\ \vdots & \ddots & \vdots & \vdots & \vdots \\ w_{(N-m)0} & \dots & w_{(N-m)N} & ; & g(x_{N-m}) \\ u_{00} & \dots & u_{0N} & ; & \lambda_0 \\ \vdots & \ddots & \vdots & \vdots & \vdots \\ u_{(m-1)0} & \dots & u_{(m-1)N} & ; & \lambda_{m-1} \end{bmatrix}.$$

If $\text{rank} \widetilde{\mathbf{W}} = \text{rank} [\widetilde{\mathbf{W}}; \widetilde{\mathbf{G}}] = N + 1$ is, the augmented matrix is written as

$$\mathbf{A} = (\widetilde{\mathbf{W}})^{-1} \widetilde{\mathbf{G}}. \quad (3.7)$$

Finally, the unknown Boole coefficients from the matrix (3.7) solution are found and placed in the series (1.5), the Boole polynomial solution is obtained as

$$y(x) \cong y_N(x) = \sum_{n=0}^N a_n R_n(x)$$

4. Residual correction and error estimation

The error estimation of the Boole collocation method for the Eq. (1.3) and the residual correction of the Boole approximate solution are given in this section. The residual function of the Boole collocation method is written as

$$\mathfrak{R}_N(x) = L[y_N(x)] - g(x),$$

where $y_N(x)$, which is the Boole polynomial solution defined by (1.5), is the approximate solution of the problem (1.3). Therefore $y_N(x)$ is improved the equation

$$L[y_N(x)] = \sum_{k=0}^m P_k(x)y_N^{(k)}(x) - \lambda \int_a^x K(x,t)y_N(t)dt = g(x) + \mathfrak{R}_N(x), \quad (4.1)$$

The error function $e_N(x)$ is defined as

$$e_N(x) = y(x) - y_N(x), \quad (4.2)$$

where $y(x)$ is the exact solution of the problem (1.3). Substituting (4.2) into (4.1), and by simplifying the error differential equation is found

$$\sum_{k=0}^m P_k(x)e_N^{(k)}(x) - \lambda \int_a^x K(x,t)e_N(t)dt = -\mathfrak{R}_N(x), \quad (4.3)$$

with homogeneous conditions

$$\sum_{k=0}^{m-1} (a_{jk}e_N^{(k)}(a) + b_{jk}e_N^{(k)}(b)) = 0, \quad j = 0, 1, 2, \dots, m-1$$

Boole collocation method is applied to Eq. (4.3), the approximation $e_{N,M}(x)$ to $e_N(x)$ is obtained, ($M \geq N$) which is the error function based on the residual function $\mathfrak{R}_N(x)$ [1,13]. The corrected Boole polynomial solution $y_{N,M}(x) = y_N(x) + e_{N,M}(x)$. The corrected Boole error function is obtained with the Boole error function $e_N(x)$ and the estimated error function $e_{N,M}(x)$ as follows

$$E_{N,M}(x) = e_N(x) - e_{N,M}(x) = y_N(x) - y_{N,M}(x).$$

5. Numerical examples

In order to demonstrate the applicability and validity of the numerical method developed in this section, first exact solution example and then approximate solution examples are given.

Example 1. In the first example, the exact solution of the linear Volterra integro differential equation given by

$$2xy''(x) - xy'(x) - y(x) = \frac{x^5}{3} - x^4 + x^3 - 3x^2 + 4x - 1 - \int_0^x x^2y(t)dt, \quad (5.1)$$

with the initial conditions $y(0) = 1$ and $y'(0) = -2$ is obtained in the interval $0 \leq x, t \leq 1$. The approximate solution $y(x)$ by the truncated Boole series

$$y(x) = \sum_{n=0}^3 a_n R_n(x),$$

where $m = 2, N = 3, a = 0, b = 1, P_0(x) = -1, P_1(x) = -x, P_2(x) = 2x, g(x) = \frac{x^5}{3} - x^4 + x^3 - 3x^2 + 4x - 1, \lambda = -1$ and $K(x,t) = x^2$. The collocation points (3.2) for $N = 3, a = 0$ and $b = 1$ are calculated as

$$\{x_0 = 0, x_1 = \frac{1}{3}, x_2 = 1, x_3 = \frac{2}{3}, x_4 = 1\}.$$

The fundamental matrix equation of the Eq. (5.1) is written as

$$[P_2 X E^2 H^T + P_1 X E^1 H^T + P_0 X E^0 H^T - \lambda \overline{X K C H^T}] A = G,$$

where

$$P_0 = \begin{bmatrix} -1 & 0 & 0 & 0 \\ 0 & -1 & 0 & 0 \\ 0 & 0 & -1 & 0 \\ 0 & 0 & 0 & -1 \end{bmatrix}_{4 \times 4},$$

$$P_1 = \begin{bmatrix} 0 & 0 & 0 & 0 \\ 0 & -\frac{1}{3} & 0 & 0 \\ 0 & 0 & -\frac{2}{3} & 0 \\ 0 & 0 & 0 & -1 \end{bmatrix}_{4 \times 4},$$

$$P_2 = \begin{bmatrix} 0 & 0 & 0 & 0 \\ 0 & \frac{2}{3} & 0 & 0 \\ 0 & 0 & \frac{4}{3} & 0 \\ 0 & 0 & 0 & 2 \end{bmatrix}_{4 \times 4}, \quad E = \begin{bmatrix} 0 & 1 & 0 & 0 \\ 0 & 0 & 2 & 0 \\ 0 & 0 & 0 & 3 \\ 0 & 0 & 0 & 0 \end{bmatrix}_{4 \times 4},$$

$$H^T = \begin{bmatrix} 1 & -\frac{1}{2} & \frac{1}{2} & -\frac{3}{4} \\ 0 & 1 & -2 & 5 \\ 0 & 0 & 1 & -\frac{9}{2} \\ 0 & 0 & 0 & 1 \end{bmatrix}_{4 \times 4}, \quad \overline{H^T} = \begin{bmatrix} H^T \\ H^T \\ H^T \\ H^T \end{bmatrix}_{16 \times 4},$$

$$\mathbf{K} = \begin{bmatrix} 0 & 0 & 0 & 0 \\ 0 & 0 & 0 & 0 \\ 1 & 0 & 0 & 0 \\ 0 & 0 & 0 & 0 \end{bmatrix}_{4 \times 4}, \bar{\mathbf{K}} = \begin{bmatrix} \mathbf{K} & 0 & 0 & 0 \\ 0 & \mathbf{K} & 0 & 0 \\ 0 & 0 & \mathbf{K} & 0 \\ 0 & 0 & 0 & \mathbf{K} \end{bmatrix}_{16 \times 16},$$

$$\bar{\mathbf{C}} = \begin{bmatrix} \mathbf{C}(0) & 0 & 0 & 0 \\ 0 & \mathbf{C}\left(\frac{1}{3}\right) & 0 & 0 \\ 0 & 0 & \mathbf{C}\left(\frac{2}{3}\right) & 0 \\ 0 & 0 & 0 & \mathbf{C}(1) \end{bmatrix}_{16 \times 16},$$

$$\mathbf{R} = \begin{bmatrix} \mathbf{R}(0) \\ \mathbf{R}\left(\frac{1}{3}\right) \\ \mathbf{R}\left(\frac{2}{3}\right) \\ \mathbf{R}(1) \end{bmatrix}_{4 \times 1}, \mathbf{G} = \begin{bmatrix} g(0) \\ g\left(\frac{1}{3}\right) \\ g\left(\frac{2}{3}\right) \\ g(1) \end{bmatrix}_{4 \times 1} \text{ and}$$

$$\bar{\mathbf{X}} = \begin{bmatrix} \mathbf{X}(0) & 0 & 0 & 0 \\ 0 & \mathbf{X}\left(\frac{1}{3}\right) & 0 & 0 \\ 0 & 0 & \mathbf{X}\left(\frac{2}{3}\right) & 0 \\ 0 & 0 & 0 & \mathbf{X}(1) \end{bmatrix}_{4 \times 16}.$$

The fundamental matrix relation is calculated, the augmented matrix is obtained as

$$[\mathbf{W}; \mathbf{G}] = \begin{bmatrix} -1 & \frac{1}{2} & -\frac{1}{2} & \frac{3}{4} & ; & -1 \\ 26 & 29 & 1342 & 17207 & ; & 991 \\ 27 & 162 & 729 & 2916 & ; & 729 \\ 19 & 143 & 5095 & 22373 & ; & 2291 \\ 27 & 162 & 1458 & 2916 & ; & 729 \\ 0 & -\frac{3}{2} & \frac{13}{3} & -\frac{21}{4} & ; & \frac{13}{3} \end{bmatrix}.$$

According to Eq. (3.6), the matrix form of the initial conditions is found as

$$[\mathbf{U}_0; \lambda_0] = \begin{bmatrix} 1 & -\frac{1}{2} & \frac{1}{2} & -\frac{3}{4} & ; & 1 \\ 0 & 1 & -2 & 5 & ; & -2 \end{bmatrix} \text{ and } [\mathbf{U}_1; \lambda_1] =$$

In that case, the new augmented matrix based on conditions is become as

$$[\mathbf{W}; \mathbf{G}] = \begin{bmatrix} -1 & \frac{1}{2} & -\frac{1}{2} & \frac{3}{4} & ; & -1 \\ 26 & 29 & 1342 & 17207 & ; & 991 \\ 27 & 162 & 729 & 2916 & ; & 729 \\ 1 & -\frac{1}{2} & \frac{1}{2} & -\frac{3}{4} & ; & 1 \\ 0 & 1 & -2 & 5 & ; & -2 \end{bmatrix}.$$

with the solution of this augmented matrix, unknown Boole coefficients are found as

$$\mathbf{A} = \begin{bmatrix} \frac{1}{2} & 0 & 1 & 0 \end{bmatrix}.$$

Finally, found Boole coefficients is placed in the solution (1.5). The Boole solution of the Eq. (5.1) for $N = 3$ is gained as $y(x) = x^2 - 2x + 1$ and this is exact solution.

Example 2. In the second example, the approximate solution of the linear Volterra integro differential equation given by

$$y^{(iv)}(x) = x(1 + e^x) + 3e^x + y(x) - \int_0^x y(t)dt, \quad 0 < x < 1 \quad (5.2)$$

with initial conditions $y(0) = 1, y(1) = 1 + e, y'(0) = 1$ and $y'(1) = 2e$ [16]. The exact solution of the problem is $y(x) = 1 + xe^x$. The results of the exact solution $y(x)$, Boole solution $y_N(x)$ and the corrected Boole solution $y_{N,M}(x)$ for the various values N, M have been calculated in the computer program. The calculated results are given in the Table 1 and compared in the Figure 1 and 2. In addition, the absolute error function $|e_N|$, the estimated error function $|e_{N,M}|$ and the corrected Boole error function $|E_{N,M}|$ have been calculated for the values N, M . The results are given Table 2.

Table 1. The comparison of the exact solution $y(x) = 1 + xe^x$, Boole solutions $y_N(x)$ and corrected Boole solutions $y_{N,M}(x)$ for the Example 2.

x_i	Exact Solution $y(x) = 1 + xe^x$	Boole Solution $y_N(x)$		Corrected Boole Solution $y_{N,M}(x)$	
		N=5	N=12	N=5, M=6	N=12, M=13
0	1.0	1.0	1.0	1.0	1.0
0.2	1.244280552	1.243648041	1.244280552	1.244203327	1.244280552
0.4	1.596729879	1.595029888	1.596729879	1.596514071	1.596729879
0.6	2.09327128	2.091228319	2.09327128	2.092994076	2.09327128
0.8	2.780432743	2.779339894	2.780432743	2.78027061	2.780432743
1.0	3.718281828	3.718281828	3.718281828	3.718281828	3.718281828

Table 2. The comparison of the error function $|e_N|$, the estimated error function $|e_{N,M}|$ and the corrected Boole error function $|E_{N,M}|$ for the Example 2.

x_i	Absolute error function $ e_N $		Estimated error function $ e_{N,M} $		Corrected Boole error function $ E_{N,M} $	
	N=5	N=12	N=5, M=6	N=12, M=13	N=5, M=6	N=12, M=13
0	0	0	0	0	0	0
0.2	6.3251e-04	3.2300e-12	5.5529e-04	3.0890e-12	7.7224e-05	1.4105e-13
0.4	1.7000e-03	9.4901e-12	1.4842e-03	9.0739e-12	2.1581e-04	4.1622e-13
0.6	2.0430e-03	1.3640e-11	1.7658e-03	1.3037e-11	2.7720e-04	6.0285e-13
0.8	1.0928e-03	1.0559e-11	9.3072e-04	1.0082e-11	1.6213e-04	4.7673e-13
1.0	0	0	3.5293e-22	1.9590e-28	0	0

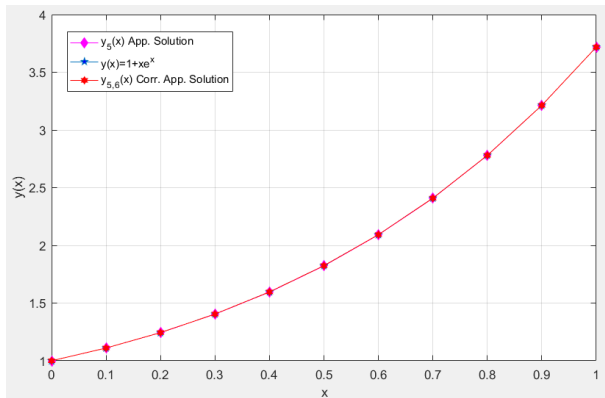


Figure 1. The comparison of the exact solution $y(x) = 1 + xe^x$, Boole solution $y_N(x)$ and corrected Boole solution $y_{N,M}(x)$ for the values $N, M = 5, 6$ for the Example 2.

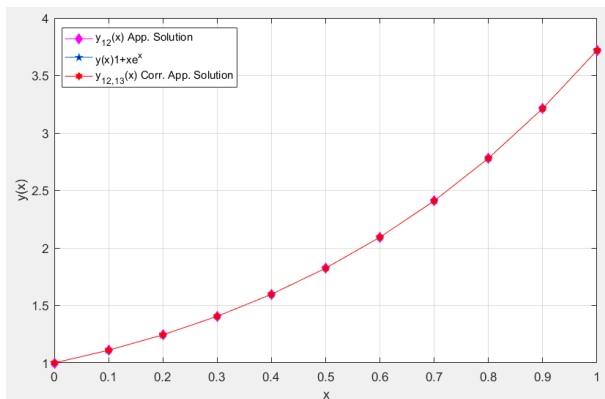


Figure 2. The comparison of the exact solution $y(x) = 1 + xe^x$, Boole solution $y_N(x)$ and corrected Boole solution $y_{N,M}(x)$ for the values $N, M = 12, 13$ for the Example 2.

Example 3. Finally, the linear Volterra integro differential equation given by

$$y''(x) + y(x) + \int_0^x x \tan(t) y(t) dt = x(1 - \cos x), \quad x \in [0, 1] \quad (5.3)$$

with initial conditions $y(0) = 1, y(1) = \cos 1$ and the analytical solution $y(x) = \cos x$ [25]. The absolute error function $|e_N|$, the estimated error function $|e_{N,M}|$ and the corrected Boole error function $|E_{N,M}|$ have been calculated in the computer program for the various values N, M and the results are given in the Table 3. Also, the results of the exact solution $y(x) = \cos x$, Boole solution $y_N(x)$ and corrected Boole solution $y_{N,M}(x)$ for the various values N, M have been compared in the Figure 3 and 4.

Table 3. The comparison of the error function $|e_N|$, the estimated error function $|e_{N,M}|$ and the corrected Boole error function $|E_{N,M}|$ for the Example 3.

x_i	Absolute error function $ e_N $		Estimated error function $ e_{N,M} $		Corrected Boole error function $ E_{N,M} $	
	N=4	N=10	N=4, M=5	N=10, M=11	N=4, M=5	N=10, M=11
0	0	0	0	0	0	0
0.2	1.3042e-04	7.5296e-07	2.7030e-04	8.8365e-12	4.0072e-04	7.5297e-07
0.4	2.5308e-04	1.4758e-06	5.3168e-04	8.3035e-13	7.8476e-04	1.4758e-06
0.6	3.6707e-04	2.1365e-06	7.4133e-04	6.3750e-13	1.1084e-03	2.1365e-06
0.8	3.8882e-04	2.5889e-06	7.1303e-04	4.8659e-12	1.1019e-03	2.5889e-06
1.0	0	0	2.6470e-23	1.0500e-24	0	3.6825e-56

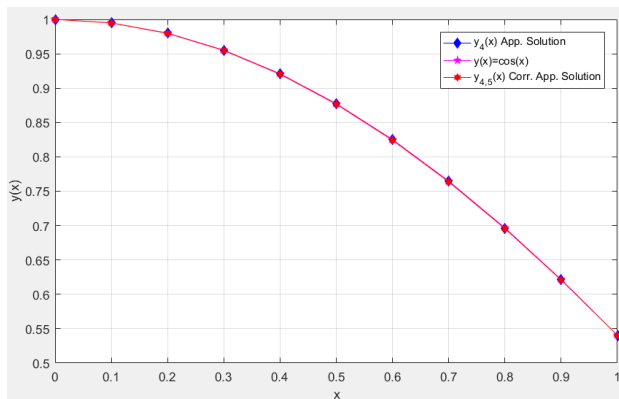


Figure 3. The comparison of the exact solution $y(x) = \cos x$, Boole solution $y_N(x)$ and corrected Boole solution $y_{N,M}(x)$ for the values $N, M = 4, 5$ for the Example 3.

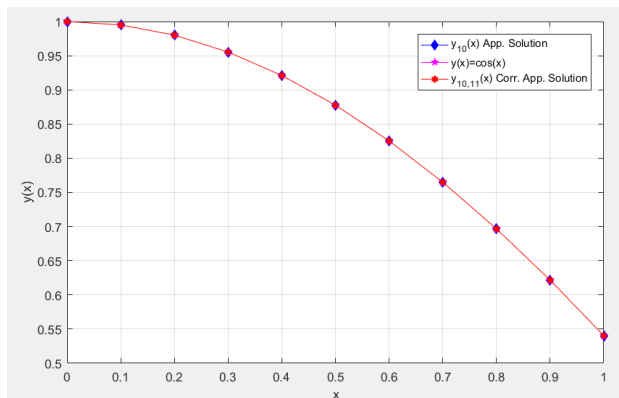


Figure 4. The comparison of the exact solution $y(x) = \cos x$, Boole solution $y_N(x)$ and corrected Boole solution $y_{N,M}(x)$ for the values $N, M = 10, 11$ for the Example 3.

Author's Contributions

Kübra Erdem Biçer Drafted and wrote the manuscript.

Ethics

There are no ethical issues after the publication of this manuscript.

6. Conclusions

In this study, a new method was developed by using the Boole polynomial to find the solution of Volterra integro differential equation. Numerical results were obtained with the developed this method. The method was used in the exact solution and approximate solution the examples. The exact solution of Example 1 was obtained using the present method for value $N = 3$. The exact solutions, Boole solutions and corrected Boole solutions of the Example 2 and 3 were gained for various values N, M . In addition, the error estimations based on residual function of the Example 2 and 3 have

been calculated. According to the tables and figures, the good results were obtained with this method. The advantage of present method is the solutions and calculations can be obtained easily the using computer code in MATLAB program. The present method can be develop to find solutions of other integro differential equation classes.

References

1. Erdem, K, Yalçınbaş, S, Sezer, M. 2013. A Bernoulli polynomial approach with residual correction for solving mixed linear Fredholm integro-differential equations. *Journal of Difference Equations and Applications*; 19: 1619-1631.
2. Laib, H, Bellour, A, Bousselsal, A. 2019. Numerical solution of high-order linear Volterra integro-differential equations by using Taylor collocation method. *International Journal of Computer Mathematics*; 96 (5): 1066-1085.
3. Chen, J, He, M, Zeng, T. 2019. A multiscale Galerkin method for second-order boundary value problems of Fredholm integro-differential equation II: Efficient algorithm for the discrete linear system. *J. Vis. Commun. Image R.*; 58: 112-118.
4. Hesameddini, E, Shahbazi, M. 2019. Solving multipoint problems with linear Volterra-Fredholm integro-differential equations of the neutral type using Bernstein polynomials Method. *Applied Numerical Mathematics*; 136: 122-138.
5. Rohaninasab, N, Maleknejad, K, Ezzati, R. 2018. Numerical solution of high-order Volterra-Fredholm integro-differential equations by using Legendre collocation method. *Applied Mathematics and Computation*; 328: 171-188.
6. Wang, Y, Zhu, L. 2017. Solving nonlinear Volterra integro-differential equations of fractional order by using Euler wavelet method. *Advances in Difference Equations*; 2017(1): 27.
7. Babayar-Razlighi, B, Soltanalizadeh, B. 2013. Numerical solution for system of singular nonlinear Volterra integro-differential equations by Newton-Product method. *Applied Mathematics and Computation*; 219: 8375-8383.
8. Roul, P, Meyer, P. 2011. Numerical solutions of systems of nonlinear integro-differential equations by Homotopy-perturbation method. *Applied Mathematical Modelling*; 35: 4234-4242.
9. Yüzbaşı, Ş. 2016. Improved Bessel collocation method for linear Volterra integro-differential equations with piecewise intervals and application of a Volterra population model. *Applied Mathematical Modelling*; 40: 5349-5363.
10. Gu, Z. 2019. Spectral collocation method for weakly singular Volterra integro-differential equations. *Applied Numerical Mathematics*; 143: 263-275.
11. Yuzbasi, S, Sahin, N, Sezer, M. 2011. Bessel matrix method for solving high-order linear Fredholm integro-differential equations, *Journal of Advanced Research in Applied Math.*; 3(23): 1-25.
12. Hosseini, SM, Shahmorad, S. 2003. Tau numerical solution of Fredholm integro-differential equations with arbitrary polynomial bases. *Applied Mathematical Modelling*; 27: 145-154.
13. Erdem, Biçer, K, Sezer, M. 2017. Bernoulli matrix-collocation method for solving general functional integro-differential equations with Hybrid delays. *Journal of Inequalities and Special Functions*; 8(3): 85-99.



14. Turkyilmazoglu, M. 2014. An effective approach for numerical solutions of high-order Fredholm integro-differential equations. *Appl. Math. Comput.*; 227: 384–398.
15. Kürkcü, ÖK, Aslan, E, Sezer, M. 2016. A numerical approach with error estimation to solve general integro-differential-difference equations using Dickson polynomials. *Applied Mathematics and Computation*; 276: 324–339
16. Yıldırım, A. 2008. Solution of BVPs for fourth-order integro-differential equations by using homotopy perturbation method. *Computers and Mathematics with Applications*; 56: 3175-3180.
17. Mirzaee, F, Hoseini, SF. 2017. A new collocation approach for solving systems of high-order linear Volterra integro-differential equations with variable coefficients. *Applied Mathematics and Computation*; 311: 272–282.
18. Yalçınbaş, S, Erdem, K. 2014. A New Approximation Method for the Systems of Nonlinear Fredholm Integral Equations. *Applied Mathematics and Physic*; 2(2): 40-48.
19. Mustafa, MM, Muhammad, AM. 2014. Numerical Solution of Linear Volterra-Fredholm Integro-Differential Equations Using Lagrange Polynomials. *Mathematical Theory and Modelin*; 4(5): 137-146.
20. Dastjerdi, HL, Maalek, Ghaini FM. 2012. Numerical solution of Volterra–Fredholm integral equations by moving least square method and Chebyshev polynomials. *Applied Mathematical Modelling*; 36: 3283–3288.
21. Maleknejad, K, Basirat, B, Hashemizadeh E. 2012. A Bernstein operational matrix approach for solving a system of high order linear Volterra–Fredholm integro-differential equations. *Mathematical and Computer Modelling*; 55: 1363–1372.
22. Yüzbaşı, Ş, Şahin, N, Yildirim, A. 2012. A collocation approach for solving high-order linear Fredholm–Volterra integro-differential equations. *Mathematical and Computer Modelling*; 55: 547–563.
23. Rashidinia, J, Tahmasebi, A. 2013. Approximate solution of linear integro-differential equations by using modified Taylor expansion method. *World Journal of Modelling and Simulation*; 9(4): 289-301.
24. Erdem, Bicer, K, Yalcinbas, S. 2016. A Matrix Approach to Solving Hyperbolic Partial Differential Equations Using Bernoulli Polynomials, *Published by Faculty of Sciences and Mathematics*, 30(4): 993–1000.
25. Cravero, I, Pittaluga, G, Sacripante, L. 2012. An algorithm for solving linear Volterra integro-differential equations. *Numer Algor*; 60: 101–114,
26. Jordan, C. *Calculus of Finite Differences*; Chelsea Publishing Company: New York, 1950; pp 318.
27. Baykus, Savaseneril, N, Sezer, M. 2016. Laguerre polynomial solution of high- order linear Fredholm integro-differential equations. *NTMSCI*; 4(2), 273-284.
28. Yüzbaşı, Ş, Şahin, N, Sezer, M. 2011. Bessel polynomial solutions of high-order linear Volterra integro-differential equations. *Computers and Mathematics with Applications*; 62: 1940–1956.
29. Balcı, MA, Sezer, M. 2016. Hybrid Euler-Taylor matrix method for solving of generalized linear Fredholm integro-differential difference equations. *Applied Mathematics and Computation*; 273: 33–41.
30. Roman, S., *The Umbral Calculus*; ACADEMIC PRESS: New York, 1984; pp 12.
31. Kim, DS. 2014. A note on Boole polynomials. *Integral Transforms and Special Functions*, 25(8): 627-633.

Existence and Uniqueness Results for a Computer Virus Spreading Model with Atangana-Baleanu Derivative

Sümeyra Uçar^{1*} 

¹Balikesir University, Faculty of Arts and Sciences, Department of Mathematics, Balikesir, Turkey

*sumeyraucar@balikesir.edu.tr

*Orcid: 0000-0002-6628-526X

Received: 8 April 2020

Accepted: 1 March 2021

DOI: 10.18466/cbayarfbe.716573

Abstract

A virus is programs that are often hidden inside a file that appears to be harmless and cause unexpected and unwanted events on the computer when the file is run. Viruses, unlike others, are software designed to maliciously damage systems. Viruses have the ability to copy themselves, jump to the files you work with, and delete files, change the file content and make it unavailable. They can do all this without the knowledge of the user and without the need for any command. Therefore, in order to better understanding of computer virus, there are many mathematical models in the literature. In the present study, we consider computer virus spreading model benefiting from Atangana-Baleanu derivative in Caputo sense with non-local and non-singular kernels. The solution properties of our fractional model are established benefiting from Arzelo-Ascoli theorem.

Keywords: Arzelo-Ascoli theorem, Atangana-Baleanu derivative, existence and uniqueness results.

1. Introduction

Computer viruses are some computer programs that can damage your computer in different ways when it works. If these programs (or virus codes) are run, they will start damaging your computer according to the way they are programmed. In addition, after viruses are activated in a system, they have the ability to reproduce, spread to other files on your computer, infect other computers over the network and many more. Many mathematical models are being studied to cope with the spread of computer viruses and for better understanding their structure such as SIR model, SEIRS model, SIRS model [1-8].

Due to memory properties of fractional derivatives, fractional operators gain increasing interest from various directions in the modeling of biological process, neural networks, engineering, physics, etc [9-20]. It is clear that Riemann Liouville and Caputo fractional derivatives have singular kernels. To cope with this problem, Atangana and Baleanu have proposed a new fractional derivative named as Atangana-Baleanu (AB) fractional derivative with Mittag-Leffler kernel. There are many extensive treatment and several applications of this recently defined AB derivatives in the literature [21-28].

Taking these motivations and AB derivative into consideration, in this article we examine the existence and uniqueness conditions for the solutions of the below computer virus spreading model presented by [29]:

$$\begin{aligned}\frac{dS}{dt} &= b - \beta SI - \mu S, \\ \frac{dE}{dt} &= (1-p)\beta SI - \gamma E + \varepsilon I - \mu E, \\ \frac{dI}{dt} &= p\beta SI + \gamma E - \varepsilon I - \alpha I - \mu I.\end{aligned}\tag{1.1}$$

We choose this model because it defines a novel virus spreading system considering the possibility of a virus outbreak on a network with restricted antivirus ability. Here, the total number of computers attached the internet are separated into four class: The number of susceptible computers $S(t)$ is the set of external not infected computers which are attached to the network, the number of exposed computers $E(t)$ is the set of all latent computers at which viruses are latent, the number of infected computers $I(t)$ is the set of infected

computers at which viruses are explode. The model parameters are: b represents the ratio where external computers are linked with the network, β stands for the ratio where having a link to one latent computer, γ shows the ratio where one latent computer explodes, μ displays the ratio where one computer is out from the network, α displays the recovery ratio of infected computers and connect to the the ability of the anti-virus software. Owing to a possible link with infected computers, susceptible computer is latent with possibility $(1-p)\beta I(t)$, or explodes with possibility $p\beta I(t)$ where $p > 0$ is a fixed parameter. Since the network's anti-virus ability is restricted, the virus is momentarily suppressed with possibility ε where $\varepsilon > 0$ is a fixed parameter.

In this paper, inspired by the above model, we give properties of the solution of our fractional model with AB derivative by Arzelò-Ascoli theorem.

2. Preliminaries

Now, we will give basic definitions related to AB fractional derivative.

Definition 2.1. Let $f \in H^1(a, b)$ be a function, $a < b$ and $r \in [0, 1]$. The AB derivative in Caputo sense of f is defined as [30]

$${}^{ABC}_0 D_t^r f(t) = \frac{K(r)}{1-r} \int_a^t f'(x) E_r \left[-r \frac{(t-x)^r}{1-r} \right] dx \quad (2.1)$$

with $K(r)$ is a normalization function with $K(0) = K(1) = 1$.

Definition 2.3. The fractional integral relevant to AB derivative is given by [30]

$${}^{AB}_0 I_t^r f(t) = \frac{1-r}{K(r)} f(t) + \frac{r}{K(r)\Gamma(r)} \int_a^t f(y)(t-y)^{r-1} dy \quad (2.2)$$

3. Existence and Uniqueness of the Solutions

Now, we remodel the system (1.1) using AB derivative in Caputo sense.

$$\begin{aligned} {}^{ABC}_0 D_t^r S &= b - \beta SI - \mu S, \\ {}^{ABC}_0 D_t^r E &= (1-p)\beta SI - \gamma E + \varepsilon I - \mu E, \\ {}^{ABC}_0 D_t^r I &= p\beta SI + \gamma E - \varepsilon I - \alpha I - \mu I. \end{aligned} \quad (3.1)$$

In this part, the existence and uniqueness of the solutions for the model (3.1) is considered and proved by using AB derivative. For this aim, we apply AB integral to the system (3.1) and we get

$$\begin{aligned} S(t) - S(0) &= K \frac{1-r}{K(r)} \{b - \beta SI - \mu S\} \\ &+ \frac{r}{K(r)\Gamma(r)} \int_0^t (t-y)^{r-1} \{b - \beta SI - \mu S\} dy, \\ E(t) - E(0) &= \frac{1-r}{K(r)} \{(1-p)\beta SI - \gamma E + \varepsilon I - \mu E\} \\ &+ \frac{r}{K(r)\Gamma(r)} \int_0^t (t-y)^{r-1} \{(1-p)\beta SI - \gamma E + \varepsilon I - \mu E\} dy, \\ I(t) - I(0) &= \frac{1-r}{K(r)} \{p\beta SI + \gamma E - \varepsilon I - \alpha I - \mu I\} \\ &+ \frac{r}{K(r)\Gamma(r)} \int_0^t (t-y)^{r-1} \{p\beta SI + \gamma E - \varepsilon I - \alpha I - \mu I\} dy. \end{aligned} \quad (3.2)$$

For the simplification of equations in (3.2), we define our kernels below:

$$\begin{aligned} s(t, S(t)) &= b - \beta SI - \mu S, \\ s(t, E(t)) &= (1-p)\beta SI - \gamma E + \varepsilon I - \mu E, \\ s(t, I(t)) &= p\beta SI + \gamma E - \varepsilon I - \alpha I - \mu I. \end{aligned} \quad (3.3)$$

Now, we will consider the operator $G: H \rightarrow H$ defined as

$$\begin{aligned} GS(t) &= \frac{1-r}{K(r)} s(t, S(t)) \\ &+ \frac{r}{K(r)\Gamma(r)} \int_0^t (t-y)^{r-1} s(y, S(y)) dy, \\ GE(t) &= \frac{1-r}{K(r)} s(t, E(t)) \\ &+ \frac{r}{K(r)\Gamma(r)} \int_0^t (t-y)^{r-1} s(y, E(y)) dy, \\ GI(t) &= \frac{1-r}{K(r)} s(t, I(t)) \\ &+ \frac{r}{K(r)\Gamma(r)} \int_0^t (t-y)^{r-1} s(y, I(y)) dy. \end{aligned} \quad (3.4)$$

Lemma 3.1. Let $M \subset H$ be a bounded set, assume that S, E and I satisfy Lipschitz condition
 $\|S(t_2) - S(t_1)\| \leq p \|t_2 - t_1\|,$
 $\|E(t_2) - E(t_1)\| \leq r \|t_2 - t_1\|,$
 $\|I(t_2) - I(t_1)\| \leq q \|t_2 - t_1\|.$

For some positive constants p, q, r . Then $\overline{G(M)}$ is compact.

Proof 3.1 Let $P = \max \left\{ \frac{1-r}{K(r)} + s(t, S(t)) \right\},$

$0 \leq S(t) \leq K_1$ for some positive constant K_1 . For $S(t) \in M$, then we get

$$\begin{aligned} \|GS(t)\| &= \frac{1-r}{K(r)} \|s(t, S(t))\| \\ &+ \frac{r}{K(r)\Gamma(r)} \int_0^t (t-y)^{r-1} \|s(y, S(y))\| dy \\ &\leq \frac{1-r}{K(r)} P + \frac{rPt^r}{K(r)\Gamma(r+1)}. \end{aligned} \quad (3.5)$$

Let $R = \max \left\{ \frac{1-r}{K(r)} + s(t, E(t)) \right\},$ $0 \leq E(t) \leq K_2$

for some positive constant K_2 . For $E(t) \in M$, then we get

$$\begin{aligned} \|GE(t)\| &= \frac{1-r}{K(r)} \|s(t, E(t))\| \\ &+ \frac{r}{K(r)\Gamma(r)} \int_0^t (t-y)^{r-1} \|s(y, E(y))\| dy \\ &\leq \frac{1-r}{K(r)} R + \frac{rRt^r}{K(r)\Gamma(r+1)} \end{aligned} \quad (3.6)$$

And similarly, we consider third equation, let

$Q = \max \left\{ \frac{1-r}{K(r)} + s(t, I(t)) \right\},$ $0 \leq I(t) \leq K_3$ for

some positive constant K_3 . For $I(t) \in M$

$$\begin{aligned} \|GI(t)\| &= \frac{1-r}{K(r)} \|s(t, I(t))\| \\ &+ \frac{r}{K(r)\Gamma(r)} \int_0^t (t-y)^{r-1} \|s(y, I(y))\| dy \\ &\leq \frac{1-r}{K(r)} Q + \frac{rQt^r}{K(r)\Gamma(r+1)}. \end{aligned} \quad (3.7)$$

Thus from equations (3.5)-(3.7) we can conclude that the operator G is bounded.

Now, we assume $t_1 < t_2$ and $S(t) \in M$. Taking into account that M is bounded, for $\varepsilon > 0$, if $|t_2 - t_1| < \delta$ we have

$$\begin{aligned} \|GS(t_2) - GS(t_1)\| &= \left\| \frac{1-r}{K(r)} s(t_2, S(t_2)) \right. \\ &+ \frac{r}{K(r)\Gamma(r)} \int_0^{t_2} (t_2-y)^{r-1} s(y, S(y)) dy \\ &- \frac{1-r}{K(r)} s(t_1, S(t_1)) \\ &- \left. \frac{r}{K(r)\Gamma(r)} \int_0^{t_1} (t_1-y)^{r-1} s(y, S(y)) dy \right\| \\ &\leq \frac{1-r}{K(r)} \|s(t_2, S(t_2)) - s(t_1, S(t_1))\| \\ &+ \left\| \frac{r}{K(r)\Gamma(r)} \int_0^{t_2} (t_2-y)^{r-1} s(y, S(y)) dy \right. \\ &- \left. \frac{r}{K(r)\Gamma(r)} \int_0^{t_1} (t_1-y)^{r-1} s(y, S(y)) dy \right\| \\ &\leq \frac{1-r}{K(r)} \|s(t_2, S(t_2)) - s(t_1, S(t_1))\| \\ &+ \frac{rK_1}{K(r)\Gamma(r)} \left\{ \int_0^{t_2} (t_2-y)^{r-1} dy - \int_0^{t_1} (t_1-y)^{r-1} dy \right\}. \end{aligned} \quad (3.8)$$

We have that

$$\begin{aligned} &\int_0^{t_2} (t_2-y)^{r-1} dy - \int_0^{t_1} (t_1-y)^{r-1} dy \\ &= \frac{(t_2-t_1)^r}{r}. \end{aligned} \quad (3.9)$$

We study the following

$$\begin{aligned} &\|s(t_2, S(t_2)) - s(t_1, S(t_1))\| \\ &\leq (\beta(a+b) + \mu) \|S(t_2) - S(t_1)\| \\ &\leq J_1 \|t_2 - t_1\|. \end{aligned} \quad (3.10)$$

Then, putting Eqs. (3.9)-(3.10) in (3.8), we obtain

$$\|GS(t_2) - GS(t_1)\| \leq \frac{1-r}{K(r)} J_1 \|t_2 - t_1\| + \frac{rK}{K(r)\Gamma(r)} \frac{\|t_2 - t_1\|^r}{r}$$

Let $\delta_1 = \frac{\varepsilon}{\frac{1-r}{K(r)} J_1 + \frac{rK_1}{K(r)\Gamma(r+1)}}$ then we get

$$\|GS(t_2) - GS(t_1)\| \leq \varepsilon.$$

In the same manner, we can get the following results for the other two functions: If we get $\varepsilon > 0$, we have

$$\delta_2 = \frac{\varepsilon}{\frac{1-r}{K(r)} J_2 + \frac{rK_2}{K(r)\Gamma(r+1)}}$$

$$\delta_3 = \frac{\varepsilon}{\frac{1-r}{K(r)} J_3 + \frac{rK_3}{K(r)\Gamma(r+1)}}$$

then we obtain

$$\|GE(t_2) - GE(t_1)\| \leq \varepsilon,$$

$$\|GI(t_2) - GI(t_1)\| \leq \varepsilon.$$

Thus $\overline{G(M)}$ is equicontinuous and so $\overline{G(M)}$ is compact by Arzelo-Ascoli Theorem. \square

Theorem 3.2. Let $S : [a, b] \times [0, \infty) \rightarrow [0, \infty)$ be increasing for each t in $[a, b]$ and be a continuous function. Suppose that one can find u, v satisfying $M(D)u \leq S(t, u)$, $M(D)v \geq S(t, v)$ for $0 \leq u(t) \leq v(t)$ and $a \leq t \leq b$. Thus, system (1.1) has a positive solution.

Proof 3.2. Now we handle the fixed point operator G . We know that the operator $G : H \rightarrow H$ is completely continuous. Let $S_1 \leq S_2, E_1 \leq E_2, I_1 \leq I_2$ then we get

$$GS_1(t) \leq \frac{1-r}{K(r)} s(t, S_1(t)) + \frac{r}{K(r)\Gamma(r)} \int_0^t (t-y)^{r-1} \|s(y, S_1(y))\| dy \leq GS_2(t). \quad (3.11)$$

Following similar steps, we obtain

$$GE_1(t) \leq \frac{1-r}{K(r)} s(t, E_1(t)) + \frac{r}{K(r)\Gamma(r)} \int_0^t (t-y)^{r-1} \|s(y, E_1(y))\| dy \leq GE_2(t) \quad (3.12)$$

and

$$GI_1(t) \leq \frac{1-r}{K(r)} s(t, I_1(t)) + \frac{r}{K(r)\Gamma(r)} \int_0^t (t-y)^{r-1} \|s(y, I_1(y))\| dy \leq GI_2(t) \quad (3.13)$$

Thus, G is increasing operator. From the conjecture, $Gm \geq m$, $Gn \leq n$. So $G : \langle m, n \rangle \rightarrow \langle m, n \rangle$ is compact and continuous from Lemma 3.1. Thus, H is a normal cone. \square

Now, we will investigate the uniqueness of solutions. To manage this, we study the followings:

$$\|GS_1(t) - GS_2(t)\| \leq \frac{1-r}{K(r)} \|s(t, S_1(t)) - s(t, S_2(t))\| + \frac{r}{K(r)\Gamma(r)} \int_0^t (t-y)^{r-1} \|s(y, S_1(y)) - s(y, S_2(y))\| dy \leq \frac{1-r}{K(r)} F_1 \|S_1(t) - S_2(t)\| + \frac{r}{K(r)\Gamma(r)} F_1 \int_0^t (t-y)^{r-1} \|S_1(y) - S_2(y)\| dy$$

which gives

$$\|GS_1(t) - GS_2(t)\| \leq \left\{ \frac{1-r}{K(r)} F_1 + \frac{rF_1 b^r}{K(r)\Gamma(r+1)} \right\} \times \|S_1(t) - S_2(t)\| \quad (3.14)$$

By a similar method, we obtain

$$\|GE_1(t) - GE_2(t)\| \leq \left\{ \frac{1-r}{K(r)} F_2 + \frac{rF_2 b^r}{K(r)\Gamma(r+1)} \right\} \times \|E_1(t) - E_2(t)\|. \quad (3.15)$$

$$\|GI_1(t) - GI_2(t)\| \leq \left\{ \frac{1-r}{K(r)} F_3 + \frac{rF_3 b^r}{K(r)\Gamma(r+1)} \right\} \times \|I_1(t) - I_2(t)\|. \quad (3.16)$$

Therefore, if the following conditions satisfy

$$\frac{1-r}{K(r)} F_1 + \frac{rF_1 b^r}{K(r)\Gamma(r+1)} < 1,$$

$$\frac{1-r}{K(r)} F_2 + \frac{rF_2 b^r}{K(r)\Gamma(r+1)} < 1,$$

$$\frac{1-r}{K(r)} F_3 + \frac{rF_3 b^r}{K(r)\Gamma(r+1)} < 1,$$

the mapping G is a contraction, so it has a fixed point by Banach fixed-point theorem. Thus the new model has a unique positive solution.

4. Numerical Results

Here, in order to observe how fractional order r affects behavior of the fractional model (1.1), some numerical simulations of this model are depicted benefiting from the numerical method presented by Toufik and Atangana in the paper [31]. We select the parameters $b=5$, $\beta = 0.007$, $\mu = 0.6$, $\gamma = 0.25$, $\varepsilon = 0.3$, $p = 0.7$ with the initial conditions $S(0)=3$, $E(0)=1$, $I(0)=1$ as given in [29]. From Figure 1, we see the behavior of susceptible, exposed and infected computers. From Figure 2, it is visible that as r goes up, the number of susceptible computers $S(t)$ increases while the number of exposed computers $E(t)$ and infected computers $I(t)$ decreases.

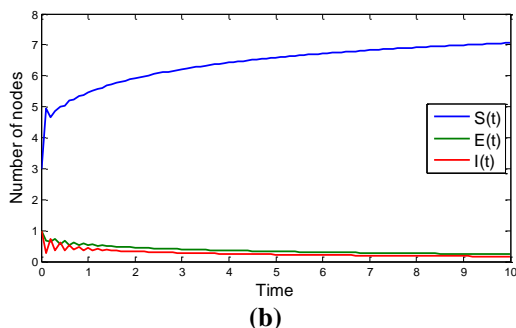
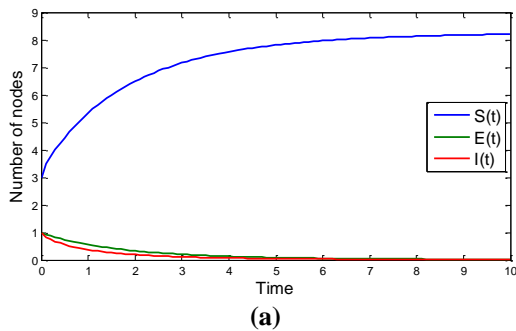


Figure 1. Numerical simulations for the model (1.1) at $r=0.95$ and $r=0.6$, respectively.

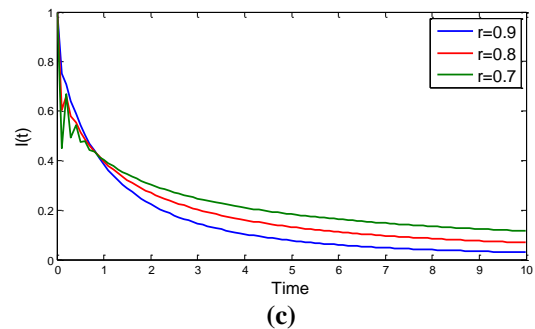
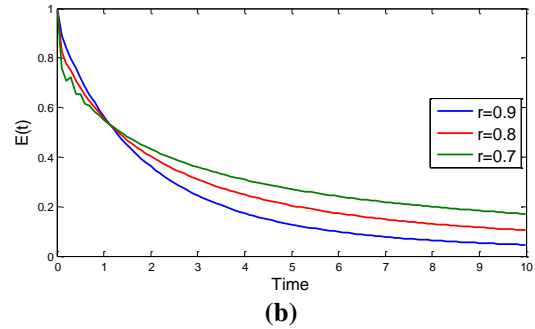
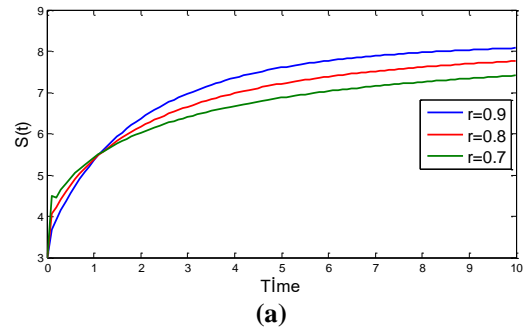


Figure 2. The behavior of the fractional computer virus spreading model components for distinct values r .

5. Conclusion

In this study, Atangana–Beleanu derivative with Mittag-Leffler kernel has been applied in reformulating the computer virus spreading model presented by Xu and Ren [29]. Then, Arzelo-Ascoli theorem is used to prove the existence and uniqueness properties of the considered model. Benefiting from Toufik-Atangana method [31], some numerical simulations are depicted with several values r and briefly interpreted. We expect that the present study will be more helpful to construct computer virus spreading model with fractional derivatives.

Author's Contributions

Sümeýra Uçar drafted the manuscript, compiled information from the literature, and designed the figures and tables.

Ethics

There are no ethical issues after the publication of this manuscript.

References

1. Piqueira, JRC, Araujo, VO. 2009. A modified epidemiological model for computer viruses, *Applied Mathematics and Computation*; 213(2): 355–360.
2. Wierman, JC, Marchette, DJ. 2004. Modeling computer virus prevalence with a susceptible-infected susceptible model with reintroduction, *Computational Statistics Data Analysis*; 45(1): 3–23.
3. Li, XZ, Zhou, LL. 2009. Global stability of an SEIR epidemic model with vertical transmission and saturating contact rate, *Chaos Solitons & Fractals*; 40(2): 874–884.
4. Li, G, Zhen, J. 2005. Global stability of an SEI epidemic model with general contact rate, *Chaos, Solitons Fractals*; 23(3): 997–1004.
5. Jin, Y, Wang, W, Xiao, S. 2007. An SIRS model with a nonlinear incidence rate, *Chaos, Solitons Fractals*; 34(5): 1482–1497.
6. Yang, LX, Yang, XF, Zhu, QY, Wen, LS. 2013. A computer virus model with graded cure rates, *Nonlinear Analysis: Real World Applications*; 14(1): 414-442.
7. Yang, LX, Yang, XF. 2012. The spread of computer viruses under the influence of removable storage devices, *Applied Mathematics and Computation*; 219(8): 3419-3422.
8. Wang, FG, Zhang, YK, Wang, CG, Ma, JF, Moon, SJ. 2010. Stability analysis of a SEIQV epidemic model for rapid spreading worms, *Computers & Security*; 29(4): 410-418.
9. Özdemir, N, Karadeniz, D, İskender, BB. 2009. Fractional optimal control problem of a distributed system in cylindrical coordinates, *Physics Letters A*; 373(2): 221-226.
10. Oldham, KB, Spanier, J. *The Fractional Calculus*; New York, Academic Press, 1974.
11. Kilbas, AA, Srivastava, HM, Trujillo, JJ. *Theory and applications of fractional differential equations*; Amsterdam, Elsevier, 2006.
12. Özdemir, N, Agrawal, OP, İskender, BB, Karadeniz, D. 2009. Fractional optimal control of a 2-dimensional distributed system using eigenfunctions. *Nonlinear Dynamics*; 55:251-260.
13. Yavuz, M, Özdemir, N. 2018. European vanilla option pricing model of fractional order without singular kernel. *Fractal Fractional*; 2(1): 3.
14. Evrigen, F. 2011. Multistage adomian decomposition method for solving NLP problems over a nonlinear fractional dynamical system, *Journal of Computational and Nonlinear Dynamics*; 6.
15. Evrigen, F. 2016. Analyze the optimal solutions of optimization problems by means of fractional gradient based system using VIM, *An International Journal of Optimization and Control: Theories & Applications (IJOCTA)*; 6(2): 75-83.
16. Atangana, A, Koca, İ. 2016. On the new fractional derivative and application to nonlinear Baggs andFreedman model, *Journal of Nonlinear Sciences and Applications*; 9(5): 2467-2480.
17. Alkahtani, BSTA, Atangana A, Koca İ. 2016. A new nonlinear triadic model of predator prey based on derivative with non-local and non-singular kernel, *Advances in Mechanical Engineering*; 8(11).
18. Mekkaoui, T, Atangana, A. 2017. New numerical approximation of fractional derivative with non-local and non-singular kernel: Application to chaotic models, *European Physical Journal Plus*; 132(10).
19. Morales-Delgado VF, Gomez-Aguilar JF, Taneco-Hernandez MA, Escobar-Jimenez RF, Olivares-Peregrino VH. 2018. Mathematical modeling of the smoking dynamics using fractional differential equations with local and nonlocal kernel, *Journal of Nonlinear Sciences Applications*; 11(8): 994-1014.
20. Özdemir, N, Yavuz M. 2017. Numerical Solution of Fractional Black-Scholes Equation by Using the Multivariate Pade Approximation, *Acta Physica Polonica A*; 132: 1050-1053.
21. Yavuz, M, Özdemir, N, Başkonuş, HM. 2017. Solutions of partial differential equations using the fractional operator involving Mittag-Leffler kernel, *The European Physical Journal Plus*; 133(6).
22. Koca, İ. 2018. Analysis of rubella disease model with non-local and non-singular fractional derivatives, *An International Journal of Optimization and Control: Theories & Applications (IJOCTA)*; 8(1): 17-25.
23. Uçar, S, Uçar E, Özdemir, N, Hammouch Z. 2019. Mathematical analysis and numerical simulation for a smoking model with Atangana Baleanu derivative, *Chaos, Solitons Fractals*; 118: 300-306.
24. Özdemir, N, Uçar E. 2020. Investigating of an immune system-cancer mathematical model with Mittag-Leffler kernel, *AIMS Mathematics*, 5(2):1519-1531.
25. Baleanu, D, Fernandez, A. 2018. On some new properties of fractional derivatives with Mittag-Leffler kernel, *Communications Nonlinear Science and Numerical Simulation*; 59: 444–462.
26. Fernandez, A, Baleanu D, Srivastava, HM. 2019. Series representations for fractional-calculus operators involving generalised Mittag-Leffler functions, *Communications Nonlinear Science and Numerical Simulation*; 67: 517-527.
27. Avcı, D, Yetim A. 2018. Analytical solutions to the advection-diffusion equation with the Atangana-Baleanu derivative over a finite domain, *Journal of Balıkesir University Institute Science and Technology*; 20(2): 382–395.
28. Yavuz, M, Bonyah E. 2019. New approaches to the fractional Dynamics of schistosomiasis disease model, *Physica A: Statistical Mechanics and its Applications*; 525: 373-393.
29. Xu, Y, Ren J. 2016, Propagation Effect of a Virus Outbreak on a Network with Limited Anti-Virus Ability; *Plos One*, Article ID: e0164415
30. Atangana, A, Baleanu, D. 2016. New fractional derivatives with non-local and non-singular kernel: theory and applications to heat transfer model, *Thermal Science*; 20(2): 763-769.
31. Toufik, M, Atangana, A. 2017. New numerical approximation of fractional derivative with non-local and non-singular kernel: Application to chaotic models, *The European Physical Journal Plus*; 132.

Attenuation of Docetaxel-induced Oxidative Stress and Apoptosis in HEK 293 Human Embryonic Kidney Cells by Curcumin Treatment

Suleyman Ilhan^{1*} 

¹Manisa Celal Bayar University, Faculty of Science and Letters, Biology Department, Manisa, Turkey

*suleyman.ilhan@cbu.edu.tr

*Orcid: 0000-0002-6584-3979

Received: 13 June 2020

Accepted: 20 February 2021

DOI: 10.18466/cbayarfbe.752495

Abstract

Docetaxel (DOC) is a chemotherapeutic that induces microtubule stabilization. It is often used in breast, prostate, lung and gastric cancers but severe side effects such as cardiotoxicity, neurotoxicity, hepatotoxicity, and nephrotoxicity limit its usage. Curcumin (CUR), a natural bioactive compound derived from turmeric. Here, the possible preventive effect of CUR against DOC-induced oxidative stress and apoptosis on HEK-293 immortalized human embryonic kidney cells. Viability was assessed via MTT assay. The generation of ROS was measured by CM-H2DCFDA dye. Phosphatidylserine externalization and caspase 3/7 activity were used to measure apoptosis. CUR pretreatment remarkably inhibited DOC-induced cell viability reduction, ROS generation, and cell apoptosis in HEK-293 cells. Moreover, this study revealed that CUR pretreatment decreased caspase-3 activity. Thus, this study highlights the novel pharmacological mechanisms of CUR and understanding the detailed mechanisms of CUR action.

Keywords: Apoptosis, curcumin, docetaxel, HEK-293, oxidative stress.

1. Introduction

Despite the novel technological and scientific developments, cancer is still one of the biggest threats to humanity for decades. Many strategies are being done to struggle with cancer [1]. Among them, chemotherapy is the most effective one and considered the backbone of the treatment. However, serious side-effects in normal tissues such as cardiotoxicity, neurotoxicity, hepatotoxicity, and nephrotoxicity limit their usages [2-5]. Thus, there is an instant need to find new adjuvant compounds to diminish the chemotherapy-induced severe side effects.

Taxanes that promote microtubule stabilization are critical chemotherapy drugs in the treatment of a wide range of solid tumors [6-9]. Of taxanes, Docetaxel (DOC) is often used in breast, lung, prostate and gastric cancers, but its frequent use often leads to nephrotoxicity, especially in lung cancer patients [10]. Chronic nephrotoxicity of anticancer drugs may have multiple causes and are mediated by various mechanisms. In this study, the effects of DOC were investigated on human kidney embryonic cells (HEK-293) which could represent the possible target tissue and widely used in *in vitro* toxicology studies. One of the most important mechanisms is reactive oxygen species

(ROS) formation and subsequently induction of hepatocyte apoptosis [11]. The induction of ROS also decreases endogenous antioxidants via activation of caspases. To avoid these harmful effects of oxidative stress, it is essential to increase the cell's antioxidant defenses with natural compounds having antioxidant activity.

Curcumin (CUR), known as diferuloylmethane, is originated from *Curcuma longa* rhizome. It has been shown to have several biological activities [12-15]. CUR is a potent oxygen free radical scavenger and can inhibit the production of ROS and prevent oxidative stress both *in vitro* and *in vivo* [16]. Previous studies demonstrated that CUR treatment can ameliorate nephrotoxicity by preventing oxidative stress caused by cisplatin, gentamicin and cyclosporine and paracetamol in rats [17-19].

Taken together, the current study was aimed to investigate the protective effect of the CUR against DOC-induced oxidative stress and apoptotic cell death on HEK-293 immortalized human embryonic kidney cells.

2. Materials and Methods

2.1. Materials

CUR was provided by Sigma Chemical Co (USA). To prepare a stock solution, CUR was dissolved in 1 mg/mL ethanol (EtOH) and stored at 4°C. DOC was purchased from Sigma Chemical Co and dissolved in dimethyl sulfoxide (DMSO). The EtOH and DMSO concentrations used in this analysis were lower than 0.1% and were not cytotoxic. All other chemicals were obtained from Sigma.

2.2. Cell culture conditions

The human embryonic kidney cell line HEK-293 (CRL-11268) was purchased from ATCC (American Type Culture Collection, USA). The cells were cultured by using Eagle's Minimum Essential Medium including 10% fetal bovine serum and 1% penicillin/streptomycin in 75 cm² polystyrene cell culture flasks (Cellstar, UK). Cell culture was maintained in a standard incubator containing 5% CO₂ at 37°C.

2.3. Cell viability and morphology

MTT assay (3-(4,5-dimethylthiazol-2-yl)-2,5-diphenyltetrazolium bromide) was conducted to evaluate cell viability. Disaggregation of cells was carried out with trypsin/EDTA. A total of 10⁴ cells were propagated onto 96-well plates in 100 µL medium per well. After 24 h cell attachment, cells were exposed to increasing concentrations of DOC, CUR, or sequentially. MTT (20 µL) was added at 24, 48 and 72 h time points. The dye was carefully drained and 200 µL DMSO was added to dissolve formed formazan crystals. The optic densities were recorded by a microplate reader at 570 nm (Tecan Infinite 200 PRO, Switzerland) [20]. Olympus IX53 inverted microscope was used to monitor HEK-293 cell morphology after DOC, CUR or sequential treatment (Tokyo, Japan).

2.4. Analysis of ROS generation

The formation of ROS in HEK-293 cells was measured by cell-permeable indicator dye [5-(and-6)-chloromethyl-2,7-dichlorodihydrofluorescein diacetate acetyl ester dye (CM-H₂DCFDA, MW 577.8 Da, Molecular Probes, Eugene, OR)]. The CM-H₂DCFDA passively enters the cells and remains non-fluorescent until oxidation occurs in the cell. After oxidation, it fluoresces in the cell. The cell suspension was (10⁵ cells/mL) transferred on 96-wells in 200 µL medium containing CM-H₂DCFDA dye. The plate was then incubated for 45 min. at 37 °C. As a control, cells were also exposed to 10 mM N-acetylcysteine (NAC) which is a ROS scavenger. The amount of fluorescence was then measured at 485-520 nm by a microplate reader (Tecan Infinite 200 PRO, Switzerland) and also

observed with fluorescence microscopy (Olympus, Tokyo, Japan).

2.5. Flow cytometric analysis of apoptosis

For analyzing apoptosis, phosphatidylserine externalization was detected via Muse™ Annexin V and Dead Cell kit (Millipore, USA). HEK-293 cells in a density of 4×10⁵ were seeded in 2 mL medium and incubated 24 h for attachment. Then, attached cells were exposed to compounds alone or sequentially for 48 h. After incubation, centrifugation was performed at 1000×g for 10 min and supernatants were removed. The remaining pellets were suspended with a culture medium. Equal amounts of cell suspension and Muse™ Annexin-V & Dead Cell kit solution were mixed and incubated for 20 min in the dark. The analysis was performed using Muse™ Cell Analyzer (Millipore, USA). For each condition at least 10,000 cells were analyzed.

2.6. Caspase 3/7 activity assay

Caspase-Glo 3/7 Assay (Promega, USA). Cells were (10⁴ cells per well) treated with the desired concentrations of the compounds. After incubation periods, CaspaseGlo 3/7 reagent (100 µL) was added and incubated for 1 h in the dark. The formed luminescence was detected by a microplate reader (Tecan Infinite 200 PRO, Switzerland).

2.7. Statistical Analysis

Each experiment was done in duplicate, and three experiments were performed for each condition. Results were presented as mean ± SD. The *Student's t-test* was performed to analyze the differences between the two groups. For analysis of three or more groups, the first one-way analysis of variance test was done and then Dunnett's t-test was performed. The half-maximal inhibitory concentration (IC₅₀) was calculated via Graph Pad Prism 5.0 (San Diego, USA). A p-value of <0.05 was considered statistically significant.

3. Results and Discussion

3.1. Preventive effect of CUR on DOC-induced cytotoxicity in HEK-293 cells

Today, CUR has attracted intense interest in the protection of normal tissues from chemotherapy-induced toxicity. Before determining the preventive effect of CUR on DOC-induced cytotoxicity in HEK-293 cells, first, the effects of single CUR or DOC on the viability of cells were investigated. For this aim, HEK-293 cells were exposed to increasing concentrations of CUR (5-100 µg/mL) or DOC (0.1-1000 nM) for different time points and viability was assessed via MTT assay. As seen in Fig. 1, the increasing concentrations of single CUR or DOC induced a time-

dependent reduction in cell viability ($p < 0.05$). The IC_{50} value of CUR calculated from cell viability data was found to be $12.5 \pm 0.52 \mu\text{g/mL}$ at 48 h ($p < 0.05$). The cell viability was 91% at $5 \mu\text{g/mL}$ CUR concentration but significantly decreased by $25 \mu\text{g/mL}$ CUR concentration (17% viability) at 48 h. Therefore, 5, 10 and $25 \mu\text{g/mL}$ concentrations were chosen as a low-, medium- and high-concentration groups, respectively. There are limited studies demonstrating the effects of CUR on HEK-293 cells in the literature. Concentration-dependent inhibition in cell viability by different incubation times was reported for HEK-293 cells and calculated IC_{50} values were quite different in these studies. Rao et al. calculated the IC_{50} value of CUR on HEK-293 cells as $5.0 \pm 0.6 \mu\text{M}$ at 72 h [21]. In different studies, the IC_{50} value of CUR was calculated at 24 h and found to be $29.8 \mu\text{M}$ and $458.14 \mu\text{M}$, respectively [22, 23]. Only Zhao et al. calculated the IC_{50} value of CUR at 48 h and found it as $11 \mu\text{M}$ which was similar to the results of the current study [24]. The IC_{50} value of DOC was also calculated in HEK-293 cells and found to be $5.5 \pm 2.5 \text{ nM}$ at 48 h. Contrary to CUR, there is no study investigating the effect of DOC on HEK-293 cells. Thus, this study is the first study revealing the effect of DOC on HEK-293 cells.

To screen the possible preventive effect of CUR on DOC-induced cytotoxic effects, cells were pretreated with 5, 10 or $25 \mu\text{g/mL}$ CUR for 48 h and then treated for an additional 48 h with 10 nM DOC. As demonstrated in Fig. 2, 5 and $10 \mu\text{g/mL}$ CUR pretreatment significantly increased cell viability compared with the 10 nM DOC treated group ($p < 0.05$). However, in the $25 \mu\text{g/mL}$ CUR pretreated group, cell viability decreased as compared to the 10 nM DOC treated group ($p < 0.05$). From these data, it can be concluded that CUR pretreatment with low and medium concentrations prevented DOC-induced cytotoxicity and cell damage in HEK-293 cells. However, this effect was not observed at high concentrations of CUR.

Nephrotoxicity is a serious and well described chemotherapy-associated side-effect limiting its clinical use. Ortega-Domínguez et al. revealed that CUR treatment prevented cisplatin-induced nephrotoxicity by diminishing mitochondrial abnormalities and necrosis [25]. *In vivo* part of the study was also revealed that pretreatment of CUR prevented all the histological abnormalities in the kidney as compared to only the cisplatin received group. In another study, mitomycin-induced kidney damage was attenuated by CUR pretreatment in mice [26]. Their results further indicate that CUR pretreatment could reduce chemotherapy-induced cytotoxicity and nephrotoxicity.

To investigate the changes in cell morphology, HEK-293 cells were also analyzed by an inverted microscope.

Observations supported the cell viability results and showed that DOC treatment of HEK-293 cells led to rounding of cells indicating cell death. Moreover, loss of cell attachment to the well plates was observed, however, the number of non-adherent cells was decreased by CUR pretreatment (Figure 3).

3.2. CUR suppresses the production of ROS in DOC-treated HEK-293 cells

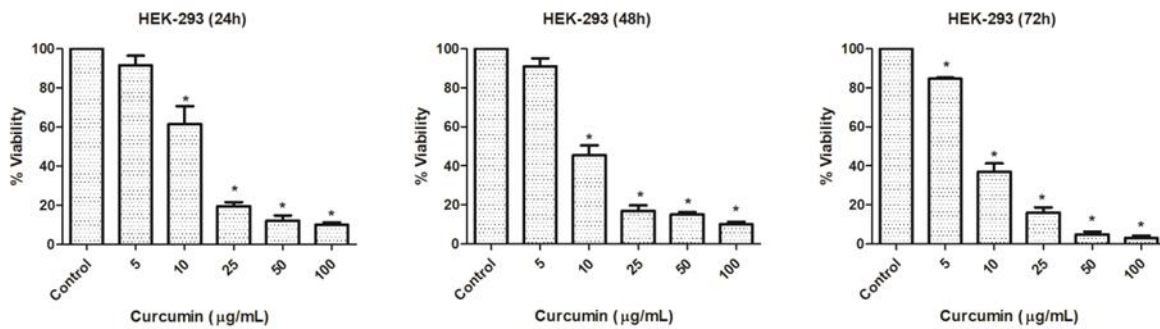
Oxidative stress and ROS accepted as the possible mechanisms responsible for DOC induced cytotoxicity and scavenging of ROS in normal tissues are known to be effective for protecting cells from chemotherapy-induced toxicity. In many studies, it was shown that CUR could inhibit cytotoxicity via diminishing cellular ROS [27, 28]. Thus, to enlighten the role of CUR in preventing DOC-induced cytotoxicity in HEK-293 cells, cellular ROS levels were measured after staining with CM-H2DCFDA and also observed with fluorescence microscopy. As shown in Fig. 4, cellular ROS was significantly induced after exposure to DOC treatment in HEK-293 cells. ROS levels were significantly diminished in CUR pretreated and NAC treated cells ($p < 0.05$).

In the study of Ortega-Domínguez et al., it has been shown that CUR can inhibit ROS as strongly as NAC. In the same study, it was also revealed that CUR attenuates cisplatin-induced mitochondrial damage via diminishing ROS production [25]. CUR not only reduces ROS levels but induces cellular defense machinery such as superoxide dismutase (SOD), catalase (CAT), and glutathione peroxidase (GTP) activities [29]. Sheu et al. showed that CUR pretreatment increased the SOD activity and, in this way, enhanced the antioxidant capacity of normal tissues [30]. From these results, it can be concluded that the possible mechanism of ROS decreasing effect in HEK-293 cells pretreated with CUR might be associated with the direct free radical scavenging activity or indirect induction of antioxidant defense systems.

3.3. The effects of CUR pretreatment on cell apoptosis in DOC-treated HEK-293 cells

Growing evidence shows that chemotherapy-induced cytotoxicity is mediated by apoptotic induction following oxidative stress. [31]. If ROS levels excessively increase in the cell, redox imbalanced cells become more vulnerable to apoptosis. To elucidate whether the preventive effects of CUR were related to the prevention of cell apoptosis, flow cytometric analysis was done. Cells undergoing early and late apoptosis after exposure to DOC were stained by Annexin V-FITC and PI and found that DOC treatment induced apoptotic cell death in HEK-293 cells.

A



B

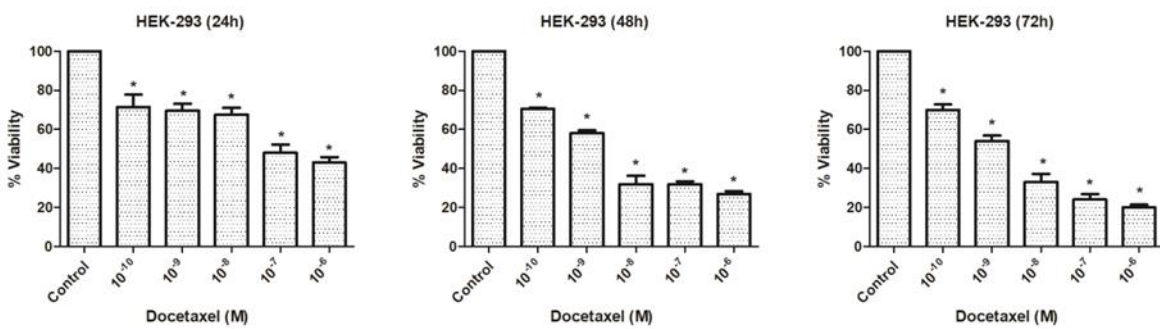


Figure 1: The effect of CUR (A) and DOC (B) on the viability of HEK-293 cells at 24, 48 and 72 h (*p<0.05 compared with the untreated control group).

However, the percentage of stained cells was significantly decreased in CUR pretreated group (p<0.05) (Figure 5).

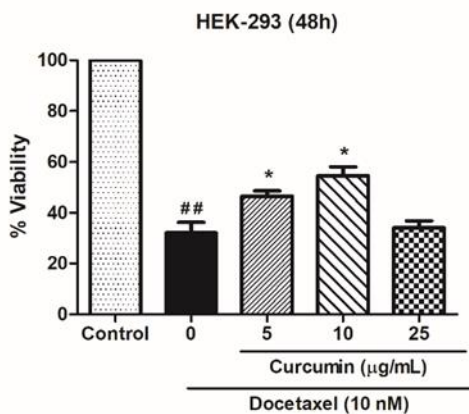


Figure 2: The effect of CUR pretreatment on the viability of HEK-293 cells under DOC exposure. Cells were treated with 5, 10 or 25 µg/mL CUR for 48 h then treated with 10 nM DOC for 48 h (##p<0.05 as compared to untreated control group, *p<0.05 as compared to 10 nM DOC treatment group).

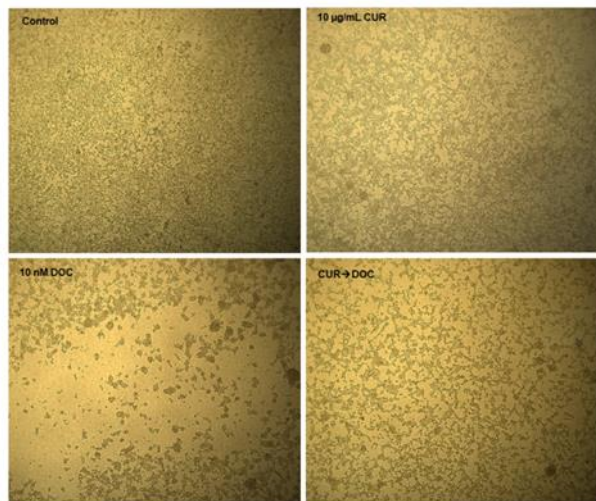


Figure 3: The effect of CUR pretreatment on the cell morphology of DOC-treated HEK-293 cells (20X).

After triggering apoptosis, the process is carried out by an enzyme family namely caspases. Among the caspase family, initiator caspases trigger effector caspases (caspases 3, 6, and 7) which are the final players that execute apoptosis [32].

After demonstrating the preventive effects of CUR pretreatment on apoptosis, caspase 3/7 activity was performed to confirm the data. According to results, pretreatment with CUR decreased the activity as compared to single DOC treatment ($p < 0.05$) (Figure 5). These observations are parallel with the previous studies that investigate the preventive effect of CUR on cell apoptosis. Benzer et al. investigated the preventive effect of CUR on doxorubicin-induced apoptosis and demonstrated that pretreatment with CUR decreased the caspase-3 activity [33]. Dai et al., demonstrated that CUR pretreatment protected cells from caspase activation and following apoptosis which was triggered by colistin [34].

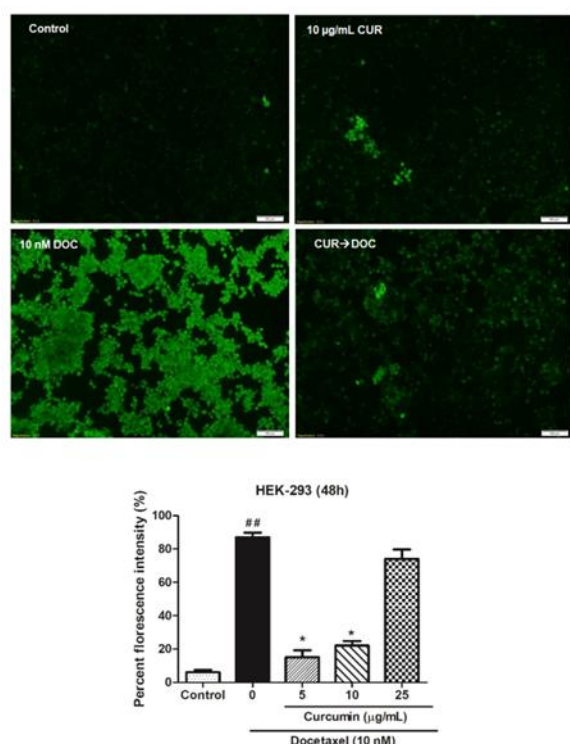


Figure 4: CUR ameliorates DOC-induced ROS in HEK-293 cells.

4. Conclusion

In summary, pretreatment with low concentrations of CUR can alleviate DOC-induced ROS levels in HEK-293 human kidney embryonic cells. The CUR treatment also protects the cell from DOC-induced apoptotic cell death through inhibition of caspases 3 and 7 and increases the viability of cells. However, the detailed protection mechanisms of the CUR in HEK-293 cells require further investigations *in vitro* and *in vivo*. Understanding the detailed mechanisms of CUR action could lead to novel renoprotective interventions.

Author's Contributions

Süleyman İlhan: Drafted and wrote the manuscript, performed the experiment and result analysis.

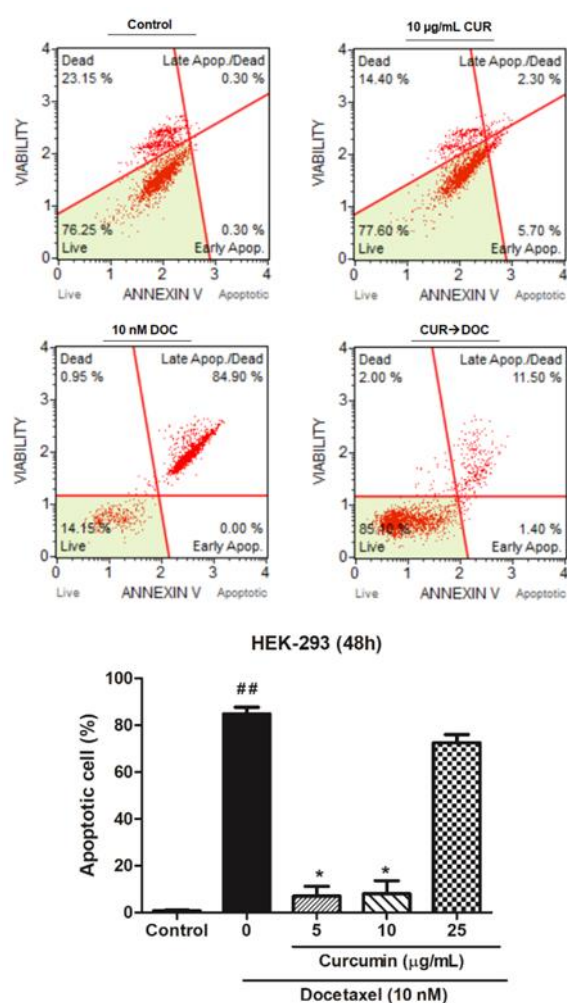


Figure 5: CUR pretreatment inhibited DOC-induced apoptosis in HEK-293 cells at 48 h (## $p < 0.05$ as compared to the untreated control group, * $p < 0.05$ as compared to 10 nM DOC treatment group).

Ethics

There are no ethical issues after the publication of this manuscript.

References

- Bray, F, Ferlay, J, Soerjomataram, I, Siegel, RL, Torre, LA, Jemal, A. 2018. Global cancer statistics 2018: GLOBOCAN estimates of incidence and mortality worldwide for 36 cancers in 185 countries. *CA: A Cancer Journal for Clinicians*; 68(6): 394-424.
- Monsuez, JJ, Charniot, JC, Vignat, N, Artigou, JY. 2010. Cardiac side-effects of cancer chemotherapy. *International Journal of Cardiology*; 144(1): 3-15.
- Love, RR, Leventhal, H, Easterling, DV, Nerenz, DR. 1989. Side effects and emotional distress during cancer chemotherapy. *Cancer*; 63(3): 604-612.



4. Oun, R, Moussa, YE, Wheate, NJ. 2018. The side effects of platinum-based chemotherapy drugs: a review for chemists. *Dalton Transactions*; 47(19): 6645-6653.
5. Cheok, CF. 2012. Protecting normal cells from the cytotoxicity of chemotherapy. *Cell Cycle*; 11(12): 2227-2227.
6. Saloustros, E, Mavroudis, D, Georgoulis, V. 2008. Paclitaxel and docetaxel in the treatment of breast cancer. *Expert Opinion on Pharmacotherapy*; 9(15): 2603-2616.
7. Saloustros, E, Georgoulis, V. 2008. Docetaxel in the treatment of advanced non-small-cell lung cancer. *Expert Review of Anticancer Therapy*; 8(8): 1207-1222.
8. Yin, H, Guo, R, Xu, Y, Zheng, Y, Hou, Z, Dai, X, Zhang, Z, Zheng, D, Xu, HE. 2012. Synergistic antitumor efficiency of docetaxel and curcumin against lung cancer. *Acta Biochimica et Biophysica Sinica*; 44(2): 147-153.
9. Baker, SD, Verweij, J, Cusatis, GA, van Schaik, RH, Marsh, S, Orwick, SJ, Franke, RM, Hu, S, Schuetz, EG, Lamba, V, Messersmith, WA, Wolff, AC, Carducci, MA, Sparreboom, A. 2009. Pharmacogenetic pathway analysis of docetaxel elimination. *Clinical Pharmacology & Therapeutics*; 85(2): 155-163.
10. Takimoto, T., Nakabori, T., Osa, A., Morita, S., Terada, H., Oseto, S., Iwazawa, T. Abe, K., 2012. Tubular nephrotoxicity induced by docetaxel in non-small-cell lung cancer patients. *International Journal of Clinical Oncology*; 17(4): 395-398.
11. Pabla, N, Dong, Z. 2008. Cisplatin nephrotoxicity: mechanisms and renoprotective strategies. *Kidney International*; 73(9): 994-1007.
12. Aggarwal, BB, Kumar, A, Bharti, AC. 2003. Anticancer potential of curcumin: preclinical and clinical studies. *Anticancer Research*; 23(1/A): 363-398.
13. Basnet, P, Skalko, BN. 2011. Curcumin: An anti-inflammatory molecule from a curry spice on the path to cancer treatment. *Molecules*; 16(6): 4567-4598.
14. Araujo, C, Leon, L. 2001. Biological activities of *Curcuma longa* L. *Memórias do Instituto Oswaldo Cruz*; 96(5): 723-28.
15. Joe, B, Vijaykumar, M, Lokesh, B. 2004. Biological properties of curcumin-cellular and molecular mechanisms of action. *Critical Reviews in Food Science and Nutrition*; 44(2): 97-111.
16. Gupta, SC, Patchva, S, Koh, W, Aggarwal, BB. 2012. Discovery of curcumin, a component of golden spice, and its miraculous biological activities. *Clinical and Experimental Pharmacology and Physiology*; 39(3): 283-299.
17. Farombi, E, Ekor, M. 2006. Curcumin attenuates gentamicin-induced renal oxidative damage in rats. *Food and Chemical Toxicology*; 44(9): 1443-1448.
18. Venkatanarayana, G, Sudhakara, G, Sivajyothi, P, Indira, P. 2012. Protective effects of curcumin and vitamin E on carbon tetrachloride-induced nephrotoxicity in rats. *EXCLI Journal*; 11: 641-650.
19. Tung, BT, Hai, NT, Son, PK. 2017. Hepatoprotective effect of Phytosome Curcumin against paracetamol-induced liver toxicity in mice. *Brazilian Journal of Pharmaceutical Sciences*, 53(1): 1-13.
20. Berridge, MV, Herst, PM, Tan, AS. 2005. Tetrazolium dyes as tools in cell biology: New insights into their cellular reduction. *Biotechnology Annual Review*; 11: 127-152.
21. Rao, DK., Liu, H, Ambudkar, SV, Mayer, M. 2014. A combination of curcumin with either gramicidin or ouabain selectively kills cells that express the multidrug resistance-linked ABCG2 transporter. *Journal of Biological Chemistry*, 289(45): 31397-31410.
22. Adahoun, MAA, Al-Akhras, MAH, Jaafar, MS, Bououdina, M. 2017. Enhanced anti-cancer and antimicrobial activities of curcumin nanoparticles. *Artificial cells, Nanomedicine, and Biotechnology*; 45(1): 98-107.
23. Nishida, M, Nishiumi, S, Mizushima, Y, Fujishima, Y, Yamamoto, K, Masuda, A, Mizuno, S, Fujita, T, Morita, Y, Kutsumi, H, Yoshida, H. 2010. Monoacetylcurcumin strongly regulates inflammatory responses through inhibition of NF- κ B activation. *International Journal of Molecular Medicine*; 25(5): 761-767.
24. Zhao, Y, Collier, JJ, Huang, EC, Whelan, J. 2014. Turmeric and Chinese goldthread synergistically inhibit prostate cancer cell proliferation and NF- κ B signaling. *Functional Foods in Health and Disease*; 4(7): 312-339.
25. Ortega-Domínguez, B, Aparicio-Trejo, OE, García-Arroyo, FE, León-Contreras, JC, Tapia, E, Molina-Jijón, E, Hernández-Pandoc, R, Sánchez-Lozada, LG, Barrera-Oviedo, D, Pedraza-Chaverri, J. 2017. Curcumin prevents cisplatin-induced renal alterations in mitochondrial bioenergetics and dynamic. *Food and Chemical Toxicology*; 107: 373-385.
26. Zhou, QM, Wang, XF, Liu, XJ, Zhang, H, Lu, YY, Huang, S, Su, SB. 2011. Curcumin improves MMC-based chemotherapy by simultaneously sensitising cancer cells to MMC and reducing MMC-associated side-effects. *European Journal of Cancer*; 47(14): 2240-2247.
27. Ramanathan, B, Jan, KY, Chen, CH, Hour, TC, Yu, HJ, Pu, YS. 2005. Resistance to paclitaxel is proportional to cellular total antioxidant capacity. *Cancer Research*; 65(18): 8455-8460.
28. Trujillo, J, Chirino, YI, Molina-Jijón, E, Andérica-Romero, AC, Tapia, E, Pedraza-Chaverri, J. 2013. Renoprotective effect of the antioxidant curcumin: Recent findings. *Redox Biology*; 1(1): 448-456.
29. Swamy, AV, Gulliaya, S, Thippeswamy, A, Koti, BC, Manjula, DV. 2012. Cardioprotective effect of curcumin against doxorubicin-induced myocardial toxicity in albino rats. *Indian Journal of Pharmacology*; 44(1): 73.
30. Sheu, MT, Jhan, HJ, Hsieh, CM, Wang, CJ, Ho, HO. 2015. Efficacy of antioxidants as a complementary and alternative medicine (CAM) in combination with the chemotherapeutic agent doxorubicin. *Integrative Cancer Therapies*; 14(2): 184-195.
31. Kim, SJ, Kim, HS, Seo, YR. 2019. Understanding of ROS-Inducing Strategy in Anticancer Therapy. *Oxidative Medicine and Cellular Longevity*; 1-12.
32. Florentin, A, Arama, E. 2012. Caspase levels and execution efficiencies determine the apoptotic potential of the cell. *Journal of Cell Biology*; 196(4): 513-527.
33. Benzer, F, Kandemir, FM, Kucukler, S, Comaklı, S, Caglayan, C. 2018. Chemoprotective effects of curcumin on doxorubicin-induced nephrotoxicity in wistar rats: by modulating inflammatory cytokines, apoptosis, oxidative stress and oxidative DNA damage. *Archives of Physiology and Biochemistry*; 124(5): 448-457.
34. Dai, C, Ciccotosto, GD, Cappai, R, Tang, S, Li, D, Xie, S, Xiao, X, Velkov, T. 2018. Curcumin attenuates colistin-induced neurotoxicity in N2a cells via anti-inflammatory activity, suppression of oxidative stress, and apoptosis. *Molecular Neurobiology*; 55(1): 421-434.

Filler Type and Particle Distribution Effect on Some Properties of Polymer Composites

Bayram Poyraz¹ , Şevki Eren^{2*} , Serkan Subaşı³ 

¹Duzce University, Faculty of Technology, Department of Civil Engineering, Düzce, 81620, Turkey

^{2*}Kırşehir Ahi Evran University, Vocational School, Department of Construction Technology, Kırşehir, Turkey

³Duzce University, Faculty of Technology, Department of Civil Engineering, Düzce, 81620, Turkey

[*seren@ahievran.edu.tr](mailto:seren@ahievran.edu.tr)

* Orcid:0000-0003-0773-4034

Received: 1 September 2020

Accepted: 1 March 2021

DOI: 10.18466/cbayarfbe.787883

Abstract

This study reports the effects of silica (S), quartz (Q), and basalt (B) fillers on the chemical, thermal, and mechanical properties of unsaturated polyester (PE) composites. In the study, fillers were selected as same class grain distribution and mixed with orthophthalic based PE resin to produce composites. The thermal characterization of the composites was determined with thermogravimetric and thermal conductivity. Chemical characterization was carried out with FT-IR. Compressive strength was investigated with Universal Testing Machine. SEM device was used to investigate the morphological alterations of the composites. Also, statistical analysis was carried out for thermal conductivity and mechanical results. At the end of the present study, some minor chemical alterations were seen in FT-IR after the interaction of the fillers and PE resin. Thermal stability decreased after adding fillers. The thermal conductivity and thermogravimetric analysis were not agreed with each other that higher thermal conductivity was seen in the PE-Q composites. The compressive strength of filler-based composites was higher than that of the neat PE composite whereas the higher compressive strength was obtained in the PE-Q. This study confirms the applicability of various fillers as a reinforcing agent in the polymer.

Keywords: Compressive strength, FT-IR, Grain distribution, Polymer composites, SEM, Silica, quartz and basalt fillers, Thermogravimetric and thermal conductivity.

1. Introduction

Composites were mostly used as a substitute for conventional materials due to the revealing high strength at a small specific weight, high rigidity as well as the ability to be tailored for specific purposes [1-4].

PE having doubled bonds and giving crosslinking are mainly used in the production of the composites for any applications due to the ease of use and the low cost easily tailoring of the mechanical and chemical properties. Several phenomena were carried out to improve the performance of PE polymers. One of the traditional methods is the pooling of a PE with inorganic substances through physical or weak phase interaction e.g., hydrogen bonding, van der Waals forces, or strong covalent bond e.g., between the organic and inorganic phases. In this way, organic-inorganic composites combine the ductility, flexibility, resistance, thermal stability, rigidity, and dielectric of their distinct properties [5-8].

Inorganic fillers are a promising reinforcing agent in the modification of polymers that if the inorganic fillers having different dimensions of a dispersed phase in PE composite would alter mechanical and thermal properties that cannot be obtained with traditional PE composites. Because fillers restrict the movement of the polymer chain and increase the formability of the material. With those properties, tensile strength, hardness, abrasion resistance, rigidity, the toughness of the composites can be improved [9-11].

Mahdi et al. [12] studied PET obtaining from waste bottles. In this study, they used methyl ethyl ketone peroxide (MEKP) and cobalt naphthenate (CoNp) as free radical initiator and the catalyst, respectively. Afterward, they mixed with inorganic aggregate (10% w/w. aggregate/resin). The maximum compressive strength was measured as 42.2 MPa that this obtained value is higher than those of the compressive strength of the neat polymer composite (28.5 MPa). Ateş and Barnes [13] prepared polymer concrete composite

specimens by using polyester and quartz as binder and filler material, in different aggregate diagrams and binder ratio. The highest compression strength was obtained as 95.8 MPa. Ateş [14] examined the change of the compressive strength properties of the polyester and epoxy resin-based composite material having quartz sand as a filler which has different grain distributions and produced by using binder material at different ratios. The highest compressive strength value was obtained as 62.8 MPa in a mixture of 18% resin + 82% quartz filler. Singh et al. [15] fabricated silica-polyester composites having 0.5-2.5% by weight in the presence of cobalt octoate and MEKP via the compression molding method cured for 24 h at room temperature. The tensile yield strength and tensile modulus increased with the filler content from 10.58 MPa to 25.99 MPa, and 1.11 GPa to 1.61 GPa for sheets containing 1.5 % colloidal silica filler content. After that point, there is a substantial decrease in the tensile modulus. Flexural strength and flexural modulus revealed a similar trend with increasing filler content as tensile properties did. That probably stems from good newly bonding and uniform dispersion of the smaller size of particles. The increase in filler content caused new bonds in the resin matrix. Besides, agglomeration which reduces the strength of the composites occurred as well. The objective of this study was to investigate how particle size distribution and type of filler influence the chemical, thermal and mechanical properties of the composites. For that purpose, silica, quartz, and basalt fillers were embedded in unsaturated orthophthalic

polyester resins. Then, polyester resins were cured in certain conditions with methyl ethyl ketone peroxide (initiator) in the presence of cobalt octoate (catalyst) to obtain polyester-filler composites. After production, FTIR, thermogravimetric analysis, thermal conductivity, and mechanical analysis were carried out.

2. Materials and Methods

2.1. Matrix Materials

In this study, the orthophthalic acid resin was used as a thermosetting composite matrix (1.12 g/cm³, 66% solid content, Polipol 3562-SR, Turkey) and MEKP (ER 59, Akperox, Turkey) and cobalt octoate (RC88, Akkobalt, Turkey) was used as initiator and catalyst, respectively. In the study, silica filler, quartz filler, and basalt filler were used in the 0-1000 µm grain size range in the composites.

2.2. Design of The Experiments

The orthophthalic acid resin having initiator and catalyst were mixed with fillers in certain conditions and those are classified as a polyester-silica filler (PE-S), polyester-basalt filler (PE-B), and polyester-quartz filler (PE-Q). Filler grain-size distribution was determined as Fuller equation. The reference "Fuller equation" is given in Equation 2.1 and in this equation, n=0.8 was taken as [16]. Filler grain-size distributions are represented in Figure 1.

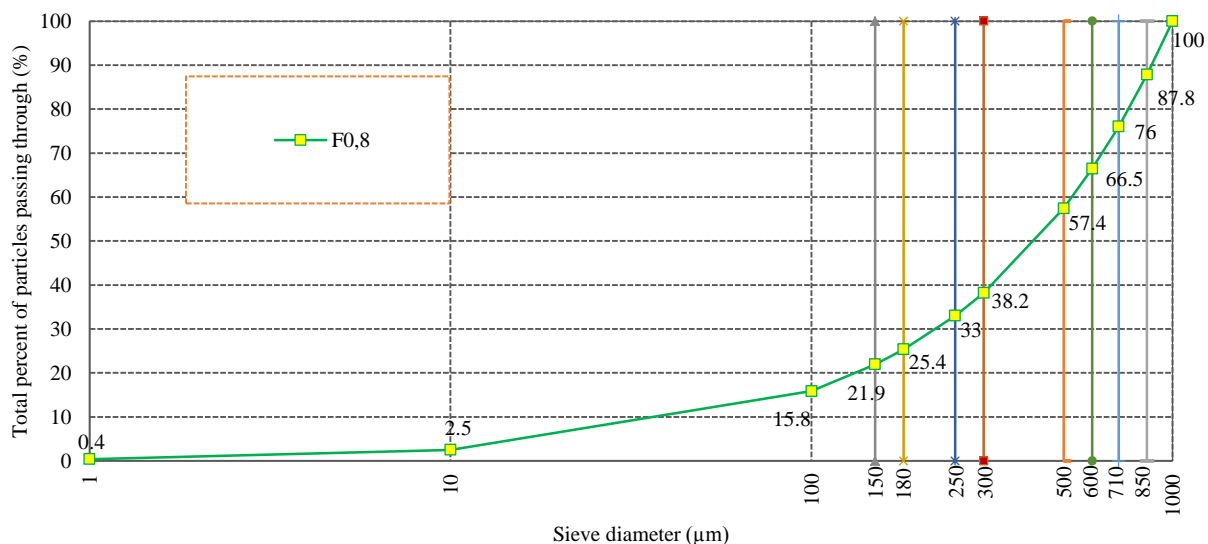


Figure 1. F 0.8 grain size distributions of the fillers

$$P\% = \left(\frac{d}{D}\right)^n \quad (2.1)$$

P%: total percent of particles passing through.
d: diameter of the current sieve (µm)
D: maximum size of aggregate (1000µm)
n: exponent of the equation (n=0.8)

Together with grain-size distribution, chemical and physical properties of the fillers are other parameters that affect the chemical, thermal and mechanical properties of the thermosetting composites. Chemical and physical parameters of the fillers are given in Table 1, and Table 2.

Table 1. Chemical compositions of filling materials.

Chemical Composition	Fillers (%)		
	Quartz	Silica	Basalt
Silicon Dioxide (SiO ₂)	99.18	98.94	61.21
Aluminium Oxide (Al ₂ O ₃)	LOD*	0.08	13.61
Iron Oxide (Fe ₂ O ₃)	0.02	0.1	5.72
Magnesium Oxide (MgO)	LOD*	LOD*	3.9
Calcium Oxide (CaO)	0.16	LOD*	6.2
Sodium Oxide (Na ₂ O)	LOD*	LOD*	2.63
Potassium Oxide (K ₂ O)	0.03	0.05	2.83
Titanium Oxide (TiO ₂)	0.04	0.12	0.76
Manganes (II) Oxide (MnO)	LOD*	LOD*	0.13
Sulphur Dioxide (SO ₂)	0.02	0.3	LOD*
Diphosphor pentaoxide (P ₂ O ₅)	0.01	0.01	LOD*
Chrome (II) Oxide (Cr ₂ O ₃)	0.004	0.053	LOD*
Manganes (III) Oxide Mn ₂ O ₃	0.0017	0.004	LOD*

*LOD: Limit of Detection

Table 2. Physical test results of filling materials.

Physical parameters	Silica	Basalt	Quartz
Moisture content (%)	0.002	0.6	0.5
Burning loss (%)	1.3	2.6	1.2
Specific gravity (gr/cm ³)	2.55	2.74	2.57
Compact unit weight (gr/cm ³)	1.79	1.72	1.76
Loose unit weight (gr/cm ³)	1.62	1.53	1.54
Water absorption ratio (%)	2.03	2.73	2.29
Specific surface area (µ)	12.07	11.31	10.42

2.3. Composite Fabrication

The orthophthalic resin, methyl ethyl ketone peroxide, and cobalt octoate were added to the beaker with a

volume ratio of 100:1:1, respectively. Afterward, the former mixture stirred 2 min at 300 rpm in the magnetic stirrer (Figure 2) and numbered experimental protocol in the manuscript.



Figure 2. Experimental demonstration

- 1-2: Preparing resin and pouring the initiator on the orthophthalic resin
 - 3: Mixing of the resin and additives in the sonicator
 - 4: Adding of the filler
 - 5: Mixing in the disperser
 - 6-7: Pouring the mixture into the steel mold, and molding
 - 8: Curing process
- Before the curing, the former prepared solution was transferred to ultrasonic homogenizer (Bandelin, RK 100 H, Germany) and sonicated for 1 min at 35 kHz to improve the homogeneity. Then the obtained mixture was transferred and the fillers that prepared according to

Fuller equation were added and mixed at 1000 rpm for 1 min in the ultraturrex disperser (Heidolph, Hei TORQUE 100, Germany) before the resin reached the gelling time. Finally, the obtained suspension poured for molding to a steel cylinder (3cm x 6 cm) with controlled leveling and kept at room temperature for 1h and afterward was transferred to an oven (Utest. UTD 1035, Turkey) to kept at 80 °C for 24h. Release agent (Poliya, Polivaks SV-6, Turkey) were applied to the molds to remove easily after curing. The production of silica (PE-S), quartz (PE-Q), and basalt (PE-B) filled polyester composites are given in Figure 3.

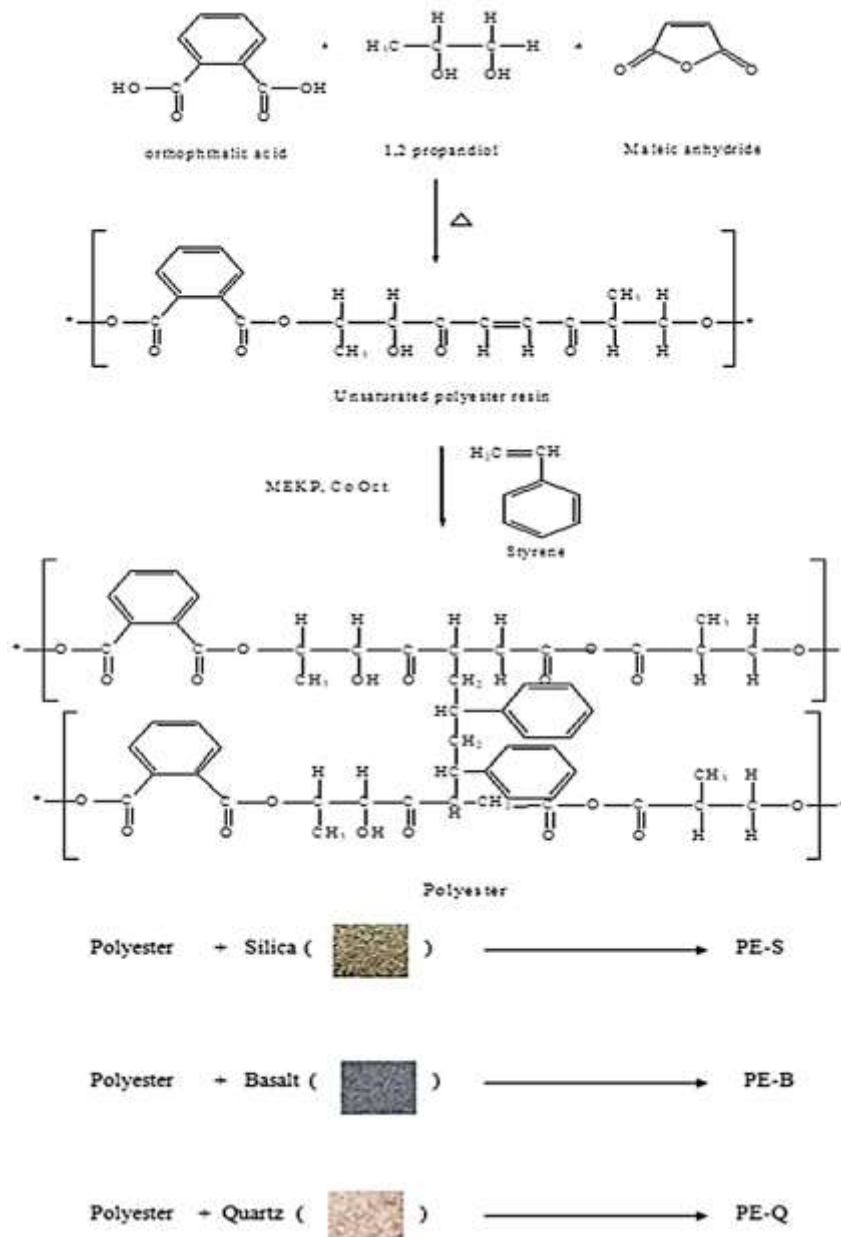


Figure 3. Production of silica (PE-S), quartz (PE-Q), and basalt (PE-B) filled polyester composites.

2.4. Polymerization Analysis (Chemical Analysis)

The IR spectra were taken via an attenuated total reflectance (ATR)-FTIR device (Shimadzu IR Prestige-21, Shimadzu Corp.). The samples were gently put in an attachment containing a diamond to evaluate molecular vibration signals in the range of 4000-600 cm^{-1} , and 20 scans with a resolution of 4 cm^{-1} were carried out.

2.5. Thermogravimetric Analysis

Thermogravimetric analysis was performed on a DTG 60 (Shimadzu) analyzer equipped with a thermal analysis data station at a heating rate of 10 $^{\circ}\text{C}/\text{min}$ under a 75 mL/min nitrogen atmosphere. The materials were first dried at room temperature overnight. 5-10 mg of the material was placed in a platinum pan and heated from room temperature to 1200 $^{\circ}\text{C}$. For SEM analysis, cross-section images were taken of the samples at 20 kV acceleration voltage (FEI, Quanta 250, Netherland). The specimens were mounted with tweezers onto a substrate with carbon tape and coated with a thin layer of gold/palladium mixture.

2.6. Thermal Conductivity Analysis

The thermal conductivity analysis, a sample having a smooth surface was prepared and put the specimen sensor, then 500 g weightiness was put over the sensor then applied current thoroughly 3 seconds and measurements are saved.

2.7. Compressive Test

After the samples were removed from the cylinder molds, they were subjected to a cutting process for pressure tests. After 7 days of waiting time, pressure tests were performed on the cut samples. The pressure test was performed according to ASTM C 579-01 [17]. Samples were produced in a cylindrical shape with a diameter to length ratio of $\frac{1}{2}$ (35mm / 70mm). Loading speed, 41 MPa / min. is set to. In order to perform the pressure test, 3 samples were produced from each mixture.

3. Results and Discussion

3.1. Chemical Characterization

The FTIR spectra were investigated to determine molecular vibrations for all composites. The obtained spectra are given in Figure 4.

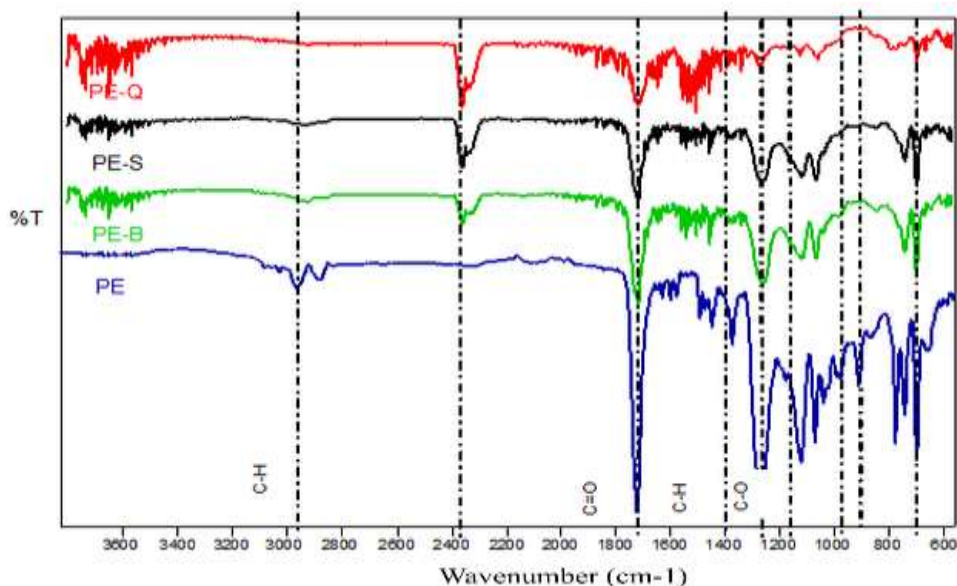


Figure 4. FTIR spectra of the PE, PE-S, PE-B, and PE-Q composites.

C-H asymmetric and symmetric stretching vibration of the methylene group found in the composites was observed at 2967 cm^{-1} [18]. However, this interaction was seen only in the PE composite. C=O stretching vibrations of the neat PE composite were observed at 1721 cm^{-1} . After the interaction of the PE and fillers, all of C=O vibration were approximately seen at 1716 cm^{-1} . C=C vibration that is related to C=C in the aromatic

ring was observed at 1599 cm^{-1} for all composites. It was encountered C-H bending vibrations at 1494 cm^{-1} for the PE whereas this vibration saw at 1491 cm^{-1} for filled composites. Another, C-H bending vibrations were seen at 1259 cm^{-1} , 1261 cm^{-1} , 1269 cm^{-1} for the PE-B, PE-S, and PE-Q, respectively. The other vibration which is for the PE at 1121 cm^{-1} was seen at

1117 cm^{-1} for PE-S and 1118 cm^{-1} for PE-B. However, it was not observed in the PE-Q.

It seems that vibration is not related to Si-C or Si-O interaction as quartz and silica are comprised of mostly from SiO_2 molecules. Besides, as well as chemical shifts, alterations in the intensity were determined between PE and fillers. The intensity of PE vibrations was significantly decreased due to decreasing resin concentration in the composites. With a similar trend, the intensity of carboxyl groups ($-\text{C}=\text{O}$) found at 1721 cm^{-1} was decreased in the composites as well as C-O vibrations. After the interaction, PE and fillers, vibration which reveals unsaturated $\text{C}=\text{C}$ bond founding in styrene and mostly seen at 910 cm^{-1} for PE, disappeared in the PE-S, PE-B, and PE-Q composites that this phenomenon revealed that polymerization and curing were carried out [20, 28]. Besides, neither asymmetric nor symmetric Si-O vibrations were

specifically seen in the spectra for the PE-B, PE-Q, and PE-S composites. Those vibrations probably overlapped with the C-O vibrations between 1150 cm^{-1} -850 cm^{-1} [19].

3.2. Thermal Characterization

3.2.1. Thermogravimetric Analysis Thermal Conductivity

The thermogravimetric analysis (TGA) and its derivative (DTG) indicate the starting and end temperatures of thermal degradation, as well as the number and content of the steps involved in the thermal degradation temperature related to the composites, are given in Figure 5. Also, the 10%, 50% weight loss, the decomposition temperature, and residue (%) are summarized in Table 3.

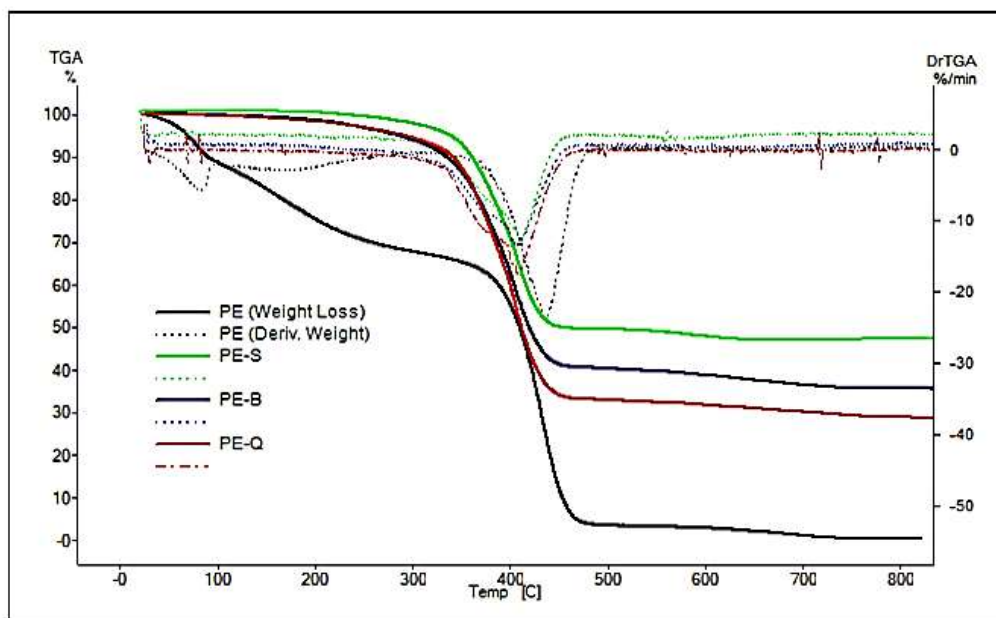


Figure 5. Thermogravimetric analysis results of the PE, PE-S, PE-B, and PE-Q composites.

Table 3. Thermal degradation temperature values of the composites.

Samples	$T_{10\%}$ (°C)	$T_{50\%}$ (°C)	T_d (°C)	Residue (%)
PE	92.1	404.1	388.5	0.2
PE-S	361.2	448.2	351.1	46.01
PE-B	336.6	421.4	343.9	35.8
PE-Q	343.4	407.9	348.3	28.9

In Figure 5, the PE-S, PE-B, and PE-Q composites revealed mostly similar thermal degradation temperature trend except for the PE. When investigated the $T_{10\%}$ values, the thermal stability of the composites increased with the fillers that the PE-S, PE-B, and PE-Q composites exhibited higher thermal stability compared

to the neat PE with an enhanced decomposition temperature about 361.2, 336.6, and 343.4 °C, respectively. Also, a similar trend continued with a $T_{50\%}$ degradation temperature that degradation was carried out in the 448.2, 421.4, and 407.9 °C for PE-S, PE-B, and PE-Q, respectively. However, PE-B degraded at a lower temperature compared to PE-S and PE-Q. It means that basalt caused lower heat transfer, thus diminishing the thermostability and leading to earlier degradation.

In contrary to Shimazaki et al, organic fillers used in that study caused higher thermostability [21]. It means that filler's structure influenced thermal stability that as organic-based fibrils decreased the thermal stability whereas minerals having inorganic chemical structure enabled higher thermostability [22-25]. This

circumstance can be explained with the organic cellulose fillers enabled chain mobility of the polymer within the composite whereas inorganic fillers restricted chain mobility in the matrix on the long-range [26]. When investigated the derivative curves, two thermal degradations were seen for PE. It was seen only PE in the first thermal degradation. Then, in the second degradation, PE-B was degraded firstly. However, the highest thermal degradation temperature was seen in PE.

Besides, solid residue is higher in the PE up to 800 °C. This is ascribed in inorganic particles. Inorganic particles comprised of a variety of metals and oxides. These metals and oxides have a higher melting point compared to organic structures. Thus, when exposed to the temperature, organic-based structures removed faster from the structure whereas inorganic based

structures remained in the structure. Therefore, PE-Q, PE-S, PE-B composites having inorganic particles remained in higher value when the solid residue of PE is lowest. Because, the melting point of the basalt mineral is at around 1200 °C whereas the melting point of the quartz and silica is at around 1650 °C and 1400 °C, respectively [29].

3.3. Thermal Conductivity

The results of the thermal conductivity of the produced composites are given in Figure 6 and the statistical analysis related to the thermal conductivity are given in Table 4. The data obtained were analyzed statistically by the variance analysis (ANOVA) and the Duncan test is given in Table 5, and Table 6.

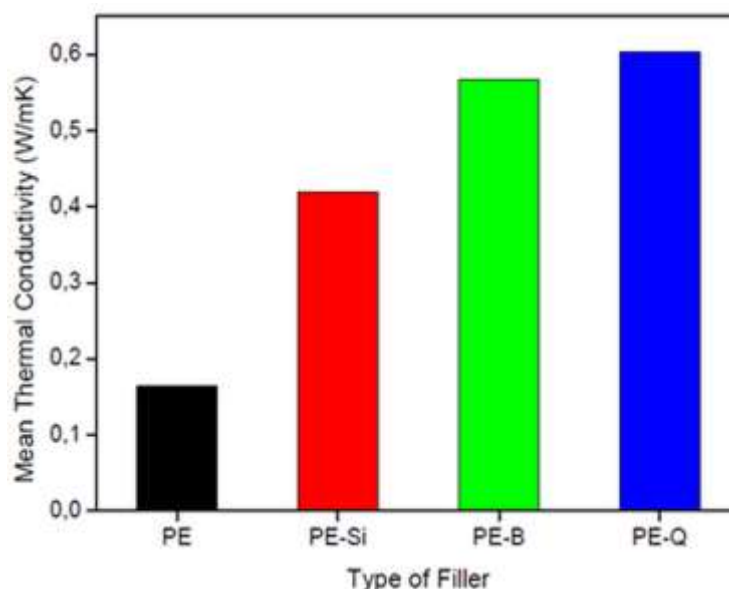


Figure 6. Thermal analysis results of the PE, PE-S, PE-B, and PE-Q composites.

Table 4. Descriptive values of thermal conductivity test results.

Composite type	N	Mean of Thermal Conductivity (W/mK)	Std. Deviation	Std. Error	95% Confidence Interval for Mean		Minimum	Maximum
					Lower Bound	Upper Bound		
PE	4	0.16	0.01291	0.00645	0.1445	0.1855	0.15	0.18
PE-S	4	0.42	0.00816	0.00408	0.4070	0.4330	0.41	0.43
PE-B	4	0.56	0.01500	0.00750	0.5436	0.5914	0.55	0.58
PE-Q	4	0.60	0.02217	0.01109	0.5672	0.6378	0.58	0.63

Table 5. Variance analysis results of thermal conductivity values.

Source of variance	Sum of Squares	Degree of freedom (df)	Mean Square	F	Significance (p≤0.05)
Between GroPEs	0.475	3	0.158	666.281	0.00001
Within GroPEs	0.003	12	0.000		
Total	0.478	15			

Table 6. Duncan test results of thermal conductivity values.

Type of Filler	N	Different GroPEs (Subset for alpha = 0.05)			
		1	2	3	4
PE	4	0.1650			
PE-S	4		0.4200		
PE-B	4			0.5675	
PE-Q	4				0.6025

Means for groPEs in homogeneous subsets are displayed. a. Uses Harmonic Mean Sample Size = 4.000.

According to the statistical analysis and evaluations of the test results, it was observed that there has been a significant change in the thermal conductivity depends on filler types. The thermal conductivity of the PE composite ascended from $0.16 \text{ Wm}^{-1}\text{K}^{-1}$ to $0.42 \text{ Wm}^{-1}\text{K}^{-1}$, which was 2.7 times higher than that of the PE-B composite. However, the highest increment was seen in the PE-Q composite with $0.60 \text{ Wm}^{-1}\text{K}^{-1}$ that nearly 4 times higher compared to composites obtained from the PE. Also, the thermal conductivity results are agreement with the TGA results that filler-based composites revealed higher thermal conductivity. However, compared to thermal conductivity levels of the PE-Q,

PE-S, and PE-B composites, the highest thermal conductivity was seen in the PE-Q composites. It is also known that quartz mineral is higher thermal conductivity property over basalt [26]. It can be concluded that inorganic fillers enabled the higher thermal conductivity results in the thermosetting composites.

3.4. Morphological Characterization

The morphology of the composites was investigated with SEM (Figure 7).

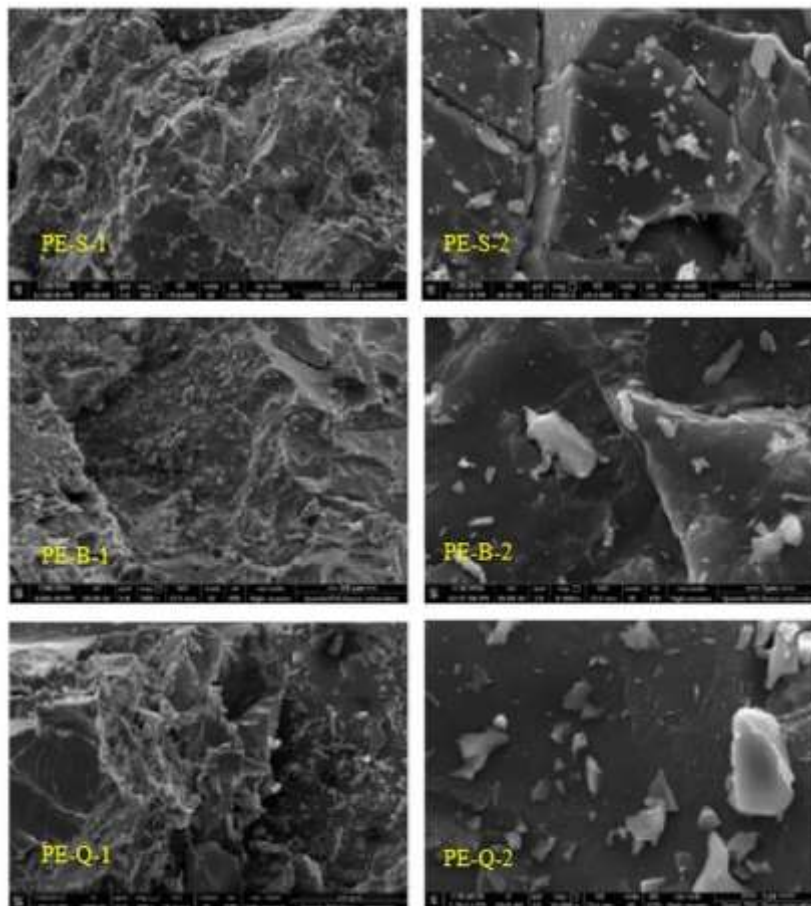


Figure 7. SEM pictures of the PE, PE-S, PE-B, and PE-Q composites.

When investigated SEM images of the composites, all of the fillers mostly dispersed homogeneously in the resin matrix and no agglomeration was observed between resin and fillers since there has been a good adherence between fillers and polyester. Also, there is not considerable cracking and void between surfaces of the fillers and matrix. This probably stems from the lower the dimension of fillers. However, although mostly fillers dispersed in the matrix, silica filler dispersed more homogeneous in the PE matrix than those of fillers and also interacted more effectively with the PE.

It has been also thought that load and energy applied to the composites caused lower fragmentation or cracking. The energy that should be applied to form cracks in the composites was higher since the filler used is low. It

was shown that fillers having high hardness carried mostly load that applied. Thanks to this, it protected to matrix against cutting. However, with increasing load, cracking began between interfacial surface and fillers, then fillers eluded from the surface of the matrix towards to sliding side.

3.5. Mechanical Characterization

The results of the compressive strength of the produced composites are given in Figure 8 and the statistical analysis related to the compressive strength are given in Table 7. The data obtained were analyzed statistically by the variance analysis (ANOVA) and the Duncan test is given in Table 8 and Table 9.

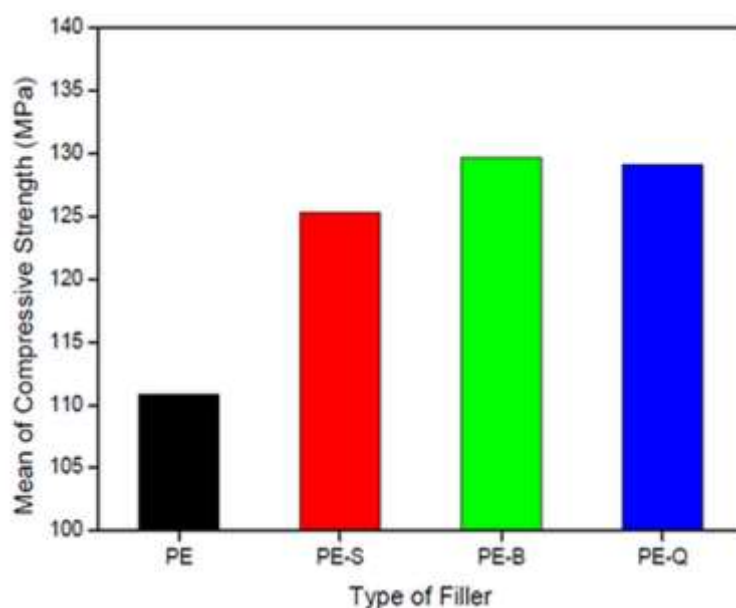


Figure 8. Compressive strength values of the PE, PE-S, PE-B, and PE-Q composites.

Table 7. Descriptive values of compressive strength test results.

Composite type	N	Mean of Compressive Strength (MPa)	Std. Deviation	Std. Error	95% Confidence Interval for Mean		Minimum	Maximum
					Lower Bound	Upper Bound		
PE	4	110.77	1.91551	0.95775	107.72	113.82	108.90	113.40
PE-S	4	125.25	1.06301	0.53151	123.55	126.94	124.40	126.80
PE-B	4	129.72	1.40801	0.70401	127.48	131.96	128.10	131.00
PE-Q	4	129.12	1.60702	0.80351	126.56	131.68	126.90	130.40

I

Table 8. Variance analysis results of compressive strength values.

Source of Variance	Sum of Squares	Degree of freedom (df)	Mean Square	F	Significance (p<0.05)
Between GroPEs	940.752	3	313.584	133.951	0.00001
Within GroPEs	28.093	12	2.341		
Total	968.844	15			

Table 9. Duncan test results of compressive strength values.

Type of Filler	N	Different Groups (Subset for alpha = 0.05)		
		1	2	3
PE	4	110.77		
PE-S	4		125.25	
PE-B	4			129.12
PE-Q	4			129.72

Means for groPEs in homogeneous subsets are displayed. a. Uses Harmonic Mean Sample Size = 4.000.

According to the statistical analysis and evaluations of the test results, filler types influenced the mechanical results that mechanical properties of the thermosetting composites may vary in comparison to inorganic materials in it.

Compressive strength is of great importance for any structural element. The difference strength values between the groups can be explained by the dependence of the strength of thermosetting composites on various factors such as resin and filling material rates, grain-size distributions, and its heterogeneous structure. It also seemed that composites are prone to fail in bending and the improvement of new composites with improved flexural characteristics is essential.

Fillers improved the compressive strength value of the composites compared to the neat polyester composite. And, the highest compressive strength result was obtained in PE-B composite whereas PE-S revealed lower compressive strength value. This is ascribed in iron oxide and titanium oxide found in the basalt. It is thought that these minerals make this structure strength. However, PE-Q composite value was so close with basalt filled composite.

4. Conclusion

This study reports the effects of silica (S), quartz (Q), and basalt (B) fillers on the chemical, thermal and mechanical properties of PE composites.

Conclusions from this study are as follows:

1. The neat PE and its composites with silica (PE-S), basalt (PE-B), and quartz (PE-Q) were successfully produced with free-radical polymerization and mechanical treatment.
2. After the interaction of filler and PE, minor chemical shifts were observed in obtained composites. The intensity of the basic vibrations of the PE was decreased due to the decrease in the concentration of the resin.
3. Filler based PE composites revealed higher thermostability compared to the neat PE composite due to the inorganic based fillers restricted chain mobility in the matrix on the long-range.
4. All of the fillers were mostly dispersed as homogeneous and no agglomeration was observed that there has also been good adherence between PE and fillers.

5. Filler based PE composites revealed higher thermal conductivity. This phenomenon was an agreement with the TGA results. However, among the filler-based composites, the highest thermal conductivity was seen in the PE-Q composite whereas PE-B revealed close value to it.

6. Filler enabled higher compressive strength over the neat PE. Also, the PE-B composite revealed the highest compressive strength value while the lowest value was observed in the PE-S composite.

This study reveals that the applicability of various filler as a reinforcing agent in polymer composites may alter depending on filler types.

Acknowledgement

The authors gratefully acknowledge the financial support of the Scientific and Technological Research Council of Turkey (TUBITAK). Project Number: 5140058.

Author's Contributions

The authors contributed to the study as follows.

Bayram Poyraz: Investigation, Writing- Original draft preparation, Methodology, Formal analysis

Şevki Eren: Investigation, Writing- Original draft preparation, Methodology, Formal analysis.

Serkan Subaşı: Methodology, Supervision, Project administration.

Ethics

There are no ethical issues after the publication of this manuscript.

References

1. Kalkan, E, Karakışla, MM, Saçak, M. 2018. Polypyrrole and silver particles coated poly (ethylene terephthalate) nonwoven composite for electromagnetic interference shielding. *Journal of Composite Materials*; 52(10): 1353-1362.
2. Kumar, V, Dev, A, Gupta, A. 2014. Studies of poly (lactic acid) based calcium carbonate nanocomposites. *Composites Part B: Engineering*; 56: 184-188.



3. Çopuroğlu, M, Şen, M, Keyf, F. 2017. A polymeric nanocomposite system for potential adhesive applications in restorative dentistry. *Journal of Adhesion Science and Technology*; 31(6): 602-612.
4. Kim, HG. 2002. Dielectric cure monitoring for glass/polyester prepreg composites. *Composite Structures*; 57(1-4): 91-99.
5. Novak, BM. 1993. Hybrid nanocomposite materials—between inorganic glasses and organic polymers. *Advanced Materials*; 5(6): 422-433.
6. Ogoshi, T, Itoh, H, Kim, KM, Chujo, Y. 2002. Synthesis of organic– inorganic polymer hybrids having interpenetrating polymer network structure by formation of ruthenium– bipyridyl complex. *Macromolecules*; 35(2): 334-338.
7. Chen, Y, Iroh, JO. 1999. Synthesis and characterization of polyimide/silica hybrid composites. *Chemistry of Materials*; 11(5): 1218-1222.
8. Demir, MM, Altın, B, Özçelik, S. 2010. Composites of reactive silica nanoparticles and poly (glycidyl methacrylate) with linear and crosslinked chains by in situ bulk polymerization. *Composite Interfaces*; 17(9): 831-844.
9. Horath, L. *Fundamentals of Materials Science for Technologists: Properties, Testing. and Laboratory Exercises*; Waveland Press: 2019.
10. Rothon, R. *Particulate-Filled Polymer Composites*; iSmithers Rapra Publishing: 2003.
11. Saba, N, Jawaid, M, Asim, M. Recent Advances in Nanoclay/Natural Fibers Hybrid Composites. In: *Nanoclay Reinforced Polymer Composites*; Springer, 2016; pp 1-28.
12. Mahdi, F, Abbas, H, Khan, A. 2010. Strength characteristics of polymer mortar and concrete using different compositions of resins derived from post-consumer PET bottles. *Construction and Building Materials*; 24(1): 25-36.
13. Ateş, E, Barnes, S. 2012. The effect of elevated temperature curing treatment on the compression strength of composites with polyester resin matrix and quartz filler. *Materials & Design*; 34: 435-443.
14. Ateş, E. 2009. Optimization of compression strength by granulometry and change of binder rates in epoxy and polyester resin concrete. *Journal of Reinforced Plastics and Composites*; 28(2): 235-246.
15. Singh, P, Kaushik, A, Kirandeep. 2006. Mechanical and transport properties of colloidal silica-unsaturated polyester composites. *Journal of Reinforced Plastics and Composites*; 25(2): 119-140.
16. Fuller WB, Thompson SE. 1907. The laws of proportioning concrete. *Journal of Transportation Engineering*; 59.
17. ASTM (2012) C579-18. Standard test methods for compressive strength of chemical-resistant mortars, grouts, monolithic surfacings and polymer concretes. ASTM International, USA.
18. Carrillo, F, Colom, X, Sunol, J, Saurina, J. 2004. Structural FTIR analysis and thermal characterisation of lyocell and viscose-type fibres. *European Polymer Journal*; 40(9): 2229-2234.
19. Heidari, A, Younesi, H, Mehraban, Z. 2009. Removal of Ni (II), Cd (II), and Pb (II) from a ternary aqueous solution by amino functionalized mesoporous and nano mesoporous silica. *Chemical Engineering Journal*; 153(1-3): 70-79.
20. Chung, CM, Cho, SY, Kim, JG, Oh, SY. 2007. Preparation of unsaturated polyester–silica nanocomposites. *Journal of Applied Polymer Science*; 106(4): 2442-2447.
21. Shimazaki, Y, et al. 2007. Excellent thermal conductivity of transparent cellulose nanofiber/epoxy resin nanocomposites. *Biomacromolecules*; 8(9): 2976-2978.
22. Khankrua, R, et al. 2013. Thermal and Mechanical Properties of Biodegradable polyester/silica Nanocomposites. *Energy Procedia*; 34: 705 – 713.
23. Farhan, AJ. 2020. Characterization the thermal degradation E kinetic of unsaturated polyester and polyester/silica nanoparticles composites by TGA and DSC Analysis. *Journal of Advanced Research in Fluid Mechanics and Thermal Sciences*; 71(1): 10-20.
24. Carrasco, F, Pages, P. 2008. Thermal degradation and stability of epoxy nanocomposites: influence of montmorillonite content and cure temperature. *Polymer Degradation and Stability*; 93: 1000-1007.
25. Chrissafis, K, Bikiaris, D. 2011. Can nanoparticles really enhance thermal stability of polymers? Part I: An overview on thermal decomposition of addition polymers. *Thermochimica Acta*; 523: 1-24.
26. Zhua, J, et al. 2011. Ionic liquid assisted electrospinning of quantum dots/elastomer composite nanofibers. *Polymer*; 52: 1954-1962.
27. Barry-Macaulay, D, et al. 2013. Thermal conductivity of soils and rocks from the Melbourne (Australia) region. *Engineering Geology*; 164: 131-138.
28. Cao, X, Lee, LJ. 2003. Control of shrinkage and residual styrene of unsaturated polyester resins cured at low temperatures: I. Effect of curing agents. *Polymer*; 44: 1893-1902.
29. Baskaran, R, Sarojadevi, M, Vijayakumar, CT. 2010. Mechanical and thermal properties of unsaturated polyester-silica nanocomposites. *Nano Science and Nano Technology An Indian journal*; 4(1): 1-5.

Metakaolin and Red-Mud Based Geopolymer: Resistance to Sodium and Magnesium Sulfate Attack

Ouiame Chakkor^{1*} , Mehmet Fatih Altan¹ , Orhan Canpolat² 

¹Civil Engineering Department, Faculty of Engineering, İstanbul Aydın University, İstanbul, Turkey

²Civil Engineering Department, Faculty of Engineering, Yıldız Technical University, İstanbul, Turkey

*ouiamechakkor@stu.aydin.edu.tr

*Orcid No: 0000-0002-9293-7284

Received: 5 September 2020

Accepted: 1 March 2021

DOI: 10.18466/cbayarfb.790946

Abstract

This paper aims to study strength properties, UPV, and weight changes exposed to sulfate attack, and microstructural properties of geopolymer mortar prepared using metakaolin and red-mud as binder materials by mixing with river sand replaced partially by limestone, marble and basalt powder with different ratios (25%, 50%, and 75%) as filler materials, the mix proposed were activated by sodium silicate and sodium hydroxide solutions (12mol). The proposed samples were exposed to 10% of magnesium and sodium sulfate solutions for various periods of 60, 120, and 180 days to investigate the durability properties of the manufactured geopolymer mortar. The experimentally obtained results uncover that the prepared geopolymer mortar's strength properties increase at 60 days for all the proposed mixes, while at 180 days; the geopolymer mortar suffers a significant loss. Change in weight increase obviously between 10.83% and 13.65% for 60 days and decrease gradually for 120 days between 9.22% and 10.19% to reach a stable value between 120 and 180 days. Furthermore, to evaluate this work, the Scanning Electron Microscopy and X-ray Diffraction methods were investigated.

Keywords: Geopolymer, binder, metakaolin, red-mud, SEM, XRD.

1. Introduction

Regarding the durability of concrete structures, the sulfate attack is one of the factors causing deterioration cement paste due to the expansion, spalling, and softening. According to some previous research, the OPC (ordinary portland cement) showed severe damage when exposed to the sulfate attack [1]. Under the effect of sulfate attack on OPC concrete the chemical reaction between the aluminate component of cement paste and C-S-H[2], help out the formation of ettringite and gypsum which is the leading cause of the concrete's expansion and cracking, furthermore the destruction of C-S-H cause the disintegration and softening for the concrete's sample[3, 4]. The geopolymer mortars, known as known, have very low emission of CO₂[5, 6]. Moreover, the geopolymer mortars using waste materials, MK (metakaolin), Fly-ash, and ferrochrome slag supply sustainable development under the effects of sulfate attack. Recently, the geopolymers' term has been viewed as the future cement, and their evolution emerged and fostered by way of Davidovits [7], due to its good mechanical properties, low permeability, and

excellent durability properties [8]. The geopolymers must be considered a new material, a new binder, and a new cement of concrete, which has no dangerous alkali-aggregate reaction reported by Davidovits. Previous researches indicated the development of strength properties and hydration products throw the effects of curing, the composition of the alkaline solution, and the ratio of water and binder, the alkaline solution generally comprise sodium silicate, sodium hydroxide. The geopolymer binder materials have lower costs and a higher reduction in CO₂ emissions than Portland cement (PC).

Moreover, the compressive strength of geopolymer samples Range is 40-70MPa [9], due to the curing Hydrothermal, which accelerates the chemical reaction between binder and alkali solution. In the case of an acid attack, some previous researches study the durability of geopolymer materials to present its processing and characterization [10], and due to the absence of high-calcium phases, the geopolymer materials have excellent resistance under the sulfate solutions effects. Nowadays, the durability and

maintenance of concrete structures become a critical issue [11] because they start to deteriorate after 20–30 years while their design life was at least 50 years [12]. The constructions in contact with seawater, sewages, tunnels, and deep foundations are exposed to external chemical attacks [13]. When subjected to sulfate attack in the environment, the ordinary Portland cement showed cases of concrete deterioration due to the involved reactions of C–H, C–S–H and the aluminate component of cement [14]; thus for the geopolymer waste materials, the sulfate attack is a vital durability concern. Several additives are used to increase the strength properties of the manufactured geopolymer concrete, such as slag. When exposed to sulfate solutions effects, the geopolymer samples with low calcium base have shown excellent durability and strength properties [15]. Besides the OPC' durability problems are associated with its main phases; calcium content, when C_3a exposed to the sulfate ions ettringite and gypsum will be formed in the presence of $Ca(OH)_2$; thus the concrete's disruptive expansion and degradation occur due to the non-cohesive particles mass [16].

The geopolymers present a high durability and strength properties resistance under the effects of sulfate attack due to its strength, low creep, and low shrinkage [17], and low phase of calcium. Furthermore, the geopolymer activating solution, especially NaOH, accelerates chemical dissolution, which inhibits the formation of ettringite and carbon-hydrogen during binder formation and promotes higher strengths at early ages of reaction, which improved excellent stability in aggressive environments due to the development of higher crystallinity [18]. However, high concentrations of NaOH caused undesirable morphology and non-uniformity of the manufactured geopolymer samples due to the excessively OH⁻ in solution.

This work presents a geopolymer mortar manufactured by MK and RM (red-mud) as binder materials activated with (NaOH and Na_2SiO_3) chemical materials, and as filler materials limestone, marble and basalt powder were used replaced river sand with different ratio (25%, 50%, and 75%). The performance of the manufactured geopolymer samples was conducted under the effect of 10% magnesium sulfate and 10% sodium sulfate solutions. Visual appearance, the strength properties, weight changes, XRD, and SEM of these samples were obtained experimentally.

2. Materials and Methods

In this purpose, metakaolin and red mud were used as a binder material while limestone, marble, and basalt powder were used as filler materials. Red mud was collected from Seydişehir Aluminum Plant (Konya/Turkey). The ground granulated blast furnace slag is manufactured by Bolu Cement Industry (Bolu/Turkey). The slag's specific weight is

$2.91g/cm^3$ and the amount remaining on the 45-micron sieve is 1.4%, and it was used in 13% of the mixture. Kaolin was extracted from Industrial Minerals San.ve Tic. Inc. (Istanbul/Turkey), the specific gravity is $2.52 g/cm^3$, The powder of this kaolin was once calcined at $700^\circ C$ for four hours at a heating rate of $1^\circ C/min$ to get a surprisingly reactive metakaolin. Silica + alumina + iron oxide ratio = $97.18\% > 70\%$, Moreover metakaolin has fine grain which increase the reaction. Slag, metakaolin, and red mud were stated in S, MK, and RM abbreviations, respectively. Liquid sodium silicate ($SiO_2/Na_2O = 3.29 M$) ratio and analytical grade sodium hydroxide (12mol) were once used for alkaline activation taken from AS Kimya (Istanbul/Turkey). Sodium hydroxide and sodium silicate were expressed in SH and SS abbreviations, respectively. The sodium hydroxide was prepared by adding 1liter of distilled water to 480g of sodium hydroxide pellets to obtain 12mol. The obtained water glass has been stored at room temperature for 24 hours before being used with sodium silicate/sodium hydroxide in a 2:1 ratio. The mix was prepared using the mixer drill using the chemicals (SS and SH) with MK and mixed for 5mins. The RM was added to the bellow mix and also mixed for 5 mins to homogenate the mortar prepared, to enhance the tenacity of mix blast furnace slag was used and mixed for just 2 mins then immediately one the filler materials (limestone, basalt powder, and marble powder) with river sand using one of the different ratio approved for this work (25%, 50%, and 75%) were added. Filler materials used in this work has a very fine grain and convert large voids to small ones. Limestone, marble, and basalt powder used in this work as filler materials. Limestone powder was provided from Gebze Rock Quarry (Gebze/Turkey), basalt samples were homogenized, dried at $105^\circ C$ for 24 hours. From INCI Group Company (Sakarya/Turkey) the basalt powder stone was extracted. Marble powder was dried the same as basalt powder, obtained from Turkan Company (Alibeykoy/Istanbul). All the filler materials used were less than $0,0063mm$ particle diameter. In this work as aggregate, the river sand with less than $0,25 mm$ particle diameter was used correspondent to TS 706 EN 12620 [19]. Limestone, marble, and basalt powder were expressed in LS, MR, and BS abbreviations, respectively. While the mixing procedure has been finished, the mortar was used to the molds $50 \times 50 \times 50 mm$ and $71 \times 71 \times 71 mm$ cubes, $40 \times 40 \times 160$ prisms, and $300 \times 150 mm$ cylinders and vibrated, and then the geopolymer samples were kept for 24h in the ambient temperature. All the specimens were held for 24 hours in the drying oven at $100^\circ C$. After the curing, the

samples were preserved in room temperature conditions. After 28 days, durability tests were performed under the effect of sulfate solutions. Moreover, the mechanical tests, compressive strength test according to ASTM C 109 was executed after 60, 120, and 180 days utilizing the 50x50x50 mm cubes, the Flexural strength test

quoted by ASTM C 348 utilizing the 40x40x160 prisms samples was carried also after 60, 120, and 180 days [20]. When the results of the exposed samples to the effect of sulfate solutions, the SEM and XRD analysis was performed.

Table 1. The MK, RM, and S chemical properties.

Chemical Analysis(%)	SiO ₂	Al ₂ O ₃	Fe ₂ O ₃	TiO ₂	CaO	MgO	K ₂ O	Na ₂ O	SO ₃
MK	56,1	40,23	0,85	0,55	0,19	0,16	0,51	0,24	-
RM	17,38	24,52	35,25	-	3,22	0,42	0,43	8,45	-
S	40,55	12,83	1,1	-	32,58	5,87	-	0,79	0,18

Table 2. SH chemical properties.

Chemical Analysis (%)	NaOH	Na ₂ CO ₃	CL	SO ₄	Al	Fe
SH	99,1	0,3	≤0,01	≤0,01	≤0,002	≤0,002

Table 3. SS chemical properties

Chemical Analysis (%)	SiO ₂	Na ₂ O	Fe (%)	Density (g/ml)	Heavymetals (%)
SS	27,0	8,2	≤0,005	1360	≤0,005

Table 4. Fine aggregate's chemical properties.

Chemical Analysis (%)	SiO ₂	Al ₂ O ₃	Fe ₂ O ₃	TiO ₂	CaO	CaO ₂	K ₂ O	Na ₂ O	SO ₃
LS	3,3	0,82	0,58	-	-	92,9	-	-	1,18
MR	1,12	0,73	0,05	-	-	83,22	-	-	0,56
BS	56,9	17,6	8,1	0,9	7	-	1,9	3,8	-

Table 5. Mix of control sample geopolymer composites (g)

Metakaolin	Red-Mud	Slag	SS (Na ₂ SiO ₃)	SH (NaOH (12 mol))	River Sand
500	500	133	667	333	2000

Table 6. The mix of the three different filler materials replacing river sand with different ratios (g)

Metakaolin	Red-Mud	Slag	Na ₂ SiO ₃	NaOH (12mol)	River Sand	Limestone or Marble or Basalt powder
500	500	133	667	333	1500 1000 500	500 1000 1500

3. Results and Discussions

Table 7. Compressive strength loss rates (%) due to magnesium and sodium sulfate effect.

Mix ID	Magnesium sulfate			Sodium sulfate		
	60 days	120 days	180 days	60 days	120 days	180 days
Control	-3,20	3,044	7,33	-3,87	2,28	3,98
25%LS	-3,08	3,215	7,59	-3,55	2,58	4,14
50%LS	-2,18	3,519	8,69	-2,50	2,98	5,43
75%LS	-1,79	4,634	9,82	-2,09	3,30	6,37
25%MR	-3,12	3,198	7,42	-3,62	2,47	4,06
50%MR	-2,31	3,407	8,42	-2,65	2,84	5,13
75%MR	-1,98	4,140	9,28	-2,16	3,20	6,21
25%BS	-3,25	2,960	7,22	-3,96	2,28	3,87
50%BS	-3,52	2,575	6,70	-4,03	2,19	3,52
75%BS	-4,19	2,176	5,67	-4,48	1,81	2,97

Geopolymer mortar specimens were exposed to 10% Sodium (Na_2SO_4) and 10% Magnesium (MgSO_4) Sulfate solutions for 60 days, 120 days, and 180 days. The results for each sample were given in (Tables 7, 8) compared with 28 days'.

3.1. The Visual Appearance

The visual appearance of the test specimens at 60 and 120 after moistening in magnesium and sodium sulfate solutions (Figs. 1 and 2). Clearly it was seen that there were no changes as surface erosion, cracking in the surface appearance of the manufactured geopolymer samples. It was mean that geopolymer mortar had a good resistance to sulfates, agreement to values limit of the expansion suggested in the ASTM C1012-13. Moreover, at 180 days after the samples were immediately removed from both magnesium and sodium sulfate solutions and kept at room temperature 25°C, a wire brush was used to clean up the



Fig.1. a) Samples after exposed to (MgSO_4), b) Samples after exposed to (Na_2SO_4) c) Samples while exposed to (MgSO_4), d) Samples while exposed to (Na_2SO_4)

accumulated salt attack scaling behind the surface of the manufactured geopolymer mortar specimens, which did not affect the integrity of specimens mechanically. Furthermore, for both magnesium and sodium sulfate solutions there were no severe damages observed similar results were reported by other there is no severe deterioration was observed. Similar observations also have been reported by other studies' [16, 21-26]. Skvara et al. [27] stated that also more than one year there was not any significant sign of surface deterioration because of their lower susceptibility to form hydration byproducts, due to the cross-linked structure of the gels in the geopolymer samples.

3.2. Strength Properties

3.2.1. Compressive strength of magnesium sulfate

According to the magnesium sulfate effect, fluctuations in the compressive strength were seen up to 120 days. The fluctuations occurred were due to the diffusion of Magnesium from the mixture of alkaline ions to the solution, resulting in diffusion to the matrix formed [16]. Furthermore, a decrease in strength was observed for up to 120 days. The microcracks presence and alkalis transition geopolymers to the solution caused the strength losses at 120 days [28]. The compressive strength increase rate of magnesium sulfate in geopolymer samples after 60 days compared to 28 days results at room temperature were between 1.79% and 4.19%. After 120 days, the compressive strength decrease was occurred between 2.17% and 4.63%, while after 180 days, the decrease was between 5.67% and 9.82%. The results are shown in table 7. The compressive strength ls and bs powder at 60 days were 58.94 MPa and 77.58 MPa respectively, while the control sample was 65.09 MPa. The results for 120 days were between 73.01 MPa and 50.25 MPa. The obtained

results for 180 days were between 69.92MPa and 42.51 for bs and mr powder specimens, respectively. According to the results, it was seen that the geopolymer samples have better behavior under the magnesium sulfate attack effects. Microstructural changes occurring in the control, bs and ls samples at 6 months after the magnesium sulfate attack. The microstructure of the samples was preserved after exposure to magnesium sulfate. The excellent resistance of geopolymeric materials to sulfates was attributed to the source material having a lower Ca content and a more stable cross-linked aluminosilicate polymer structure while for the material having a higher Ca

content as limestone and marble powder exhibited a new phase of gypsum (Y: gypsum), through the chemical reaction happened between Ca and ($MgSO_4$) occurring the decomposition of the C-A-S-H, the notion proposed was identified by XRD and SEM. Besides, the geopolymer materials are less susceptible to attack's sulfate than standard cement hydration products. Low Ca content was found to be a significant feature in the durability of metakaolin. In this case, the reaction manufacture is an alkali gel (aluminosilicate) with a three-dimensional structure, which was significantly different from the hydrated calcium silicate gel formed in GPC hydration [29].

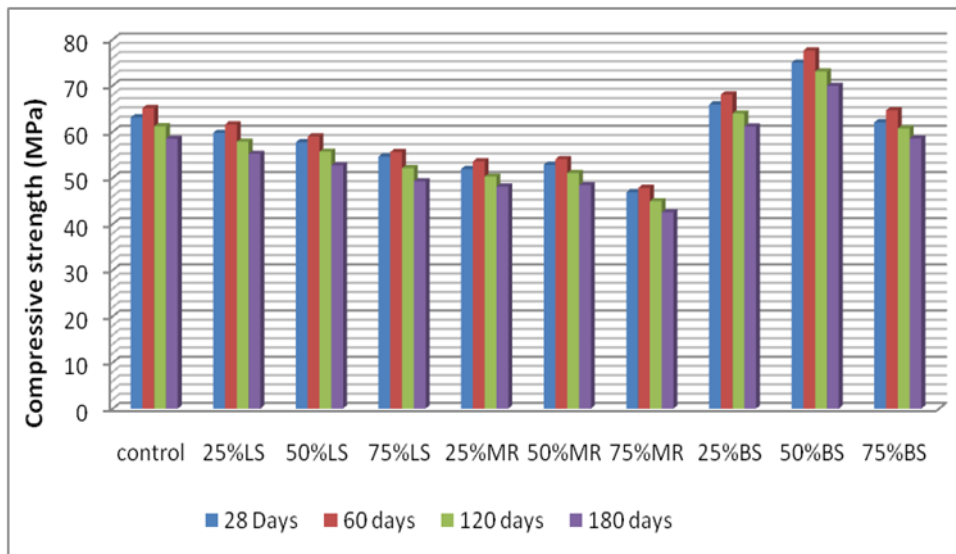


Fig. 2. Compressive strength results of geopolymers samples exposed to magnesium sulfate

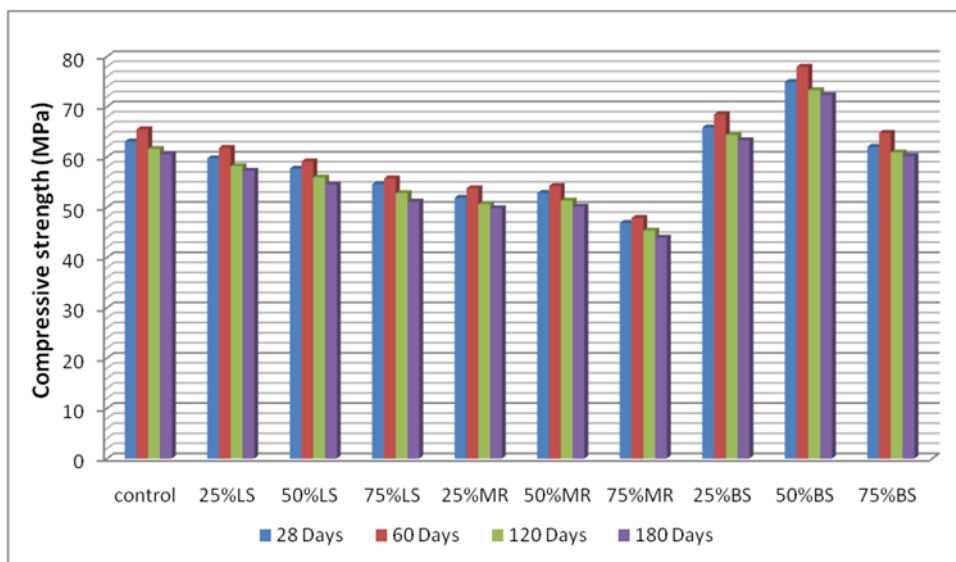


Fig. 3. Compressive strength results of geopolymers samples exposed to sodium sulfate.

3.2.2. Compressive strength of sodium sulfate

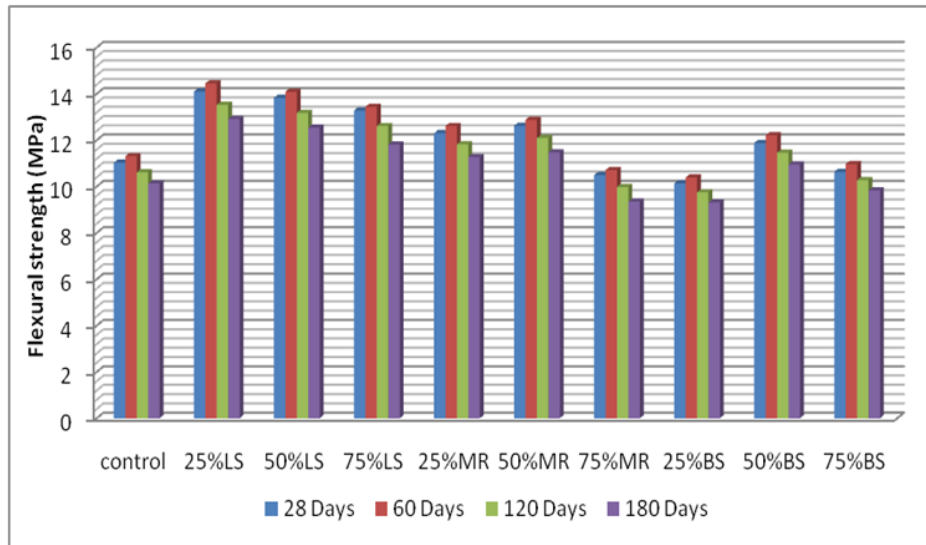


Fig. 4. Flexural strength results of geopolymers samples exposed to magnesium sulfate.

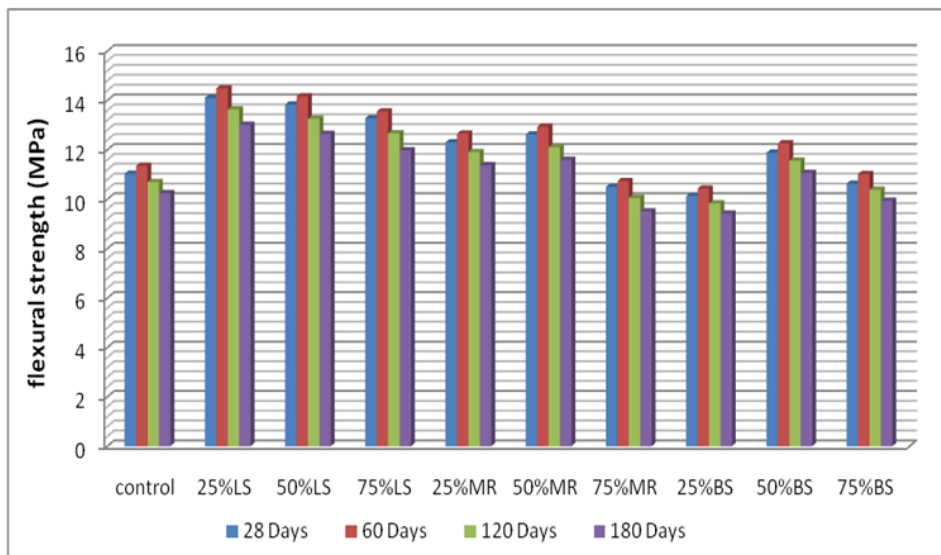


Fig. 5. Flexural strength results of geopolymers samples exposed to sodium sulfate.

Table 8. Flexural strength loss rates (%) due to magnesium and sodium sulfate effect

Mix ID	Magnesium sulfate			Sodium sulfate		
	60 Days	120 Days	180 Days	60 days	120 Days	180 Days
Control	-2,54	3,81	8,16	-2,90	3,08	7,16
25%LS	-2,48	4,04	8,44	-2,77	3,33	7,73
50%LS	-1,88	4,70	9,33	-2,39	4,19	8,60
75%LS	-1,20	5,05	11,07	-2,03	4,59	9,79
25%MR	-2,52	3,90	8,37	-2,85	3,17	7,56
50%MR	-2,06	4,12	9,11	-2,46	4,12	8,16
75%MR	-2,00	4,95	10,95	-2,19	4,29	9,43
25%BS	-2,57	3,75	8,09	-2,96	2,96	7,11
50%BS	-2,78	3,54	7,83	-3,20	2,69	6,90
75%BS	-3,20	3,29	7,53	-3,67	2,35	6,59

The geopolymer samples showed fluctuations in compressive strength of up to 120 days in the results with sodium sulfate. The geopolymerization reaction continued with exposure time to the sulfate, resulting in increased compressive strength [24] since sodium sulfate has the ability to act as an activation factor. Calcium (Ca) expansion products combined with sulfate continuously fill the pore structure for up to 120 days. After this period, a decrease in resistance was observed for up to 180 days. Remarkable cracks and high porosity ratio after 120 days resulted in decreased strength. Magnesium sulfate is a more aggressive solution than sodium sulfate [30]. After 120 days, the loss of strength was lower in sodium sulfate effect than in magnesium sulfate effect. After 60 days, the increase in the compressive strength of geopolymer samples was 2.09% and 4.48%. At 120 days, there was a decrease in strength between 1.81% and 3.30 %, and after 180 days, the decrease was between 2.87% and 6.37%. The compressive strength of 61.84 MPa, 58.18 MPa, and 57.25 MPa was obtained in 25LS in 60 days, 120 days, and 180 days, respectively. In the 50BS sample, the compressive strength 77.96 MPa, 73.36 MPa, and 72.31MPa were obtained in 60 days, 120 days, and 180 days, respectively. Besides, the compressive strength results of 50MR were 54.23 MPa, 51.33 MPa, and 50.12 MPa in 60 days, 120 days, and 180 days, respectively. The compressive strength results were shown in fig. 2. According to the results, it has been observed that the geopolymer samples have excellent behavior under sodium sulfate better magnesium sulfate.

3.2.3. Flexural strength of magnesium and sodium sulfate

The flexural strength results of the geopolymer specimen's exposure to the solution were obtained and

compared with 28-day results (Figure 4 and 5), the maximum deterioration of the manufactured samples was observed in the 180 days exposure time. Decreases in bending strengths were observed with the effect of magnesium sulfate and sodium sulfate and [28]. As known, the magnesium sulfate is a more aggressive solution than sodium sulfate [29]. Thus, the flexural strength decrease rate is formed in the lowest sodium sulfate and then magnesium sulfate, respectively. According to the results, it has been observed that the geopolymer samples have a better behavior under sodium sulfate than magnesium sulfate due to its aggressive. After 60 days, the flexural strength geopolymer samples increases under magnesium sulfate effect were between 1.20% and 3.21% and decrease between 3.29% and 5.05% after 120 days and between 7.53% and 11.07% after 180 days (table. 8). The flexural strength of 14.45 MPa, 13.53 MPa, and 12.91 MPa was obtained in 25LS in 60, 120, 180 days, respectively. In the 50MR samples, the flexural strength results of 12.88 MPa, 12.1 MPa, and 11.47 MPa were obtained in 60, 120, 180 days, respectively. The results of magnesium sulfate flexural strength were shown in fig. 4. The flexural strength of geopolymer samples increases with sodium sulfate effect at 60 days; the obtained results were between 2.03% and 3.67%. After 120 days, the geopolymer samples' results decrease significantly between 2.35% and 4.59%, while after 180 days, the decrease was between 6.59% and 9.79% (table.8). The flexural strength results obtained of 25LS geopolymer samples were 14.49 MPa, 13.63 MPa, and 13.01 MPa in 60, 120, 180 days, respectively. Besides the 50MR samples, the flexural strength results obtained were 12.93 MPa, 12.1 MPa, and 11.59 MPa in 60, 120, 180 days, respectively. The results of sodium sulfate flexural strength were shown in fig. 5.

3.3 Ultrasonic Pulse Velocity (UPV) Results

Table 9. UVP loss rates (%) due to magnesium and sodium sulfate effect.

Mix ID	Magnesium sulfate			Sodium sulfate		
	60 Days	120 Days	180 Days	60 days	120 Days	180 Days
Control	-2,00	3,92	7,63	-2,33	3,98	7,34
25%LS	2,04	7,89	11,15	1,87	8,04	11,09
50%LS	3,17	9,39	12,47	3,22	9,36	12,42
75%LS	-0,73	5,36	8,44	-0,79	5,30	8,53
25%MR	-3,17	3,65	6,59	-3,20	3,56	6,53
50%MR	-2,87	3,32	6,64	-2,81	3,29	6,52
75%MR	-1,22	4,55	7,55	-1,28	4,58	7,67
25%BS	0,99	7,12	10,87	1,28	7,29	10,75
50%BS	2,26	8,29	11,97	2,01	8,20	11,89
75%BS	2,82	8,14	11,77	2,48	8,20	11,83

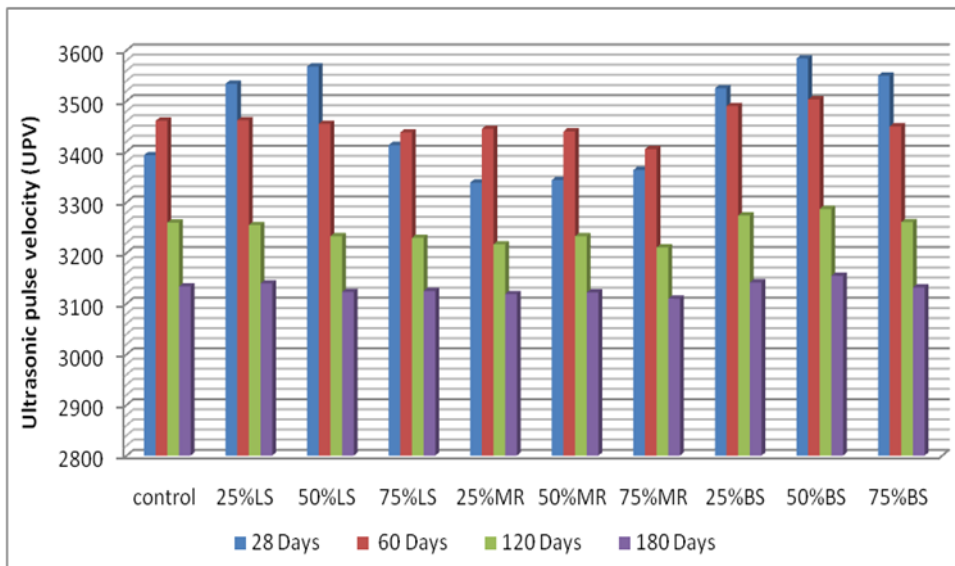


Fig. 6. UPV results of magnesium sulfate.

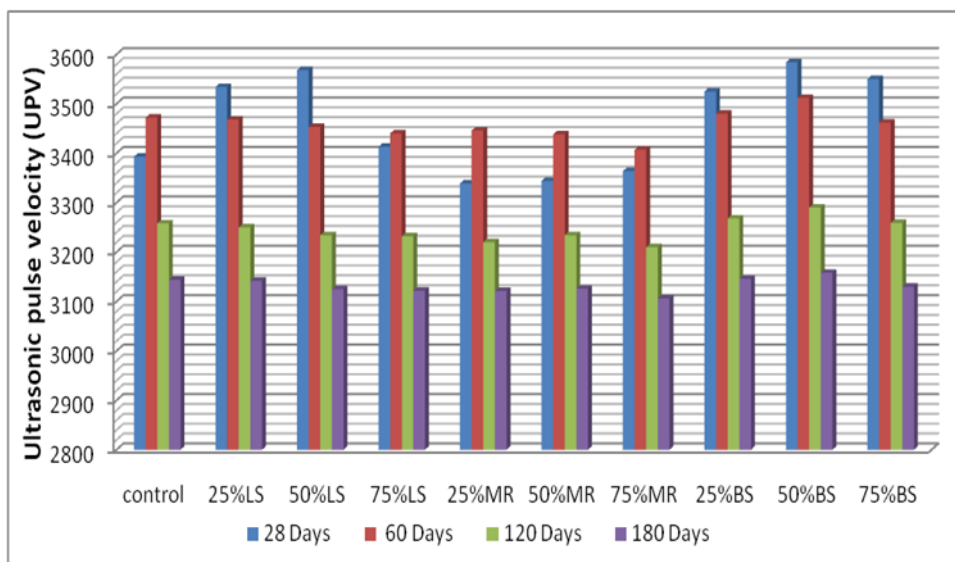


Fig. 7. UPV results of sodium sulfate.

The UPV results obtained under exposure to the solution effects were compared with the results of 28 days (Figure 6 and 7). The UPV test's change was obtained from the UPV results of the samples after exposure to the solution effects (Table. 9) With the effect of magnesium sulfate and sodium sulfate, there was an increase in the UPV test results up to 60 days, due to the filling of voids with sulfate salts and hydration products under the action of solution [16]. The results were reduced with the effect of the microcracks formed later [27]. Magnesium sulfate is a more aggressive solution than sodium sulfate [26]. Thus, the UPV test increase rate was formed in the highest sodium sulfate and magnesium sulfate. According to the results, it has been observed that the geopolymer samples have better behavior under the

effect of sulfate solutions. After 60 days, UPV results increase rates were between 0.99% and 3.17% with the effect of magnesium sulfate in geopolymer samples. At the end of 120 days, there was a decrease between 3.32% and 9.39%; moreover, after 180 days was between 6.59% and 10.87%. The geopolymer manufactured 25LS specimens, UPV results of 3462 m / s, 3255 m / s, and 3140 m / s were obtained in 60 days, 120 days, and 180 days, respectively. Furthermore, for 50BS specimens, UPV results were 3503 m / s, 3287 m / s, and 3155 m / s obtained in 60 days, 120 days, and 180 days, respectively. The geopolymer samples' UPV results that increase at 60 days under the sodium sulfate effect were between 0.79% and 3.22%. At 120 days, there was a decrease of between 3.29% and 9.36%; thus, after 180 days, the decrease was between 6.53% and

10.75%. The geopolymer 25LS sample, UPV results of 3468 m / s, 3250 m / s, and 3142 m / s were obtained in 60 days, 120 days, and 180 days, respectively. 60 days, 120 days, and 180 days, respectively. Moreover, for the 50BS sample, UPV results were 3512 m / s, 3290 m / s, and 3158 m / s obtained in 60 days, 120 days, and 180 days, respectively.

3.4. Weight Changes after Magnesium and Sodium Solution Effects

Under the effect of magnesium sulfate and sodium sulfate, there has been an increase in weight up to 60 days. Thus, to the filled voids with sulfate salts and hydration products under the action of a solution [16]. The results were reduced with the effect of the microcracks formed later [27]. Magnesium sulfate is a

more aggressive solution than sodium sulfate [26]. For these reasons, the rate of weight increase occurs in the highest in sodium sulfate and magnesium sulfate, respectively. Moreover, placing the samples before the experiment in the oven for 24 hours at 105 ° C provided better sulfate solutions to be absorbed and more effective. The effect of magnesium sulfate in geopolymer mortars, the weight increase rates in 60 days were between 10.83% and 13.65%, the weight increase rates in 120 days were between 9.22% and 10.19%, and in the 180 days weight increase rates were between 7.19% and 8.16% (Figure. 8) according to the 28 days sample. The sodium sulfate effect in the weight of geopolymer mortars increases in 60 days, 120 days, 180 days, the results obtained were between 12.64% and 15.05%, 11.59%, and 14.23%, 8.43%, and 11.23% at 60 days, 120 days, 180 days, respectively.

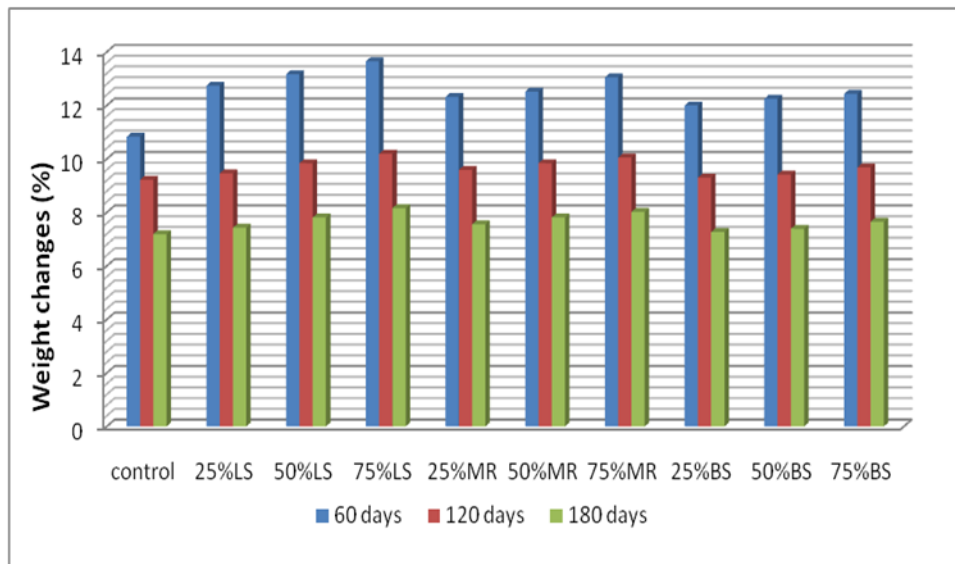


Fig. 8. Weight changes of magnesium sulfate.

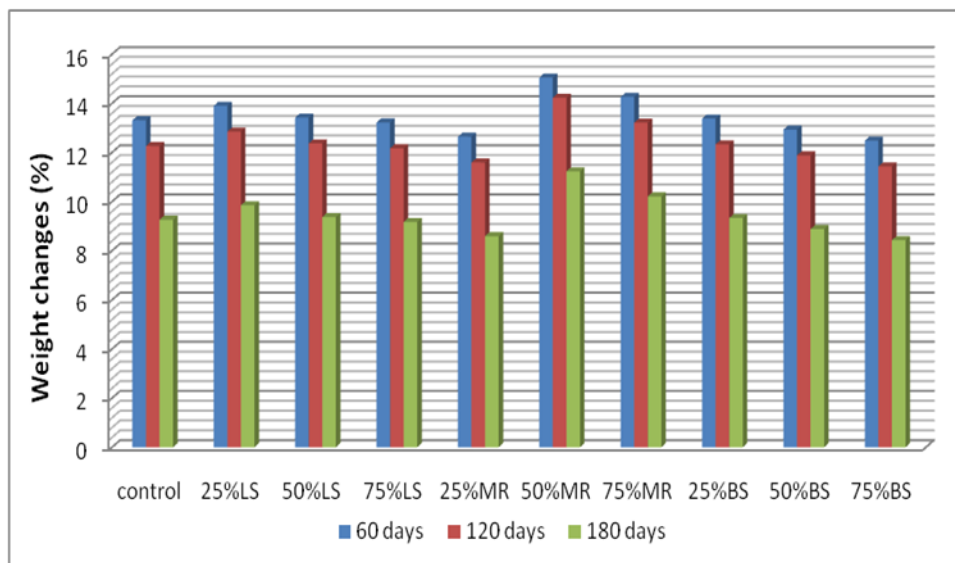


Fig. 9. Weight changes of sodium sulfate.

3.4. XRD Analysis

The XRD analysis of geopolymer samples after exposure to Na_2SO_4 and MgSO_4 over 180 days. The geopolymer samples XRD analysis uncover the crystalline phases of the raw materials.

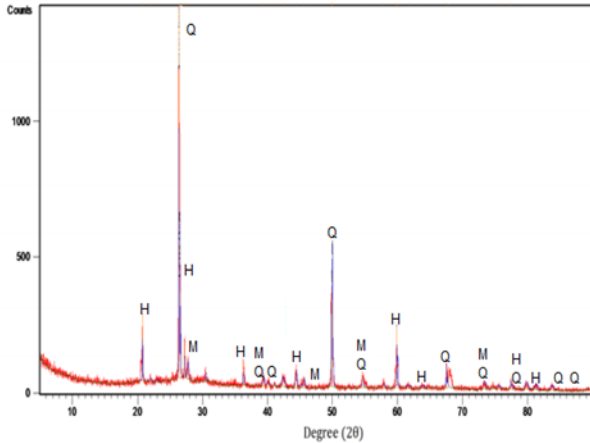


Fig. 10. X-ray diffractograms of control sample after 180days exposed to sodium sulfate exposure.

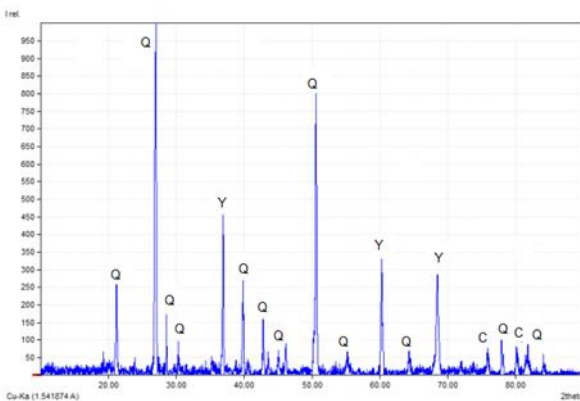


Fig. 11. X-ray diffractograms of 50%LS sample after 180 days of magnesium sulfate exposure.

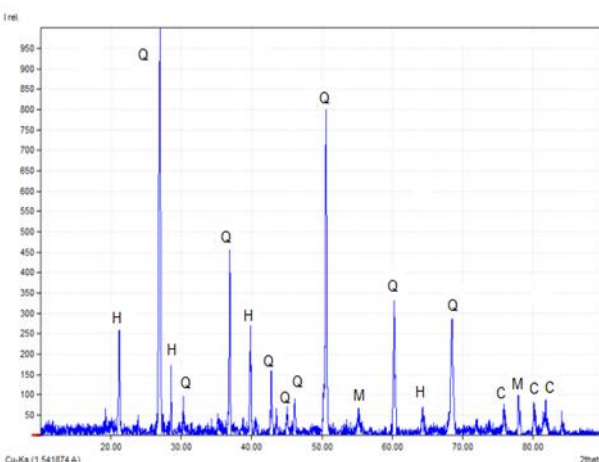


Fig. 12. X-ray diffractograms of 50%BS sample after 180 days of magnesium sulfate exposure.

The limestone and marble powder specimens exposed to MgSO_4 exhibited a new phase of gypsum with elevated intensity, produced by atomization of the C-(A)-S-H phase by the interfere of calcite with (CSH) of low crystallinity [30]. C-(A)-S-H phase peak were location at($30^\circ 2\theta$) indicating the low [36]. besides there was no sever damages seen in the control and basalt powder samples due to the lower Ca content which is almost insignificant and the existence of SiO_2 glass content obstructing the chemical reaction with MgSO_4 . Regarding to the geopolymer sample's exposure to Na_2SO_4 solution there was no different crystalline phases from the any immersed samples for this a small almost insignificant mechanical losses were observed similar to those previously mentioned by other researchers [8].The MgSO_4 solution attack were more aggressive than Na_2SO_4 , especially for the limestone and marble powder samples due to the reaction of MgSO_4 and Ca producing gypsum and magnesium hydroxide (brucite) which reduce the stability of CSH and poorly alkaline insoluble phase. Furthermore, at long term the sulfate attack progresses, and decalcification occurs due to the calcium extracted of CSH.

C: calcite (CaCO_3), Q: quartz (SiO_2), M : mullite, H : hermatite

3.4. The SEM Micrographs

The SEM micrographs of the geopolymer specimens that were exposed to Na_2SO_4 and MgSO_4 solutions for 180 days. The limestone and marble powder samples immersed in MgSO_4 exhibited the establishment of gypsum crystals in the geopolymer phase (Fig. 17), XRD analysis confirmed the presence of gypsum in the specimen, as shown in (Fig. 11).

While for the control and basalt specimens there was no significant changes occurred. Besides the manufactured geopolymer samples of this work immersed in Na_2SO_4 solutions, it was impossible to recognize the new phases formed because any XRD analysis changes were found, the results founded were in accordance with the research described by [28].

In addition to SEM analysis, EDS analysis was performed for control sample to examine the distribution of the elements within the matrices (Fig. 14). In general, spectra showed an expected distribution of elements. The main elements in the spectrum are Si, Fe and Al, which show a particular geopolymerization reaction and provide a good correlation with the relevant results.

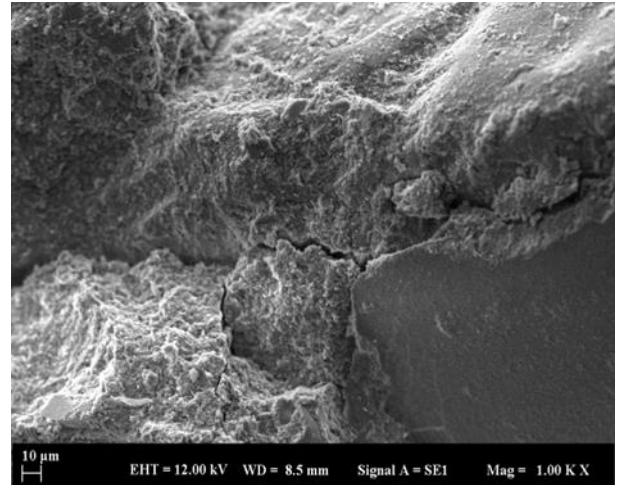
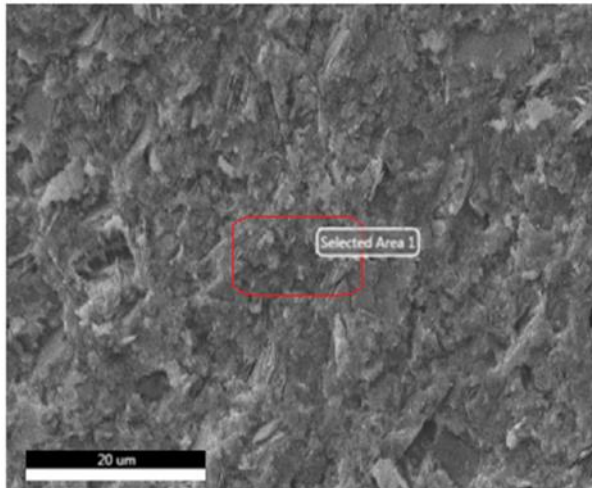


Fig. 15. The 50% BS sample after exposing to magnesium sulfate solution.

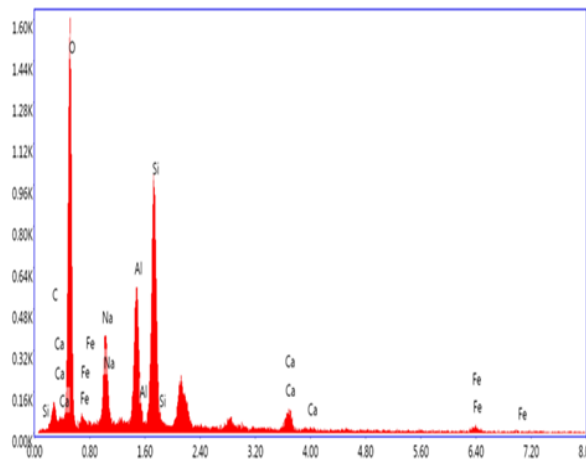


Fig. 13. EDS spectroscopy of the control sample before exposing to sulfate solution

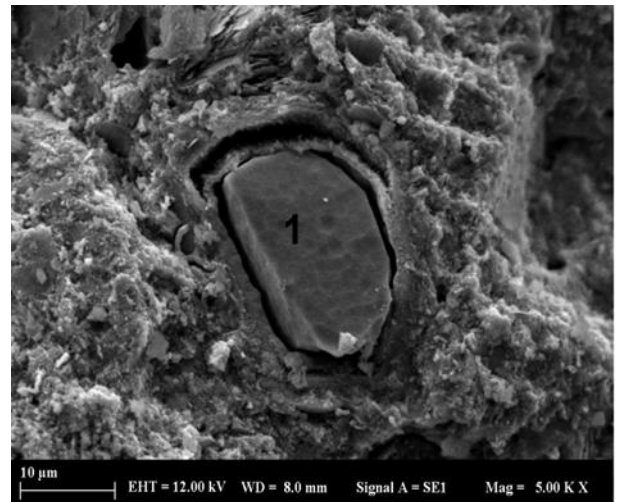


Fig. 16. The 50% LS sample after exposing to magnesium sulfate solution (1: gypsum).

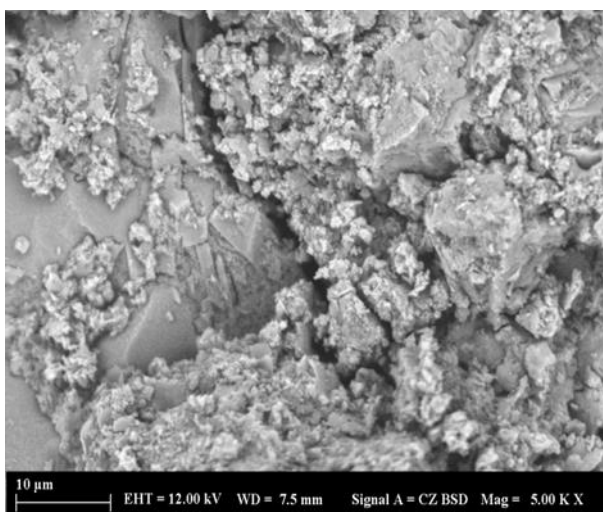


Fig. 14. The control sample after exposing to magnesium sulfate solution.

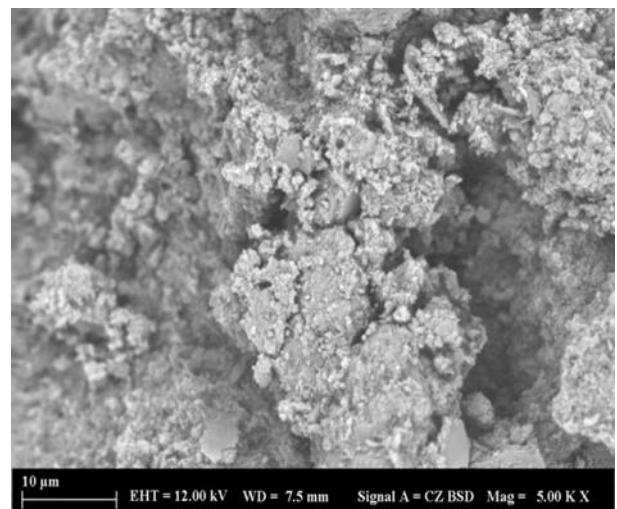


Fig. 17. The 50% LS sample after exposing to sodium sulfate solution.

4. Conclusion

The purpose of this work was to look into the durability, mechanical properties and microstructural composition impact of adding three different types of filler materials limestone, marble, and basalt powder, with the primary binder materials of this study Red-Mud and Metakaolin, based on geopolymer composites under the effect of magnesium and sodium sulfate solutions:

- After exposure to magnesium sulfate the compressive and flexural strengths of samples increase at 60 days then decrease after 120 days, especially limestone and marble powder due to the establishment of gypsum crystals in the geopolymer structure.
- There was no severe damages seen in the control and basalt powder samples due to the lower Ca content which is almost insignificant and the existence of SiO_2 glass content obstructing the chemical reaction with MgSO_4 .
- The replacement of waste filler materials increased the strength properties, especially the basalt powder, with a 75% ratio.
- The MgSO_4 solution attack was more aggressive than Na_2SO_4 , especially for the limestone and marble powder samples due to the reaction of MgSO_4 and Ca which reduce the stability of CSH and poorly alkaline insoluble phase.
- The weight changes increase due to the filled voids with sulfate salts and hydration products under the action of a solution
- About the mechanical properties, there was a considerable increase estimate observing compressive and flexural strength was obtained at 60 days, then a decrease after 120 days. For instance, the 60 days, compressive and flexural strength of basalt powder and control samples, were higher when compared to the marble and limestone powder geopolymer samples.
- About the manufactured geopolymer samples immersed in Na_2SO_4 solutions, it was impossible to recognize the new phases formed because any XRD analysis changes were found.

As an established conclusion growing waste materials, as filler replacing river sand with different ratios, contributed the development of the durability and mechanical properties and microstructural behaviors of the composite, especially basalt powder concerning the control composites. Furthermore, the ratio (50%-50%) metakaolin and red-Mud as a binder material was given good results. Moreover, the mix of Metakaolin and Red-Mud is more durable and able to be used. Finally, the use of Red-Mud and the waste filler materials in manufacturing geopolymers are economical and environmentally friendly.

Acknowledgment

This work was supported by İstanbul Aydın University and the research fund of the Yildiz Technical University-Turkey. The authors would like to express their sincere gratitude to the scientific research coordination unit for their financial support (Project number: FBA-2019-3558).

Author's Contributions

Name Surname: Ouiame CHAKKOR

Name Surname: Prof. Dr. Mehmet Fatih ALTAN and Assoc. Prof. Dr. Orhan CANPOLAT

Ethics

There are no ethical issues after the publication of this manuscript.

References

- [1] E.E. Hekal, E. Kishar, H. Mostafa, Magnesium sulfate attack on hardened blended cement pastes under different circumstances, *Cement and Concrete Research*, 32 (2002) 1421-1427.
- [2] M. Santhanam, M.D. Cohen, J. Olek, Mechanism of sulfate attack: a fresh look: Part 2. Proposed mechanisms, *Cement and concrete research*, 33 (2003) 341-346.
- [3] D. Bonen, M.D. Cohen, Magnesium sulfate attack on Portland cement paste-I. Microstructural analysis, *Cement and concrete research*, 22 (1992) 169-180.
- [4] D. Bonen, M.D. Cohen, Magnesium sulfate attack on portland cement paste—II. Chemical and mineralogical analyses, *Cement and concrete research*, 22 (1992) 707-718.
- [5] N.B. Singh, B. Middendorf, Geopolymers as an alternative to Portland cement: An overview, *Construction and Building Materials*, 237 (2020) 117455.
- [6] N. Singh, B. Middendorf, Geopolymers as an alternative to Portland cement: An overview, *Construction and Building Materials*, 237 (2020) 117455.
- [7] C. Villa, E.T. Pecina, R. Torres, L. Gómez, Geopolymer synthesis using alkaline activation of natural zeolite, *Construction and Building Materials*, 24 (2010) 2084-2090.
- [8] B. Singh, G. Ishwarya, M. Gupta, S. Bhattacharyya, Geopolymer concrete: A review of some recent developments, *Construction and building materials*, 85 (2015) 78-90.
- [9] A. Palomo, M. Grutzeck, M. Blanco, Alkali-activated fly ashes: A cement for the future, *Cement and concrete research*, 29 (1999) 1323-1329.
- [10] P.K. Mehta, R.W. Burrows, Building durable structures in the 21st century, *Concrete international*, 23 (2001) 57-63.
- [11] E.M.S. Mulapeer, Strength And Absorption Characteristics Of Fly Ash Based Geopolymer Composite Reinforced With Glass Fiber, Hasan Kalyoncu Üniversitesi, 2016.
- [12] R. El-Hachem, E. Rozière, F. Grondin, A. Loukili, Multi-criteria analysis of the mechanism of degradation of Portland cement based mortars exposed to external sulphate attack, *Cement and Concrete Research*, 42 (2012) 1327-1335.
- [13] T. Bakharev, Durability of geopolymer materials in sodium and magnesium sulfate solutions, *Cement and Concrete Research*, 35 (2005) 1233-1246.
- [14] S. Thokchom, D. Dutta, S. Ghosh, Effect of incorporating silica fume in fly ash geopolymers, *World Academy of Science, Engineering and Technology*, 60 (2011) 243-247.
- [15] A. Fernández-Jiménez, I. García-Lodeiro, A. Palomo, Durability of alkali-activated fly ash cementitious materials, *Journal of Materials Science*, 42 (2007) 3055-3065.
- [16] V. Sata, A. Sathonsaowaphak, P. Chindaprasirt, Resistance of lignite bottom ash geopolymer mortar to sulfate and sulfuric acid attack, *Cement and Concrete Composites*, 34 (2012) 700-708.

- [17] R. Martynkova, M. Mavroulidou, Properties of Alkali-Activated Concrete Based On Industrial Wastes Or By Products, Proceedings of the 14th International conference on Environmental Science and Technology Athens, Greece, 2015, pp. 3-5.
- [18] R.I. Iacobescu, G.N. Angelopoulos, P.T. Jones, B. Blanpain, Y. Pontikes, Ladle metallurgy stainless steel slag as a raw material in Ordinary Portland Cement production: a possibility for industrial symbiosis, *Journal of Cleaner Production*, 112 (2016) 872-881.
- [19] A. ASTM, C348-14 Standard Test Method for Flexural Strength of Hydraulic-Cement Mortars, ASTM Int, West Conshohocken, DOI.
- [20] K. Scrivener, J.F. Young, Mechanisms of chemical degradation of cement-based systems, CRC Press 1997.
- [21] P.K. Sarker, Bond strength of reinforcing steel embedded in fly ash-based geopolymer concrete, *Materials and structures*, 44 (2011) 1021-1030.
- [22] F. Puertas, R. Gutierrez, A. Fernández-Jiménez, S. Delvasto, J. Maldonado, Alkaline cement mortars. Chemical resistance to sulfate and seawater attack, *Materiales de Construcción*, 52 (2002) 55-71.
- [23] I. Ismail, S.A. Bernal, J.L. Provis, S. Hamdan, J.S. van Deventer, Microstructural changes in alkali activated fly ash/slag geopolymers with sulfate exposure, *Materials and structures*, 46 (2013) 361-373.
- [24] T. Aye, C.T. Oguchi, Resistance of plain and blended cement mortars exposed to severe sulfate attacks, *Construction and Building Materials*, 25 (2011) 2988-2996.
- [25] N. Rajamane, M. Nataraja, J. Dattatreya, N. Lakshmanan, D. Sabitha, Sulphate resistance and eco-friendliness of geopolymer concretes, *Indian Concrete Journal*, 86 (2012) 13.
- [26] F. Škvára, T. Jílek, L. Kopecký, Geopolymer materials based on fly ash, *Ceram.-Silik*, 49 (2005) 195-204.
- [27] S. Thokchom, P. Ghosh, S. Ghosh, Performance of fly ash based geopolymer mortars in sulphate solution, *Journal of engineering science and technology review*, 3 (2010) 36-40.
- [28] B.A. Salami, M.A.M. Johari, Z.A. Ahmad, M. Maslehuddin, Durability performance of palm oil fuel ash-based engineered alkaline-activated cementitious composite (POFA-EACC) mortar in sulfate environment, *Construction and Building Materials*, 131 (2017) 229-244.
- [29] F.N. Değirmenci, Effect of sodium silicate to sodium hydroxide ratios on durability of geopolymer mortars containing natural and artificial pozzolans, DOI (2017).
- [30] H. Manzano, R. González-Teresa, J. Dolado, A. Ayuela, X-ray spectra and theoretical elastic properties of crystalline calcium silicate hydrates: comparison with cement hydrated gels, *Materiales de Construcción*, 60 (2010) 7-19.

1.1.1 Celal Bayar University Journal of Science

Metakaolin and Red-Mud Based Geopolymer: Resistance to Sodium and Magnesium Sulfate Attack

Ouiame Chakkor^{1*}, Mehmet Fatih Altan¹, Orhan Canpolat²

¹Civil Engineering Department, Faculty of Engineering, İstanbul Aydın University, İstanbul, Turkey

²Civil Engineering Department, Faculty of Engineering, Yıldız Technical University, İstanbul, Turkey

*ouiamechakkor@stu.aydin.edu.tr

*Orcid No: 0000-0002-9293-7284

Received: 5 September 2020

Accepted: 1 March 2021

DOI: 10.18466/cbayarfbe.790946

Abstract

This paper aims to study strength properties, UPV, and weight changes exposed to sulfate attack, and microstructural properties of geopolymer mortar prepared using metakaolin and red-mud as binder materials by mixing with river sand replaced partially by limestone, marble and basalt powder with different ratios (25%, 50%, and 75%) as filler materials, the mix proposed were activated by sodium silicate and sodium hydroxide solutions (12mol). The proposed samples were exposed to 10% of magnesium and sodium sulfate solutions for various periods of 60, 120, and 180 days to investigate the durability properties of the manufactured geopolymer mortar. The experimentally obtained results uncover that the prepared geopolymer mortar's strength properties increase at 60 days for all the proposed mixes, while at 180 days; the geopolymer mortar suffers a significant loss. Change in weight increase obviously between 10.83% and 13.65% for 60 days and decrease gradually for 120 days between 9.22% and 10.19% to reach a stable value between 120 and 180 days. Furthermore, to evaluate this work, the Scanning Electron Microscopy and X-ray Diffraction methods were investigated.

Keywords: Geopolymer, binder, metakaolin, red-mud, SEM, XRD.

2. Introduction

Regarding the durability of concrete structures, the sulfate attack is one of the factors causing deterioration cement paste due to the expansion, spalling, and softening. According to some previous research, the OPC (ordinary portland cement) showed severe damage when exposed to the sulfate attack [1]. Under the effect of sulfate attack on OPC concrete the chemical reaction between the aluminate component of cement paste and C-S-H[2], help out the formation of ettringite and gypsum which is the leading cause of the concrete's expansion and cracking, furthermore the destruction of C-S-H cause the disintegration and softening for the concrete's sample[3, 4]. The geopolymer mortars, known as known, have very low emission of CO₂[5, 6]. Moreover, the geopolymer mortars using waste materials, MK (metakaolin), Fly-ash, and ferrochrome slag supply sustainable development under the effects of sulfate attack. Recently, the geopolymers' term has been viewed as the future cement, and their evolution emerged and fostered by way of Davidovits [7], due to its good mechanical properties, low permeability, and

excellent durability properties [8]. The geopolymers must be considered a new material, a new binder, and a new cement of concrete, which has no dangerous alkali-aggregate reaction reported by Davidovits. Previous researches indicated the development of strength properties and hydration products throw the effects of curing, the composition of the alkaline solution, and the ratio of water and binder, the alkaline solution generally comprise sodium silicate, sodium hydroxide. The geopolymer binder materials have lower costs and a higher reduction in CO₂ emissions than Portland cement (PC).

Moreover, the compressive strength of geopolymer samples Range is 40-70MPa [9], due to the curing Hydrothermal, which accelerates the chemical reaction between binder and alkali solution. In the case of an acid attack, some previous researches study the durability of geopolymer materials to present its processing and characterization [10], and due to the absence of high-calcium phases, the geopolymer materials have excellent resistance under the sulfate solutions effects. Nowadays, the durability and

maintenance of concrete structures become a critical issue [11] because they start to deteriorate after 20–30 years while their design life was at least 50 years [12]. The constructions in contact with seawater, sewages, tunnels, and deep foundations are exposed to external chemical attacks [13]. When subjected to sulfate attack in the environment, the ordinary Portland cement showed cases of concrete deterioration due to the involved reactions of C–H, C–S–H and the aluminate component of cement [14]; thus for the geopolymer waste materials, the sulfate attack is a vital durability concern. Several additives are used to increase the strength properties of the manufactured geopolymer concrete, such as slag. When exposed to sulfate solutions effects, the geopolymer samples with low calcium base have shown excellent durability and strength properties [15]. Besides the OPC' durability problems are associated with its main phases; calcium content, when C_3A exposed to the sulfate ions ettringite and gypsum will be formed in the presence of $Ca(OH)_2$; thus the concrete's disruptive expansion and degradation occur due to the non-cohesive particles mass [16].

The geopolymers present a high durability and strength properties resistance under the effects of sulfate attack due to its strength, low creep, and low shrinkage [17], and low phase of calcium. Furthermore, the geopolymer activating solution, especially NaOH, accelerates chemical dissolution, which inhibits the formation of ettringite and carbon-hydrogen during binder formation and promotes higher strengths at early ages of reaction, which improved excellent stability in aggressive environments due to the development of higher crystallinity [18]. However, high concentrations of NaOH caused undesirable morphology and non-uniformity of the manufactured geopolymer samples due to the excessively OH⁻ in solution.

This work presents a geopolymer mortar manufactured by MK and RM (red-mud) as binder materials activated with (NaOH and Na_2SiO_3) chemical materials, and as filler materials limestone, marble and basalt powder were used replaced river sand with different ratio (25%, 50%, and 75%). The performance of the manufactured geopolymer samples was conducted under the effect of 10% magnesium sulfate and 10% sodium sulfate solutions. Visual appearance, the strength properties, weight changes, XRD, and SEM of these samples were obtained experimentally.

3. Materials and Methods

In this purpose, metakaolin and red mud were used as a binder material while limestone, marble, and basalt powder were used as filler materials. Red mud was collected from Seydişehir Aluminum Plant (Konya/Turkey). The ground granulated blast furnace slag is manufactured by Bolu Cement Industry (Bolu/Turkey). The slag's specific weight is

$2.91g/cm^3$ and the amount remaining on the 45-micron sieve is 1.4%, and it was used in 13% of the mixture. Kaolin was extracted from Industrial Minerals San.ve Tic. Inc. (Istanbul/Turkey), the specific gravity is $2.52 g/cm^3$, The powder of this kaolin was once calcined at $700^\circ C$ for four hours at a heating rate of $1^\circ C/min$ to get a surprisingly reactive metakaolin. Silica + alumina + iron oxide ratio = $97.18\% > 70\%$, Moreover metakaolin has fine grain which increase the reaction. Slag, metakaolin, and red mud were stated in S, MK, and RM abbreviations, respectively. Liquid sodium silicate ($SiO_2/Na_2O = 3.29 M$) ratio and analytical grade sodium hydroxide (12mol) were once used for alkaline activation taken from AS Kimya (Istanbul/Turkey). Sodium hydroxide and sodium silicate were expressed in SH and SS abbreviations, respectively. The sodium hydroxide was prepared by adding 1liter of distilled water to 480g of sodium hydroxide pellets to obtain 12mol. The obtained water glass has been stored at room temperature for 24 hours before being used with sodium silicate/sodium hydroxide in a 2:1 ratio. The mix was prepared using the mixer drill using the chemicals (SS and SH) with MK and mixed for 5mins. The RM was added to the bellow mix and also mixed for 5 mins to homogenate the mortar prepared, to enhance the tenacity of mix blast furnace slag was used and mixed for just 2 mins then immediately one the filler materials (limestone, basalt powder, and marble powder) with river sand using one of the different ratio approved for this work (25%, 50%, and 75%) were added. Filler materials used in this work has a very fine grain and convert large voids to small ones. Limestone, marble, and basalt powder used in this work as filler materials. Limestone powder was provided from Gebze Rock Quarry (Gebze/Turkey), basalt samples were homogenized, dried at $105^\circ C$ for 24 hours. From INCI Group Company (Sakarya/Turkey) the basalt powder stone was extracted. Marble powder was dried the same as basalt powder, obtained from Turkan Company (Alibeykoy/Istanbul). All the filler materials used were less than $0,0063mm$ particle diameter. In this work as aggregate, the river sand with less than $0,25 mm$ particle diameter was used correspondent to TS 706 EN 12620 [19]. Limestone, marble, and basalt powder were expressed in LS, MR, and BS abbreviations, respectively. While the mixing procedure has been finished, the mortar was used to the molds $50 \times 50 \times 50 mm$ and $71 \times 71 \times 71 mm$ cubes, $40 \times 40 \times 160$ prisms, and $300 \times 150 mm$ cylinders and vibrated, and then the geopolymer samples were kept for 24h in the ambient temperature. All the specimens were held for 24 hours in the drying oven at $100^\circ C$. After the curing, the

samples were preserved in room temperature conditions. After 28 days, durability tests were performed under the effect of sulfate solutions. Moreover, the mechanical tests, compressive strength test according to ASTM C 109 was executed after 60, 120, and 180 days utilizing the 50x50x50 mm cubes, the Flexural strength test

quoted by ASTM C 348 utilizing the 40x40x160 prisms samples was carried also after 60, 120, and 180 days [20]. When the results of the exposed samples to the effect of sulfate solutions, the SEM and XRD analysis was performed.

Table 1. The MK, RM, and S chemical properties.

Chemical Analysis(%)	SiO ₂	Al ₂ O ₃	Fe ₂ O ₃	TiO ₂	CaO	MgO	K ₂ O	Na ₂ O	SO ₃
MK	56,1	40,23	0,85	0,55	0,19	0,16	0,51	0,24	-
RM	17,38	24,52	35,25	-	3,22	0,42	0,43	8,45	-
S	40,55	12,83	1,1	-	32,58	5,87	-	0,79	0,18

Table 2. SH chemical properties.

Chemical Analysis (%)	NaOH	Na ₂ CO ₃	CL	SO ₄	Al	Fe
SH	99,1	0,3	≤0,01	≤0,01	≤0,002	≤0,002

Table 3. SS chemical properties

Chemical Analysis (%)	SiO ₂	Na ₂ O	Fe (%)	Density (g/ml)	Heavymetals (%)
SS	27,0	8,2	≤0,005	1360	≤0,005

Table 4. Fine aggregate's chemical properties.

Chemical Analysis (%)	SiO ₂	Al ₂ O ₃	Fe ₂ O ₃	TiO ₂	CaO	CaO ₂	K ₂ O	Na ₂ O	SO ₃
LS	3,3	0,82	0,58	-	-	92,9	-	-	1,18
MR	1,12	0,73	0,05	-	-	83,22	-	-	0,56
BS	56,9	17,6	8,1	0,9	7	-	1,9	3,8	-

Table 5. Mix of control sample geopolymer composites (g)

Metakaolin	Red-Mud	Slag	SS (Na ₂ SiO ₃)	SH (NaOH (12 mol))	River Sand
500	500	133	667	333	2000

Table 6. The mix of the three different filler materials replacing river sand with different ratios (g)

Metakaolin	Red-Mud	Slag	Na ₂ SiO ₃	NaOH (12mol)	River Sand	Limestone or Marble or Basalt powder
500	500	133	667	333	1500 1000 500	500 1000 1500

4. Results and Discussions

Table 7. Compressive strength loss rates (%) due to magnesium and sodium sulfate effect.

Mix ID	Magnesium sulfate			Sodium sulfate		
	60 days	120 days	180 days	60 days	120 days	180 days
Control	-3,20	3,044	7,33	-3,87	2,28	3,98
25%LS	-3,08	3,215	7,59	-3,55	2,58	4,14
50%LS	-2,18	3,519	8,69	-2,50	2,98	5,43
75%LS	-1,79	4,634	9,82	-2,09	3,30	6,37
25%MR	-3,12	3,198	7,42	-3,62	2,47	4,06
50%MR	-2,31	3,407	8,42	-2,65	2,84	5,13
75%MR	-1,98	4,140	9,28	-2,16	3,20	6,21
25%BS	-3,25	2,960	7,22	-3,96	2,28	3,87
50%BS	-3,52	2,575	6,70	-4,03	2,19	3,52
75%BS	-4,19	2,176	5,67	-4,48	1,81	2,97

Geopolymer mortar specimens were exposed to 10% Sodium (Na_2SO_4) and 10% Magnesium (MgSO_4) Sulfate solutions for 60 days, 120 days, and 180 days. The results for each sample were given in (Tables 7, 8) compared with 28 days'.

3.1. The Visual Appearance

The visual appearance of the test specimens at 60 and 120 after moistening in magnesium and sodium sulfate solutions (Figs. 1 and 2). Clearly it was seen that there were no changes as surface erosion, cracking in the surface appearance of the manufactured geopolymer samples. It was mean that geopolymer mortar had a good resistance to sulfates, agreement to values limit of the expansion suggested in the ASTM C1012-13. Moreover, at 180 days after the samples were immediately removed from both magnesium and sodium sulfate solutions and kept at room temperature 25°C , a wire brush was used to clean up the

accumulated salt attack scaling behind the surface of the manufactured geopolymer mortar specimens, which did not affect the integrity of specimens mechanically. Furthermore, for both magnesium and sodium sulfate solutions there were no severe damages observed similar results were reported by other there is no severe deterioration was observed. Similar observations also have been reported by other studies' [16, 21-26]. Skvara et al. [27] stated that also more than one year there was not any significant sign of surface deterioration because of their lower susceptibility to form hydration byproducts, due to the cross-linked structure of the gels in the geopolymer samples.

3.2. Strength Properties

3.2.1. Compressive strength of magnesium sulfate

According to the magnesium sulfate effect, fluctuations in the compressive strength were seen up to 120 days. The fluctuations occurred were due to the diffusion of Magnesium from the mixture of alkaline ions to the solution, resulting in diffusion to the matrix formed [16]. Furthermore, a decrease in strength was observed for up to 120 days. The microcracks presence and alkalis transition geopolymers to the solution caused the strength losses at 120 days [28]. The compressive strength increase rate of magnesium sulfate in geopolymer samples after 60 days compared to 28 days results at room temperature were between 1.79% and 4.19%. After 120 days, the compressive strength decrease was occurred between 2.17% and 4.63%, while after 180 days, the decrease was between 5.67% and 9.82%. The results are shown in table 7. The compressive strength ls and bs powder at 60 days were 58.94 MPa and 77.58 MPa respectively, while the control sample was 65.09 MPa. The results for 120 days were between 73.01 MPa and 50.25 MPa. The obtained



Fig.1. a) Samples after exposed to (MgSO_4), b) Samples after exposed to (Na_2SO_4) c) Samples while exposed to (MgSO_4), d) Samples while exposed to (Na_2SO_4)

results for 180 days were between 69.92MPa and 42.51 for bs and mr powder specimens, respectively. According to the results, it was seen that the geopolymer samples have better behavior under the magnesium sulfate attack effects. Microstructural changes occurring in the control, bs and ls samples at 6 months after the magnesium sulfate attack. The microstructure of the samples was preserved after exposure to magnesium sulfate. The excellent resistance of geopolymeric materials to sulfates was attributed to the source material having a lower Ca content and a more stable cross-linked aluminosilicate polymer structure while for the material having a higher Ca

content as limestone and marble powder exhibited a new phase of gypsum (Y: gypsum), through the chemical reaction happened between Ca and ($MgSO_4$) occurring the decomposition of the C-A-S-H, the notion proposed was identified by XRD and SEM. Besides, the geopolymer materials are less susceptible to attack's sulfate than standard cement hydration products. Low Ca content was found to be a significant feature in the durability of metakaolin. In this case, the reaction manufacture is an alkali gel (aluminosilicate) with a three-dimensional structure, which was significantly different from the hydrated calcium silicate gel formed in GPC hydration [29].

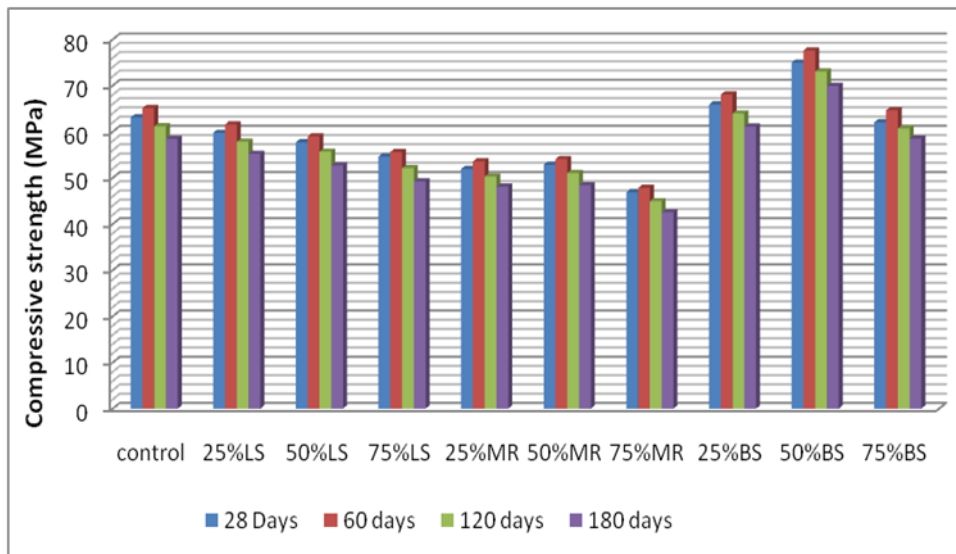


Fig. 2. Compressive strength results of geopolymers samples exposed to magnesium sulfate

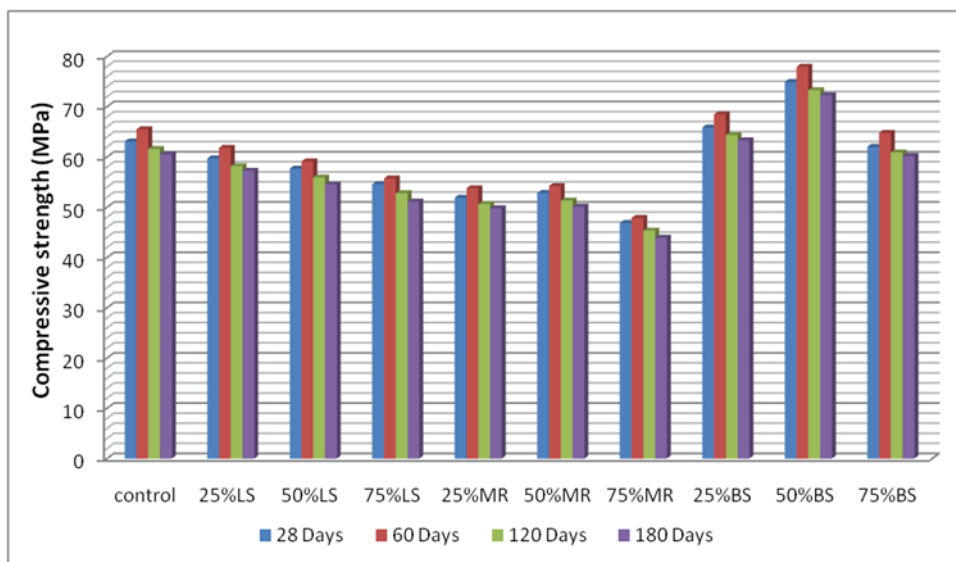


Fig. 3. Compressive strength results of geopolymers samples exposed to sodium sulfate.

3.2.2. Compressive strength of sodium sulfate

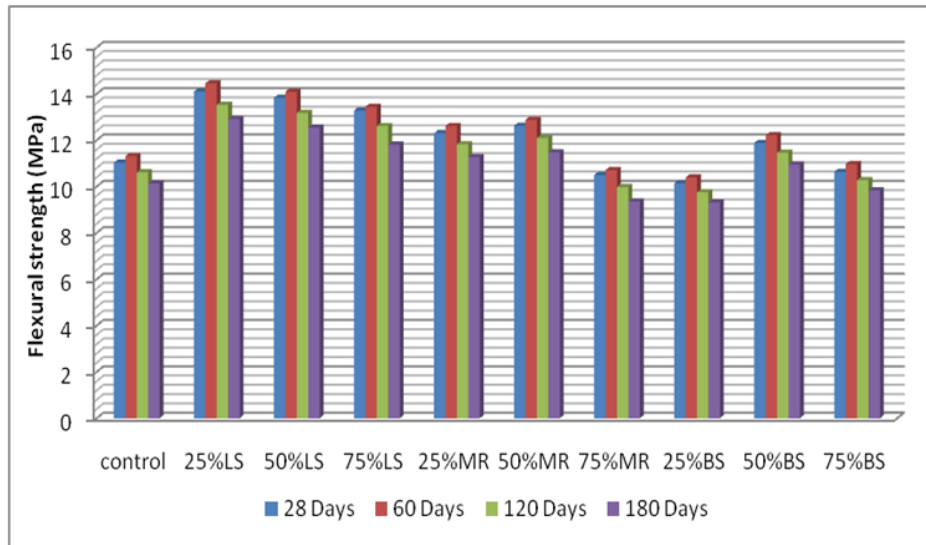


Fig. 4. Flexural strength results of geopolymers samples exposed to magnesium sulfate.

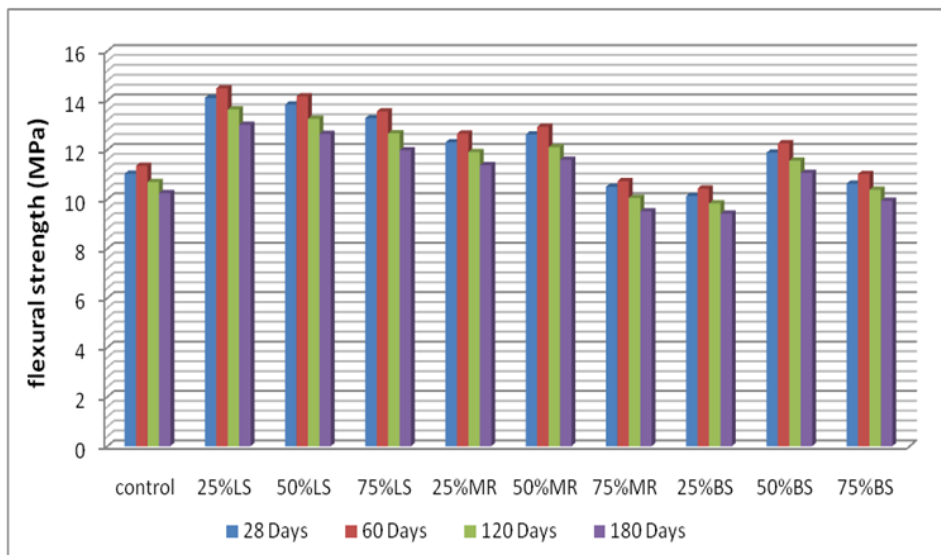


Fig. 5. Flexural strength results of geopolymers samples exposed to sodium sulfate.

Table 8. Flexural strength loss rates (%) due to magnesium and sodium sulfate effect

Mix ID	Magnesium sulfate			Sodium sulfate		
	60 Days	120 Days	180 Days	60 days	120 Days	180 Days
Control	-2,54	3,81	8,16	-2,90	3,08	7,16
25%LS	-2,48	4,04	8,44	-2,77	3,33	7,73
50%LS	-1,88	4,70	9,33	-2,39	4,19	8,60
75%LS	-1,20	5,05	11,07	-2,03	4,59	9,79
25%MR	-2,52	3,90	8,37	-2,85	3,17	7,56
50%MR	-2,06	4,12	9,11	-2,46	4,12	8,16
75%MR	-2,00	4,95	10,95	-2,19	4,29	9,43
25%BS	-2,57	3,75	8,09	-2,96	2,96	7,11
50%BS	-2,78	3,54	7,83	-3,20	2,69	6,90
75%BS	-3,20	3,29	7,53	-3,67	2,35	6,59

The geopolymer samples showed fluctuations in compressive strength of up to 120 days in the results with sodium sulfate. The geopolymerization reaction continued with exposure time to the sulfate, resulting in increased compressive strength [24] since sodium sulfate has the ability to act as an activation factor. Calcium (Ca) expansion products combined with sulfate continuously fill the pore structure for up to 120 days. After this period, a decrease in resistance was observed for up to 180 days. Remarkable cracks and high porosity ratio after 120 days resulted in decreased strength. Magnesium sulfate is a more aggressive solution than sodium sulfate [30]. After 120 days, the loss of strength was lower in sodium sulfate effect than in magnesium sulfate effect. After 60 days, the increase in the compressive strength of geopolymer samples was 2.09% and 4.48%. At 120 days, there was a decrease in strength between 1.81% and 3.30 %, and after 180 days, the decrease was between 2.87% and 6.37%. The compressive strength of 61.84 MPa, 58.18 MPa, and 57.25 MPa was obtained in 25LS in 60 days, 120 days, and 180 days, respectively. In the 50BS sample, the compressive strength 77.96 MPa, 73.36 MPa, and 72.31MPa were obtained in 60 days, 120 days, and 180 days, respectively. Besides, the compressive strength results of 50MR were 54.23 MPa, 51.33 MPa, and 50.12 MPa in 60 days, 120 days, and 180 days, respectively. The compressive strength results were shown in fig. 2. According to the results, it has been observed that the geopolymer samples have excellent behavior under sodium sulfate better magnesium sulfate.

3.2.3. Flexural strength of magnesium and sodium sulfate

The flexural strength results of the geopolymer specimen's exposure to the solution were obtained and

compared with 28-day results (Figure 4 and 5), the maximum deterioration of the manufactured samples was observed in the 180 days exposure time. Decreases in bending strengths were observed with the effect of magnesium sulfate and sodium sulfate and [28]. As known, the magnesium sulfate is a more aggressive solution than sodium sulfate [29]. Thus, the flexural strength decrease rate is formed in the lowest sodium sulfate and then magnesium sulfate, respectively. According to the results, it has been observed that the geopolymer samples have a better behavior under sodium sulfate than magnesium sulfate due to its aggressive. After 60 days, the flexural strength geopolymer samples increases under magnesium sulfate effect were between 1.20% and 3.21% and decrease between 3.29% and 5.05% after 120 days and between 7.53% and 11.07% after 180 days (table. 8). The flexural strength of 14.45 MPa, 13.53 MPa, and 12.91 MPa was obtained in 25LS in 60, 120, 180 days, respectively. In the 50MR samples, the flexural strength results of 12.88 MPa, 12.1 MPa, and 11.47 MPa were obtained in 60, 120, 180 days, respectively. The results of magnesium sulfate flexural strength were shown in fig. 4. The flexural strength of geopolymer samples increases with sodium sulfate effect at 60 days; the obtained results were between 2.03% and 3.67%. After 120 days, the geopolymer samples' results decrease significantly between 2.35% and 4.59%, while after 180 days, the decrease was between 6.59% and 9.79% (table.8). The flexural strength results obtained of 25LS geopolymer samples were 14.49 MPa, 13.63 MPa, and 13.01 MPa in 60, 120, 180 days, respectively. Besides the 50MR samples, the flexural strength results obtained were 12.93 MPa, 12.1 MPa, and 11.59 MPa in 60, 120, 180 days, respectively. The results of sodium sulfate flexural strength were shown in fig. 5.

3.3 Ultrasonic Pulse Velocity (UPV) Results

Table 9. UVP loss rates (%) due to magnesium and sodium sulfate effect.

Mix ID	Magnesium sulfate			Sodium sulfate		
	60 Days	120 Days	180 Days	60 days	120 Days	180 Days
Control	-2,00	3,92	7,63	-2,33	3,98	7,34
25%LS	2,04	7,89	11,15	1,87	8,04	11,09
50%LS	3,17	9,39	12,47	3,22	9,36	12,42
75%LS	-0,73	5,36	8,44	-0,79	5,30	8,53
25%MR	-3,17	3,65	6,59	-3,20	3,56	6,53
50%MR	-2,87	3,32	6,64	-2,81	3,29	6,52
75%MR	-1,22	4,55	7,55	-1,28	4,58	7,67
25%BS	0,99	7,12	10,87	1,28	7,29	10,75
50%BS	2,26	8,29	11,97	2,01	8,20	11,89
75%BS	2,82	8,14	11,77	2,48	8,20	11,83

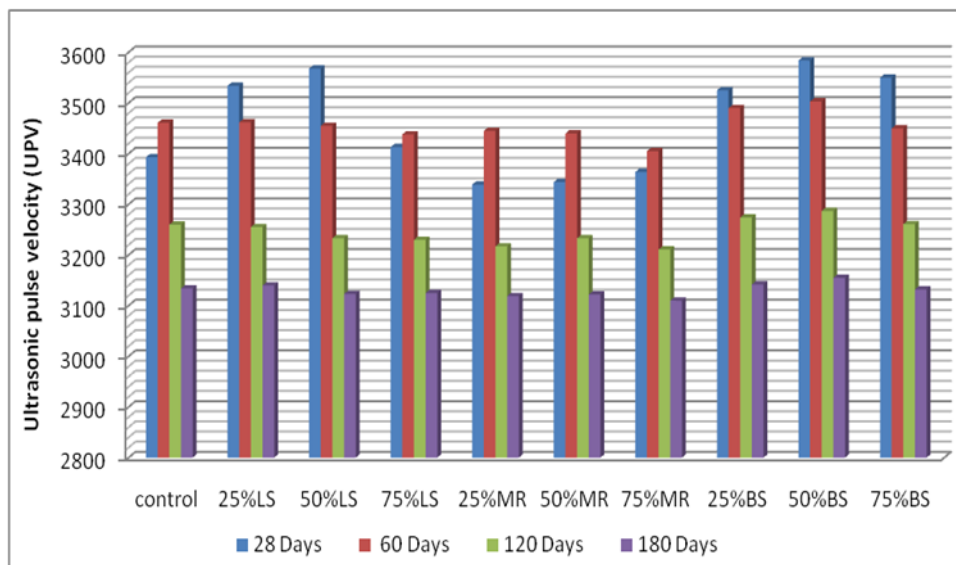


Fig. 6. UPV results of magnesium sulfate.

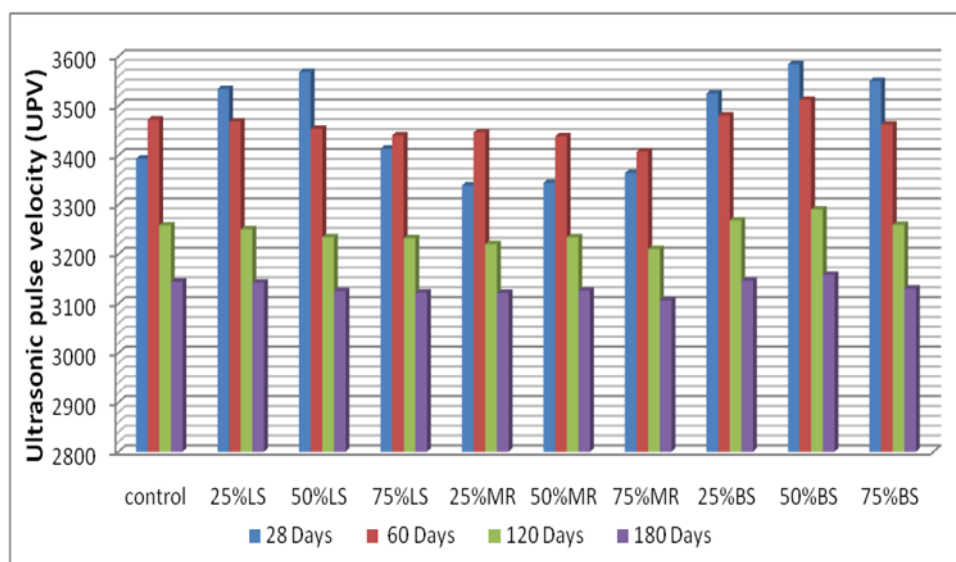


Fig. 7. UPV results of sodium sulfate.

The UPV results obtained under exposure to the solution effects were compared with the results of 28 days (Figure 6 and 7). The UPV test's change was obtained from the UPV results of the samples after exposure to the solution effects (Table. 9) With the effect of magnesium sulfate and sodium sulfate, there was an increase in the UPV test results up to 60 days, due to the filling of voids with sulfate salts and hydration products under the action of solution [16]. The results were reduced with the effect of the microcracks formed later [27]. Magnesium sulfate is a more aggressive solution than sodium sulfate [26]. Thus, the UPV test increase rate was formed in the highest sodium sulfate and magnesium sulfate. According to the results, it has been observed that the geopolymer samples have better behavior under the

effect of sulfate solutions. After 60 days, UPV results increase rates were between 0.99% and 3.17% with the effect of magnesium sulfate in geopolymer samples. At the end of 120 days, there was a decrease between 3.32% and 9.39%; moreover, after 180 days was between 6.59% and 10.87%. The geopolymer manufactured 25LS specimens, UPV results of 3462 m / s, 3255 m / s, and 3140 m / s were obtained in 60 days, 120 days, and 180 days, respectively. Furthermore, for 50BS specimens, UPV results were 3503 m / s, 3287 m / s, and 3155 m / s obtained in 60 days, 120 days, and 180 days, respectively. The geopolymer samples' UPV results that increase at 60 days under the sodium sulfate effect were between 0.79% and 3.22%. At 120 days, there was a decrease of between 3.29% and 9.36%; thus, after 180 days, the decrease was between 6.53% and

10.75%. The geopolymer 25LS sample, UPV results of 3468 m / s, 3250 m / s, and 3142 m / s were obtained in 60 days, 120 days, and 180 days, respectively. 60 days, 120 days, and 180 days, respectively. Moreover, for the 50BS sample, UPV results were 3512 m / s, 3290 m / s, and 3158 m / s obtained in 60 days, 120 days, and 180 days, respectively.

3.4. Weight Changes after Magnesium and Sodium Solution Effects

Under the effect of magnesium sulfate and sodium sulfate, there has been an increase in weight up to 60 days. Thus, to the filled voids with sulfate salts and hydration products under the action of a solution [16]. The results were reduced with the effect of the microcracks formed later [27]. Magnesium sulfate is a

more aggressive solution than sodium sulfate [26]. For these reasons, the rate of weight increase occurs in the highest in sodium sulfate and magnesium sulfate, respectively. Moreover, placing the samples before the experiment in the oven for 24 hours at 105 ° C provided better sulfate solutions to be absorbed and more effective. The effect of magnesium sulfate in geopolymer mortars, the weight increase rates in 60 days were between 10.83% and 13.65%, the weight increase rates in 120 days were between 9.22% and 10.19%, and in the 180 days weight increase rates were between 7.19% and 8.16% (Figure. 8) according to the 28 days sample. The sodium sulfate effect in the weight of geopolymer mortars increases in 60 days, 120 days, 180 days, the results obtained were between 12.64% and 15.05%, 11.59%, and 14.23%, 8.43%, and 11.23% at 60 days, 120 days, 180 days, respectively.

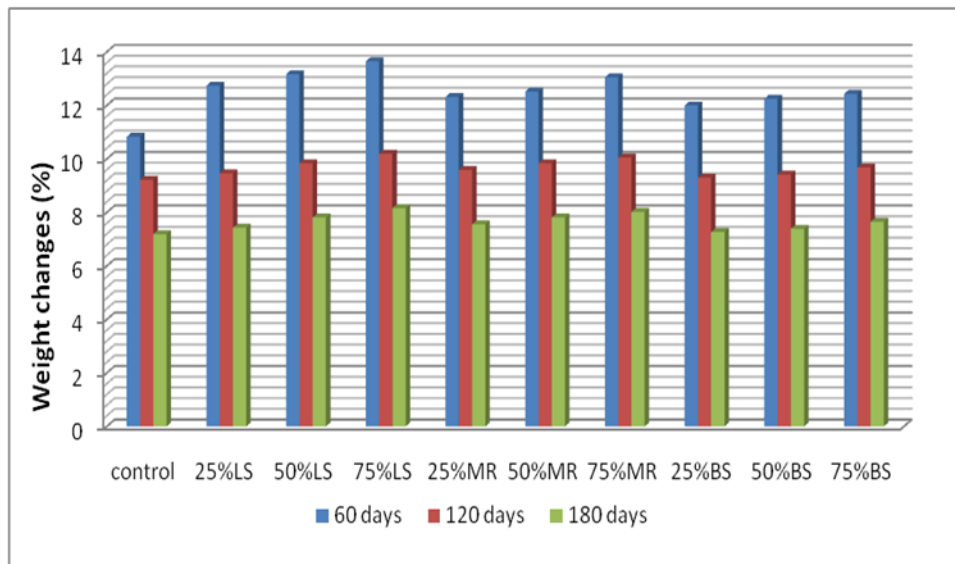


Fig. 8. Weight changes of magnesium sulfate.

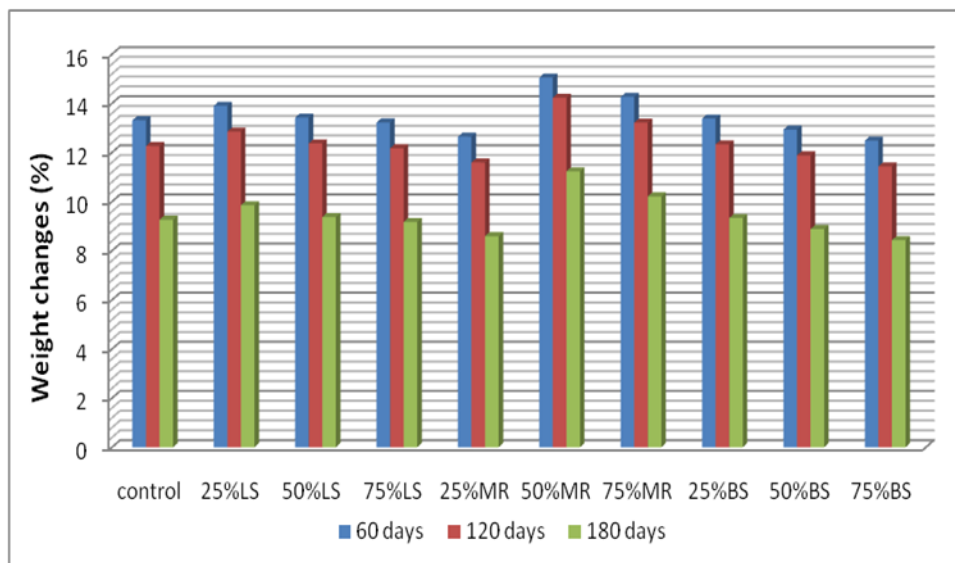


Fig. 9. Weight changes of sodium sulfate.

3.4. XRD Analysis

The XRD analysis of geopolymer samples after exposure to Na_2SO_4 and MgSO_4 over 180 days. The geopolymer samples XRD analysis uncover the crystalline phases of the raw materials.

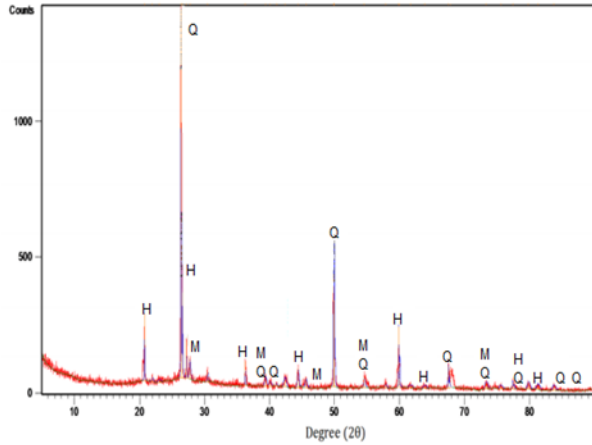


Fig. 10. X-ray diffractograms of control sample after 180days exposed to sodium sulfate exposure.

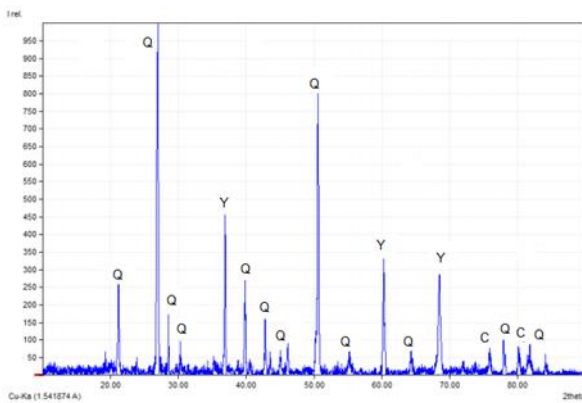


Fig. 11. X-ray diffractograms of 50%LS sample after 180 days of magnesium sulfate exposure.

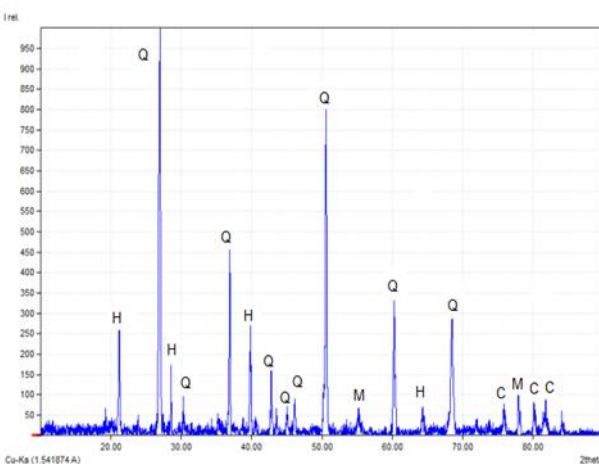


Fig. 12. X-ray diffractograms of 50%BS sample after 180 days of magnesium sulfate exposure.

The limestone and marble powder specimens exposed to MgSO_4 exhibited a new phase of gypsum with elevated intensity, produced by atomization of the C-(A)-S-H phase by the interfere of calcite with (CSH) of low crystallinity [30]. C-(A)-S-H phase peak were location at($30^\circ 2\theta$) indicating the low [36]. besides there was no sever damages seen in the control and basalt powder samples due to the lower Ca content which is almost insignificant and the existence of SiO_2 glass content obstructing the chemical reaction with MgSO_4 . Regarding to the geopolymer sample's exposure to Na_2SO_4 solution there was no different crystalline phases from the any immersed samples for this a small almost insignificant mechanical losses were observed similar to those previously mentioned by other researchers [8].The MgSO_4 solution attack were more aggressive than Na_2SO_4 , especially for the limestone and marble powder samples due to the reaction of MgSO_4 and Ca producing gypsum and magnesium hydroxide (brucite) which reduce the stability of CSH and poorly alkaline insoluble phase. Furthermore, at long term the sulfate attack progresses, and decalcification occurs due to the calcium extracted of CSH.

C: calcite (CaCO_3), Q: quartz (SiO_2), M : mullite, H : hermatite

3.4. The SEM Micrographs

The SEM micrographs of the geopolymer specimens that were exposed to Na_2SO_4 and MgSO_4 solutions for 180 days. The limestone and marble powder samples immersed in MgSO_4 exhibited the establishment of gypsum crystals in the geopolymer phase (Fig. 17), XRD analysis confirmed the presence of gypsum in the specimen, as shown in (Fig. 11).

While for the control and basalt specimens there was no significant changes occurred. Besides the manufactured geopolymer samples of this work immersed in Na_2SO_4 solutions, it was impossible to recognize the new phases formed because any XRD analysis changes were found, the results founded were in accordance with the research described by [28].

In addition to SEM analysis, EDS analysis was performed for control sample to examine the distribution of the elements within the matrices (Fig. 14). In general, spectra showed an expected distribution of elements. The main elements in the spectrum are Si, Fe and Al, which show a particular geopolymerization reaction and provide a good correlation with the relevant results.

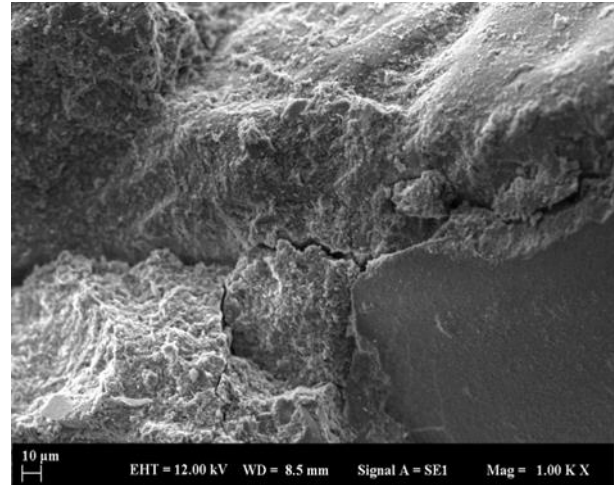
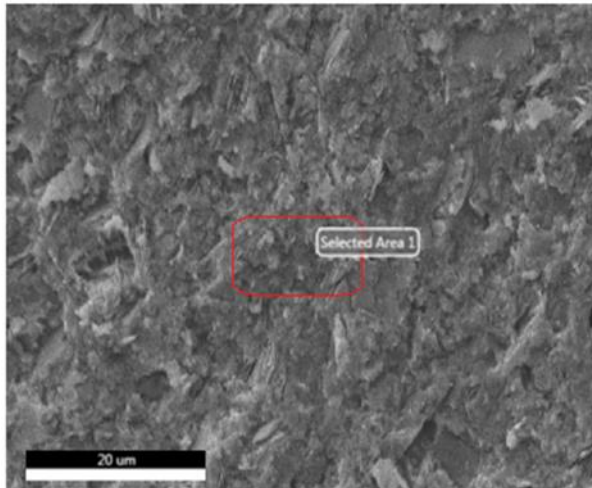


Fig. 15. The 50% BS sample after exposing to magnesium sulfate solution.

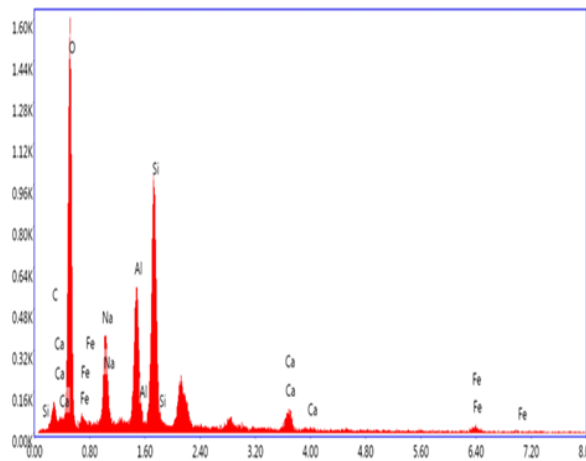


Fig. 13. EDS spectroscopy of the control sample before exposing to sulfate solution

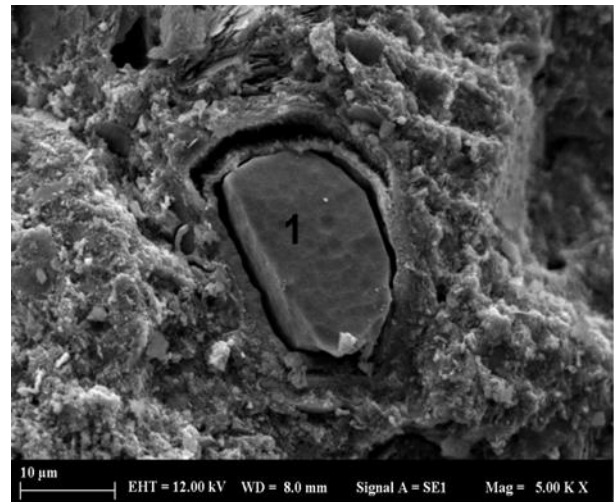


Fig. 16. The 50% LS sample after exposing to magnesium sulfate solution (1: gypsum).

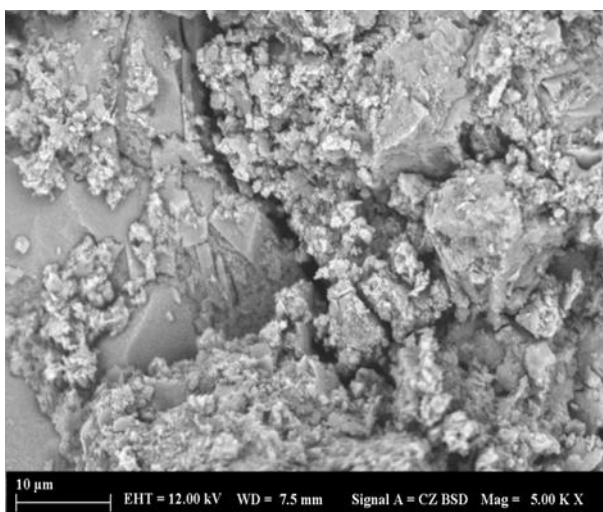


Fig. 14. The control sample after exposing to magnesium sulfate solution.

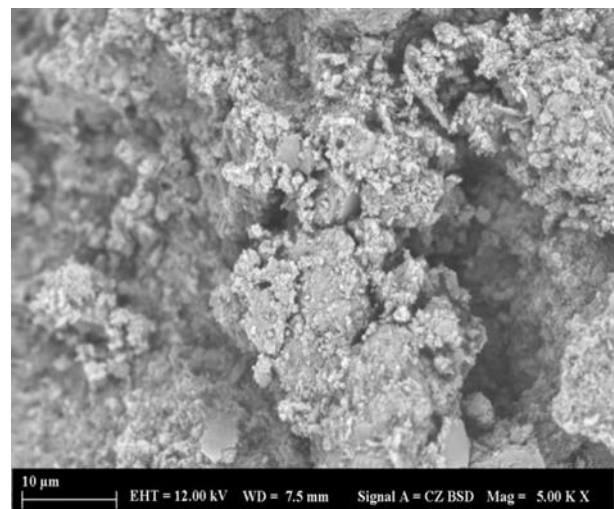


Fig. 17. The 50% LS sample after exposing to sodium sulfate solution.

5. Conclusion

The purpose of this work was to look into the durability, mechanical properties and microstructural composition impact of adding three different types of filler materials limestone, marble, and basalt powder, with the primary binder materials of this study Red-Mud and Metakaolin, based on geopolymer composites under the effect of magnesium and sodium sulfate solutions:

- After exposure to magnesium sulfate the compressive and flexural strengths of samples increase at 60 days then decrease after 120 days, especially limestone and marble powder due to the establishment of gypsum crystals in the geopolymer structure.
- There was no severe damages seen in the control and basalt powder samples due to the lower Ca content which is almost insignificant and the existence of SiO_2 glass content obstructing the chemical reaction with MgSO_4 .
- The replacement of waste filler materials increased the strength properties, especially the basalt powder, with a 75% ratio.
- The MgSO_4 solution attack was more aggressive than Na_2SO_4 , especially for the limestone and marble powder samples due to the reaction of MgSO_4 and Ca which reduce the stability of CSH and poorly alkaline insoluble phase.
- The weight changes increase due to the filled voids with sulfate salts and hydration products under the action of a solution
- About the mechanical properties, there was a considerable increase estimate observing compressive and flexural strength was obtained at 60 days, then a decrease after 120 days. For instance, the 60 days, compressive and flexural strength of basalt powder and control samples, were higher when compared to the marble and limestone powder geopolymer samples.
- About the manufactured geopolymer samples immersed in Na_2SO_4 solutions, it was impossible to recognize the new phases formed because any XRD analysis changes were found.

As an established conclusion growing waste materials, as filler replacing river sand with different ratios, contributed the development of the durability and mechanical properties and microstructural behaviors of the composite, especially basalt powder concerning the control composites. Furthermore, the ratio (50%-50%) metakaolin and red-Mud as a binder material was given good results. Moreover, the mix of Metakaolin and Red-Mud is more durable and able to be used. Finally, the use of Red-Mud and the waste filler materials in manufacturing geopolymers are economical and environmentally friendly.

Acknowledgment

This work was supported by İstanbul Aydın University and the research fund of the Yıldız Technical University-Turkey. The authors would like to express their sincere gratitude to the scientific research coordination unit for their financial support (Project number: FBA-2019-3558).

Author's Contributions

Ouiame Chakkor: Made literature search, prepared the samples used in the experimental work, and wrote the manuscript.

Mehmet Fatih Altan: Supervised the experiment work and analyze the results.

Orhan Canpolat: Edited the revisions, and helped in manuscript preparation.

Ethics

There are no ethical issues after the publication of this manuscript.

References

1. E.E. Hekal, E. Kishar, H. Mostafa, Magnesium sulfate attack on hardened blended cement pastes under different circumstances, *Cement and Concrete Research*, 32 (2002) 1421-1427.
2. M. Santhanam, M.D. Cohen, J. Olek, Mechanism of sulfate attack: a fresh look: Part 2. Proposed mechanisms, *Cement and concrete research*, 33 (2003) 341-346.
3. D. Bonen, M.D. Cohen, Magnesium sulfate attack on Portland cement paste-I. Microstructural analysis, *Cement and concrete research*, 22 (1992) 169-180.
4. D. Bonen, M.D. Cohen, Magnesium sulfate attack on portland cement paste—II. Chemical and mineralogical analyses, *Cement and concrete research*, 22 (1992) 707-718.
5. N.B. Singh, B. Middendorf, Geopolymers as an alternative to Portland cement: An overview, *Construction and Building Materials*, 237 (2020) 117455.
6. N. Singh, B. Middendorf, Geopolymers as an alternative to Portland cement: An overview, *Construction and Building Materials*, 237 (2020) 117455.
7. C. Villa, E.T. Pecina, R. Torres, L. Gómez, Geopolymer synthesis using alkaline activation of natural zeolite, *Construction and Building Materials*, 24 (2010) 2084-2090.
8. B. Singh, G. Ishwarya, M. Gupta, S. Bhattacharyya, Geopolymer concrete: A review of some recent developments, *Construction and building materials*, 85 (2015) 78-90.
9. A. Palomo, M. Grutzeck, M. Blanco, Alkali-activated fly ashes: A cement for the future, *Cement and concrete research*, 29 (1999) 1323-1329.
10. P.K. Mehta, R.W. Burrows, Building durable structures in the 21st century, *Concrete international*, 23 (2001) 57-63.
11. E.M.S. Mulapeer, Strength And Absorption Characteristics Of Fly Ash Based Geopolymer Composite Reinforced With Glass Fiber, Hasan Kalyoncu Üniversitesi, 2016.
12. R. El-Hachem, E. Rozière, F. Grondin, A. Loukili, Multi-criteria analysis of the mechanism of degradation of Portland cement based mortars exposed to external sulphate attack, *Cement and Concrete Research*, 42 (2012) 1327-1335.
13. T. Bakharev, Durability of geopolymer materials in sodium and magnesium sulfate solutions, *Cement and Concrete Research*, 35 (2005) 1233-1246.

14. S. Thokchom, D. Dutta, S. Ghosh, Effect of incorporating silica fume in fly ash geopolymers, *World Academy of Science, Engineering and Technology*, 60 (2011) 243-247.
15. A. Fernández-Jiménez, I. García-Lodeiro, A. Palomo, Durability of alkali-activated fly ash cementitious materials, *Journal of Materials Science*, 42 (2007) 3055-3065.
16. V. Sata, A. Sathonsaowaphak, P. Chindapasirt, Resistance of lignite bottom ash geopolymer mortar to sulfate and sulfuric acid attack, *Cement and Concrete Composites*, 34 (2012) 700-708.
17. R. Martynkova, M. Mavroulidou, Properties of Alkali-Activated Concrete Based On Industrial Wastes Or By Products, *Proceedings of the 14th International conference on Environmental Science and Technology Athens, Greece, 2015*, pp. 3-5.
18. R.I. Iacobescu, G.N. Angelopoulos, P.T. Jones, B. Blanpain, Y. Pontikes, Ladle metallurgy stainless steel slag as a raw material in Ordinary Portland Cement production: a possibility for industrial symbiosis, *Journal of Cleaner Production*, 112 (2016) 872-881.
19. A. ASTM, C348-14 Standard Test Method for Flexural Strength of Hydraulic-Cement Mortars, ASTM Int, West Conshohocken, DOI.
20. K. Scrivener, J.F. Young, *Mechanisms of chemical degradation of cement-based systems*, CRC Press 1997.
21. P.K. Sarker, Bond strength of reinforcing steel embedded in fly ash-based geopolymer concrete, *Materials and structures*, 44 (2011) 1021-1030.
22. F. Puertas, R. Gutierrez, A. Fernández-Jiménez, S. Delvasto, J. Maldonado, Alkaline cement mortars. Chemical resistance to sulfate and seawater attack, *Materiales de Construcción*, 52 (2002) 55-71.
23. I. Ismail, S.A. Bernal, J.L. Provis, S. Hamdan, J.S. van Deventer, Microstructural changes in alkali activated fly ash/slag geopolymers with sulfate exposure, *Materials and structures*, 46 (2013) 361-373.
24. T. Aye, C.T. Oguchi, Resistance of plain and blended cement mortars exposed to severe sulfate attacks, *Construction and Building Materials*, 25 (2011) 2988-2996.
25. N. Rajamane, M. Nataraja, J. Dattatreya, N. Lakshmanan, D. Sabitha, Sulphate resistance and eco-friendliness of geopolymer concretes, *Indian Concrete Journal*, 86 (2012) 13.
26. F. Škvára, T. Jílek, L. Kopecký, Geopolymer materials based on fly ash, *Ceram.-Silik*, 49 (2005) 195-204.
27. S. Thokchom, P. Ghosh, S. Ghosh, Performance of fly ash based geopolymer mortars in sulphate solution, *Journal of engineering science and technology review*, 3 (2010) 36-40.
28. B.A. Salami, M.A.M. Johari, Z.A. Ahmad, M. Maslehuddin, Durability performance of palm oil fuel ash-based engineered alkaline-activated cementitious composite (POFA-EACC) mortar in sulfate environment, *Construction and Building Materials*, 131 (2017) 229-244.
29. F.N. Değirmenci, Effect of sodium silicate to sodium hydroxide ratios on durability of geopolymer mortars containing natural and artificial pozzolans, DOI (2017).
30. H. Manzano, R. González-Teresa, J. Dolado, A. Ayuela, X-ray spectra and theoretical elastic properties of crystalline calcium silicate hydrates: comparison with cement hydrated gels, *Materiales de Construcción*, 60 (2010) 7-19.